Geographisches Institut der Universität Bonn

Influences of Snow Cover on Thermal and Mechanical Processes in steep Permafrost Rock Walls

Dissertation

zur Erlangung des Doktorgrades (Dr. rer. nat.)

der

Mathematisch-Naturwissenschaftlichen Fakultät

der

Rheinischen Friedrich-Wilhelms-Universität Bonn

vorgelegt von

Daniel Draebing

aus

Remagen

Bonn, den 18.07.2014

Angefertigt mit Genehmigung der Mathematisch-Naturwissenschaftlichen Fakultät

der Rheinischen Friedrich-Wilhelms-Universität Bonn

Gutachter: 1. Prof. Dr. R. Dikau

2. Prof. Dr. M. Krautblatter

3. Prof. Dr. L. Schrott

4. PD Dr. G. Welp

Tag der Promotion: 13.11.2014

Erscheinungsjahr: 2015

Comment:

This Ph.D.-thesis was written in accordance with the rules for "Kumulative Dissertationen" issued on the 17th of June, 2011. Text of articles is printed in the original version in British English (Geomorphology, The Cryosphere) or American English (JGR). The following articles have been incorporated in the thesis:

- Draebing, D., Krautblatter, M. and R. Dikau (in review): Interaction of thermal and mechanical processes in steep permafrost rock walls: a conceptual approach. Geomorphology.
- Draebing, D. and M. Krautblatter (2012): P-wave velocity changes in freezing hard low-porosity rocks: a laboratory-based time-average model, The Cryosphere 6, 1163–1174.
- Krautblatter, M. and D. Draebing (2014): Pseudo 3D - P-wave refraction seismic monitoring of permafrost in steep unstable bedrock, Journal of Geophysical Research – Earth Surface 119, 278-299.

Content

1 Abstract

Degradation of rock permafrost can cause instability due to influences on rock- and ice-mechanical properties. Permafrost conditions can be altered by thermal processes and, thus, also mechanical properties of rocks. Snow cover controls the seasonal occurrence of thermal processes.

A conceptual approach is presented to explain snow cover influences on steep permafrost rock walls. This approach combines snow cover with thermal processes, e.g. conductive, convective and advective heat transport, shear strengths and shear forces. On a seasonal scale, two critical time windows of instability can be identified. In the first window in early summer, combined hydrostatic and cryostatic pressure cause a peak in shear force exceeding shear resistance. In the second time window in autumn, shear force increases faster than shear resistance. On a system scale, the system state is important for the understanding of permafrost rock wall stability. The system state can change path-dependent from a rock-mechanical into an ice-mechanical system state, which is more sensitive to seasonal permafrost thaw. Climate change can amplify this impulse, leading to higher magnitudes of active-layer thawing. System stability can be exceeded by internal processes, e.g. weathering processes, or external processes, e.g. active-layer thaw. To support the conceptual approach, empirical data is presented to evaluate snow cover, the thermal and the mechanical regime.

A combination of temperature data loggers and photos of automatic cameras allows the reconstruction of the temporal and spatial development of snow cover. Avalanche probe measurements deliver spatial snow height data at the time of measurement. The four snow stages developed by Luetschg (2005) can be distinguished. Stage IV in autumn or winter 2012 has a cooling effect on the underground. The thin-snow cover enhances ground cooling (Stage I). Prolonged Stage II possesses a cooling influence by preserving cold underground temperatures and delay warming. Stage III is dependent on aspect and is characterized by a zero-curtain effect, occurring for 1-4 weeks on the north-facing slope and for 1-3 months on the south-facing slope of the Steintaelli rock wall. Stage IV in summer 2013 has a warming effect on the subsurface.

In laboratory measurements, p-wave velocities of 22 different alpine rocks are tested and the influence of ice pressure on seismic velocities is evaluated. P-wave velocity increases dependent on lithology due to freezing. Parallel to cleavage/bedding, this increase ranges from 418 ±194 m/s for gneiss to 2290 ±370 m/s for carbonate rocks and. For perpendicular measurements, p-wave velocity

increase is between 414 ±210 m/s for other metamorphic rocks and 2745 ±1444 m/s for carbonate rocks. This increase is dominated by an increase of the velocity of the rock matrix due to ice pressure, which closes cracks and, thus, decreases anisotropy up to 45 %. These results are incorporated into a novel time-average equation based on Timur's (1968) 2-phase equation with a lithology dependent variable to increase the matrix velocity. The findings provide the basis for the applicability of refraction seismics in permafrost rock walls.

In 2006 and 2007, Seismic Refraction Tomography (SRT) was successfully applied in a steep permafrost rock wall in the Steintaelli. Glacier onfreezing, the position of snow accumulations and deep-reaching ice-filled fractures seem to have a systemic and locally dominant impact on spatial and temporal permafrost development. The influence was investigated in more detail in 2012 and 2013 with the use of SRT, Electrical Resistivity Tomography (ERT) and thermal modelling. Air temperature in the summers 2012 and 2013 were comparable, but snow cover differed significantly. Long lasting snow cover in 2013 delayed heat transport processes by insulating the underground and prevented active-layer thaw. Thus, snow cover plays a key role of permafrost evolution on slope facet scale. Topography leads to deeper thawing on south-facing slopes, while blocky material seems to produce a permafrost-favouring microclimate on the toe of NE-slope.

Inter-annual extensometer measurements show divergent and convergent displacements. Intra-annual extensometer rates are one to two magnitudes higher than inter-annual rates, suggesting a short-term displacement in summer. Active-layer thaw and freezing are potential causes of displacement and seasonally change of rock stability. Snow cover is the main controlling factor of discontinuity movement and rock decay. The snow cover controls the occurrence of thermal expansion/contraction and volumetric expansion as it prevents these processes, while favouring ice segregation due to isolation. Volumetric expansion increases short-term cryostatic pressure, whereas ice segregation leads to seasonal cryostatic pressure. Active-layer thaw decreases shear strengths during summer and increases instability seasonally.

Crackmeter data confirms the critical time window in autumn. Five crackmeters show sudden opening of discontinuities due to volumetric expansion with coincident thermal contraction. The second time window during early summer snow melt cannot be confirmed but was observed at Jettan rockslide in Norway by Blikra and Christiansen (2014). Based on stability analysis without including ice or permafrost, the Steintaelli rock wall should be stable and currently in phase I (stable rock, no warming). Inter-annual discontinuity movements are small but significant, indicating that the rock wall moved into phase II (warming, fracture opening). Ice segregation can crack rock bridges and can change the system status from rock-mechanical to more sensitive ice-mechanical status. Climate change can increase active-layer thaw depth, and, thus, seasonal sensitivity to rock wall failure. Path-dependent system change and increased seasonal thawing both will increase sensitivity to instability in the future. The conceptual approach explains rock stability on seasonal and system scale. Therefore, this study delivers the basis in the understanding of stability of permafrost rock walls.

2 Zusammenfassung

Die Degradation von Fels-Permafrost kann durch den Einfluss auf fels- und eismechanische Eigenschaften Felsinstabilität verursachen. Thermale Prozesse können die Permafrost-Bedingungen verändern und dadurch auch die mechanischen Eigenschaften von Felsen. Die Schneedecke kontrolliert das saisonale Auftreten dieser thermalen Prozesse.

Ein konzeptioneller Ansatz wird vorgestellt, um den Einfluss der Schneedecke auf steile Permafrost-Felswände zu erklären. Dieser Ansatz kombiniert die Schneedecke mit thermalen Prozessen, wie beispielsweise konduktivem, konvektivem sowie advektivem Wärmetransport, Scherfestigkeiten und Scherkräften. Auf saisonaler Skale können zwei kritische Zeitfenster der Instabilität identifiziert werden. Im ersten Zeitfenster im Frühsommer verursacht die Kombination von hydrostatischen und kryostatischen Druck einen Scherkrafthöchststand, der die Scherfestigkeit übersteigt. Im zweiten Zeitfenster im Herbst steigt die Scherkraft stärker an als die Scherfestigkeit. Auf Systemskale ist der Systemstatus wichtig zum Verständnis der Fels-Permafrost-Stabilität. Der Systemzustand kann sich pfadabhängig von einem felsmechanischen in einen eismechanischen Systemzustand verändern, der sensitiver gegenüber saisonalem Permafrost-Auftauen ist. Klimawandel kann diese Impulse verstärken und zu verstärktem Auftauen der Auftauschicht führen. Die Stabilität des Systems kann durch interne Prozesse wie exemplarisch Verwitterungsprozesse oder durch externe Prozesse wie beispielweise das Auftauen der Auftauschicht überschritten werden. Um den konzeptionellen Ansatz zu belegen, werden empirische Daten zur Schneebedeckung, zum thermalen und mechanischen Regime ausgewertet.

Die Kombination von Temperaturdatenloggern und automatischen Kamerafotos ermöglicht die Rekonstruktion der zeitlichen und räumlichen Schneedeckenentwicklung. Lawinensonden-Messungen liefern räumliche Schneehöhendaten zum Messzeitpunkt. Die vier Schneephasen nach Luetschg (2005) können unterschieden werden. Phase IV im Herbst oder Winter 2012 hat einen kühlenden Effekt auf den Untergrund. Die dünne Schneedecke ermöglicht eine verstärkte Auskühlung des Untergrundes (Schneestadium I). Das lang anhaltende Schneestadium II besitzt einen kühlenden Einfluss durch den Erhalt kalter Untergrundtemperaturen und der zeitlichen Verzögerung der Erwärmung des Untergrundes. Schneestadium III ist expositions-abhängig und charakterisiert durch einen 1-4 Wochen auf dem nordexponierten Hang sowie 1-3 Monate auf dem südexponierten Hang auftretenden „zero-curtain“-Effekt. Schneestadium IV im Sommer 2013 hat einen wärmenden Einfluss auf den Untergrund.

In Labormessungen wurden P-Wellengeschwindigkeiten an 22 alpinen Felsproben getestet und der Einfluss des Eisdrucks auf seismische Geschwindigkeiten evaluiert. P-Wellengeschwindigkeiten steigen in Abhängigkeit der Lithologie durch Gefrieren. Dieser Anstieg reicht von 418 ±194 m/s bei Gneis bis zu 2290 ±370 m/s bei Kalksteinen, gemessen parallel zur Schieferung/Schichtung. Bei perpendikularen Messungen wurde ein P-Wellengeschwindigkeitsanstieg zwischen 414 ±210 m/s bei metamorphen Gesteinen und 2745 ±1444 m/s bei Kalkgesteinen festgestellt. Dieser Anstieg wird dominiert durch einen vom Eisdruck verursachten Anstieg der Felsmatrixgeschwindigkeit, der zum Schließen von Rissen führt, was wiederum eine Abnahme der Anisotropie in Höhe von 45% verursacht. Die Ergebnisse sind in eine neue Durchschnittszeit-Gleichung basierend auf Timur‘s (1968) 2-Phasen-Gleichung mit einer Lithologie-abhängigen Variable zur Anhebung der Matrixgeschwindigkeit eingeflossen. Die Erkenntnisse stellen die Basis für die Anwendung der Refraktionsseismik in Permafrost-Felswänden dar.

In 2006 und 2007 wurde die Refraktionsseismik-Tomographie (SRT) erfolgreich in einer steilen Permafrost-Felswand im Steintälli angewendet. Das Anfrieren von Gletschereis, die Position von Schneeablagerungen und tiefreichende eisgefüllte Klüfte scheinen eine systematische und lokal dominante Auswirkung auf die räumliche und zeitliche Permafrost-Entwicklung zu haben. Der Einfluss wurde detaillierter in 2012 und 2013 mit Hilfe von SRT, elektrischer Widerstandstomographie (ERT) und thermaler Modellierung untersucht. Lufttemperaturen in den Sommern 2012 und 2013 waren durchaus vergleichbar, jedoch unterschied sich die Schneedecke signifikant. Lang anhaltende Schneebedeckung in 2013 verzögerte Wärmetransportprozesse durch Isolierung des Untergrundes und verhinderte das Auftauen der Auftauschicht. Die Schneedecke spielt folglich eine Schlüsselrolle in der Entwicklung des Permafrostes auf der Hang-Fazies-Skale. Topographie führte zu einem tieferen Auftauen südexponierter Hänge. Blockiges Material scheint ein Permafrost begünstigendes Mikroklima an den Hangfüßen nordost-exponierter Hänge zu verursachen.

Zwischenjährliche Extensometer-Messungen zeigen divergente und konvergente Bewegungen. Innerjährliche Extensometer-Raten sind ein bis zwei Magnituden größer als zwischenjährliche Raten und suggerieren das Auftreten von kurzfristigem Versatz im Sommer. Crackmeter bestätigen dieses kurzzeitige Auftreten. Auftauen und Gefrieren der Auftauschicht sind potentielle Ursachen für diesen Versatz und verändern saisonal die Felsstabilität. Die Schneedecke ist der Hauptkontrollfaktor von Trennflächenbewegungen und Felszersatz und kontrolliert das Auftreten thermaler Expansion/Kontraktion sowie Volumenexpansion. Sie verhindert diese Prozesse, während die Eissegregation durch die Isolierungswirkung des Schnees begünstigt wird. Volumenexpansion führt zum kurzfristigen Anstieg kryostatischen Drucks, wohingegen die Eissegregation zu einem saisonalem kryostatischen Druckanstieg führt. Das Auftauen der Auftauschicht verringert die Scherfestigkeiten im Sommer und verursacht saisonal Instabilität.

Crackmeter-Daten bestätigen das kritische Zeitfenster im Herbst. Fünf Crackmeter zeigen eine plötzliche Trennflächenöffnung, verursacht durch Volumenexpansion mit gleichzeitig auftretender thermaler Kontraktion. Das zweite Zeitfenster während der frühsommerlichen Schneeschmelze kann nicht bestätigt werden, wurde allerdings von Blikra und Christiansen (2014) an der Jettan-Hangrutschung beobachtet. Basierend auf Stabilitätsanalysen, ohne Eis oder Permafrost einzuschließen, sollte die Felswand im Steintälli stabil sein und sich in Phase I (stabiler Fels, keine Erwärmung) befinden. Zwischenjährliche Diskontinuitätsbewegungen sind klein, jedoch signifikant und indizieren eine Bewegung der Felswand hin zu Phase II (Erwärmung, Kluftöffnen). Eissegregation kann Felsbrücken zerstören und den Systemstatus von einem felsmechanischen zu einem sensitiveren eismechanischen Status verändern. Der Klimawandel kann die Auftautiefe der Auftauschicht erhöhen und dadurch die saisonale Sensitivität gegenüber Felswand-Versagen erhöhen. Pfadabhängige Systemwechsel und ansteigendes saisonales Auftauen erhöhen beide zukünftig die Sensitivität gegenüber Instabilität. Der konzeptionelle Ansatz erklärt Felsstabilität auf saisonaler wie auch Systemskale. Diese Studie liefert damit die Grundlage zum Verständnis der Felsstabilität in Permafrost-Felswänden.

3 Introduction

Thermal influences on rock instability is supported by high regional rock fall activity in warmer decades (Fischer, 2010; Ravanel and Deline, 2010) or in extreme warm seasons like summer 2003 (Gruber et al., 2004a). Observations of ice in rock fall accumulations or rock scarps indicate that permafrost is involved in this process (Dramis et al., 1995; Pirulli, 2009; Fischer et al., 2010; Ravanel and Deline, 2010; Kenner et al., 2011). A lot of case studies focus on permafrost involvement in rock-ice avalanches in the volume range of bergsturz (>1 x10^7 m³) or cliff fall (10^4-10^6 m³) events, e.g. at Mt. Stellar, Alaska 2005 (Huggel et al., 2008), Monte Rosa, Italian Alps 2005 (Fischer et al., 2006), Dzimarai-Khokh, Russian Caucasus 2002 (Haeberli et al., 2004; Huggel et al., 2005), Mt. Steele, Yukon 2007 (Lipovsky et al., 2008), Harold Prince, British Columbia 2002 (Geertsema et al., 2006), Brenva, Italian Alps 1997 (Bottino et al., 2002) and Punta Thurwieser, Italian Alps 2004 (Sosio et al., 2008). Some studies show a high activity of cliff falls (10^4-10^6 m³), block falls (10^2-10^4 m³), boulder falls (10^1-10^2 m³) and debris falls (<10 m³) in permafrost rock walls (Fischer et al., 2007; Krautblatter and Dikau, 2007; Rabatel et al., 2008; Ravanel and Deline, 2008; Deline, 2009; Ravanel et al., 2010; Ravanel and Deline, 2010).

The frequency and magnitude of rockfalls from permafrost–affected rock walls seem to increase and Huggel et al. (2012) argued the responsibility of climate change. According to Gobiet et al. (in press) and based on the A1B emission scenario, climate change lead to a 0.25°C warming per decade until the mid of the 21st century for the European Alps. For the second half of the century, warming will accelerate by 0.36°C per decade (Gobiet et al., in press). Additionally, the frequency of short term warm air temperature extreme events will increase (Huggel et al., 2010; Marmy et al., 2013). The heat summer 2003 is considered as the trigger for enhanced rockfall from permafrost-affected rock walls due to exceeding of maximum active-layer thaw depths (Gruber et al., 2004a). Salzmann et al. (2007) downscaled Regional Climate Models (RCM) to model future development of permafrost in rock walls. They argue that duration and thickness of snow will probably be the most important factor influencing the thermal regime. Snow is a form of precipitation and snow cover will change as a result of climate change. At higher elevations in mountains, the precipitation will decrease in summer and increase in winter (Gobiet et al., in press). Additionally, the threshold deciding about rain or snow is currently at 1400 ±200 m, but the threshold altitude will increase due to climate change (Morán-Tejeda et al., 2013). Precipitation will shift to higher elevations and the snow season will shorten (Bavay et al., 2009).

Several authors modelled the effects of this changed snow season and temperature increase by climate change on underground temperatures for rock glaciers and debris-covered rock slopes (Luetschg and Haeberli, 2005; Luetschg et al., 2008; Engelhard et al., 2010; Marmy et al., 2013; Scherler et al., 2013). Climate change will increase the snow cover but not prolong the snow cover duration (Marmy et al., 2013). An increased snow height during warm periods can produce a critical input of water due to more snow melt, which can result in an increased advective heat transfer and an increased hydrostatic pressure (Huggel et al., 2010; Marmy et al., 2013). The shortening of the snow season results in an earlier active-layer thaw, a longer snow-free period and increased active-layer thaw depths (Luetschg et al., 2008). At the debris-covered rock slope of Schilthorn and Murtèl rock glacier, Scherler et al. (2013) distinguished two phases of climate sensitivity. In the first phase, the slow warming of the permafrost body will result in a slight increase of active-layer thaw depth, combined with an absence of complete freezing in winter. In the second phase, permafrost will degrade gradually and active-layer depth will strongly increase. Due to lower porosities and lower ice content, the sensitivity of rock permafrost to climate change is higher than permafrost in debris-covered slopes or rock glaciers.

This is relevant as degradation of rock permafrost can endanger infrastructure and can cause casualties due to both rockfall activity and slow rock deformation. Therefore, it has to be considered as a major hazard. However, high-alpine regions are extensively used for recreational subject like tourism-related sports in winter and summer (Messerli, 2006) and hydro-power generation and water storage, without considering hazards from thawing permafrost (Haeberli et al., 1997).

Unfortunately, there is little knowledge “why permafrost rocks become unstable”. This question was asked and mechanically answered by Krautblatter et al. (2013). Their work presents the mechanical basis of this thesis and explains, why warming results in instability of rock walls. Krautblatter et al. (2013) identified critical fracture toughness K_C, the uniaxial compressive strength σ_u, the temperature of ice at failure T_C and the temperature of ice T_K as sensitive to warming. Until to today, warming is mostly explained by conductive heat transport, which is included in process-based permafrost models e.g. TEBAL or COMSOL (Gruber et al., 2004b; Noetzli et al., 2007). However, other heat transport processes like advective or convective heat transfer could be identified in rock walls (Krautblatter, 2010; Hasler et al., 2011b). Unfortunately, little knowledge exists, how advection works in rock walls. Gruber & Haeberli (2007) argue that the effect of advection in rock walls is an important unknown due to earlier and faster propagation of advective thawing along fractures.

Convective and advective heat transport work along discontinuities, while conductive heat is transported along the intact rock. The differentiation between intact rock and discontinuities is the fundamental basis of rock mechanics, thus, the idea of this thesis is to combine mechanical and thermal regime in a conceptual approach. Snow cover is assumed to be the most important factor of the thermal regime (Salzmann et al., 2007) on one hand, and on the other hand a source of meltwater influencing rock stability due to hydrostatic pressure increase. As a consequence, snow cover is included in the conceptual approach of this thesis. This approach is introduced in Chapter 5.3 after a short review of fundamental thermal (Chapter 5.1) and mechanical (Chapter 5.2) processes and properties. Hypotheses are derived from the conceptual approach and are presented in Chapter 6. The study site is not described in an individual chapter and will be introduced in the following chapters if information is necessary for the understanding of the thesis.

In Chapter 7, methods to investigate snow cover are introduced; data results are presented and discussed. The methods using seismic velocities are important methods in both permafrost and stability studies. Influences of permafrost on rocks are tested in the laboratory (Chapter 8.2) and findings are transferred to field conditions in the Steintaelli (Chapter 8.3). Seismic methods are combined with geoelectrical measurement and thermal modelling techniques to describe the thermal regime of Steintaelli rock wall in 2012 and 2013 (Chapter 8.4). Response of the mechanical regime to thermal forcing is divided in inter-annual dynamics of discontinuity movements (Chapter 9.2), intra-annual dynamics of discontinuity movements (Chapter 9.3) and seasonal dynamics of rock decay (Chapter 9.4). The hypotheses are discussed in a synoptic way (Chapter 10) before the thesis is concluded (Chapter 11).

4 Scales and scale effects

4.1 Introduction

Scales contain a spatial and temporal aspect (de Boer, 1992). The implications of scales for geomorphology are described in the fundamental work of Schumm and Lichty (1965), by Brunsden and Thornes (1979) or more recently by Church (1996). Geomorphic systems are nested and hierarchal organized, thus, they contain smaller systems and are at the same time parts of larger systems (de Boer, 1992). The hierarchy concept was founded originally in ecology (O'Neill et al., 1986) and is transferable from biologic to geomorphic systems according to Graf (1988). On each level of hierarchy, different properties and variables can be defined. The higher level consists of the sum of components of the next lower level. There are additionally new processes and structures of form that cannot be derived from the lower level (Dikau, 2006). These objects and properties are emergent (Dikau, 2006) and prohibit simple upscaling approaches. Harrison (2001) gives a comprehensive overview of emergence in geomorphology.

Therefore geomorphic systems are scale dependent (Phillips, 1999). Transferred to the Steintaelli, the following levels of hierarchy are of interest (Fig. 4.1).

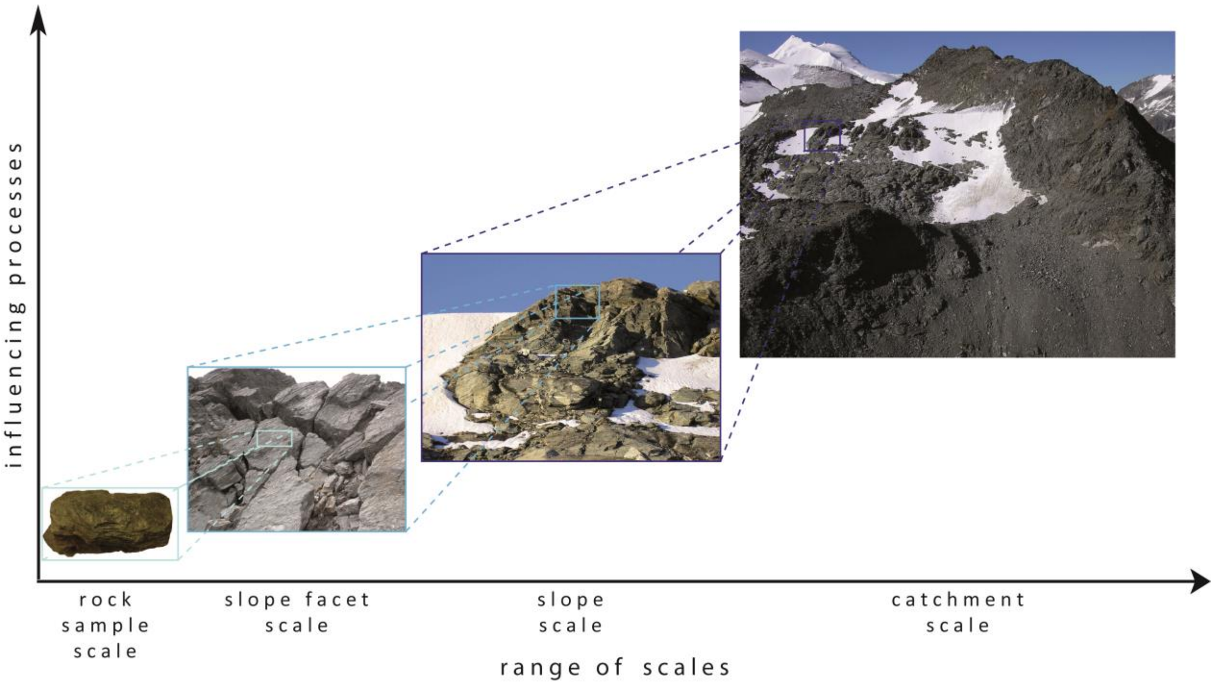

Fig. 4.1 Levels of hierarchy exemplary from Steintaelli. The number of influencing processes increases with enlargement of scale within the hierarchy.

4.2 Scales and hierarchy in the Steintaelli

For the different levels, the following properties and variables can be distinguished:

- Rock sample scale: material properties (lithology, hydrological, thermal, mechanical), micro fissures.
- Slope facet scale: sum of properties/variables at rock sample scales, plus: form of discontinuities.
- Slope scale: sum of properties/variables of all slope facets, plus: slope morphology and topography (aspect), hydrology, downward movement of snow and rocks.
- Catchment scale: sum of all slope scale properties/variables, plus: storage effects, connectivity, network paths.

On the rock sample scale, material properties like lithological, hydrological, thermal and mechanical properties are important and control processes. Rocks consist of mineral grains, pores and micro fissures. Pore infill and connectivity determine the hydrological properties of rocks such as saturation. Minerals determine mechanical properties like rock strength (Edelbro, 2003). Combined minerals and pores influence thermal conductivity of rocks. In addition, on the slope facet scale, discontinuities are an expression of change in the rock mass (Hencher, 1987). Discontinuities represent preferred paths of advective or convective heat transport (Dietrich et al., 2005) and influence the thermal regime (Gruber and Haeberli, 2007). Due to mechanical properties, discontinuities control rock wall stability at slope facet scale.

On the slope scale, in addition to slope facet processes transport between slope facets occurs. Snow can be redistributed upslope by wind or downslope by avalanches. Debris or blocks can be transported slope downslope due to gravitative processes. Connectivity between slope facets is an important factor. On the catchment scale, in addition to slope scale processes, climate conditions and glacial conditions influence the processes. For example, glacial recession can influence rock wall stability due to debuttressing (McColl, 2012). Climate change can influence snow distribution and thermal forcing.

4.3 Measurement approaches at the Steintaelli

Different methods or techniques enable the measurement of properties and variables on different levels of hierarchy. To interpret the collected data, it is always necessary to consider the observed level. Simple upscaling approaches are impossible due to emergent features. The methods or techniques to measure snow cover, thermal and mechanical properties of rock walls are presented in the following schematic image (Fig. 4.2). In the following chapter, the methods are described from rock sample scale up to catchment scale.

Snow height is measured discontinuously using avalanche probes. Avalanche probe measurements are point measurements at rock sample scale limited to snow height lower than 2.25 m due to probe length. The simplicity and the low time-consumption allow the sampling of a high number of snow height measurements. This high number of heights and the spatial distribution of the sampled points incorporate the spatial variability and allow upscaling (bottom-up) by using interpolation techniques (kriging) to achieve snow height distribution. Snow cameras continuously take photos of the catchment area. Photo analysis allows differentiating snow-covered and non-snow-covered areas.

Ground Surface Temperature (GST) measurements using data loggers are a low-cost technique and provide continuous information at rock sample scale. By using a diffusivity model, temperature can be extended to higher depths. However, this also includes uncertainties due to assumptions and processes, like advective or convective heat transport, which are not incorporated in the model. Standard deviation of rock surface temperature (RST) is used to evaluate existence of snow cover due to isolating properties of snow, which switch-off diurnal variations of RST.

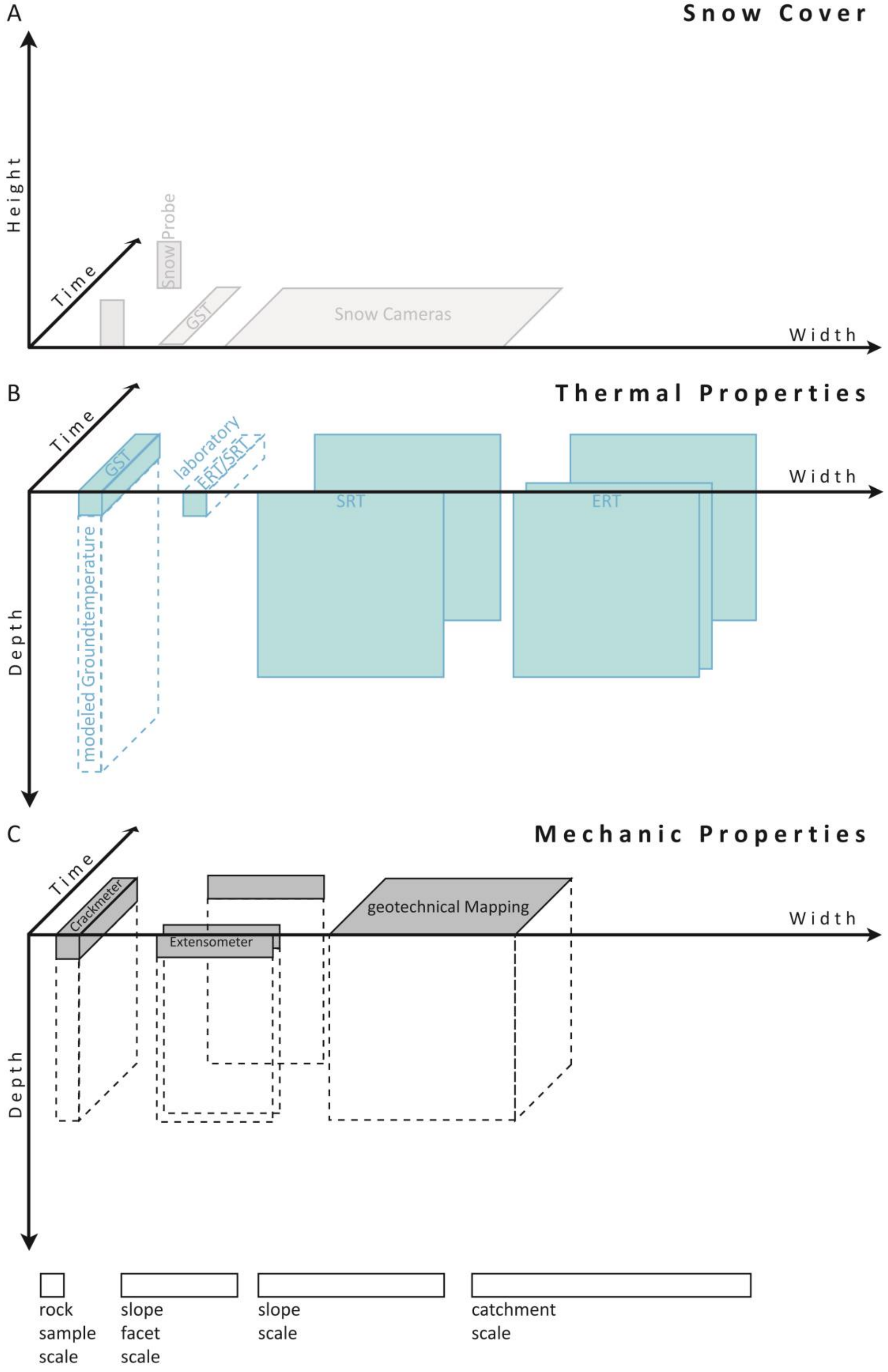

Fig. 4.2 Schematic illustration of methods to measure (A) snow cover, (B) thermal and (C) mechanical properties and their temporal and spatial (depth and width) distribution.

Geophysical methods provide only indirect information about the subsurface thermal regime, but in 2D/3D on a slope scale. Calibration on sample scale by laboratory measurements, where thermal properties can be controlled, is necessary to distinguish frozen and unfrozen rock. Simple upscaling of laboratory results to field conditions is difficult. Scenario building for seismic measurement is exemplarily presented by Krautblatter and Draebing (2014). Scenarios incorporate the additional properties arising from transfer to higher level of hierarchy. They comprehend uncertainties and give an upper and lower limit of property. Automatic Electric Resistivity Tomography allows continuous monitoring on a slope scale.

A crackmeter continuously measures dilation and shortening of one discontinuity and rock surface temperature. Measurements are restricted on short distances of maximum of the crackmeter length. The result is information on rock sample scale; by distributing crackmeters on a rock wall we receive a result on a slope scale. Extensometer measurements enable a low-cost method to evaluate rock wall kinematics. The measurements are conducted manually once a year before maximum thawing and once at thawing. Extensometers provide data on a slope facet scale. The measurement integrates several discontinuities. Spatial distribution of extensometers enables interpretation on a slope scale. Geotechnical mapping evaluating rock mass stability by using GSI (Hoek and Brown, 1997) and discontinuity stability by using scanline measurements (Priest, 1993) allow stability interpretation on a slope scale.

5 The permafrost rock system

For the first time, Krautblatter (2009) investigated the thermal, hydrologic and mechanical properties of permafrost-affected rock walls and their interaction and included his findings in a geomorphic system view. Constituted on this approach, the effects of snow and interactions are considered in the following chapter.

5.1. Thermal regime

5.1.1 Permafrost

Permafrost is defined as a thermal condition below 0°C of underground material for at least two consecutive years (NRC-Permafrost-Subcommitee, 1988; Muller, 2008) or one year (Hoelzle, 1994). Permafrost does not contain ice per definition. Especially in rocks, equilibrium freezing point depressions occur caused by solutes, pressure, pore diameter or pore material (Lock, 2005). Freezing point depression can lead to unfrozen water content and unfrozen water can exist in supercooled form in rocks at temperatures of up to -10°C (Mellor, 1970). Here, the term supercooled refers to the range between the equilibrium and the spontaneous freezing point. Water or moisture may or may not be present so French (2007) suggests to differentiate permafrost between temperature (thermal) and status (frozen or unfrozen). He further introduces the terms cryotic and non-cryotic for status differentiation. Thermal conditions below 0°C with no or little ice are called dry permafrost existing particularly in Antarctica (French, 2007). In this thesis, permafrost refers to a frozen underground material below 0°C because the existence of ice plays a significant role for the mechanical behaviour.

Permafrost is horizontally limited by the permafrost table and permafrost base (Fig. 5.1). The upper boundary, the permafrost table, delimits the permafrost from the active-layer. The permafrost is perennially frozen while the active-layer thaws seasonally. The lower boundary, the permafrost base, represents the border between permafrost and unfrozen ground. If the active-layer increases or the permafrost base ascends, exemplarily caused by climate change, permafrost degrades.

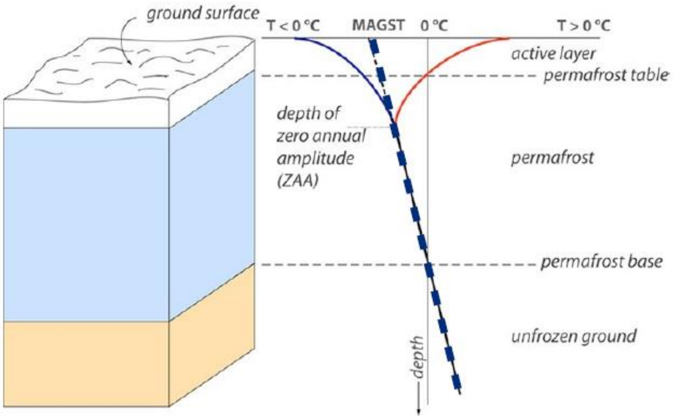

Fig. 5.1 Schematic illustration of a permafrost body (Noetzli and Gruber, 2012).

Permafrost can be further classified according to extent as continuous (90-100 %), discontinuous (50-90 %), sporadic (10-50 %) or isolated (0-10 %) (French, 2007). Alpine permafrost is controlled by climate but also by steep slopes which alter solar radiation, aspect and snow (French, 2007). It is distinguished from latitudinal (polar) and plateau permafrost.

Permafrost is investigated on different temporal and spatial scales. If the active-layer thaw is the focus, the temporal scale is one year and the following components of the energy balance should be investigated in the same time range. Dynamic reactions to altered environmental conditions as climate change operate with fast response times for permafrost degradation at the permafrost table and longer response times for permafrost degradation at the permafrost base (Hoelzle, 1994). The reaction at the permafrost base depends on thermal conductivity and permafrost thickness (Osterkamp, 1983).

Oke (1987) classified spatial scales for energy and mass exchanges:

Micro-scale 10^{-2} to 10^{3} m

Local scale 10^{2} to 5×10^{4} m

Meso-scale 10^{4} to 2×10^{5} m

Macro-scale 10^{5} to 10^{8} m

Hoelzle (1994) advises to use these scales for permafrost modelling. From a geomorphological point of view, landforms size and extent will determine spatial and also temporal scales (Brunsden, 1996; Dikau, 1996). The rock wall in the Steintaelli is in the climatological micro-scale class (10^{-2} – 10^{3} m) but in the geomorphologically meso-scale class (10^{2} - 10^{3} m).

5.1.2 Energy balance and net radiation

The thermal regime of the surface is regulated by heat and mass exchange processes. The ground surface temperature (GST) is determined by the following components of the energy balance (Hoelzle, 1994):

$$Q_R \pm Q_H \pm Q_{LE} \pm Q_G \pm Q_M = 0 \qquad (5.1)$$

where Q_R is the net radiation, Q_H is the sensible heat flux, Q_{LE} is the latent heat flux in the underground, Q_G is the ground thermal heat flux and Q_M is the energy stored in the snowpack or used in the process of fusion. The sensible heat flux displays energy exchange between ground surface and atmosphere resulting from temperature differences. If atmosphere is warmer than ground surface, then sensible heat flux is positive. Warmer ground surface than atmosphere temperatures result in a negative sensible heat flux, respectively. Latent heat is released by evaporation or melting processes while negative Q_{LE} are observable during condensation. The heat for snowmelt Q_M is positive during melting of snow or ice and negative during refreezing. The ground thermal heat flux Q_G determines the heat transport in the ground. All components of the energy balance (Fig. 5.2) affect the thermal regime of the underground and, thus, the ground temperature.

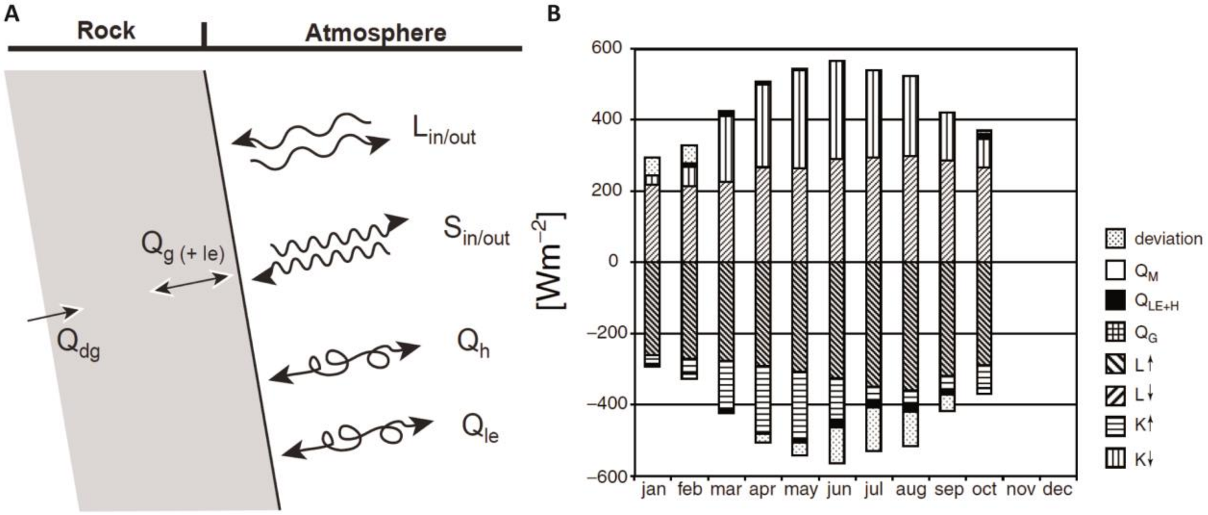

Fig. 5.2 A: Schematic illustration of energy balance components in a snow-free steep rock wall (Gruber, 2005); B: Comparison of all energy balance components for 1998 measured at the Murtèl rock glacier (Mittaz et al., 2000); $S_{in}/K^{\downarrow}$, $S_{out}/K^{\uparrow}$ is short-wave incoming and reflected radiation; $L_{in}/L^{\downarrow}$, $L_{out}/L^{\uparrow}$, long-wave incoming and outgoing radiation; Q_h/Q_H, Q_{le}/Q_{LE}, sensible and latent heat flux; Q_M, snowmelt energy; Q_g/Q_G, ground heat flux, Q_{dg}, geothermal ground heat flux .

The net radiation is composed by the short-wave radiation and the long-wave radiation balance:

$$Q_R = S_{in}(1-\propto) + L_{in-}L_{out} \tag{5.2}$$

where S_{in} is the incoming short-wave radiation, α is the surface albedo, L_{in} is the incoming long-wave radiation and L_{out} is the long-wave emission.

The incoming short-wave radiation S_{in} is a sum of direct irradiance and diffuse irradiance and strongly dependent on azimuth and zenith angle of the sun in proportion to the horizon, cloud cover and optical thickness of the atmosphere (Hoelzle, 1994). Direct irradiance depends on sunshine duration, aspect, angle and horizon and is, thus, highly variable in time and space (Hoelzle, 1994). Diffuse irradiance results from scattering due to atmospheric as well as surface properties (albedo) and lies between 10% (cloud-free conditions) and 100% (cloudy) of total S_{in} (Hoelzle, 1994). Topography in combination with aspect leads to spatial variation of radiation and, thus, to energy balance differences (Oke, 1987).

Outgoing short-wave radiation (S_{out}) depends on albedo of the surface. Albedo is the proportion between S_{in} and reflected radiation and depends on material and surface roughness. Rock surfaces possess an albedo in the range of exemplary 0.12 for basalt or sandstone), 0.18 for granite and 0.25 for chalk (McGreevy, 1985) while snow albedo ranges from 0.60 for wet up to 0.85-0.90 for fresh snow (Zhang, 2005). The differences of albedo and changing snow and ice conditions result in a highly temporal and spatial variability of S_{out}.

Incoming long-wave radiation emitted by the atmosphere depends on temperature of atmospheric air layers and their emissivity. It is described by Stefan-Boltzmann-Law:

$$L_{in} = \varepsilon_L \sigma T_L^4 \tag{5.3}$$

where ε_L is the emissivity of atmospheric air layer, σ is the Stefan-Boltzmann constant and T_L is the temperature of an atmospheric air layer. The incoming long-wave radiation depends on large-scale atmospheric conditions, varies little during the year and decreases with increasing altitude (Hoelzle, 1994).

Outgoing long-wave radiation can be described by:

$$L_{out} = \varepsilon_S \sigma T_S^4 \tag{5.4}$$

where ε_S is the emissivity of the surface and T_S is the temperature of the surface, respectively. Emissivity is dependent on material and surface roughness. Emissivity of rocks ranges from 0.45

(granite) to 0.90 (limestone) (Krautblatter, 2009) while emissivity of snow lies between 0.96 to 0.99 and snow acts almost as a "black body" (Zhang, 2005). Higher emissivity implies higher absorptivity that means snow surfaces absorb more energy than other surface conditions (Zhang, 2005). Temporal snow cover changes and spatial heterogeneity of material results in a mean temporal and spatial variability of L_{out}.

5.1.3 Sensible and latent heat fluxes

The sensible heat can be described as

$$Q_H = -\rho_a \, c_a K_H \left(\frac{\delta T}{\delta z}\right) \tag{5.5}$$

where ρ_a is the density of air, c_a is the heat capacity of air, K_H is the turbulent transport coefficient, $\delta T/\delta z$ is the temperature gradient. The turbulent transport depends on wind velocity, surface roughness and the difference between atmospheric and ground temperature (Hoelzle, 1994). This process tries to minimize these temperature differences.

The latent heat flux can be expressed as

$$Q_L = -\rho_a \, L_V K_V \left(\frac{\delta e}{\delta z}\right) \tag{5.6}$$

where L_V is the heat of evaporation, K_V is the turbulent transport coefficient, $\delta e/\delta z$ is the water vapour pressure gradient. Evaporation can result in cooling of the surface depending on heat balance and water content of the surface. Hoelzle (1994) states that latent heat fluxes are negligible because of fast run-off due to high topography in alpine environments.

5.1.4 Melting heat flux and snow cover as a term in the energy-balance

Snow cover can be regarded as snow pack with a surface, a base and a certain thickness. The physical properties of snow acting at the surface are described above. Snow cover is a porous medium consisting primarily of ice and air. These components determine the thermal conductivity of snow. Pure ice at 0°C has a thermal conductivity of 2.24 W m^{-1} K^{-1} and a density of 917 kg m^{-3} while the thermal conductivity of air is only 0.025 W m^{-1} K^{-1} with a density of 1.2 kg m^{-3} (Zhang, 2005). The thermal conductivity of snow ranges from 0.10 W m^{-1} K^{-1} (fresh snow) to 0.5 W m^{-1} K^{-1} (ripened snow)

(Zhang, 2005). Low thermal conductivity of snow causes excellent insulator properties. Thermal conductivity strongly depends on density (Fig. 5.3 A) but also grain size type, bonding and temperature can lead to range of thermal conductivity at equal densities (Phillips, 2000). The relationship between density and conductivity is caused by the pre-existing relationship between density and microstructure (Sturm et al., 1997). Densification by settling and snow metamorphosis leading to fluctuations of conductivity and, thus, fluctuations of insulation (Lehning, 2005). Ice has a heat capacity of 2.1 J g^{-1} K^{-1} and the latent heat fusion is about 334 J g^{-1}. To melt ice, an immense amount of latent heat is necessary; therefore, snow melt is a heat sink. Refreezing of meltwater releases the same amount of latent heat and warms the snow pack. The consummation or release of latent heat results in an isothermal state, the temperature remains at 0°C, thus, this effect is called zero-curtain effect.

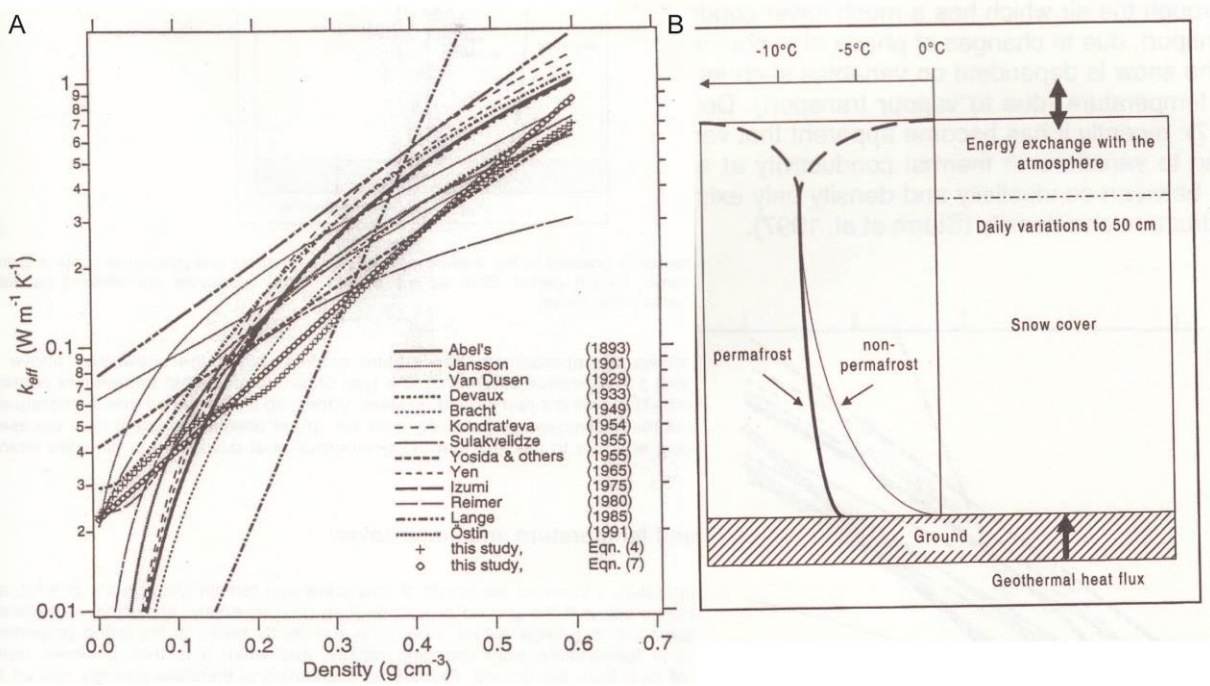

Fig. 5.3 A: Regression equations of thermal conductivity of snow versus snow density (Sturm et al., 1997); B: Schematic temperature gradient in the snow cover over non-permafrost and permafrost ground at the winter cooling period (Phillips, 2000).

5.1.5 Snow cover and the interaction between permafrost and snow cover

Additionally to internal snow pack changes, external factors influence differences of snow distribution in space and time. The spatial distribution of snow is highly variable on rock walls. Wind processes and slope morphometry interact and in combination they influence snow cover variability of the rock walls (Wirz et al., 2011). Snow cover depends on slope morphometry and roughness of the underground's surface while aspect and wind alter snow cover distribution (Phillips, 2000). Schmidt (2009) showed that morphometric factors influence snow distribution more during the period of snow accumulation than during snow depletion. Snow distribution is affected by snow fall and wind as well as to lesser extent by slope angle (Wirz et al., 2011). Avalanches and wind redistributes snow. Morphometric features like ridges, small gullies or toe of slopes prefer snow accumulation, maximum accumulation is observed behind ridges on steep rock walls (Wirz et al., 2011). In less inclined alpine catchment areas, snow is distributed heterogeneously where maximum snow depths develop in snow cornices and snow-free areas regularly occur on ridges and knolls (Grünewald et al., 2010). Snow remains longer in areas of high snow accumulation (Grünewald et al., 2010) because melting increase from snow-free areas to the edges of snow patches due to albedo and surface temperatures and melt out areas with low accumulation first (Essery and Pomeroy, 2004; Grünewald et al., 2010).

The ground thermal heat fluxes determine the energy balance at the base of the snow cover (Haeberli, 1973). Permeability and moisture in the subsurface beneath the snow cover determine the latent heat exchange. When underground releases latent heat during freezing, the temperature at the snow surface remains colder than at the base (Phillips, 2000). If there is no latent heat release due to already frozen underground, the ground cools the base of the snow cover (Fig. 5.3 B). This effect exists in spring, when permafrost ground cools the snow base while air temperature warms the snow surface. Dry ground reduces latent heat release and heat flow from the ground into the base of the snow cover occurs leading to enhanced cooling called thin-snow cover effect (Phillips, 2000). Colder ground prevents or postpones the melting of snow and in reverse a sufficient thick snow cover prevents thermal warming of the underground by an insulation effect. A snow depth of 0.6 m (Hanson and Hoelzle, 2004) or 0.8 m (Keller and Gubler, 1993) is the lower boundary of isolation, this relationship was established on the Murtèl rock glacier.

5.1.6 Ground thermal heat flux

Ground heat fluxes can be divided into geothermal heat fluxes from earth interior influencing the permafrost base and heat fluxes near the surface influenced by the energy balance components. Transient effects of past climate changes persist in several decameters depth observed in boreholes (Lachenbruch and Marshall, 1986; Wegmann, 1998; Kukkonen and Safanda, 2001). Alpine topography modifies the temperature signal in depth up to hundreds of meters (Kohl, 1999). The transient effects existing on Holocene and quaternary scale due to Little Ice Age or medieval climatic optimum and Late Glacial Maximum need to be included in present heat flux analysis (Wegmann et al., 1998; Kohl and Gruber, 2003; Noetzli, 2008; Noetzli and Gruber, 2009). Due to these transient and topographic effects the geothermal heat fluxes is unknown and in modelling often assumed as zero at the lower boundary of permafrost models (Gruber et al., 2004b).

Ground heat flux near the surface can be subdivided into conductive, advective and convective heat transport.

5.1.6.1 Conductive heat transport

Conductive heat transport is a flux of heat from regions of high energy with high temperatures to regions of low temperatures proportional to the local temperature gradient. This relationship is described by Fourier's law:

$$Q_{cond} = -k\,\frac{\delta T}{\delta x} \qquad (5.7)$$

where Q_{cond} is conductive heat flux, k is thermal conductivity, T is temperature and x is the direction of the local gradient of temperature. The minus sign indicates that heat travels down the gradient. The Fourier-equation can be simplified by assuming uniform conductivity in a material and can be changed into the diffusion equation (see Anderson & Anderson (2012) for details):

$$\frac{\delta T}{\delta t} = \kappa\frac{\delta^2 T}{\delta x^2} \qquad (5.8)$$

where $\kappa = k/cp$ and with κ is thermal diffusivity, c is specific heat capacity and p is density. Vosteen and Schellschmidt (2003) measured specific heat capacity for 26 Alpine rocks, c ranges between 0.75 – 0.8 kJ kg^{-1} K^{-1} for magmatic and metamorphic rocks and between 0.8 – 0.9 kJ kg^{-1} K^{-1} for sedimentary rocks. Air possess specific heat capacity of 1.01 kJ kg^{-1} K^{-1}, water at 4°C 4.18 kJ kg^{-1} K^{-1}

and pure ice at 0°C 2.1 kJ kg^{-1} K^{-1} (Oke, 1987). Thermal conductivity ranges from 1 to 3.5 W m^{-1} K^{-1} for magmatic and metamorphic rocks and from 2 to 4 W m^{-1} K^{-1} for sedimentary rocks (Vosteen and Schellschmidt, 2003). The thermal conductivity is very low for air (0.025 W m^{-1} K^{-1}) and water (0.57 W m^{-1} K^{-1}) and relatively high for pure ice (2.24 W m^{-1} K^{-1}) (Oke, 1987). Rocks contain pores filled with air, water and/or ice, thus, thermal conductivity of rocks depends on k of the rock material itself and of the pore infill. Phase transitions in water-filled pores can consume or release large amounts of latent heat as described in the chapter of snowpack processes. Latent heat consummation while thawing slows down significantly conductive heat flow and increases response times of active-layer thawing.

In intact rock, heat will flow in a conductive way but only on a scale smaller than a macro-discontinuity. In real rock walls, macro-discontinuities affect the thermal regime of the rock mass by additional convective and advective heat fluxes. Mechanical effects of discontinuities on rock mass are well known and described in the mechanical chapter. Discontinuity infills of air, water or ice influence conductive processes in discontinuities. As long as no phase transitions occur, ice is a good cold heat conductor. Conductive heat transport of still and not moving water or air is insignificantly low compared to conductive heat flow in the intact rock, however, the occurrence of not moving water or air is theoretically possible but unlikely.

5.1.6.2 Convective heat transport

Convective heat flux is combined with movement of particles. Convection is a movement of gaseous particles by air resulting from temperature or density differences (Kamai et al., 2009), from pressure differences like chimney effects and from barometric pressure changes. Local air convection cells can develop themselves in wide deep fractures (Weisbrod and Dragila, 2006; Weisbrod et al., 2009). Convective heat flux is far from being understood. The process was observed in a permafrost-free slope at Randa (Moore et al., 2011) as well in the active-layer of permafrost-affected rock walls at Jungfraujoch and Matterhorn (Hasler et al., 2011b). The influence of convective heat flux is evaluated comparing conductive heat flux models with actual measurements (Moore et al., 2011).

5.1.6.3 Advective heat transport

In meteorology, advection is a special case of horizontal convection while convection is in vertical direction (Oke, 1987). In alpine environments, transport is preferentially in vertical direction due to strong gradients (Forster and Smith, 1989). In addition, horizontal transport is difficult to evaluate in rock walls. Advective transport is heat transport by percolating water fluid along fractures (Gruber and Haeberli, 2007); I use the term advection the same way without determining a direction. The effect of water and heat transport by water is determined by the fluid velocity (Dietrich et al., 2005) which depends on infiltration and, thus, permeability. Infiltration can be classified according to Gray et al. (1985) in restricted, limited and unlimited. Infiltration is restricted if ice lenses at or below the surface pond water which evaporates or runs off at the surface. Limited infiltration is given when snow melt infiltrates partially and infiltration rate depends on ground water content, ground temperature and surface saturation during infiltration. If the underground possesses air filled macropores (soil) at snowmelt time infiltration is unlimited. Infiltration in macropores of soil is the key role factor (Stähli, 2005) unless ice blocks the macropores (Seyfried and Murdock, 1997). In soils, flow in unsaturated macropores is turbulent and the degree of connectivity decides lateral water flow downward the slope (Beven and Germann, 1982). In rock, discontinuities are the counterpart of macropores in soils.

Water flow in porous media can be described using the Darcy-equation:

$$Q = -A\,K\,\frac{\delta h}{\delta l} \qquad (5.9)$$

where Q is volume discharge, A is the cross-sectional area of the column, K is the hydraulic conductivity, δh is the difference in hydraulic head and δl is the distance between measurement points.

$$K = \frac{k\rho g}{\mu} \qquad (5.10)$$

Hydraulic conductivity is dependent on fluid density ρ, gravitational acceleration g, permeability k and dynamic viscosity μ (Dietrich et al., 2005; Anderson and Anderson, 2012). The Darcy equation is valid for Reynolds numbers lower than 1 to 10 (Bear, 1972). Permeability values of quartz slate and schist quartz slate samples of the Steintaelli are 0.087 ±0,032 µD and 0.816 ±0.07 µD (Krautblatter, 2009). Discontinuities increase the permeability by several magnitudes compared to pores and determine the hydrologic properties of rock walls due their distribution, size, permeability, orientation, distance, density, roughness and filling (Dietrich et al., 2005). High relief of rock walls in

Alpine environments enhance the vertical flow of water and, thus, the influence of advection on the thermal regime (Forster and Smith, 1989). The parallel-plate concept to model flow in a fracture between two parallel planes is a strong simplified approach (Dietrich et al., 2005) but the only approach that finds acceptance (Berkowitz, 2002). Assuming laminar flow, flow can be modelled using the Navier-Stokes equation where permeability is dependent on the square of aperture width (Dietrich et al., 2005). Fracture roughness increases the transition from laminar to turbulent flow (Witherspoon, 2013).

There is little knowledge, how advection works in rock walls. Gruber & Haeberli (2007) argue that the effect of advection in rock walls is an important unknown. They further assume an earlier and faster propagation of advective thawing than conductive thawing resulting in discrete thaw zones and corridors along fractures. These thaw corridors were quantified with geoelectrical measurements (Krautblatter and Hauck, 2007; Krautblatter, 2010). Hasler et al. (2011a) conducted a first laboratory study to simulate how ice erosion by advective processes works.

The temporal development of ground heat flux and interaction between intact rock and discontinuities are described in Chapter 5.3.

5.1.7 Feedbacks and Response Times

The ground thermal heat fluxes described above allow formulation of findings concerning response times. (1) The temporal dimension is governed by the speed of conductive, convective and advective heat transport processes. (2) Thermal gradients govern the dynamic and direction of conductive heat transport while discontinuities and their distribution govern the dynamic of convective and advective processes. (3) Latent heat fusion necessary for melting ice will slow down active-layer thawing or permafrost degradation. (4) Higher ice content slows down permafrost degradation. Landforms with high ice content like rock glaciers respond slower than debris-covered slopes (Scherler et al., 2013). Low-porosity rock walls possess lesser ice content and should respond faster to increased warming.

5.2 Mechanical regime

5.2.1 Mechanical properties

In the following chapter, mechanical properties and their alteration by permafrost and active-layer thaw will be shortly described. For more detailed description of general mechanical properties, text books by Jaeger (2009), Wyllie and Mah (2004) or Prinz and Strauß (2011) are highly recommended. The influence of permafrost is described in the fundamental paper by Krautblatter et al. (2013).

5.2.1.1 General mechanical properties

Rock type can be described based on geological properties like abundance, texture, involved minerals, deformation and degree metamorphosis and based on mechanically properties like strength, stiffness, anisotropy, porosity, grain size or shape (Edelbro, 2003). A discontinuity is a break or boundary in a rock mass which displays a change or is the result of a change in mass properties (Hencher, 1987). The term discontinuity amalgamates all mechanical defects known as joints, bedding planes, faults, fissures and fractures (Priest, 1993) and avoids any mode of origin of the feature or inferences according geological origin (Edelbro, 2003). The term joint compass mechanical types of structural weakness (Edelbro, 2003). In this dissertation discontinuities and joints are equally used which is common in literature (Hencher, 1987).

Two failure mechanisms of solids can be distinguished (Fig. 5.4 A and B). Brittle failure occurs when stress increases, at a stress threshold (σ_{limit}) elastic deformation change to plastic permanent deformation, a strength peak (σ_{peak}) is reached and a sudden strength loss can be observed down to a residual strength (σ_{res}) (Edelbro, 2003). Ductile behaviour shows smaller loss of strength after crossing the strength threshold (Edelbro, 2003). Igneous and metamorphic rocks show more often brittle behaviour while certain sedimentary rocks behave more in a ductile way (Edelbro, 2003).

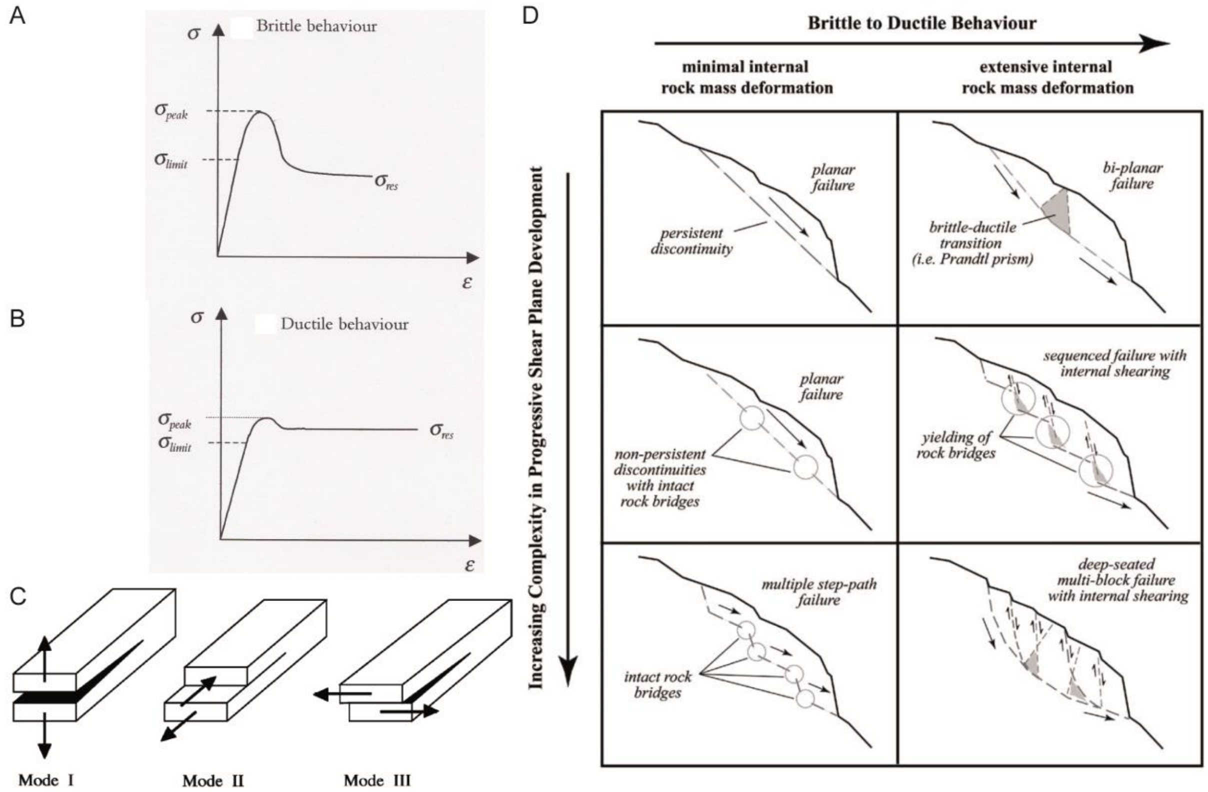

Fig. 5.4 Strain (*ε*) plotted against stress (*σ*) for A: brittle and B: ductile failure (Edelbro, 2003); C: Basic modes of failure (Chang et al., 2002); D: Massive rock slope sliding mechanisms as controlled by progressive shear plane development and internal rock mass deformation/damage (Eberhardt et al., 2004).

In fracture mechanics, the stress intensity factor K dependent on mean stress applied to a crack and crack length (Erismann and Abele, 2001). For given material, K possesses a critical maximum value called critical stress intensity factor or, in other terms, fracture toughness K_C (K_{IC}, K_{IIC}, K_{IIIC}; roman letter indicates the mode). This strength-limiting parameter is influenced by temperature, humidity, corrosion and, gradually decreases by weathering (Erismann and Abele, 2001). Due to the effects of subcritical fracture growth, fracture toughness can decrease with time even at a subcritical stress intensity factor (Kemeny, 2003). Three basic failure modes developing under different applied stress directions can be distinguished. In the tensile opening mode (Mode I) the crack opens in a right angle to crack, in the sliding/shearing mode (Mode II) crack faces shears in direction normal to the crack front and in the tearing/out of plane mode (Mode III) crack faces shears parallel to crack front (Fig. 5.4 C) (Erismann and Abele, 2001; Chang et al., 2002). Massive sliding mechanisms are controlled by strength degradation by developing of a shear plane (brittle behaviour), internal slide mass deformation (ductile behaviour) and damage mechanisms (Fig. 5.4 D) (Eberhardt et al., 2004).

The influence of these controlling factors vary depending on complexity of rock mass geology and subsurface structure (Eberhardt et al., 2004). Rock mass is defined as material with complex rock breakdown processes. On a scale smaller than discontinuities, intact rock determines rock stability (Fig. 5.5 A).

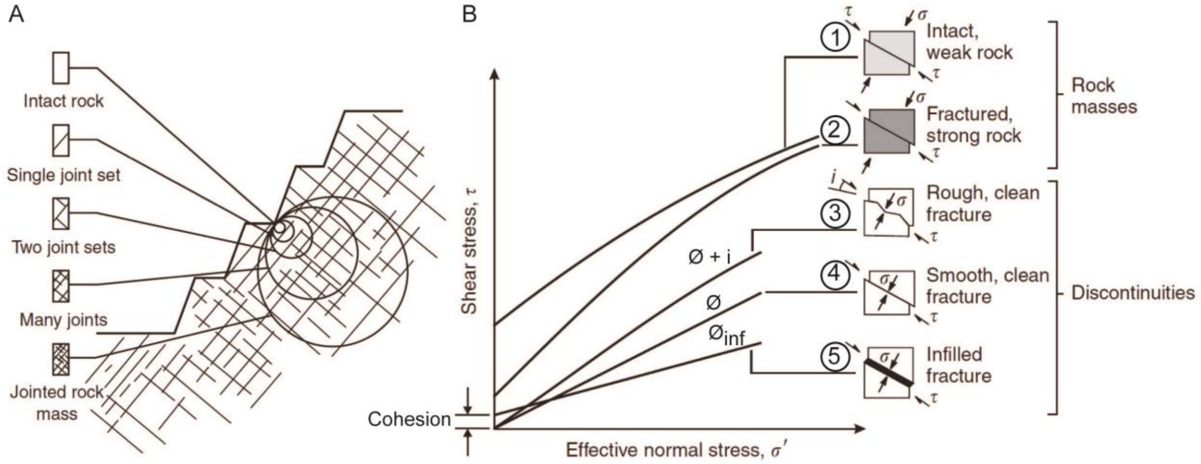

Fig. 5.5 A: Idealized diagram showing transition from intact rock to jointed rock mass (Wyllie and Mah, 2004); B: Relationship between shear and normal stress on sliding surface for five different geologic conditions (Wyllie and Mah, 2004).

If the bank height is equal to a single joint, stability is controlled by the properties of this joint (Wyllie and Mah, 2004). The stability of the rock mass is determined by the jointed rock mass where dimensions of the rock mass are bigger than the length of discontinuities (Wyllie and Mah, 2004). Intact rock properties are affected by weathering processes. Properties of discontinuities, e.g. form, roughness, weathered or fresh rock and filling, determine shear strength on discontinuity scale. Both intact rock properties such as compressive and tensile strength and the base angle of friction as well as rock mass properties such as spacing and surface properties affect shear strength on rock mass scale. Based on scale effects and geologic conditions, sliding surfaces develop along discontinuities and in the rock mass (Fig. 5.5 B) by developing new fractures.

The relationship between shear stress (τ) at failure and normal stress (σ) can be described by the Coulomb-Mohr equation:

$$\tau = c + \sigma' * \tan\varphi \quad (5.11)$$

with $\sigma' = \sigma - \mu$

where c is cohesion, σ' is effective normal stress, ϕ is the friction angle and μ is the pore water pressure. In Fig. 5.5 B, the ascending slope of the line describes the friction angle and intersection of the ordinate the cohesion, respectively.

The friction angle of an infilled fracture (ϕ_{inf}; Fig. 5.5 B-5) is low but cohesion of fracture filling is significant. Discontinuities without filling in tough rocks have no cohesion and the friction angle of the rock surface (ϕ_r; Fig. 5.5 B-4) increases with increasing roughness of asperities (i, Fig. 5.5 B-3) (Patton, 1966). The slope angle is steeper at rough surfaces because the slope angle is equal to the sum of angles of internal friction and mean angle of roughness (Patton, 1966). Equation 5.11 can be adapted to

$$\tau = \sigma' * tan\,(\varphi + i) \tag{5.12}$$

To estimate the influence of i, Barton and Choubey (1977) developed the empirical measure called Joint Roughness Coefficient (*JRC*). The *JRC* can be incorporated in Equation 5.12:

$$\tau = \sigma' * tan\,(\varphi + JRC * \log 10\left(\frac{\sigma_c}{\sigma'}\right)) \tag{5.13}$$

where σ_c is the compressive rock strength of the rough surface.

The described discontinuities (Fig. 5.5 B-3-5) and their behaviour are valid for existing shear planes (Fig. 5.4 D upper left figure). Intact rock bridges increase cohesion in discontinuities (Kemeny, 2003) and need to be broken for shear plane development (Fig. 5.4 D e.g. middle left figure). For the sliding mode II (Fig. 5.4 C), Kemeny (2003) shows that cohesion depends on mode II fracture toughness (K_{IIC}), the size of the rock bridge a and the size of the cracks on both sides of the rock bridge w. Chang et al. (2002) show resembling behaviour of mode I and mode II fracture toughness, K_{IC} strongly depends on uniaxial compressive strength σ_c. According to Krautblatter (2009) Equation 5.12 can be adapted to:

$$\tau = \frac{K_C\sqrt{\pi a}}{2w} + \sigma' * tan\,(\varphi + i) \tag{5.14}$$

If effective normal stress increases by e.g. increasing loading, irregularities can be sheared off and angle of friction decreases. In fractured rock mass, shear strength is determined by discontinuities and intact rock (e.g. intact rock bridges). Cohesion is comparable low but the angle of friction is high dependent on normal stress (Fig. 5.5 B-2). Intact weak rock e.g. consisting of fine-grained material possesses a higher cohesion but a low angle of friction (Fig. 5.5 B-1).

5.1.1.2 Alteration of mechanical properties by permafrost

In his early laboratory work, Mellor (1971, 1973) described the alteration of tensile and uniaxial strength due to thawing or freezing (Fig. 5.6). Only the saturation mode is described, the existence of the air-dry mode is restricted to laboratory conditions.

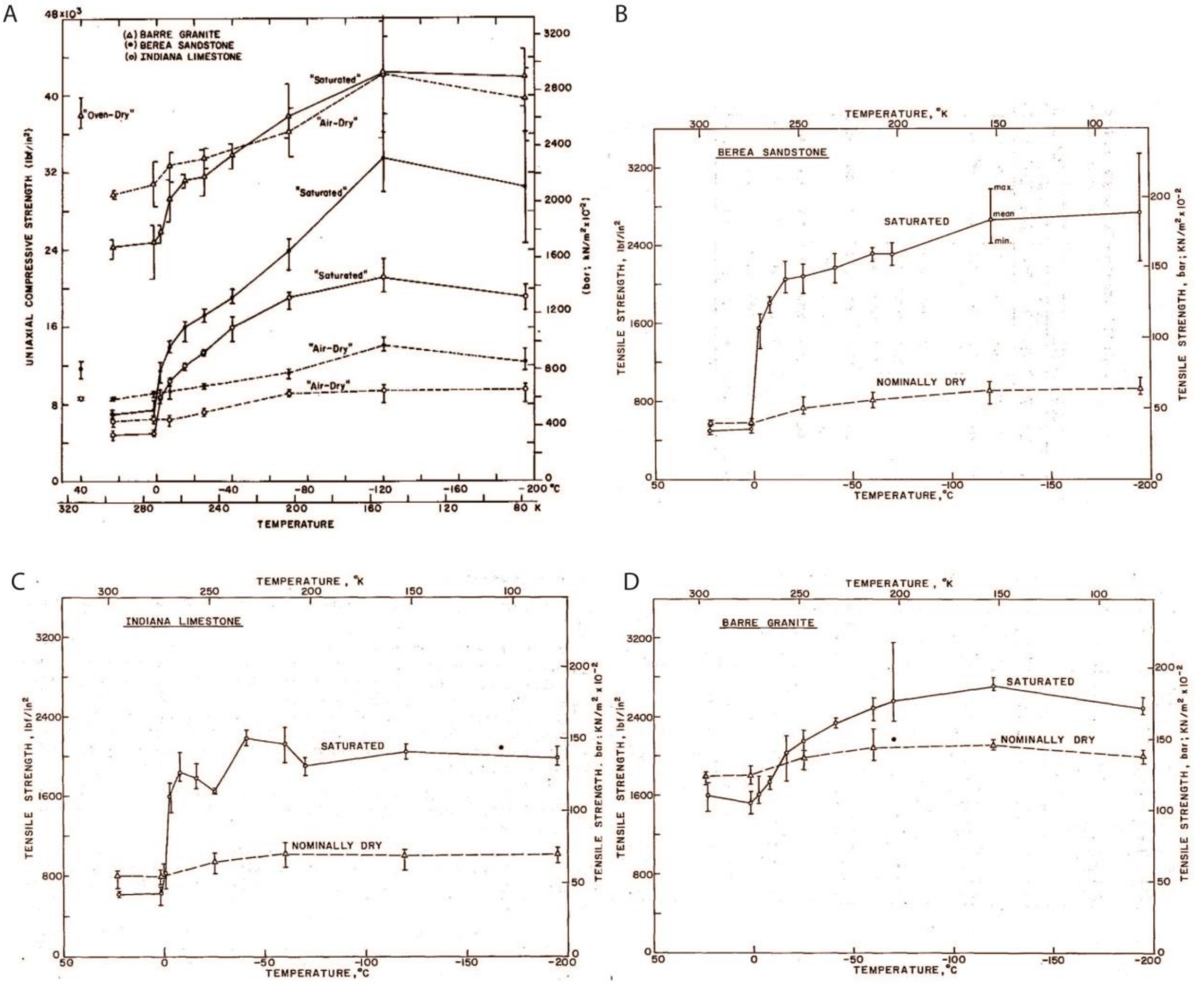

Fig. 5.6 Temperature-dependence of A: uniaxial strength (Mellor, 1973) and tensile strength of B: Berea Sandstone, C: Indiana Limestone and D: Barre Granite (Mellor, 1971).

Mean uniaxial compressive strength increases due to freezing from 1.5° to -7°C in a range between 16 to 100 % (Fig. 5.6 A). Due to freezing from 1.65°C to -2.5°C, mean tensile strength increases between 6 % (Fig. 5.6 B-D) and 300 % (Fig. 5.6 B-D), respectively. This behaviour implicates strong influences of active-layer thawing or permafrost degradation on stability. Krautblatter (2009) argues that there is probably no other environmental factor reducing rock mass stability such fast as thawing. In permafrost rocks, instability can be caused by an increase of shear forces or a decrease of shear resistances (Krautblatter et al., 2013).

A stability-relevant discontinuity is represented in Fig. 5.7 A. Permafrost can increase hydrostatic pressure (*B*) by decreasing the permeability in the order of 1-3 magnitudes (Pogrebiskiy and Chernyshev, 1977), and thus, sealing the underground which enhances water pressure building in unfrozen fractures (Terzaghi, 1962). The efficiency of hydrostatic pressure will increase with depth of the shear plane (Fig. 5.7 B) (Krautblatter et al., 2013). Cryostatic pressure (*C*) can be derived by volumetric expansion (Wegmann and Gudmundsson, 1999; Matsuoka and Murton, 2008) and/or ice segregation (Walder and Hallet, 1985; Murton et al., 2006; Matsuoka and Murton, 2008). Ice segregation is more efficient in the first 2 decameters, in deeper areas the rock overload causes a shut-off pressure (Fig. 5.7 B) (Krautblatter et al., 2013). Seasonal changes of shear forces and resistances are described in Chapter 5.3.

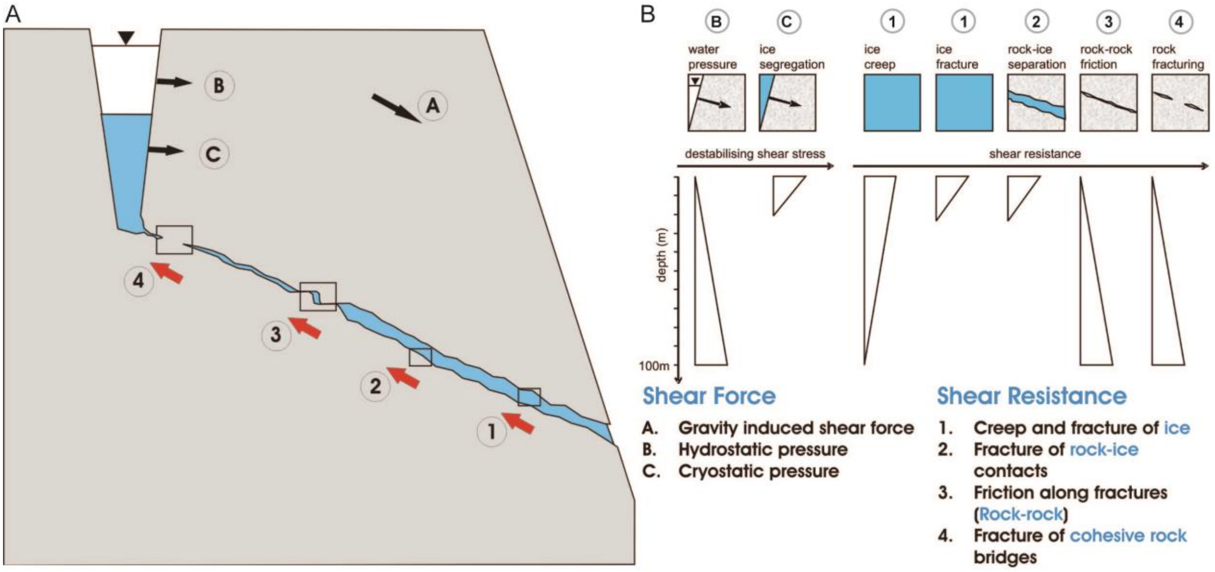

Fig. 5.7 A: Schematic illustration of the rock-ice mechanical model; B: The efficiency of shear force and shear resistance with depth of the shear plane (adapted from Krautblatter et al. (2013)).

Krautblatter et al. (2013) identify four components of shear resistance: the creep and fracture of ice (*1*), the fracture of rock-ice contents (*2*), the friction along rock-rock contact (*3*) and the fracture of cohesive rock bridges *(4)* (Fig. 5.7). Creep of ice (*1*) depends on temperature and can be exemplified as:

$$\tau_{\mathrm{p}} = \frac{\epsilon_{\mathrm{w}}}{A_0} \exp\left(-\frac{16700}{T_{\mathrm{K}}}\right) \tag{5.15}$$

where ε_{w} is the shear strain rate of ice, A_0 is the temperature independent Arrhenius factor and T_{K} is the temperature of ice. Efficiency of creep and fracture of ice decrease with increasing shear plane depth (Fig. 5.7 B) (Krautblatter et al., 2013). The decrease of shear strength of ice-filled joints with increasing ice temperature dependent on normal stress and temperature was shown by several authors (Davies et al., 2000; Davies et al., 2001, 2003; Guenzel, 2008). Based on their laboratory experiments, Krautblatter et al. (2013) transferred their findings into an empirical relationship:

$$\tau_{\mathrm{p}} = (-144\, T_{\mathrm{C}} + 0.42\sigma' + 41.3) \tag{5.16}$$

where T_{C} is the temperature of ice at failure and σ' is effective normal stress. The efficiency of rock-ice contacts decrease with increasing shear plane depth due to increasing normal stress by the higher overloading rock mass (Fig. 5.7 B) (Krautblatter et al., 2013). Along frictional rock-rock contacts without rock bridges, asperities influence the shear strength and the influence can be estimated by the *JRC* of Barton and Choubey (1977) (Eq. 5.13). Upon warming, the compressive strength (σ_{u}) decreases significantly according to laboratory results of Mellor (1971, 1973). Krautblatter et al. (2013) further use Kemeny's (2003) intact rock bridge-approach (Eq. 5.14). The fracture toughness decreases with increasing temperature (Dwivedi et al., 2000). Both, the efficiency of friction along rock-rock contacts and fracture toughness of cohesive rock bridges increase with increasing shear plane depth due to increasing normal stress originated by higher overloading rock mass (Fig. 5.7 B) (Krautblatter et al., 2013).

For detailed derivations of the rock-ice mechanical model see Krautblatter et al. (2013); the model can be formulated as:

$$\begin{aligned} \left|\tau_{\mathrm{p}}\right| = {} & \frac{\epsilon_{\mathrm{w}}}{A_0} \exp\left(-\frac{16700}{T_{\mathrm{K}}}\right) \\ & + (-144\, T_{\mathrm{C}} + 0.42\sigma' + 41.3) \\ & + \sigma' \tan\left(JRC\ \log_{10}\left(\frac{\sigma_{\mathrm{u}}}{\sigma'}\right) + \varphi_{\mathrm{r}}\right) \\ & + \frac{K_{\mathrm{C}}\sqrt{\pi a}}{2w}. \end{aligned} \tag{5.17}$$

Krautblatter et al. (2013) identified critical fracture toughness K_C, the uniaxial compressive strength σ_u and temperature T_C and T_K as sensitive to warming. The instability in time will be explained in a Chapter 5.3.

Guenzel (2012) measured shear strength behaviour of an artificial concrete sample with a sand-filled discontinuity. Her results show a stronger temperature dependency of peak shear strength of frozen sand-filled joints (370 kPa) than ice-filled joints (180 kPa). After melting, former ice-filled joints come into contact and shear strength increases (Davies et al., 2001) (compare Fig. 5.5 B-3 or B-4). Sand-filled joints are still affected by the sand infill after melting and show lower shear strength (compare Fig. 5.5 B-5).

5.2.2 Weathering and rock decay

The use of the term “weathering” is questioned and discussed by Hall et al. (2012). The authors argue that the term “weathering” implies that climate is the primary driver and rock properties play a secondary role. Classic definition of weathering by Chorley et al. (1984) determine weathering as response of minerals to conditions at or near the interface between earth and atmosphere. The definition highlights the role of rock properties. Hall et al. (2012) consider rock properties as dominant control, summarize terminology synonymous for weathering (e.g. rock breakdown, rock decomposition) and advise to use the term “rock decay” alternatively. To acknowledge the role of rock properties the terminologies rock decay (Hall et al., 2012) is used synonymously for weathering in this dissertation. For scale issues in weathering studies, Viles (2001; 2013a) provides a comprehensive overview. Weathering occurs at timescales from instantaneous to tens of millions of years, rates and types of weathering vary during these timescales (Viles, 2013a). Also weathering variability in space is huge, different conditions lead to variability of weathering rates and process synergies (Viles, 2013a). At all temporal and spatial scales synergies between weathering processes occur (Viles, 2013a). Exemplarily, biofilms can cause stabilization effects and negative feedbacks or destabilization effects and positive feedbacks (Viles et al., 2008). Synergy and scale effects explain up-scaling problems. A good overview about the linkage between weathering and rock instability is given by Viles (2013b). The instability of rock slopes can be regarded in terms of ratio between stress and strength like factor of safety (Dikau, 2004a). Rock slope strength is a measure of resistance to stress, degree of weathering influences strength (Viles, 2013b) and is incorporated into different rock mass classification systems (Selby, 1980; Bieniawski, 1987). The rate of weathering determines the frequency of stress acting on the rock wall (Viles, 2013b). The links between weathering and rock instability are dynamic and nonlinear due to e.g. storage effects, thresholds, etc. (Viles, 2013b).

According to Hall (2013), the assumption that the most important weathering process in cold environments like periglacial regions is freeze-thaw action and that debris produced from freeze-thaw processes possesses an angular form is not justified. Climatic geomorphologists like Tricart (1970) introduced a process-product scale relationship into freeze-thaw process, long-term macrogélivation produces blocks of several cubicmeters and short-term microgélivation results in small products. Matsuoka (2001b) differentiates micro- and macrogelivation according to porosity of rock, scale of fragmentation and prevailing process. Prevailing process of microgelivation is ice-segregation and volumetric expansion causes macrogelivation, respectively (Matsuoka, 2001b; Matsuoka and Murton, 2008). Hall and Thorn (2011) argue that other weathering processes e.g. thermal stress/fatigue, chemical weathering or biological weathering or synergies of weathering processes are ignored. In this dissertation, I follow the arguments of Hall and Thorn (2011) and I will not use micro- and macrogelivation. In the following chapter, processes associated with freeze-thaw action and thermal changes will be introduced which affects rock kinematics. Weathering was not the main focus of this study, to differentiate weathering processes is a difficult task. For detailed overview about mechanical weathering in cold regions see Hall (2013) and chemical weathering Dixon (2013), respectively.

5.2.2.1 Frost weathering

Frost weathering strongly depends on lithology and discontinuities, zones of weakness influence the size and form of the weathered product and enhance moisture and temperature transport (Wegmann, 1998). Two different frost weathering processes are distinguished: volumetric expansion and ice segregation. The type of frost weathering process depends on properties of rocks, temperature and moisture regimes of the rock wall (Matsuoka, 1991; Prick, 1997) as well as duration and intensity of frost conditions (Wegmann, 1998).

With freezing of in situ water, volumetric expansion of 9 % occurs developing freezing pressure up to 207 MPa (Matsuoka and Murton, 2008). Tensile strength of rock is theoretically smaller than freezing pressure (Wegmann, 1998). To develop such freezing pressures, certain preconditions need to be fulfilled. Saturation needs to be high, Walder and Hallet (1986) argue a threshold of > 91 % and Matsuoka (1990a) calculated > 92 % as a saturation threshold. Rock breakdown is observed in laboratory tests at much lower degrees of saturation (Mellor, 1970; Matsuoka, 1990a) implying that volumetric expansion does not occur alone or it is sufficient that certain parts of the pores in a rock are fully filled with water. Uniaxial compressive strength and tensile strength increase with decreasing temperatures (Mellor, 1971). Intensity of rock deformation increases with increasing freezing rate and freezing intensity (Mellor, 1970), thus, a high freezing rate is required for volumetric expansion. Fast freezing prevents evaporation, ice extrusion (Davidson and Nye, 1985), ice expansion into free spaces or ice relaxation with time (Tharp, 1987). Unfrozen water can exist at temperatures up to -10°C (Mellor, 1970). If the water is sealed, the water is under pressure (Davidson and Nye, 1985) and confined water can increase ice pressure by an order of a magnitude (Tharp, 1987). High freezing rates can be expected during short-term (e.g. diurnal) freezing cycles and affect the uppermost 30 cm (Matsuoka et al., 1998; Matsuoka and Murton, 2008); areas below 30 cm depth are not affected by short-term cycles due to low rock conductivity. McGreevy and Whalley (1985) argue that saturation is the limiting factor of volumetric expansion. In rock walls, Sass (2005a) showed that rock moisture fluctuates between 0 and 100 % in the uppermost 15 cm, rocks are wetter in summer than winter and wetter in the inside than close to the surface. Short-term frost cycles seldom penetrates to high saturated areas (> 15 cm) (Sass, 2003) and water which not freezes instantaneously is pushed away from the freezing front due to freezing-generated hydraulic pressure (Sass, 2004).

Frost heaving in arctic soils is observed to be larger than 9 % (Taber, 1929, 1930) indicating that ice pressure is not generated by volumetric expansion alone. Ice segregation occurs when unfrozen liquid water migrates through a porous medium towards the freezing front. The migration results from temperature-induced suction in freezing ground, a temperature drop of 1° C can induce a cryosuction of 1.2 MPa (Williams and Smith, 1989). Several preconditions are needed for ice segregation. Walder and Hallet (1985) developed a theoretical thermodynamic model to explain ice segregation. They assume penny-shaped cracks, water migrates along grain boundaries in an unfrozen water film towards the cracks. If water encounters cracks or ice lenses, surface forces suddenly decrease and water can freeze onto the surface. Phase change to ice enlarges the ice lens in the crack, can promote crack growth and develop tension on unfrozen water films. Calculated crack growth rates were highest between -5 and -15 °C (Walder and Hallet, 1985) but acoustic emission measurements on Berea Sandstone show 90 % of cracking occurs between -3°C and -6°C (Hallet et al., 1991). The temperature range where cracking occurs is called frost cracking window (Walder and Hallet, 1985). This temperature range exists because at higher temperatures water in films or microcracks is thermodynamically stable and will not freeze, while at lower temperatures effective viscosity of water increases and slows down the water transport towards the freezing front (Anderson and Anderson, 2012). Murton et al. (2001) observed ice segregation at temperature ranges between -0.2°C and -2.5°C in high-porosity Tuffeau Limestone (39.8 %). The higher temperature range is probably caused by lower strength of Tuffeau Limestone (Murton et al., 2001) than Berea Sandstone (Hallet et al., 1991), Westerly Granite or St. Pons Marble (Walder and Hallet, 1985). Ice segregation occurs most during thawing of the active-layer when water is released and can migrate towards the permafrost table (Murton et al., 2000) and frostcracking is more effective in simulated permafrost conditions (bi-directional freezing) than in freezing from the surface (uni-directional freezing) (Murton et al., 2006). Preconditions for ice segregation are (1) subzero temperature gradient to cause a thermomolecular pressure gradient, (2) warm temperatures (slightly sub-zero) to increase permeability and (3) an intra-crack pressure slightly above stress-corrosion limit (Murton et al., 2006). Annual frost cycles with seasonal freezing and long time spans in the critical temperature range favour ice segregation (Murton et al., 2006; Matsuoka and Murton, 2008).

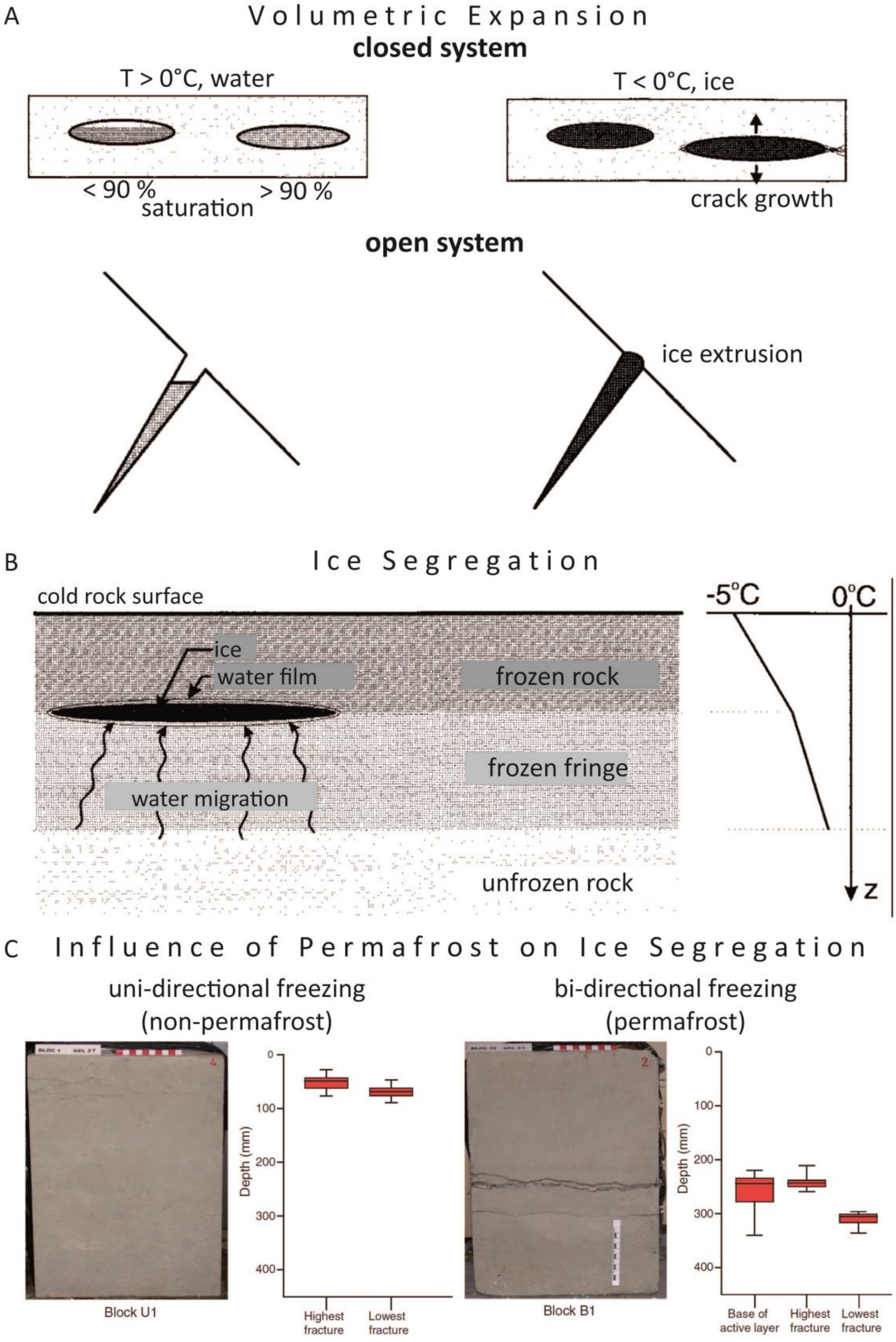

Fig. 5.8 A: Schematic representation of volumetric expansion in pores (closed system) and discontinuities (open system)(adapted from Wegmann (1998)); B: Schematic representation of ice segregation (adapted from Wegmann (1998)); C: The influence of permafrost (bi-directional freezing) on frost cracking by ice segregation (Murton et al., 2006).

5.2.2.2 Thermal weathering

Rocks expand when heated and contract when cooled. Non-uniform contraction and expansion of rock compartments or rock minerals cause stress which can exceed rock strength. High temperature gradients are required for thermally induced strain sufficient to produce fractures, high temperature gradients are confined close to the surface (Anderson and Anderson, 2012). Thermal volumetric expansion can be expressed by

$$\alpha = \frac{1}{V\left(\frac{\delta V}{\delta T}\right)_P} \tag{5.18}$$

with α is the thermal expansion coefficient, V is the volume, T is temperature and the subscript P indicates constant pressure (Anderson and Anderson, 2012). Thermal expansion coefficients range from 1-10 x 10^{-6} °C^{-1} (Anderson and Anderson, 2012), Wegmann (1998) mentions 13.2 x 10^{-6} °C^{-1} for Limestone and 9.5 x 10^{-6} °C^{-1} for granitoide orthogneiss at Jungfraujoch. Rock minerals possess different values of α and anisotropic behaviour, e.g. quartz expands and contracts 7.7 x 10^{-6} °C^{-1} parallel to c-axis and 13.3 x 10^{-6} °C^{-1} in perpendicular direction (Hall et al., 2008; Siegesmund et al., 2008). Due to differences in orientation and varying albedo, rock heats non-uniformly (Anderson and Anderson, 2012). This non-uniformity can lead to mineral disintegration due to daily cycles (Gomez-Heras et al., 2006). Thermal stress can be distinguished into thermal fatigue and thermal shock (Hall and Thorn, 2014). Thermal fatigue is produced by repeated temperature changes and subsequent stresses (Hall and Thorn, 2014). These stresses are normally below rock strength but repetitive and cumulative nature can lead to failure along pre-existing zones of weakness (Richter and Simmons, 1974; Mahmutoglu, 1998). Thermal shock is instantaneous and singular sudden temperature change leading to stress exceeding the rock strength and resulting in fracturing (Hall and Thorn, 2014). Fractures cutting pre-existing lines of weakness and show polygonal and rectilinear patterns (Hall and Thorn, 2014). Temperature thresholds that need to be exceeded vary in literature (Hall and Thorn, 2014) and a threshold of ≥2°C min^{-1} seems reasonable (Richter and Simmons, 1974). For a detailed review of thermal fatigue and thermal stress see Hall & Thorn (2014).

5.3 Interaction of thermal and mechanical processes in steep permafrost rock walls

This chapter is currently under revision in the Journal “Geomorphology” under the title: “Interaction of thermal and mechanical processes in steep permafrost rock walls: a conceptual approach” written by D. Draebing, M. Krautblatter and R. Dikau. Formatting, pagination and numbering of equations and figures has been modified for production of this thesis. The introduction (Chapter 5.3.2) defines permafrost and summarizes papers on rockfall from permafrost rock walls. In the next step, the heat transport processes and influence of snow cover are introduced. In Chapter 5.3.3, the authors construct a rock model with increasing complexity starting with a simple homogenous rock model, adding a stability-relevant discontinuity and changing the discontinuity infill from air via water to ice and ending in a dynamic model with snow cover influence. The alterations of thermal and mechanical properties across the different model steps are described qualitatively. In Chapter 5.3.4, feedbacks between rock matrix and discontinuity are described. Seasonal development of snow cover, heat transport processes, shear forces and shear strengths are reviewed in Chapter 5.3.5. Empirical field evidences are introduced in Chapter 5.3.6 and are used to validate the conceptual approach (Chapter 5.3.8). These chapters are a short example of results presented in the latter chapters of dissertation. The reviewers of this article required an empirical validation of the conceptual approach. This validation is the main topic of this dissertation. Chapter 5.3.7 describes the system behaviour on a long-term scale and presents a conceptual long-term stability model. The Paper ends with a conclusion (Chapter 5.3.9) summarizing the main findings.

5.3.1 Abstract

Degradation of permafrost rock wall decreases stability and can initiate rock slope instability of all magnitudes. Rock instability is controlled by the balance of shear forces and shear resistances. The sensitivity of slope stability to warming results from a complex interplay of shear forces and resistances. Conductive, convective and advective heat transport processes act to warm, degrade and thaw permafrost in rock walls. On a seasonal scale, snow cover changes are a poorly understood key control of the timing and extent of thawing and permafrost degradation. We identified two potential critical time windows where shear forces might exceed shear resistances of the rock. In early summer combined hydrostatic and cryostatic pressure can cause a peak in shear force

exceeding high frozen shear resistance and in autumn fast increasing shear forces can exceed slower increasing shear resistance. On a multiannual system scale, shear resistances change from predominantly rock-mechanically to ice-mechanically controlled. Progressive rock bridge failure results in an increase of sensitivity to warming. Climate change alters snow cover and duration and, hereby, thermal and mechanical processes in the rock wall. Amplified thawing of permafrost will result in higher rock slope instability and rock fall activity. We present a holistic conceptual approach connecting thermal and mechanical processes, validate parts of the model with geophysical and kinematic data and develop future scenarios to enhance understanding on system scale.

5.3.2 Introduction

Permafrost is a thermally defined phenomenon for underground material remaining under 0°C for at least two consecutive years (NRC-Permafrost-Subcommitee, 1988; Muller, 2008). In rocks, freezing point depression caused by solutes, pressure, pore diameter or pore material can lead to a mobile supercooled unfrozen water content down to temperatures of -10°C (Mellor, 1970; Lock, 2005). Thermal conditions influence rock instability on different temporal scales, e.g. on a multiannual scale like the observed increase of regional rock fall activity (Fischer, 2010; Ravanel and Deline, 2010) or on a seasonal scale like hot summers like 2003 (Gruber et al., 2004a). Field evidences of ice in rock scarps and rock fall talus slopes indicate that permafrost is involved in these processes (Dramis et al., 1995; Pirulli, 2009; Fischer et al., 2010; Ravanel and Deline, 2010; Kenner et al., 2011). Rock slope failures can be classified according to volume introduced by Whalley (1974, 1984) and for bergsturz size by Heim (1932). Numerous case studies focus on permafrost influence on rock-ice avalanches with magnitudes >1 x10^7 m³ or cliff fall events (magnitude 10^4-10^6 m³) (Bottino et al., 2002; Haeberli et al., 2004; Huggel et al., 2005; Fischer et al., 2006; Geertsema et al., 2006; Huggel et al., 2008; Lipovsky et al., 2008; Sosio et al., 2008). Other studies show higher activities of fall processes of different magnitudes (cliff falls 10^4-10^6 m³, block falls 10^2-10^4 m³, boulder falls 10^1-10^2 m³ and debris falls <10 m³) in permafrost-influenced rock walls (Sass, 2005b; Fischer et al., 2007; Krautblatter and Dikau, 2007; Rabatel et al., 2008; Deline, 2009; Ravanel et al., 2010; Ravanel and Deline, 2010). Recently, Krautblatter et al. (2013) introduced a comprehensive rock- and ice-mechanical model to explain why permafrost rocks become unstable on different temporal and spatial scales. The authors identify and quantify rock- and ice-mechanical properties responsible for decreasing stability in degrading permafrost-affected rock slopes. In this article, we add relevant heat transfer processes and the timing of these processes.

The thermal influence on rock walls can be subdivided into three different processes: conduction, convection and advection. Conduction is heat diffusion in a solid or static fluid as a result of a temperature gradient based on the principles of thermodynamics. Convection is a heat current in combination with particle transport, where the energy is transported by liquid or gaseous particles in a discrete way. Advective heat transport is a continual heat transport through a moving fluid. Gruber & Haeberli (2007) describe the degree of material fracturing, the ice and snow cover of the surface and the availability of water as the thermal key controls on rock walls. Fracturing affects infiltration capacity and water content. Ice and snow cover controls rock temperature and water availability. Water availability affects the advective heat transport, rock weathering and turbulent exchange of latent energy at the rock surface.

Snow cover changes the energy balance of the surface by increasing albedo, long-wave emissivity and absorptivity, and by decreasing thermal conductivity in comparison to rock surfaces (Zhang, 2005). Due to latent heat processes, snow melt is an energy sink. As result of its properties snow cover possesses an insulation effect which influences the ground thermal regime. This influence of snow cover on permafrost strongly depends on the spatial and temporal snow distribution (Luetschg et al., 2008) and could be identified on flat terrain, rock glaciers and gentle slopes (Keller and Gubler, 1993; Keller, 1994; Phillips, 2000; Ishikawa, 2003; Luetschg et al., 2003; Luetschg et al., 2004; Luetschg and Haeberli, 2005). The spatial distribution of snow cover on steep rock walls is highly variable caused by interactions between wind processes and slope morphometry (Wirz et al., 2011). These interactions result in preferentially snow accumulation behind ridges, in small gullies or at the toe of slopes (Wirz et al., 2011). During the period of snow accumulation morphometric factors are more important than during snow depletion (Schmidt, 2009).

Previous research focussed on either rock stability, snow cover influence or permafrost distribution. However, previous studies have not assessed the influence of snow cover on thermal and mechanical processes in steep permafrost rock walls. Here we present (1) our conceptual model which connects thermal and mechanical processes on a seasonal scale and establishes a framework for joint thermo-hydro-mechanical forcing. (2) We present geophysical and kinematic data to validate parts of our model and (3) develop future scenarios to enhance understanding on system scale.

5.3.3 The model approach

In Chapter 5.3.3, we discuss Fig. 5.9 from the top (homogeneous rock wall) to the middle (heterogenic rock model) and then to the bottom (dynamic rock model with snow cover). Our approach is based on the factor of safety (*FS*) model:

$$FS = \frac{shear\ strength}{shear\ stress} \tag{5.19}$$

relating the sum of resisting forces (shear strength) to the sum of driving forces (shear stress). For this, we adopt the rock-ice mechanical model developed by Krautblatter et al. (2013). The model includes a mechanical representation of the fracture toughness of rock bridges, friction of rough rock-rock contacts in fractures, the deformability of ice in fractures and the performance of rock-ice interfaces in fractures. In our model, the rock wall is represented by a cubic body with vertically inclined slopes. To simplify the model, rock material is assumed to be homogeneous and no influences of topography, aspect, snow cover and spatial variability on permafrost thaw are incorporated (Gruber et al., 2004a, 2004b; Wirz et al., 2011). This provides us with a model with the three components rock mass, rock discontinuities and snow cover (Fig. 5.9).

5.3.3.1 Homogeneous rock walls

Intact rock contains air-, water- or ice-filled pores and material as well pores determine thermal properties. Heat transfer occurs primarily in a conductive way. Thermal conductivity (*k*) of metamorphic and igneous rocks approaches 1.5-3.5 W m^{-1} K^{-1}, while sedimentary rocks approach 2-4 W m^{-1} K^{-1} (Vosteen and Schellschmidt, 2003). If a phase transition occurs, latent heat transfer needs to be included because it slows down the conductive heat transfer. The stability of the rock wall is determined by intact rock-shear strength. Warming of frozen rock from -10°C to 0°C decreases uniaxial compressive strength by 20-50 % and tensile strength by 15-70 % (Mellor, 1971, 1973).

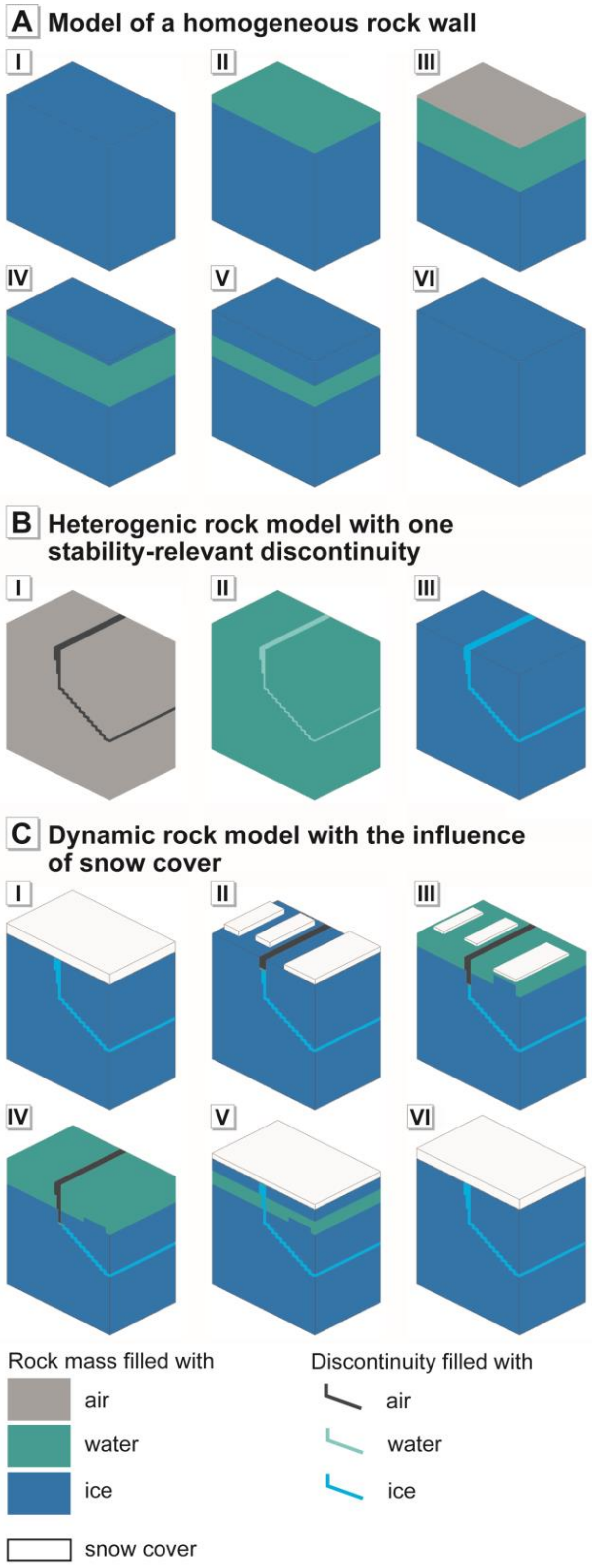

Fig. 5.9 Graphical representation of the three model components in different periods of temporal development: A: Temporal permafrost development in a homogeneous rock mass. B: Heterogenic rock mass with a rock discontinuity (fracture) filled with air (I), water (II) and ice (III). C: Temporal development of a rock mass and of rock discontinuity influenced by snow cover.

In a rock wall, active-layer distribution and permafrost thaw varies during the year. In winter (Fig. 5.9 A, periods I and VI), the entire rock wall is frozen and uniaxial compressive strength and tensile strength are high. In late spring (Fig. 5.9 A, period II), an active-layer develops due to thawing. The stability of the thawing rock wall components decreases as a result of decreasing compressive and tensile strength. Active-layer depth increases until late summer (Fig. 5.9 A, period III) and near surface areas can dry out. Downward freezing from the surface to the rock interior in late autumn and early winter (Fig. 5.9 A, period IV - V) results in an increase of shear resistance.

5.3.3.2 Heterogenic rocks with a critical path discontinuity

Discontinuity patterns and mechanical properties of discontinuities are a key controls of stability. A rock wall with a critical path discontinuity, the stability of the separated block is controlled by discontinuity properties.

5.3.3.2.1 Air-filled discontinuity

Rock model I in Fig. 1 B shows an air-filled discontinuity. The conductive thermal heat transfer in the rock mass is disturbed by seasonal patterns of convective heat flow in the discontinuity (Moore et al., 2011). The daily and seasonal air circulation is dependent on density contrast (Kamai et al., 2009), pressure contrast between air in discontinuities, the atmosphere and barometric pressure changes as sources of convective heat flow. In winter, the convective heat flow cools the discontinuity and warms it in summer. Mechanic properties are determined by gravity-induced shear force (*A)*, fracture of cohesive rock bridges (*a*) and friction along fractures with rock-rock contact (*b*), so that equation (5.19) can be extended to:

$$FS = \frac{a+b}{A}\,. \qquad (5.20)$$

For derivation of fracture of cohesive rock bridges (*a*) and total friction along fractures with rock-rock contact (*b*) see Krautblatter et al. (2013) Equations (5) and (6), respectively. The authors identified the compressive strength (σ_u) and the fracture toughness (K_C) as temperature sensitive.

Conductive and convective heat transfer can transmit thermo-elastic heat stresses to larger depths and can cause deformations and critical stresses at greater depths (Moore et al., 2011). Gischig et al. (2011a, 2011b) observed this phenomenon in a non-permafrost slope at the Randa rockslide.

5.3.3.2.2 Water-filled discontinuity

Rock model II in Fig. 1 B shows the water-saturated rock wall with a water-filled discontinuity. We assume the existence of an aquiclude that seal the discontinuity and prevent seepage. Without movement, water transports heat in a conductive way (k = 0.5 W m^{-1} K^{-1}). If the water flows, heat will be transported as advective process. Changing water columns causes changes in hydrostatic pressure (B) and can act to seasonally and abruptly increase the shear force. Equation (5.20) can be extended to:

$$FS = \frac{a+b}{A+B}. \tag{5.21}$$

The high relief of mountain areas increases the rates of vertical groundwater flow and, thus, the perturbation of the thermal regime due to advective processes (Forster and Smith, 1989). Water infiltration depends on groundwater level. High groundwater levels result in surface run-off, unsaturated underground leads to vertical water transport to the groundwater level (Forster and Smith, 1989). The permeability of discontinuities is orders of magnitude higher than the pore system and depends on discontinuity aperture, roughness and filling material (Dietrich et al., 2005). To simplify our model, we exclude infilled discontinuities. Open discontinuities are preferential paths of water flow (Dietrich et al., 2005) and permafrost sealing significantly alters flow paths. In addition, turbulent flow in rough fractures is presumably highly effective in terms of heat exchange (Beven and Germann, 1982; Witherspoon, 2000).

5.3.3.2.3 Ice-filled discontinuity

When water in discontinuities freezes, phase transition occurs, latent heat is released and discontinuity infill change to ice (Rock model III in Fig. 5.9 B). Ice transports heat in a conductive way (k = 2.5 W m^{-1} K^{-1}) and without occurring phase transitions ice is an effective thermal conductor of cold thermal impulses. Ice can act like an aquiclude and seals the discontinuities. Perched water above permafrost can exhibit enormous localized hydrostatic pressures (*B*) as described in equation (5.21). The freezing of water to ice results to a volume expansion of 9% and a freezing pressure (*C*) (Equation 5.22) up to 207 MPa develops (Matsuoka and Murton, 2008). To develop effective ice pressures, a high saturation degree (Walder and Hallet, 1986) and high cooling rates (Matsuoka, 1990a) are necessary. Cryostatic strain relaxes with time (Tharp, 1987). Ice deformation and ice extrusion into free spaces or into other open discontinuities reduces ice pressure (Davidson and Nye, 1985; Tharp, 1987), whereupon confining water increases ice pressure (Tharp, 1987). Unfrozen water can exist at temperatures at -10°C (Mellor, 1970). This water is able to migrate to freezing centre of rocks (Everett, 1961; Fukuda, 1983). It is responsible for ice segregation (Walder and Hallet, 1985; Murton et al., 2006). This process is most effective in the temperature range between -3° and -6°C (Hallet, 2006) and develops pressures (*C*) up to 20 to 30 MPa (Hallet et al., 1991). For deep shear planes (> 10 m), reduced temperature gradients and water availability combined with increased normal stress will counteract formation of ice (Konrad and Morgenstern, 1982; Nixon, 1982; Clark and Phillips, 2003). Wegmann & Gudmundsson (1999) assume that ice in discontinuities works like frost-wedging but ice segregation models and frost-wedging were never investigated in natural surroundings. Cryostatic pressure increase corresponds with expansion of clefts, thawing and cryostatic pressure decrease with contraction observed at the Jungfraujoch (Wegmann and Gudmundsson, 1999) and the Matterhorn (Hasler et al., 2012) in Switzerland.

If ice thaws, ice pressure will decrease but hydrologic pressure increase due to ice meltwater. Equation (5.21) can be expended to equation (5.22):

$$FS = \frac{a+b+c+d}{A+B+C}. \qquad (5.22)$$

Freezing significantly increases K_C and σ_u (see Krautblatter et al. (2013) Equation (5) and (6) for details). Shear strength of ice-filled fractures is a function of normal stress and temperature and declines with increasing temperature of ice (Davies et al., 2000; Davies et al., 2001, 2003; Guenzel, 2008). Krautblatter et al. (2013) developed an empirical relationship for failure of ice-rock contacts (*c*) based on experiments and developed a temperature dependence of creep of ice (*d*). In summary, the critical fracture toughness K_C, the uniaxial compressive strength σ_u and temperature T_C and T_K are sensitive to warming in their rock-ice mechanical model (see Equations (2-3) and (5-8) herein).

5.3.3.3 Dynamic rock model with influence of snow cover

In winter (Fig. 5.9 C, period I and VI), the rock wall is frozen and the discontinuity is ice-filled. The rock surface is covered by a thick snow cover (>80 cm) with high thermal resistance insulates the underground (Keller and Gubler, 1993; Luetschg et al., 2008). Due to frozen status, the sensitive parameters of shear resistance of critical fracture toughness, uniaxial compressive strength and temperature T_C and T_K are higher than in unfrozen status. Shear force is dominated by gravity and cryostatic pressure while hydrostatic pressure is absent. In rock walls, snow cover depends on slope morphometry, roughness of the underground's surface, aspect and wind (Phillips, 2000). The spatial distribution is affected by snow fall and wind as well as to lesser extent by slope angle (Wirz et al., 2011). Avalanches and wind redistribute snow. On rock walls, snow accumulates in patterns with maximum accumulation behind ridges. In a less inclined alpine catchment area, Grünewald et al. (2010) observed a heterogeneous snow cover distribution with maximum snow depth as snow cornices and snow-free areas on ridges and knolls. Snow cornice and effects on permafrost in steep rock walls are observed by Krautblatter and Draebing (2014). Snow remains longer in areas of higher snow accumulation (Grünewald et al., 2010). Based on these empirical evidences it seems reasonable to include snow depth distribution in studies concerning snow influence on permafrost.

In late spring or early summer (Fig. 5.9 C, period II and III), solar energy is consumed by snow melting. Areas with low snow depth melt out faster and melting increases from snow-free areas to the edges of snow patches due to albedo and surface temperatures (Essery and Pomeroy, 2004; Grünewald et al., 2010). Snow melting results in zero-curtain effects, the underground surface temperature stagnates at 0°C (Luetschg et al., 2008), and no thawing of the underground occurred. Permafrost can influence the duration of snow cover and snow cover insulates permafrost (Phillips, 2000). If meltwater flows over snow-free rock, the water can heat the underground and transport advective heat to the discontinuity system leading to ice erosion in fractures (Hasler et al., 2011a). This ice erosion process is controlled by the amount of water (Hasler et al., 2011a) and decreases the shear resistance of ice-ice and rock-ice contacts and reduces the cryostatic pressure (C in equation 4). If the water is trapped in the rock mass, meltwater fills the fracture system, builds up hydrostatic pressure (B) and can eventually refreeze and cause cryostatic pressure (C). Such behaviour like advective water transport in fractured permafrost rock as well as fracture opening coincident with meltwater onset and infiltration was observed by several authors (Wegmann and Gudmundsson, 1999; Krautblatter, 2010; Hasler et al., 2012).

In late summer (Fig. 5.9 C, period IV), permafrost thaws up to several meters. The permafrost thawing pattern is affected by snow distribution. The duration of snow cover affects depth and intensity of permafrost thaw (Luetschg et al., 2008). Permafrost thaw decreases the mechanical strength of the rock mass. Ice erosion continues to larger depths and further decreases shear resistance of the ice itself and rock-ice contacts.

When air temperatures decrease in late autumn (Fig. 5.9 C, period V), freezing from the surface into the rock wall occurs. Convective heat transfer transports cold air into the discontinuity (Moore et al., 2011). Water in fractures freezes and cryostatic pressure increases resulting in dilation of the cleft system (Wegmann and Gudmundsson, 1999; Hasler et al., 2012). Thin snow cover causes enhanced ground cooling (Keller, 1994; Phillips, 2000). In summary, we use equation (5.22) to describe these coupled processes. Freezing of rock increases the uniaxial compressive strength of the rock mass, of rock bridges (*a*) and rock-rock contacts (*b*). Cleft ice cooling increases rock-ice contacts (*c*) and ice stability (*d*) itself. Cleft water changes from water to ice resulting in a cryostatic pressure (*C*) increase which temporarily exceeds the hydrostatic pressure (*B*) decrease. A snow cover accumulates in time and insulates the underground from further cooling (Fig. 5.9 C, period VI). Our model assumes a complete freezing of the underground.

5.3.4 Coupling of the rock matrix with rock discontinuity

To simplify the model, only the effects of discontinuity filling with air, water or ice in terms of thermal or mechanical effects were considered. The discontinuity is coupled with the rock matrix and feedbacks between the system components occur by exchange processes between the discontinuities and the rock matrix. In relation to the rock, matrix diffusion processes (Dietrich et al., 2005) and effective porosity (Sass, 2005a) are relevant. If, due to advective processes ice in fractures thaws faster than the surrounding rock, a thermal gradient develops. Conductive processes will occur and heat will be transmitted from the fracture to the surrounding rock mass. Additionally, advective heat transport in fractures can warm up the surrounding rock to a certain degree (Hasler et al., 2011a). Ice erosion consumes energy and water in fractures cools down due to surrounding rock temperatures (Krautblatter, 2010). Refreezing of water can occur and produce cryostatic pressure. If fracture walls provide sufficient thermal energy, the cooling of melt water is prevented and the process of ice erosion amplifies. Effects of fracture opening and closure have been observed in the field (Wegmann and Gudmundsson, 1999), modelled and tested in the laboratory (Davidson and Nye, 1985; Tharp, 1987; Hasler et al., 2011a).

5.3.5 Seasonal scale

In this section we discuss Fig. 5.10 from the left (spring) to the right (winter). The temporal evolution of snow cover is described in a 4-stage model by Luetschg et al. (2008) including (i) the fully insulating snow stage, (ii) the range of time shift of total snow melt, (iii) the snow-free stage and (iv) the early winter thin-snow cover stage.

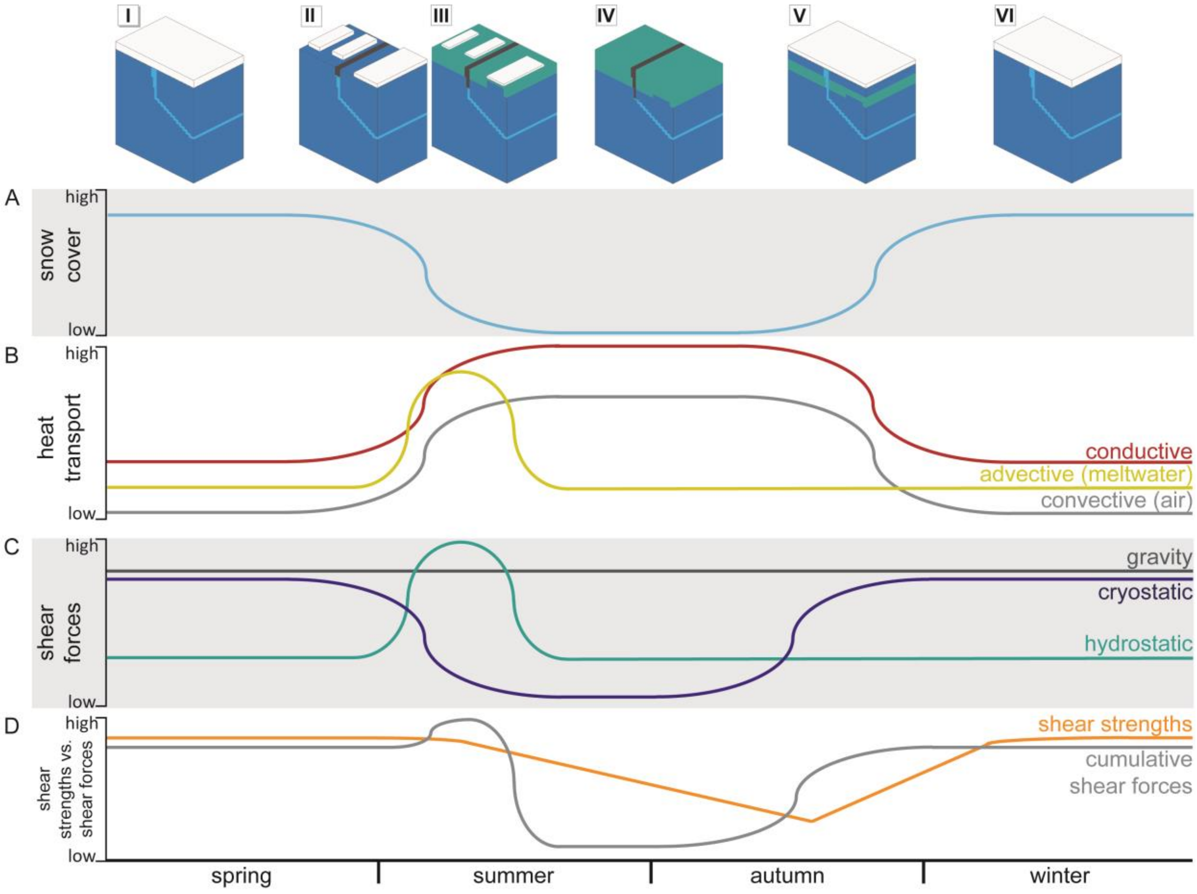

Fig. 5.10 Temporal evolution of snow cover, thermal heat transfer, shear forces and shear resistance using the graphic representation of Fig. 5.9 C in 4 seasons.

The shear force driven by gravity is virtually constant on a seasonal scale. Cryostatic pressure is driven by ice segregation and volumetric expansion. Ice segregation is effective in a temperature window of -3 to -6°C (Hallet et al., 1991) and significantly concentrates in the transition zone between active-layer and permafrost due to downward migration of water in summer and upward migration of freezing in winter (Murton et al., 2001; Murton et al., 2006). Volumetric expansion is most effective at a high degree of saturation (Walder and Hallet, 1986) and a high cooling rate (Matsuoka, 1990a). High saturated areas in rock walls, which are affected by near the surface during short-time freeze-thaw cycles, are between 10 and 30 cm depth (Sass, 2005a; Matsuoka and Murton, 2008). Shear force will increase due to cryostatic pressure resulting in rock breakdown in the range of debris fall. Annual cycles reaching depths up to 5 m (Matsuoka et al., 1998) conducting significant higher rock breakdown sizes. Freezing can cause water suction (Everett, 1961) which causes ice lens growth and, thus, enhanced cryostatic pressure.

During the fully insulated stage, the snow cover (Fig. 5.10 A) insulates the underground and prevents conductive or advective processes (Fig. 5.10 B) in the underground (Luetschg et al., 2008) and convective cooling in fractures (Hasler et al., 2011b). The underground is frozen and cryostatic pressure (Fig. 5.10 C) due to volumetric expansion and ice segregation occurs. Shear strengths (Fig. 5.10 D) are high due to the frozen status and low temperatures.

When the snow cover melting starts (Fig. 5.10 A), the advective warming of the underground begins coincidently (Fig. 5.10 B). Advective warming is more effective if water can heat up above snow-free warm rock causing ice erosion in fractures (Hasler et al., 2011a). The process can be amplified when fracture walls are conductively warmed-up. Conductive warming of the underground starts but is very slow in this period due to latent energy consumption. Convective heat transfer in snow-free and ice-free fractures can result in additional warming (Hasler et al., 2011b; Moore et al., 2011). Snow melt delivers water that causes hydrostatic pressures (Fig. 5.10 C) (Huggel et al., 2008) especially in fractures sealed by permafrost ice. Shear strength (Fig. 5.10 D) decreases due to thawing and increasing of ground temperatures (Huggel et al., 2010).

With decreasing snow melt, advective heat transport decreases coincidently and hydrostatic pressure increase is stopped. Active-layer thaw can slow-down this decrease by water delivery. During the snow-free period (Fig. 5.10 A), conductive and convective warming (Fig. 5.10 B) are dominant, advective warming-up only occurs due to permafrost thaw or as response to summer rainfall. Thawing of the active-layer increases the water availability at the base of the active-layer, refreezing of water causes ice lenses growth amplified by developing water gradients towards the freezing ice lenses resulting in cryostatic pressure increase (Fig. 5.10 C) (Murton et al., 2006). With maximum active-layer thaw, shear strengths (Fig. 5.10 D) are on the lowest seasonal level.

In the early winter thin-snow cover stage (Fig. 5.10 A), thin snow cover enhances ground cooling due to conductive processes (Fig. 5.10 B) (Keller, 1994; Phillips, 2000). Snow cover prevents convective processes due to insulating (Hasler et al., 2011b; Moore et al., 2011) and advective processes by storing water as snow. Water storage prevents the hydrostatic pressure (Fig. 5.10 C) increase. Freezing of subsurface water causes volumetric expansion and cryostatic pressure increase, while hydrostatic pressure decreases. Cooling and freezing of the underground increases shear strengths (Fig. 5.10 D). With further snow accumulation maximum insulation is achieved again and conductive cooling is finished.

In summary, two theoretical critical time windows can be observed (Fig. 5.10 D): (i) in early summer, high hydrostatic and imminent cryostatic pressure cause enhanced shear forces which might even exceed the high shear resistance of frozen rock. (ii) In autumn, shear forces might increase faster than the shear resistance and cause a second peak of instability.

5.3.6 Empirical field observations

To validate our conceptual approach, we use geophysical and kinematic data from our study site Steintaelli. The Steintaelli is located on the crestline between Turtmann Valley and Matter Valley (3050 – 3150m a.s.l.) in the Swiss Alps (Fig. 5.11 A). Lithology consists of slaty paragneis and deep 30 cm wide and many meters deep ice-filled discontinuities are common. For detailed study site description and methodological background of Seismic Refraction Tomography (SRT) see Krautblatter and Draebing (2014). Rock mass and discontinuity analysis by purely mechanical methods indicate stable conditions (Halla et al., 2014). In 2012, Mean Air Temperature (MAT) was average in July (4.0°C), but August (6.4°C) was the second warmest since the heat summer 2003 (Fig. 5.11 B). MAT was comparable warm in July (6.0°C) and August 2013 (5.1°C). Snow depth was measured manually with snow poles along the SRT transect before the seismic measurement. A 4 m wide and up to 1.4 m thick snow cornice occupied the crestline in August 2012 (Fig. 5.11 C). In August 2013 (Fig. 5.11 D), a 7 m wide, up to 1.6 m thick snow patch covered the lower north slope, while a 5 m wide, up to 1.85 m thick cornice covered the crestline. According to SRT active-layer thawed up to 15 m on the north facing slope and more than 10 m on the south facing slope (Fig. 5.11 E) in 2012. On the crestline, near surface frozen areas and permafrost in 10 m depth were preserved. In 2013, the snow covered areas were frozen up to the surface (Fig. 5.11 F). In snow-free areas, active-layer thawed up to 5 m depth on the north face and more than 10 m on the south slope.

A crackmeter with incorporated temperature logger was installed to monitor crack movement on the crestline (Fig. 5.11 E-F). Rock Surface Temperature (RST) (Fig. 5.11 G) and crack movement (Fig. 5.11 H) were recorded. Timing of snow cover was reconstructed using 24h standard deviation threshold of 0.3 K developed by Schmidt et al. (2009). RST fluctuates until a -15°C temperature drop on October 27th 2012 occurred. Coincidently discontinuity opened 0.6 cm. RST increase close to 0°C resulted in 0.2 cm closing of the discontinuity. From end of November on, snow cover insulated the underground until mid of July 2013 (light grey area in Fig. 5.11 G-H). Discontinuity opened 0.05 cm as a possible result of segregation ice during this period. From mid-July on, a zero-curtain established (dark grey area in Fig. 5.11 G-H) indicating meltwater activity. Discontinuity closed continuously 0.1 cm until a sudden 0.1 cm discontinuity closing occurred on August the 3rd.

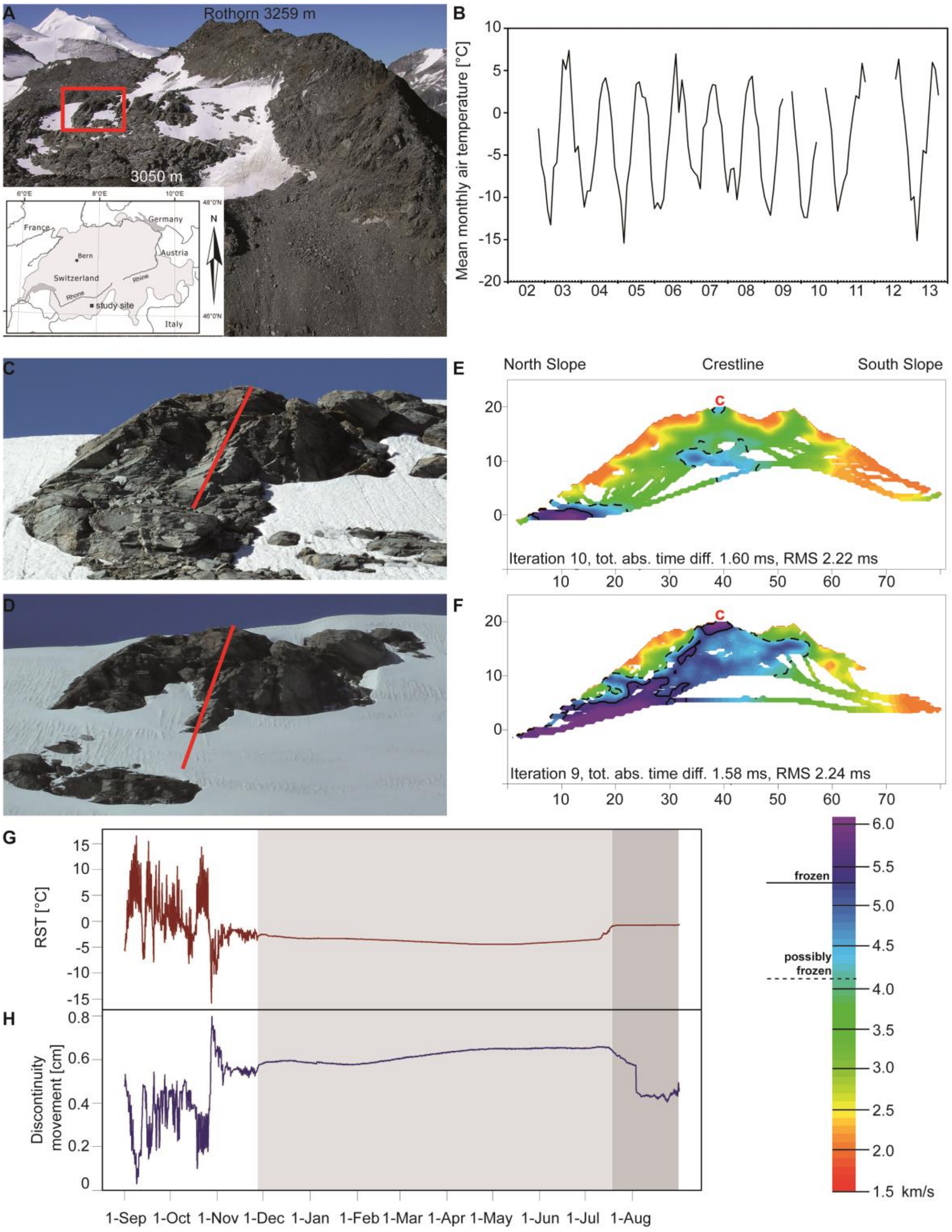

Fig. 5.11 Examples from Steintaelli. A: View of Steintaelli in southern direction, red rectangle shows location of the observed rock wall; B: Mean monthly air temperature in the Steintaelli 2002-2013; C and D: Snow cover in 2012 and 2013, E and F: Seismic Refraction Tomography of north slope (red line in C and D), crestline and south slope with legend below, c shows location of the crackmeter; G: Rock Surface Temperature and H: Discontinuity movement of crackmeter for September 2012 until August 2013.

5.3.7 Time scale and path dependence

The conceptual framework of our model approach is related to classical geomorphic concepts. Verleysdonk et al. (2011) transferred the geomorphic sensitivity concept developed by Brunsden & Thornes' (1979) to mountain permafrost systems. Sensitivity is described by a system's predisposition towards change and its ability to absorb impulses of disturbing events. This sensitivity concept can be applied to our approach of system resistivity using the factor of safety (equation 1) as failure criterion. The temporal development of the rock and ice mechanical system status is based on the approach of path dependence (historicity) of slope instability suggested by Schumm (1973) (Fig. 5.12). The rock-mechanical system status depends on slope morphometry, material properties and processes. Material properties are lithology, discontinuity patterns and permafrost structure and status (Verleysdonk et al., 2011). Discontinuity patterns are developed by tectonic processes, glacial debuttressing, ambient stress patterns and weathering (Matsuoka, 2001b; Murton et al., 2006; McColl et al., 2010; McColl, 2012). Internal processes, e.g. ice segregation, can alter the system status causing sensitivity increase, which alter the rock-mechanical system status and result in slope failure at time A due to passing the internal instability threshold (Fig. 5.12).

External impulses, e.g. air temperature change, snow cover and snow melt, lead to complex internal responses resulting in different active-layer thaw depth. Active-layer thaw (4 in Fig. 5.12) changes the shear forces and decreases the shear resistances of the system. The magnitude of thawing can result in failure at time B due to passing an external threshold. "Threshold passing" is dependent on system status resulting in non-linear behaviour of rock instability. Active-layer freezing (5 in Fig. 5.12) results in increasing shear strength and increasing cryostatic pressure. Active-layer thawing and active-layer freezing operate on a seasonal scale with different processes (Fig. 5.10).

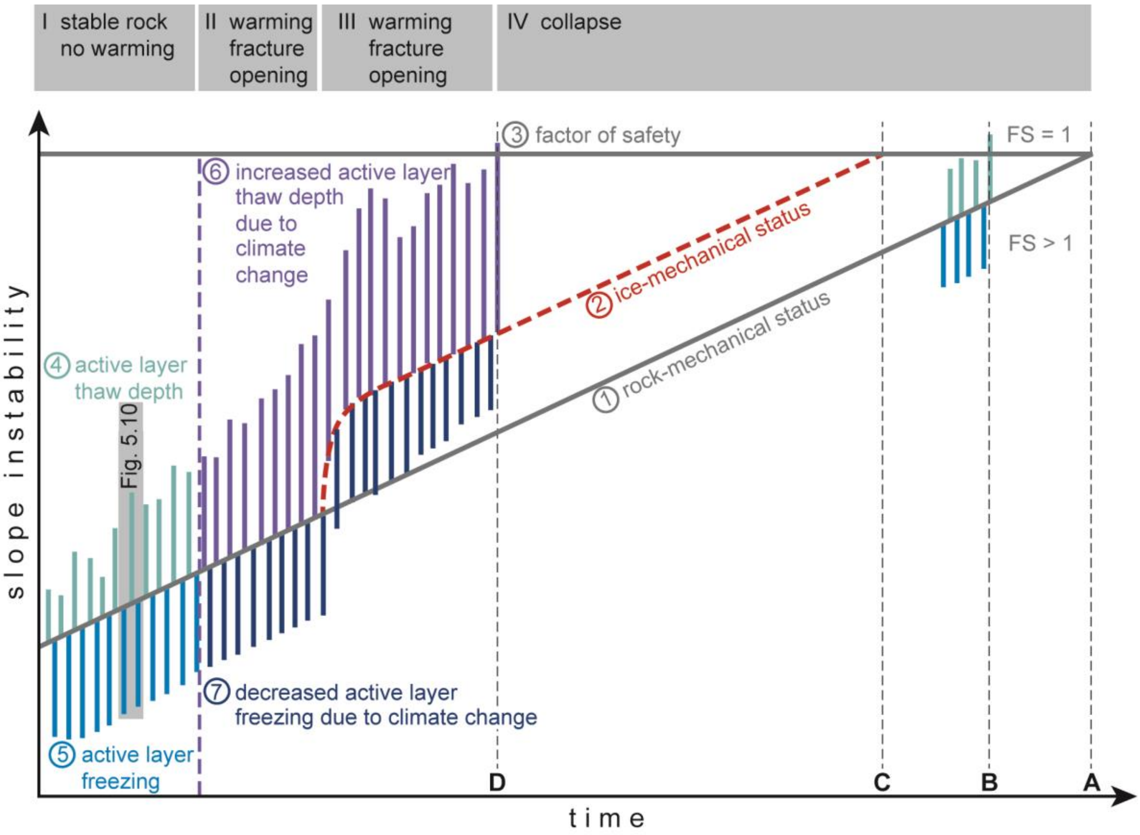

Fig. 5.12 Development of slope instability through time of a permafrost rock system. In longer time scales the rock-mechanical instability (1) increases in time and is amplified by the influences of the ice-mechanical system status (2). Failure occurs when the factor of safety (3) equals 1. On an annual time scale active-layer thaw (4) and active-layer freezing (5) seasonally change the instability of the rock-mechanical system. If the rock system is significantly affected by cleft ice rise of air temperature leads to active-layer thaw (6) increase and active-layer freezing decrease (7) (after Schumm (1973)). Seasonal scale of Fig. 5.10 is denoted by a grey rectangle.

Krautblatter et al. (2013) point out that slow rock deformation at the beginning of the rock decay processes is caused by the progressive failure of rock bridges and changing frictional resistance. After the fatigue of rock bridges, acceleration of dislocations will be governed by creep of ice, failure of rock-ice contacts and friction of rock-rock contacts. Warming of permafrost will promote the development of new shear planes and accelerating failures occur controlled by ice mechanics (2 in Fig. 5.12). The system status is transferred from a rock-mechanical to a more sensitive ice-mechanical state. The system leaves the attractor’s phase space and develops a new trajectory as response to rock bridge failures. This means, that historicity (Schumm, 1991) and processes with long relaxation times, the e.g. paraglacial cycle (Church and Ryder, 1972; Ballantyne, 2002), has to be considered as two different types of path dependence. The internal system development changes the condition for failure and results in failure at time C.

Climate change anticipates a 0.25°C warming per decade until mid of the 21st century and an accelerated 0.36°C warming for the second half for the European Alps based on the A1B emission scenario (Gobiet et al., in press). Additionally, frequency of short term warm air temperature extreme events will increase (Huggel et al., 2010; Marmy et al., 2013). Warming will increase anomalously at higher elevations, precipitation will decrease in summer and increase in winter (Gobiet et al., in press). Above 1400 ±200 m precipitation is more important than temperature for snow pack variability, but threshold altitude will increase due to atmospheric warming (Morán-Tejeda et al., 2013). The shift of precipitation corresponds with a shortening of the snow season (Bavay et al., 2009). Effects of a changed snow season and climate change on underground temperatures are simulated by several authors for rock glaciers and debris-covered rock slopes (Luetschg and Haeberli, 2005; Luetschg et al., 2008; Engelhard et al., 2010; Marmy et al., 2013; Scherler et al., 2013). The authors argue that timing and duration of snow cover is the key control of active-layer thickness. The impact of climate change on the snow-covered period will increase the snow cover but not necessarily prolong the snow cover duration (Marmy et al., 2013). The higher snow cover and short duration warm periods can produce a critical input of water due to more snow melt and coincidently more advective heat transfer as well as hydrostatic pressure (Huggel et al., 2010; Marmy et al., 2013). Due to shorter snow season, ablation and coincidently active-layer thaw can begin earlier, the snow free period prolongs and active-layer thaw reaches larger depths (Luetschg et al., 2008).

Most sensitive is the autumn, when warming of the air temperature can be close to the transition temperature between rain and snow (Marmy et al., 2013). Instead of enhanced cooling due to thin-snow cover effect, rain in combination with positive temperature will prolong the snow-free period and increase active-layer thaw by delivering heat due to increasing advective and conductive heat transfer. Scherler et al. (2013) distinguish two phases of climate sensitivity. In the first phase, slow warming of permafrost body begins with slightly increasing active-layer thaw combined with absence of complete freezing in winter. Permafrost degradation starts in the second phase by gradually active-layer depth increase. Sensitivity of rock permafrost is higher than permafrost in debris-covered slopes or rock glaciers due to lower porosities and, thus, lower ice content. Active-layer will thaw to deeper depth and shear resistance will coincidently decrease (6 in Fig. 5.12). Freezing of the active-layer increases the shear resistance (7 in Fig. 5.12) and can stabilize the system seasonally. Cryostatic pressure will be reduced and spatial occurrence of ice segregation will dislocate to deeper depths as a result of deeper active-layer thawing (Murton et al., 2001; Murton et al., 2006; Matsuoka and Murton, 2008).

The shift from a rock-mechanic system status to a more sensitive ice-mechanic system status as well as the combination with high-magnitude impulses due to temperature increase and snow cover length decrease resulting from climate change will achieve a deeper active-layer permafrost thaw and, thus, an earlier condition of failure due to external threshold crossing. This results in failure at time D (Fig. 5.12).

5.3.8 Model validation

High snow cover (Fig. 5.10 A) isolates the underground and decreases heat transport processes (Fig. 5.10 B). Decreased heat transport results in lower active-layer thaw and higher shear strength (Fig. 5.10 D). In 2012 and 2013, climate forcing by temperature were in a comparable range (Fig. 5.11 B) in the Steintaelli but snow cover differed significantly (Fig. 5.11 C-D). The snow cornice and snow patches (Fig. 5.11 D) insulated the underground and decreased heat transport while in snow-free areas heat transport was significantly higher. As a result, active-layer thawed to higher depths in snow-free areas in August 2012 and 2013 (Fig. 5.11 E-F). A thicker active-layer resulted in shear strength decrease of the thawed rock mass.

With decreasing snow cover (Fig. 5.10 A), heat transport processes increase (Fig. 5.10 B) active-layer thaw while cryostatic pressure (Fig. 5.10 C) and shear strength decrease (Fig. 5.10 D). Timing and duration of snow cover is a key control of active-layer thaw sensitivity (Luetschg et al., 2008; Marmy et al., 2013; Scherler et al., 2013). In 2012 (Fig. 5.11 C), snow cover melted earlier than August 2013 (Fig. 5.11 D) and as a result heat transport processes started earlier. Active-layer thawed to a higher depth (Fig. 5.11 E).

During low snow cover (Fig. 5.10 A), cooling of the underground starts in autumn results in freezing and cryostatic pressure increase (Fig. 5.10 C), while shear strength is still low (Fig. 5.10 D) due to deep active-layer thaw. The rapid cooling on October 27th 2012 (Fig. 5.11 G) refroze the water in the discontinuity; cryostatic pressure developed resulting from volumetric expansion. Shear strength of the unfrozen active-layer was low and the discontinuity opened (Fig. 5.11 H), thus, the discontinuity opening confirms the critical time window of instability in late autumn. With freezing of the active-layer shear strength increases (Krautblatter et al., 2013), while cryostatic pressure could not counter the shear strength increase, as a result the discontinuity closed slightly until late November (Fig. 5.11 H). Snow cover insulates the underground (Fig. 5.10 A) preserving high shear strength (Fig. 5.10 D) and high cryostatic pressure (Fig. 5.10 C). Crackmeter showed a discontinuity opening of 0.05 cm during the snow cover period (Fig. 5.11 H) reflecting high cryostatic pressure and high shear strength.

In early summer, snow cover melts (Fig. 5.10 A) and as a result hydrostatic pressure increases while cryostatic pressure decreases (Fig. 5.10 C). The sudden discontinuity closing during zero-curtain observed by the crackmeter on August the 3rd (Fig. 5.11 H) may imply cryostatic pressure decrease due to ice erosion. However, hydrostatic pressure increase was apparently not adequate or cryostatic pressure decreased too much coincidently to enlarge the discontinuity. Below the crackmeter, subsurface was totally frozen (Fig. 5.11 F) indicating high shear strength while snow-free areas thawed due to earlier and, thus, deeper reaching heat transfer processes. Frozen active-layer increased shear strengths which eventually counteract discontinuity opening and a critical time window of instability was not observable. However, Blikra and Christiansen (2014) observed increased deformation during snowmelt and assume ice warming and thaw as a trigger of deformation at Jettan rockslide. Hydrostatic pressure increased due to snowmelt while shear strength was reduced by ice warming (Krautblatter et al., 2013). Huggel et al. (2010) suggest hydrostatic pressure increase and shear strength decrease due to snowmelt as a trigger of the Mt. Stellar rock failure in 2005.

The data confirms our conceptual approach. Stability changes seasonally and is lowest during active-layer thaw. On a long scale, the sensitivity of the system depends on system status (Fig. 5.12). The crackmeter showed discontinuity opening but also equivalent reverse deformation by closing, thus, discontinuity remained on a same level on an annual scale. The Steintaelli rock wall is actually stable (Phase I in Fig. 5.12), however, climate change can alter snow conditions (Bavay et al., 2009; Gobiet et al., in press) and increase active-layer depth (Luetschg et al., 2008; Marmy et al., 2013) and seasonal instability. Data by Blikra and Christiansen (2014) suggest that Jettan rockslide is probably in an ice-mechanical status (Phase II). Discontinuities opened in a non-reversible way during snowmelt periods by ice thawing or warming.

5.3.9 Conclusion

In this paper, we present a conceptual approach for snow cover influences on steep permafrost rock walls. This approach is based on the 4-stage snow cover model by Luetschg et al. (2005; 2008), heat transfer due to conductive, convective and advective processes and mechanical response conceptualized by Krautblatter et al. (2013).

(1) On seasonal scale, two theoretical critical seasonal instability time windows can be observed in early summer, where combined hydrostatic and cryostatic pressure cause a peak in shear force exceeding high frozen shear resistance and in autumn, where shear forces increase faster than the shear resistance. Crackmeter measurements at Steintaelli showed an increasing instability in autumn due to rapid refreezing and probably coincident volumetric expansion of ice in discontinuities.
(2) On a system scale, the system state is important. The rock-mechanic trajectory can change path-dependent into an ice-mechanical system state more sensitive to seasonal permafrost thaw. Climate change can amplify the impulse leading to higher magnitude active-layer thawing. System stability can be excessed by internal processes, e.g. weathering processes, or external processes, e.g. active-layer thaw.

Our holistic approach enhances the understanding of participating and interacting processes. This approach represents the frame work for future studies and facilitates the placement of these studies in the system context.

Acknowledgements

This study is part of ISPR (Influences of Snow Cover on thermal and mechanical processes in steep permafrost rock walls)-project (KR 3912/1-1) financed by German Research Foundation (DFG). The authors thank G. Storbeck for improving the figures and both reviewers for significantly improving the manuscript.

5.4. Synthesis of the geomorphological system

Rock slopes can be regarded as paraglacial geomorphic systems. To avoid misunderstandings, the terms periglacial, paraglacial and proglacial need to be defined. According to Slaymaker (2009) or Worsley (2004), the term periglacial is on the one hand used for an environment, where frequent freeze-thaw cycles and deep seasonal freezing occurs, and on the other hand for a permafrost environment following the definition of French (2007). The term encompasses processes, landforms and landscapes (Worsley, 2004). Proglacial is used for processes and landforms in proximity to the glacier margin (Slaymaker, 2009), the proglacial zone moves with the glacier front (Embleton-Hamann, 2004). Unfortunately, there is no consistent use in literature (Embleton-Hamann, 2004). The paraglacial concept was introduced by Church and Ryder (1972) (Fig. 5.13 A); they describe paraglacial processes as non-glacial processes that are directly conditioned by glaciation or deglaciation.

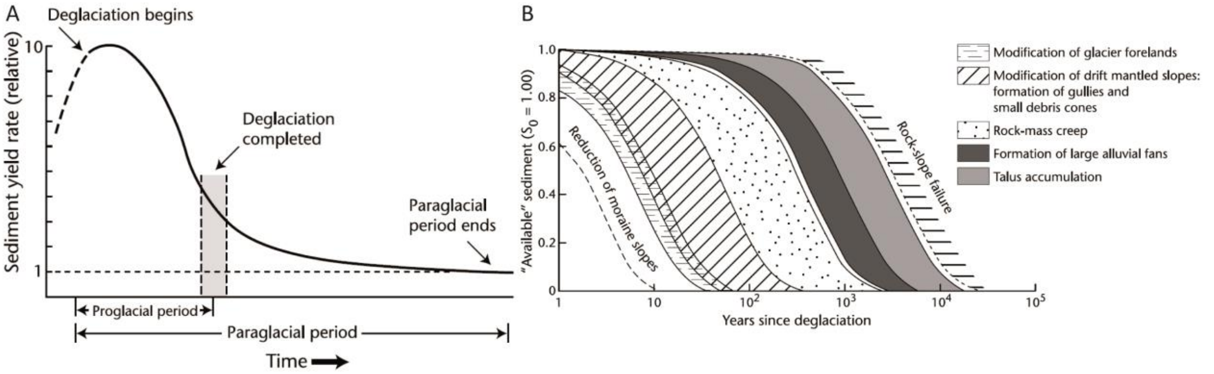

Fig. 5.13 A: The paraglacial concept according to Church and Ryder (1972) (Slaymaker and Kelly, 2007); B: Exhaustion curves for paraglacial subsystems according to Ballantyne (2002) (Slaymaker and Kelly, 2007).

Ballantyne (2002) extended the concept to sediments, landforms, landsystems and landscapes. He further divided the paraglacial system into several subsystems (Fig. 5.13 B); the rock slope system is affected by rock slope failures and possesses the longest response time of all subsystems. Paraglacial rock slope failures are reviewed in detail by McColl (2012); he distinguished preconditioning, preparatory factors and triggers. Permafrost and weathering both were classified as a preparatory factor and as trigger. Other prepatory factors are debuttressing and glacial erosion, while lithology, intact rock strength, rock mass quality, joint characteristics are preconditioning factors (McColl, 2012). Verleysdonk et al. (2011) transferred the sensitivity concept by Brunsden and Thornes (1979) to mountain permafrost systems. Sensitivity describes the predisposition of a system towards change. System state is path-dependent (Schumm, 1973) and influenced by preconditioning and predisposing factors. If a threshold is crossed by an external trigger (extrinsic threshold) or an internal factor (intrinsic threshold) (Schumm, 1973), the system changes in terms of landform change (geomorphic threshold). On a seasonal scale, active-layer thaw is controlled by climatic conditions as well as snow and increases sensitivity short-term. Permafrost degradation increases sensitivity on a long-term scale. This thesis tries to improve the theory how snow influences the thermal and mechanical regime of permafrost rock walls and delivers new insights into system understanding.

6 Hypothesis

6.1 Theory

1) Snow is a major control of permafrost evolution on a slope facet scale.

2) Snow is a key control of rock decay and the near-surface mechanical regime.

3) Slope instability occurs in critical time windows.

6.2 Methodology

4) P-wave velocity is highly sensitive to freezing in rocks.

5) P-wave velocity can be used for high-resolution active-layer monitoring in steep rock walls.

6) Combined kinematics, piezometric measurements and thermal observation allow for an attribution of discontinuity displacements to different forcing processes.

6.3 System understanding

7) Insights gained by p-wave velocity measurements help to assess and anticipate critical stages of permafrost degradation in steep rock walls.

8) In critical stages, snow and ice distribution have a high impact on the spatial and temporal pattern of degradation.

9) These insights can be used to understand thresholds for critical system changes.

7 Snow Cover

The influence of snow cover on permafrost could be identified on flat terrain (Ishikawa, 2003), rock glaciers (Keller and Gubler, 1993; Keller, 1994; Hanson and Hoelzle, 2004) and gentle slopes (Phillips, 2000; Ishikawa, 2003; Luetschg et al., 2003; Luetschg et al., 2004; Luetschg and Haeberli, 2005). The influence strongly depends on the spatial and temporal snow distribution (Luetschg et al., 2008). Snow cover can be expressed as height and depth. On flat terrain, snow depth and snow height are identical. Snow height is considered normal to underground surface while snow depth is in gravitational direction (Luetschg, 2005). Due to slope angle, there can exist a significant difference between snow height and snow depth.

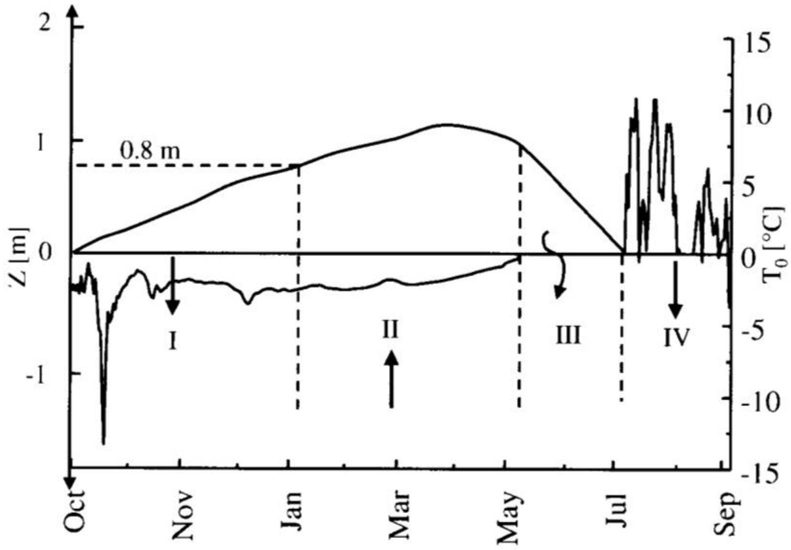

Fig. 7.1 Schematic ground surface temperature (T_0) with snow height (Z) plotted against time for snow stages I-IV (Luetschg, 2005).

Luetschg and Haeberli (2005) developed a four-stage model to describe the interaction between snow cover and permafrost (Fig. 7.1). During Stage I (thin-snow cover stage), a thin snow cover accumulates and the ground surface temperature (GST) is affected by cold air temperatures; this effect is called thin-snow cover effect (Phillips, 2000). After achieving a threshold snow height, the snow cover insulates the underground and GST is influenced by the thermal regime of the underground (Stage II). For Murtèl rock glacier, this threshold snow height is estimated as 0.6 m (Hanson and Hoelzle, 2004) or 0.8 m (Keller and Gubler, 1993), respectively. During Stage III meltwater percolates into the underground and a zero-curtain develops as a result of freezing and melting in the active-layer. In the snow-free Stage IV, the GST is affected by the incoming solar radiation and air temperature. Hanson and Hoelzle (2004) use a comparable 5-phase model with identical phases except Stage IV is further distinguished into two stages. Based on GST measurements Ishikawa (2003) classified four thermal regimes above permafrost under snow cover: (i) no sub-zero ground cooling throughout winter, (ii) direct atmospheric cold heat penetration throughout winter, (iii) ground cooling before the onset of snow accumulation and (iv) cold air funnelling and concentrating through blocky materials.

7.1 Methods for monitoring snow cover and effects

There are stratigraphic, thermal, geophysical, remote sensing and photogrammetric methods to monitor snow cover and effects. Stratigraphic methods include digging of snow pits to quantify snow height or depth, layering and physical snow properties. These properties comprise grain size, snow crystal morphology and density. Methods are described in the "International Classification for Seasonal Snow on Ground" (Fierz et al., 2009). Stratigraphic observations are used to quantify thermal effects (Pielmeier and Schneebeli, 2003) on a point scale. Pits located on different topographic locations of the slope can be used to quantitatively analyse spatial variability of snow cover. Repeated digging allows the evaluation of the temporal variability. The simplest method to quantify snow depth is by using an avalanche probe. Information is obtained on a point scale but a high amount of spatial measurements give information up to catchment scale (Anderton et al., 2002, 2004).

Meteo stations can automatically record snow depth with ultrasonic sensors on a point scale. Wind redistribution can bias the measurements. In the Swiss Alps, snow cover monitoring meteo stations like Interkantonales Mess- und Informationssystem (IMIS) or Ergänzungsnetz (ENET) are located on flat terrain and not on steep permafrost slopes (Luetschg, 2005; Egli, 2008).

The technique bottom temperature of the snow cover (BTS) developed by Haeberli (1973) is used as an indicator for permafrost occurrence. Snow depth and GST are manually measured in late winter. BTS values below -3°C of an insulating snow cover in February indicates probable permafrost occurrence (Haeberli, 1973; Keller, 1994). The manually derived BTS measurements are only valid for Ishikawa's (2003) thermal regime-type (iii) where ground cools before snow accumulation . Data loggers can be used to continuously monitor GST (Hoelzle et al., 1999) but without snow depth information. Several authors use statistical analysis of daily amplitude (Schneider et al., 2012), variance (Danby and Hik, 2007) or standard deviation (Schmidt, 2009; Schmidt et al., 2009; Schmid et al., 2012) of the measured data as indicator of insulating snow cover. Schmidt (2009) and Schmidt et al. (2009) established a standard deviation of lower than 0.3 K for 24 h of data recorded with data loggers. Snow occurrence was verified by terrestrial photography (Schmidt, 2009; Schmidt et al., 2009).

Ground Penetrating Radar (GPR) as a geophysical method is widely used to quantify snow depth and firn spatially; for reviews see Berthling and Melvold (2008) and Woodward and Burke (2007). Most applications are located on flat terrain in polar regions (Sand and Bruland, 1998; Marchand et al., 2001; Marchand and Killingtveit, 2001; Jaedicke and Sandvik, 2002; Jaedicke, 2003; Sand et al., 2003; Melvold, 2008), evaluate snow accumulations on glaciers and sea ice (Pälli et al., 2002; Machguth et al., 2006; Woodward and Burke, 2007; Galley et al., 2009) or snow water equivalent (Bradford et al., 2009). Continuous application of GPR was developed by Heilig et al. (2008; 2009) to monitor snow cover temporarily on a point scale. This application needs manual snow density measurements for calibration.

Remote sensing techniques are applicable for snow monitoring, but temporal and spatial resolution are insufficient for mountainous areas (Aschenwald et al., 2001). For a comprehending overview of remote sensing techniques see Derksen and LeDrew (2000) and Rees (2006). With a higher spatial and temporal resolution, photogrammetric approaches are applied to monitor snow cover distribution (Aschenwald et al., 2001; Mittaz et al., 2002; Luetschg, 2005; Schmidt, 2009; Schmidt et al., 2009; Schmidt, 2010; Eckerstorfer et al., 2013a; Eckerstorfer et al., 2013b), snow surface albedo (Corripio, 2004) and snow transport (Corripio et al., 2004). Snow poles were used to get additional information on snow depth (Christiansen, 2001; Christiansen, 2005; Vogel et al., 2012). Terrestrial Laserscanning with near-infrared scanners are used to measure snow depth distribution with high spatial resolution by comparing snow cover scans with snow-free reference scans (Prokop, 2008; Prokop et al., 2008). This technique was used in flat alpine terrain (Schaffhauser et al., 2008; Grünewald et al., 2010; Mott et al., 2010) and in steep rock walls (Wirz et al., 2011).

Several snow models exist which model snow on a 1D-scale, like CROCUS, SYNTHERM or SNOWPACK, 2D like SnowSim, or 3D like ALPINE3D. The Swiss model SNOWPACK enables local snow cover simulation and includes processes like snow settlement, heat transport, water vapour, liquid water and phase transition processes in the snow cover as well as bulk and energy exchange processes between snow and atmosphere (Bartelt and Lehning, 2002; Lehning et al., 2002). To investigate the interaction between snow cover and permafrost, SNOWPACK was extended with an underground tool and applied on a moderately inclined slope (Luetschg et al., 2003; Luetschg et al., 2004; Luetschg, 2005; Luetschg and Haeberli, 2005; Luetschg et al., 2008). On 3D scale, ALPINE3D is used to model spatial snow distribution (Lehning et al., 2006) and to evaluate snow transport processes (Lehning et al., 2008; Mott et al., 2008; Mott et al., 2010).

7.2 Data collection at Steintaelli

To analyse snow cover, snow distribution was detected continuously by automatic cameras. A meteo station was used to measure snow height, air temperature, wind speed and wind direction. Rock temperature loggers recorded GST continuously. Snow height was manually measured by avalanche probes before starting geophysical measurements.

In August 2012, two automatic snow cameras were installed at Steintaelli to monitor snow distribution on the NE-slope and the SW-slope (see Fig. 7.6 for pictures). Additionally, 17 rock temperature loggers were installed at different slope positions along a transect reaching from NE-slope across the crestline to the SW-slope by the WSL-Institut für Schnee- und Lawinenforschung (SLF) (Fig. 7.2). Five data loggers are located on the NE-Slope (N2-N6), five on the crestline (N1, C1-C4) and seven on the SW-slope (S1-S7), mostly along geophysical Transect 5. The temperature data loggers are iButtons DS1922L with an accuracy of ±0.5°C. They were installed in plastic tubes in 10 cm rock depth and record temperature every two hours from August 14th 2012 onwards. On October 18th 2012, the data loggers S6 and S7 were moved to the NE-slope (N7-N8). On September 28th 2012, a Sensorscope meteo station was installed north of the rock wall on top of the snow camera by the SLF to measure snow height, air temperature, wind speed and wind direction in a 1 h-resolution. Rock temperature data, meteo station data and snow camera photos are provided by Marcia Phillips and Anna Haberkorn (both SLF) for this work. Snow cover existence is calculated using the 24 h standard deviation threshold of < 0.3 K by Schmidt et al. (2009). The technique by Schmidt et al. (2009) was developed on a slope in the near-by Lötschental and snow cover existence was validated temporally and spatially with automatic cameras. The other techniques to derive snow cover from temperature data are purely empirical-derived on flat terrain and validation is missing. According to GST development and existence of snow cover, the GST are classified into the four stages of Luetschg and Haeberli (2005) (Fig. 7.1). Due to missing snow height measurements and an unknown threshold for isolation of snow cover in steep rock walls, Stage I and II are differentiated qualitatively.

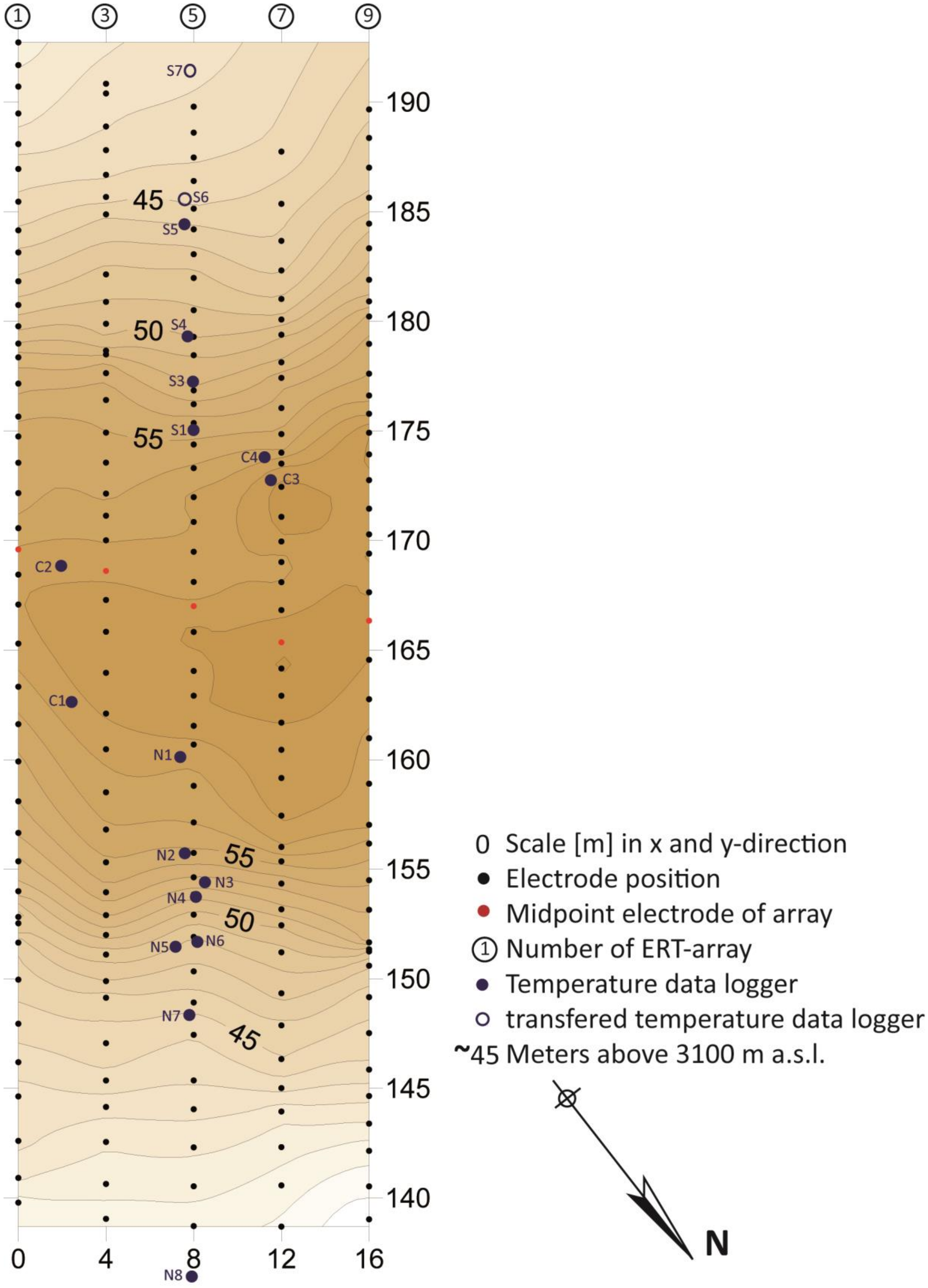

Fig. 7.2 Location of rock temperature data loggers (blue dots) in the Steintaelli rock wall; black dots indicate location of ERT electrodes based on tachymetric measurements by Krautblatter (2009).

If temperature decrease during snow cover is significant, the period is classified as Stage I. Additionally, GST measured by data loggers are classified into the thermal regimes of Ishikawa (2003) and compared to BTS by Haeberli (1973) to evaluate the applicability of BTS measurements in steep permafrost rock walls. Mean Annual Ground Surface Temperature (MAGST) is calculated for the period September 2012 to August 2013 from all loggers with a complete temperature data set. MAGST is used to compare variation between data loggers and as input data for thermal modelling in Chapter 8.

Snow height was measured with avalanche probes by Bierbaum (2013) on Aug 7th 2012 and by the author between Aug 1st and 3rd 2013. The measurements were conducted along the geophysical transects (Fig. 7.2 with 1 m spacing to receive a snow cover information at slope scale. Avalanche probe measurements allow a height measurement with an accuracy of ± 5 cm. The probe has a length of 2.25 m, which determines the maximum measurable snow height. Impenetrable ice lenses lead to underestimation of the snow height. In 2013, transects were dug along the geophysical transects allowing probe measurement correction. Transect 9 at 16m was covered by snow more than pole length and no digging was performed. Measured data is interpolated using the kriging algorithm by SURFER 8.05. The aim of data collection is to get snow cover information for the period of the following geophysical measurements.

7.3 Results

7.3.1 Air temperature, wind speed and wind direction

The meteo station recorded snow height but unfortunately, the wind blew away the snow below the sensor. Therefore, measured snow height was not representative for the area during the measurement period and data was not analysed. Air temperature data from the meteo station shows a negative temperature trend between September and beginning of November 2012 (Fig. 7.3 A). In November 2012, temperature drops to -20°C and shows no daily fluctuations, which are maybe caused by a sensor error. In December, air temperatures increase and a period with positive temperatures is observed at the turn of the year. Temperatures show a negative trend with strong daily fluctuations until February 2013. From March 2013 onwards, a positive temperature trend can be observed with phases of positive air temperature. Between March and April, an unusual phase without daily fluctuations occurs, maybe caused by a sensor error. From July 2013 onwards temperatures seldom drop below 0°C.

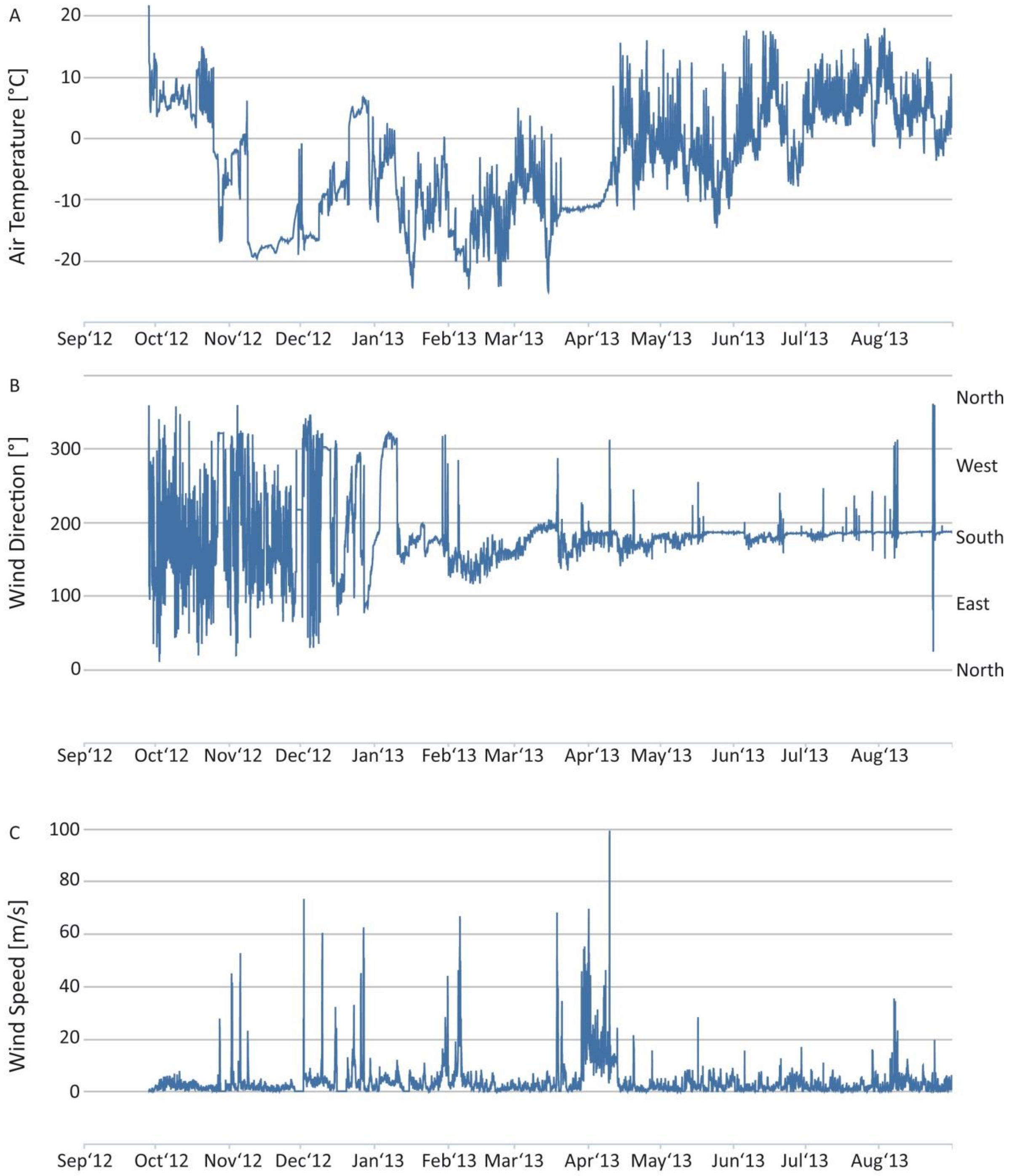

Fig. 7.3 (A) Air temperature, (B) wind direction and (C) wind speed measured at the SLF meteo station in the Steintaelli between September 30th 2012 and August 31st 2013.

Wind direction shows strong fluctuations between September 2012 and beginning of January 2013 (Fig. 7.3 B). From January 2013 onwards, the wind direction stays relatively constant with a dominating southern direction and, especially in February and March, south-eastern direction. Wind speed is constant during the whole year with speeds between 0 and 10 m/s (Fig. 7.3 C). In autumn 2012, a few events of wind with speeds up to 55 m/s occur. In winter 2012/13, six events with wind speeds between 40 and 65 m/s occur. A phase of high wind speeds is observed in March and April 2013 with speeds up to 100 m/s. During summer 2013 wind speed is lower, it sometimes reaches up to 20 m/s and two times more than 20 m/s.

7.3.2 Ground surface temperature

Rock temperature loggers can be distinguished according to location and, thus, different aspect into north (N), south (S) and crestline (C) loggers. The north-facing loggers N8 – N2 show a decreasing rock temperature trend from the beginning of August until the beginning of snow cover period (Stage IV) (Fig. 7.4). A trend of temperature decrease is not visible at loggers N7 and N8 because the loggers were installed in late September 2012. Logger N2 shows an increasing temperature trend from February until the beginning of the snow-cover period in April 2013. The Loggers N5 to N8 show a phase of temperature decrease during the first months of the snow cover period from October to Mid-December 2012, highly pronounced at Logger N8 (Stage I). Loggers (N2 – N4) with late starting snow cover show lower rock temperatures. Zero-curtain effects are visible at Loggers N4-N8, longest (1 month) at Logger N7 (Stage III). During the measurement period (August 2012 - September 2013), temperatures range from -18°C to 22°C at Logger N2, -8°C to 18°C at Logger N8 and -20°C to 12°C at Loggers N2-N7. The duration of snow cover shows a decreasing trend between Logger N8 located at the toe of the north-facing slope and Logger N2 at the top of the slope (Stage I+II). Despite missing data in August and September 2012, N8 and N7 are long-time snow-covered (259 days/286 days; Fig. 7.5). Duration of snow-cover decreases from 287 days at Logger N6 to 55 days at Logger N2. A constant snow cover starts first at Logger N8 in Mid-October 2012 and latest at Logger N2 in late April 2013 and shows a trend of increasing later accumulation between N8 and N2. Ablation shows an opposing trend starting first in Mid-June at Logger N2 and latest in Mid-August at Logger N7. During snow cover, rock temperatures persist at more or less negative temperatures. At Logger N8 snow ablates one month earlier than at Logger N7. The loggers show negative rock temperatures from October 2012 until the end of the snow cover. Only Logger N2 shows positive rock temperatures during a snow-free period in April 2013. After the end of snow cover period temperatures increase directly to values up to 12° (Logger N3-N7) and up to 20°C (Logger N2 and N8) (Stage IV), respectively.

At the crestline, five rock temperature loggers were installed; Loggers N1 and C1 facing in northern direction while Loggers C2-C4 facing in southern direction (Fig. 7.2). All loggers show a decreasing temperature trend until the beginning of the snow cover period (N1) or the beginning of December 2012 (Stage IV) (Fig. 7.4). Logger N1 shows decreasing temperatures despite snow cover until the end of January 2013 (Stage I). Stage I with decreasing temperatures despite snow cover is only observed at Logger N1. At Loggers C1-C4, temperatures increase from the beginning of December until the turn of the year and decrease until the beginning of the snow cover period (C1, C2, C4) (Stage IV). Logger C3 shows no snow cover period and temperature fluctuates with a decreasing trend until the end of November. The logger shows a small increase at the turn of the year. From Mid-February onwards an increasing temperature trend with high fluctuations can be observed (Stage IV). The loggers show a decreasing trend of snow cover duration between the north-facing Logger N1 (247 snow cover days) and the south-facing logger C4 (147 days) with exception of Logger C3 (snow-free the whole period). The period of constant snow cover (Stage II) starts in Mid-November 2012 (N1), late January or beginning of February 2013 (C1, C2, C4), respectively. Snow cover duration lasts to Mid-June (C4), end of June (C2) or Mid-July (N1, C1), respectively. A zero-curtain occurs in the range of one week at the north-facing Logger C1 and between two and four weeks at the south-facing Loggers C2 and C4 (Stage III). Loggers N1 and C1 show negative rock temperatures between late-October and late-November, respectively, until the end of the snow-covered period. Loggers C2-C4 show positive rock temperatures during the turn of the year. After the end of snow cover (Stage IV), rock temperatures fluctuate daily with maximum temperatures of up to 30°C. Logger C3 shows strong daily temperature fluctuations during the whole period and temperatures range from -20°C to 30°C. All the other loggers at the crestline show similar temperature amplitudes beside during the snow cover period.

Four data loggers record temperatures at the south-facing slope (Fig. 7.2). Logger S1 stopped recording in Mid-July 2013. All Loggers show a decreasing temperature trend from August 2012 to the beginning of the snow cover period (Stage IV) and temperatures decrease below 0°C from the end of November 2012 until the end of the snow cover period at Loggers S1-S4 (Fig. 7.4). Rock temperatures at Logger S5 decrease only slightly below 0°C during the snow cover period and show the shortest period of negative temperatures of all loggers on the south slope (Stage II). The duration of snow cover shows an increasing trend from Logger S5 located at the toe of the slope (277 snow-covered days) to Logger S1 (153 days) located at the top of the slope (Stage II+III).

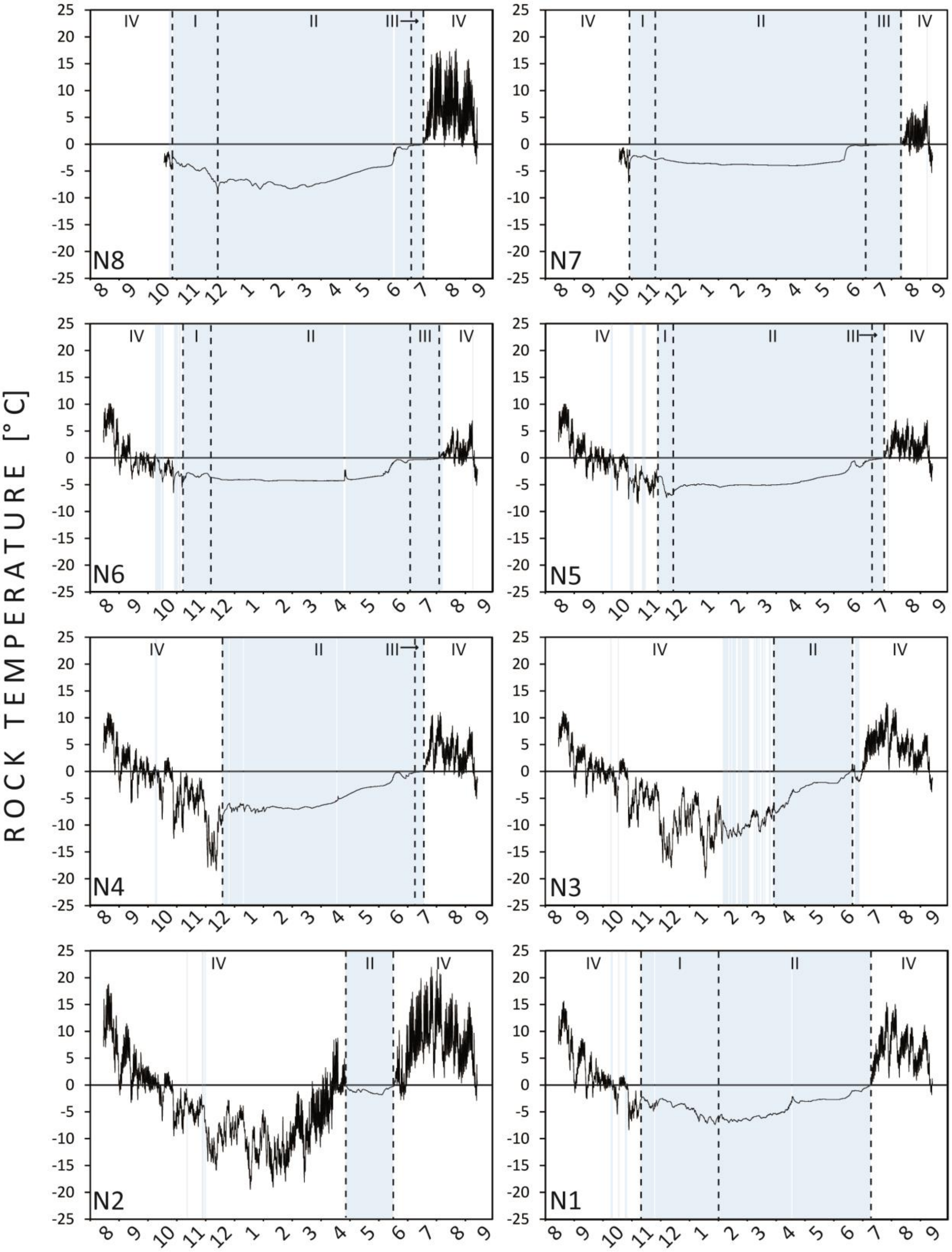

Fig. 7.4 Rock temperature from August 2012 until September 2013 and period with snow cover (light blue) on the NE-slope (N2-N8), crestline (N1, C1-C4) and SW-slope (S1-S5) plotted against time. Roman letters indicate snow cover stage.

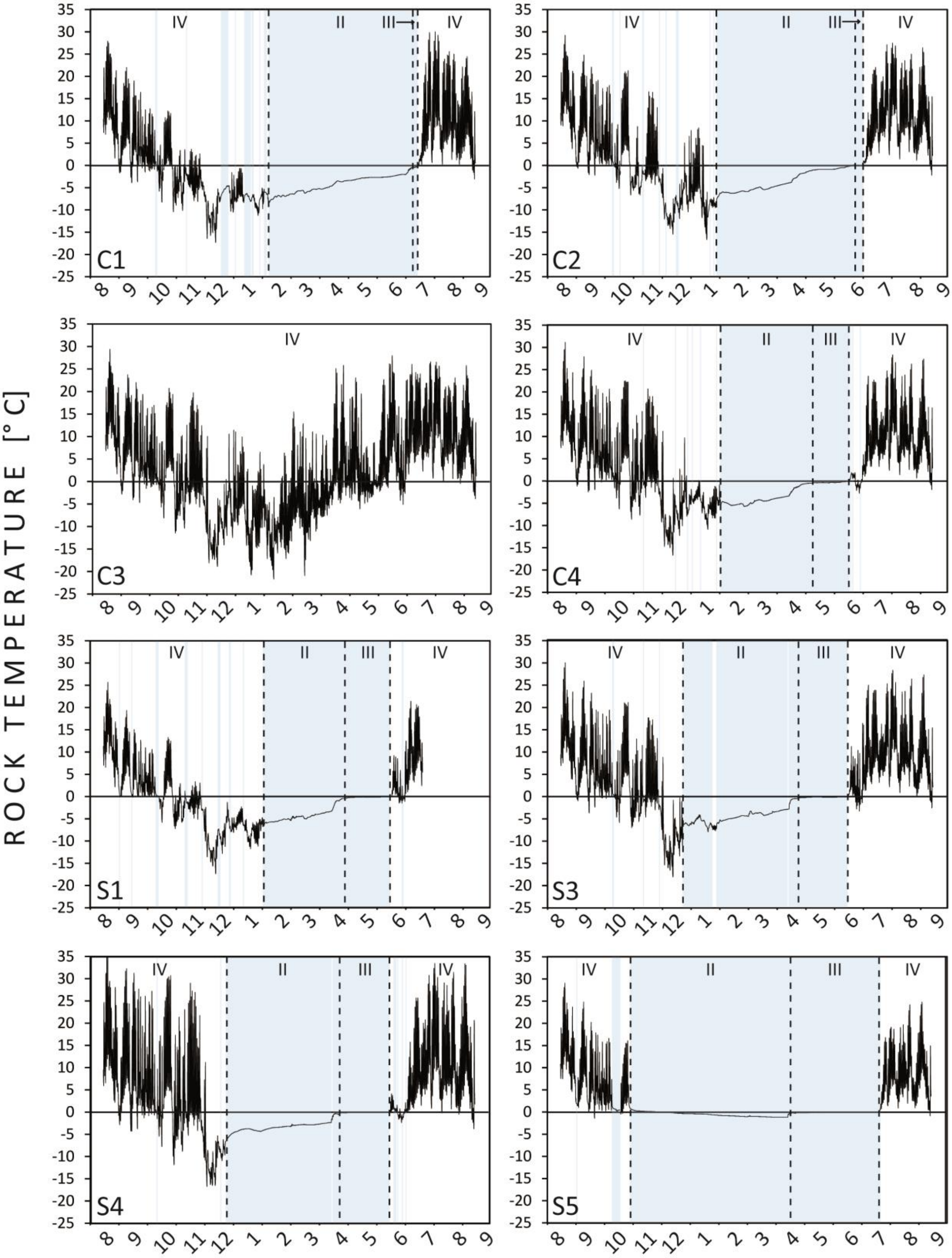

Fig. 7.4 Continued.

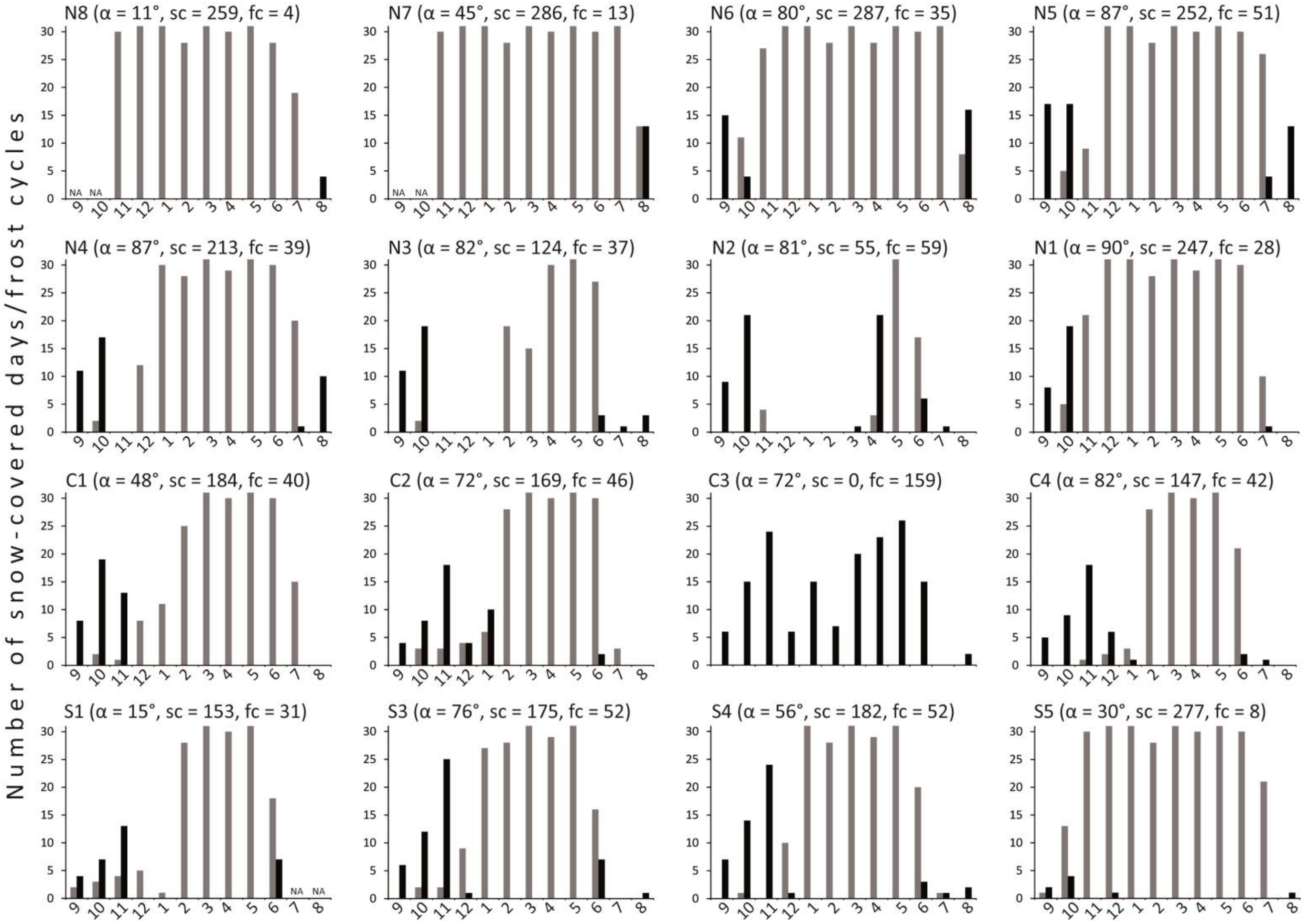

Fig. 7.5 Number of days with snow cover (sc; grey columns) and frost cycles (fc; black columns) plotted against time (September 2012- August 2013); α indicates slope angle of the rock wall at logger position.

The period of constant snow cover starts in late October 2012 at Logger S5, Mid-December 2012 at Loggers S3 and S4 as well at the beginning of February 2013 at Logger S1. Logger S5 is snow-covered for a week in October 2012 and Logger S3 is probably snow-free for a short period of several days in January 2013. All loggers on the south slope show long-lasting zero-curtain effects in the range of 1-3 months (Stage III). Snow cover period ends in Mid-June (S1-S4) or Mid-July (S5), respectively. After the end of snow cover period, temperatures increase to positive values. During the whole measurement period except the snow-covered stage, rock temperatures fluctuate between -18°C and 35°C on the south-facing slope, except from Logger S5 where rock temperatures decrease to only -1°C.

Tab. 7.1 Mean annual ground surface temperatures (MAGST) for the time period September 2012 to August 2013.

NE-slope		**Crestline**		**SW-slope**	
Logger	MAGST [°C]	Logger	MAGST [°C]	Logger	MAGST [°C]
N6	-2.6	N1	-1.7	S3	0.5
N5	-2.9	C1	-1.6	S4	1.3
N4	-3.5	C2	0.0	S5	1.4
N3	-3.7	C3	1.2		
N2	-2.2	C4	0.8		

Temperature loggers show MAGSTs ranging from -3.7°C to 1.4°C (Tab. 7.1). MAGSTs of all loggers on the NE-slope and the north-facing loggers on the crestline remain below 0°C while loggers on SW-slope and south-facing loggers on the crestline show positive MAGSTs.

According to the GST-classification by Ishikawa (2003), GST of Logger S5 is consistent with type (i) because GST shows no significant cooling. The Logger N2 lacks long-term snow cover and the Logger C3 is snow-free which corresponds to type (ii). All other loggers show more or less cooling before the onset of snow accumulation and are classified as type (iii). For loggers of type (iii), the use of BTS method is valid according to Ishikawa (2003). All these loggers show GST values around -3°C during late winter which indicate permafrost occurrence according to Haeberli (1973). BTS values will be discussed in Chapter 8.4.3.3.

7.3.3 Automatic snow cameras

The snow cameras capture the spatial distribution of snow cover at four different times between October 2012 and February 2013 and allow a rough estimate of snow distribution development. In August 2012 (Fig. 7.7 A-B), only a small snow cornice exists, which probably melts completely during September 2012. North and south-facing rock walls are snow-free.

On the north-facing slope, snow accumulates first at the toe of the slope (Fig. 7.6 A) and on top of small ledges. Steep parts of the rock wall stay snow-free. Between October 21st and November 12th high accumulation of snow can be observed. Snow cover increases in form of a snow patch from the toe upwards (Fig. 7.6 B). Additionally, small snow patches accumulate on the ledges. Development of a snow cornice on top of the crestline is slightly visible. Between November 12th and December 24th 2012, immense snow amounts accumulate especially visible by the burying of the container in the front of Fig. 7.6 C. The snow patch further increases from the top upwards and all the ledges are snow-covered.

Only the steepest parts close to the top of the north-facing rock wall stay snow-free. A massive snow cornice covers the crestline. Between December 24th 2012 and February 5th 2013, snow only accumulates slightly further (Fig. 7.6 D). On August 7th 2013, a thick snow patch covers the north-facing slope and a massive snow cornice covers the crestline (Fig. 7.7 C-D).

On the south-facing slope, snow cover first accumulates on the big ledges (Fig. 7.6 E). Figure 7.6 F shows the snow accumulation on November 12th 2012. All ledges are snow-covered, only the steepest parts stay snow-free. Snow accumulates further and on December 24th 2012, most of the south-facing rock wall is snow-covered (Fig. 7.6 G). Few steep parts remain snow-free even in January 30th 2013 (Fig. 7.6 H). The massive growth of the snow cornice is visible between November 12th 2012 and January 30th 2013. On August 7th 2013, only a small snow patches persist on the south-facing slope (Fig. 7.7 E).

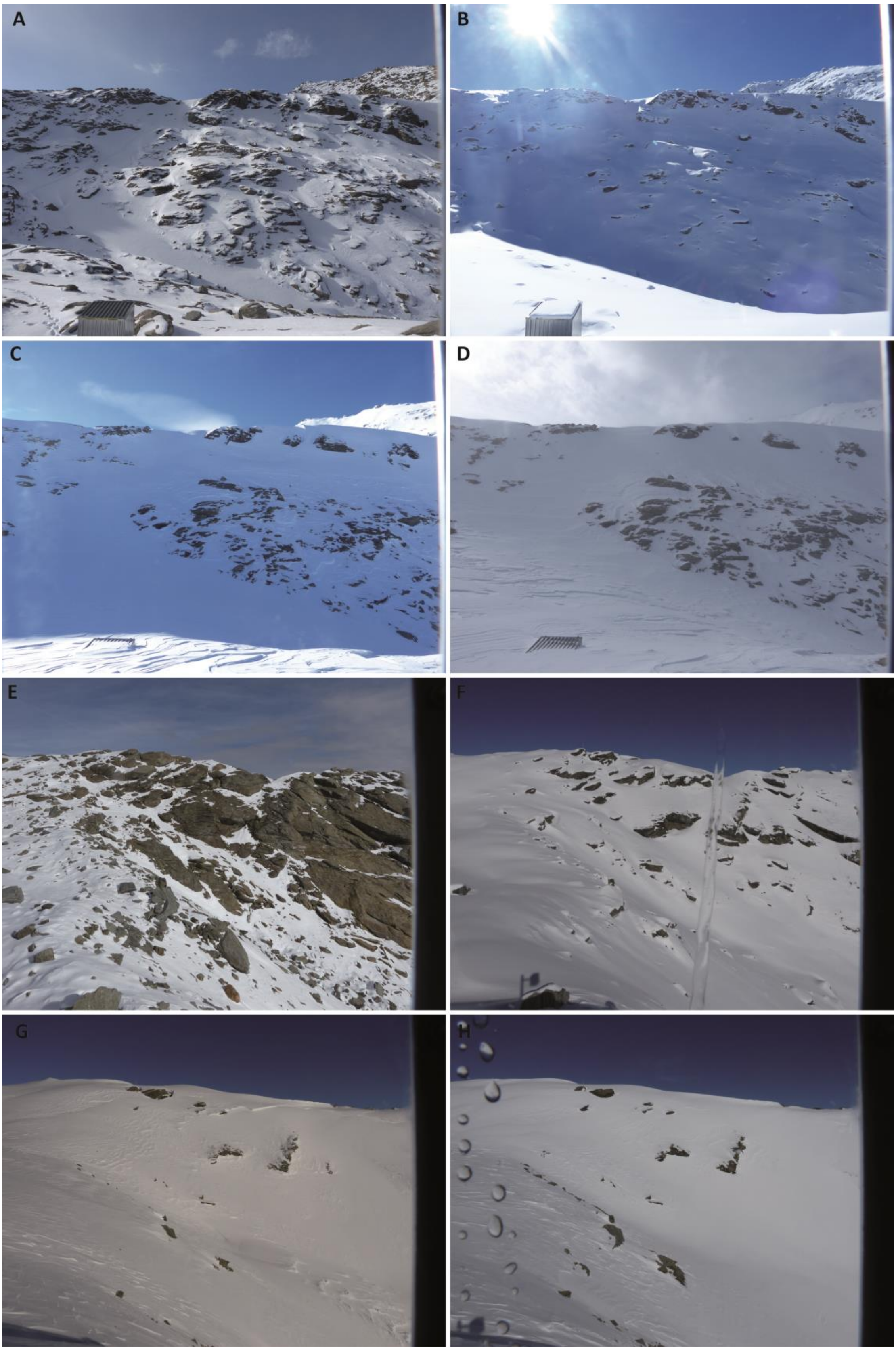

Fig. 7.6 Photos from the snow cameras of SLF at Steintaelli. A-D: North-facing rock wall on Oct 21st (A), Nov 12th (B), Dec 24th 2012 (C) and Feb 5th 2013 (D). E-H: South-facing rock wall on Oct 20th (E), Nov 12th (F), Dec 24th 2012 (G) and Jan 30th 2013 (H). All pictures by SLF.

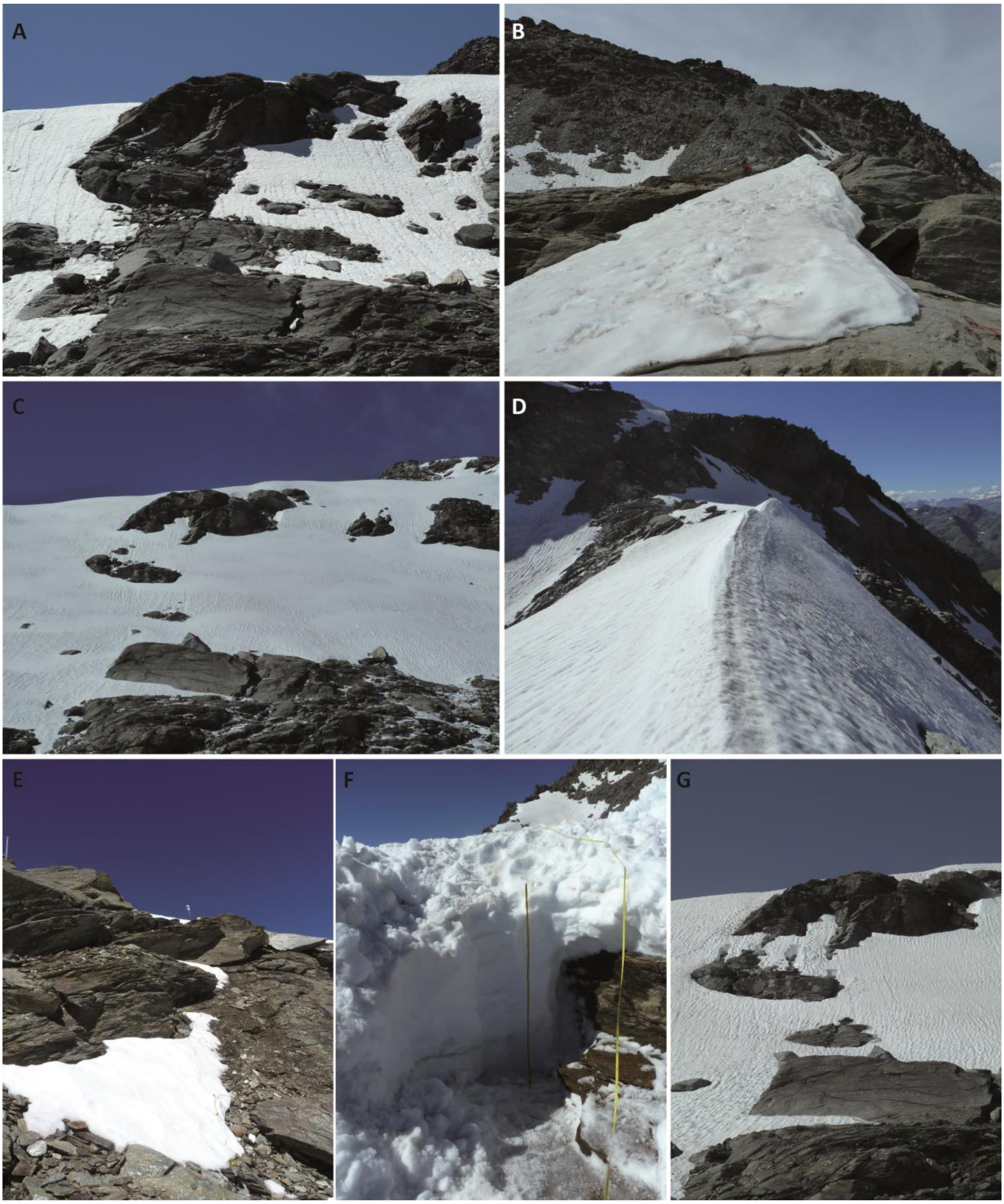

Fig. 7.7 A: Snow-free north face and small visible part of the snow cornice on Aug 7th 2012; B: Snow cornice on Aug 9th 2012; C: Snow-covered north face with immense snow cornice on July 30th 2013; D: Snow cornice with wind ripple marks on July 31st 2013; E: Snow patch on south-facing rock wall on July 31st 2013; F: Snow pit in a 2.5 m deep snow cornice in Transect 5 on Aug 2nd 2013. There is a visible thick ice lens in the bottom part of the cornice and several small ice lenses in the middle to upper part. The rock face is covered by a 10 cm thick ice cover. G: North-facing rock wall with four dug pits in the area of the geophysical transects on Aug 3rd 2013. In Transect 9, the snow cover is preserved due to high thickness.

7.3.4 Snow height measurements

On August 7th 2012, snow cover is limited to the crestline between Transect 3 (4 m) and 9 (16 m) in form of a small cornice with maximum height of 1.4 m (Fig. 7.7 B, 7.8). In the following days, the cornice ablates as a result of solar radiation and digging. On August 1st and 3rd 2013, the cornice is more pronounced and covers the whole crestline (Fig. 7.7 D, 7.8). Maximum snow heights are around 2.5 m. A snow patch is covering the less inclined part and the toe of the north-facing rock wall with maximum heights up to 2.25 m (Fig. 7.7 C). Small snow patches on the south-facing slope up to 0.7 m are preserved (Fig. 7.7 E). Small ice lenses inside the snow cover (Fig. 7.7 F) and an up to 20 cm thick ice cover on the top of the rock surface complicated the snow pole measurements and might lead to underestimation of snow height. Digging of snow pits along the geophysical transects allowed the correction of snow heights (Fig. 7.7 G). In Transect 1, the glacier advances at transect length 145 – 150 m (Fig. 7.8) into the transect line and approximately 1 m thick ice covers the rock wall. This situation was observed before in August 2007 (Krautblatter and Draebing, 2014).

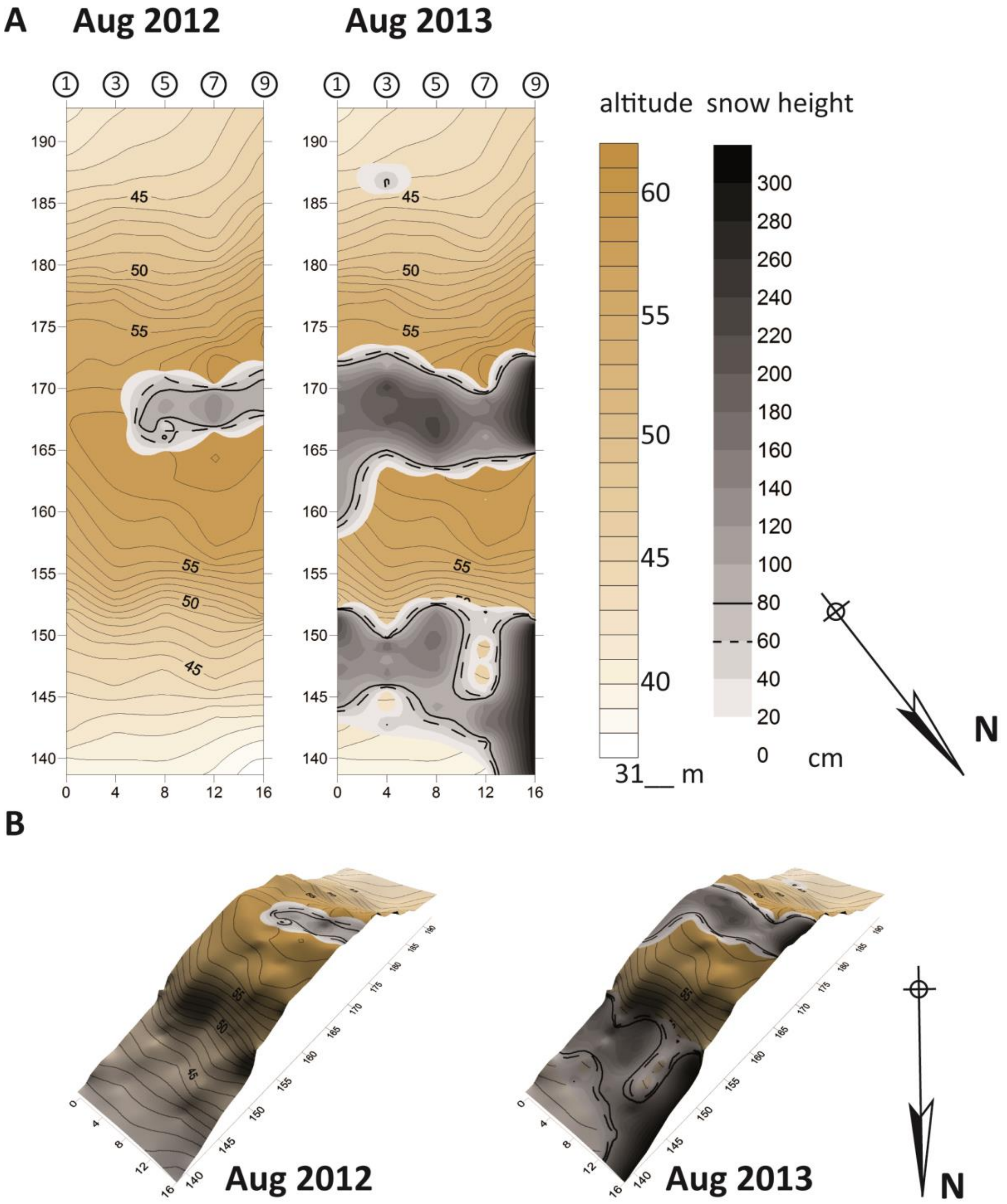

Fig. 7.8 A: Snow height distribution maps with encircled numbers indicating location of the geophysical transects; B: DEMs of snow conditions in August 2012 and August 2013.

7.4 Discussion

7.4.1 Applied methods

The meteo station was installed in a wind-exposed location to avoid high amounts of snow cover which has the potential to damage the sensors of the meteo station. Due to the location, the data from the snow height sensor of the meteo station shows no snow cover, thus, automatic measurement of snow height at a point scale is not applicable in steep permafrost terrain. The air temperature sensor shows no daily fluctuations despite the 1 h-resolution of measurement during two phases in November 2012 and March/April 2013. Data of snow-free rock temperature loggers show daily fluctuation of rock surface temperature during this period. A snow amount of more than 2 m would be necessary to cover the sensor. In this case, the north-facing camera would not be able to take images of the rock wall and wind sensors would not be able to record fluctuating data. The camera worked and, thus, snow cover can be excluded as cause of lack of daily temperature fluctuations. Therefore, a technical error remains as a single cause.

Rock surface temperature is measured at 10 cm depth with iButtons. The manufacturer stated the accuracy ±0.5°C but Gubler et al. (2011) determined near 0°C a higher accuracy of ±0.125°C. The accuracy of UTL III-loggers for example is stated as ±0.25°C (Gruber et al., 2003). The costs of an iButton logger are only a tenth of the costs of an UTL-logger, therefore more loggers can be installed for the same cost allowing a more spatial coverage of the rock wall. The installation in 10 cm depth is common practice and avoids difficult direct measurements of daily fluctuations (Gruber et al., 2003). Snow accumulation was derived from standard deviation threshold of lower 0.3 K for 24 h. This threshold was developed in the near-by Lötschental on a NE-slope and SW-slope with slope angles between 2° and 40° and snow cover was validated with automatic camera photos (Schmidt et al., 2009). The use of thresholds for standard deviation is common practice in GST analysis. Danby and Hik (2007) used a variance of ≤ 1 K as snow threshold in Southwest Yukon. Schmid et al. (2012) differentiated mean daily GST and used a standard deviation threshold of 0.1°C for positive mean daily GST and 0.3°C for negative mean daily GST in the Corvatsch area, Engadin. However, only the threshold by Schmidt et al. (2009) was used at inclined slopes and was validated, thus, this threshold was preferred for data analysis.

7.4.2 Ground surface temperatures and snow cover

Rock temperatures differ highly due to aspect, slope angle and location on the rock wall, which influence the amount of solar radiation and alters the snow cover (Gruber, 2005). The north-facing slope (-3.7°C to -1.6°C) shows lower MAGST than the south facing rock wall (0°C to 1.4°) probably due to differences of solar radiation caused by the aspect. Snow cover in winter increases the MAGST (Phillips, 2000) while long-lasting snow cover decreases MAGST. This explains the decreasing trend of MAGST with decreasing number of snow-covered days observed on NE-slope and SW-slope. Snow-free Logger C3 show highest MAGST of all loggers located on the crestline due to the absence of snow in spring and summer. The MAGST varies 5.1°C in an elevation range of 20-30 m. Gubler et al. (2011) observed a variation of 6°C in an elevational band of 300 m in the Corvatsch area, Engadin, with highest variation on steep slopes.

According to Salzmann et al. (2007) are thickness and duration of snow cover probably the most important influences on the thermal regime of the underground. Snow cover exists for up to three quarters of the year and influences strongly rock temperatures. During snow-free conditions, the rock temperatures follow the trend of air temperature. A long-lasting snow-free period (Stage IV) enables cooling of the underground (Luetschg et al., 2008) down to -10° or -15°C, thus, a decreasing temperature trend is observable in Stage IV in autumn. The length of Stage IV is dependent on geomorphometric and topographic factors (Schirmer et al., 2011; Wirz et al., 2011). Snow patches build up from the toe of the rock wall, thus, longer snow-free conditions can be observed at high-lying locations in the rock wall (Loggers N2 and S1). Meteorological conditions like wind speed redistribute snow (Schweizer et al., 2008) away from exposed locations, as consequence the exposed crestline is more affected by wind and a prolonged snow-free period can be observed at Loggers C1-C4. When air temperatures show an increasing trend (Fig. 7.3) and turn positive, the cooling effect of Stage IV changes into a warming effect. Loggers N2 and C2-C4 show positive GST values in April 2013 or December 2012/January 2013, respectively, as a result of air temperature increase and lack of snow cover. The snow-free conditions are caused by combination of topographic and meteorological factors. Logger C3 is located in a steep part of the rock wall (72°) high above an underlying ledge and close to the top. Wind speeds at the top can redistribute the snow away from the logger position, thus, Logger C3 shows snow-free conditions the whole period between August 2012 and September 2013 and remains in Stage IV. Meteorological conditions are similar at Logger N1, however, the topographic factors differ. Rock wall is vertical (90°), but the low height above a ledge allows snow accumulation growths upwards from the ledge towards the logger.

In Stage I, the thin-snow cover effect enhances ground cooling (Keller, 1994; Phillips, 2000; Luetschg and Haeberli, 2005) and cools the ground from -2° down to -7°. The cooling effect represents 5°C at Loggers N5-N8 and N1. Stage I lasts from late October, early November 2012 until Mid-December 2013 (N6-N8), from Mid-November to Mid-December (N5) or end of January (N1), respectively. Snow accumulation, topographic and meteorological conditions influence thin-snow cover effect. The accumulation of snow is influenced by geomorphometric factors like slope angle (Wirz et al., 2011), thus, the thin-snow cover effect starts first at less-inclined areas at the toe of the slope (N8, 11°) and later at high-inclined areas (N5, 87°). Wind direction was fluctuating strongly during Stage I. The snow patch at the northern slope is wind-protected, wind probably redistributes the snow from the flat areas towards the wall and forms the snow patch, as a consequence prevents the wind high snow accumulation at flat areas (N8) and transports snow to high-inclined areas (N1, N5-N7). This is confirmed by snow camera photos on November 12th and December 24th (Fig. 7.6 B-C), which show high snow accumulation between these dates of photography on the north-facing slope. The evolution of the snow patch between October 21st and December 24th is visible on Fig. 7.6 A-C and supports the pattern of snow patch up-built observed by the loggers.

Stage II shows a cooling effect especially if the ground has cooled down in Stage IV or Stage I before. The cooling effect of these stages is preserved (Luetschg et al., 2008), thus, Loggers N1, N3-N8, C1, C2, C4 and S1-S4 show longer low rock temperatures. If ground cooling was insufficient the cooling effect is less-pronounced, as a consequence Logger N2 shows rock temperatures only slightly below 0°C. If no ground cooling occurred, relatively high temperatures are preserved and cooling is prevented (Ishikawa, 2003), thus, Stage II then shows a warming effect, which is confirmed by Logger S5.

In Stage III, a zero-curtain effect is caused by meltwater infiltration and latent heat processes conjunct with melting and refreezing (Luetschg and Haeberli, 2005). The length of Stage III is affected by aspect and, thus, solar radiation. North-facing loggers (C1, N4-N8) except N1-N3 show a zero-curtain effect and Stage III lasts for 1-4 weeks. Zero-curtain effects occur much longer (1-3 months) at all south facing loggers which reflects higher solar radiation (Schmidt, 2009). Logger C2 shows a short Stage III of 2 weeks length and Logger C3 shows no zero-curtain because of the lack of snow cover. Geomorphometric factors are more important during snow accumulation in Stage II than during snow ablation at the end of Stage II or Stage III (Schmidt, 2009), respectively. However, loggers located in steep parts of the rock wall and on top of the crestline show an earlier end of snow cover of approximately up to one month than loggers located in flat terrain because higher inclined areas become snow-free earlier (Schmidt, 2009). The observed trend of increasing end of snow cover from Logger N2 to N8 and S1 to S5 indicates that melting starts from the edges of the snow patches. Melting decreases the albedo from high snow albedo to low rock albedo and amplifies melting from the edges (Essery and Pomeroy, 2004; Grünewald et al., 2010), however, earlier melting due to aspect and conjunct higher solar radiation on south-facing rock walls cannot significantly be observed. Logger N7 was manually exposed by snow pit digging at the beginning of August 2013 and, thus, Stage III at this logger position ended ahead of time. Air temperature turns positive in April 2013 while snow-covered loggers show negative GSTs, thus, Stage III has an important cooling effect if the stage lasts long and prevents warming by positive temperatures (Luetschg et al., 2008).

Stage IV in summer 2013 shows an increasing temperature trend and, thus, warming effect. GSTs show directly positive values indicating warming of the underground.

7.4.3 Snow accumulation and provenance

Wind direction shows strong fluctuations between all directions for the period from September 2012 to January 2013 (Fig. 7.3). Camera photos show massive snow accumulation on the rock wall during the same period (Fig. 7.6). Snow can be redistributed by wind from northern direction towards the north-facing rock wall. Wind speed is reduced at the wall due to wind-protection property of the rock wall (Mott et al., 2010), thus, snow can be deposited and forms a snow patch. The snow patch is a combination of autochthonous snow by snow fall and allochthonous snow by redistribution. On the southern slope contrary wind directions enhance snow patch up-built.

Cornices can be distinguished by formation, duration and topographic location (Vogel et al., 2012), the cornice in Steintaelli is classified as a ridge cornice. The snow cornice up-built is favoured, if a dominant wind direction exists (Mott et al., 2010) and snow cornice can develop typical roll cavities, however, the alteration of wind direction prevents the formation of roll cavities which could not be observed during the snow trench digging. In contrary the changing wind directions can favour the mount up of the cornice. Snow can be allochthonously accumulated by snow fall and additionally autochthonously redistributed by snow up-drift from the less inclined south-facing rock wall (Fig. 7.6 G-H). Redistribution by avalanche activity was not observed but cannot be excluded due to high topography. The snow patch on the steep north-facing rock wall could be fed autochthonous by small snow avalanches.

7.4.4 Snow height

Snow height was measured in August before geophysical measurements take place to potentially establish a relationship between snow cover and frozen underground conditions. At this time of the year, snow Stages II, III or IV occur. The low density of early winter snow conducts heat inferior to high-density snow. Snow settling leads to densification of snow (Lehning, 2005). In August, snow cover is settled and dense which leads to higher thermal conductivity (Sturm et al., 1997). Snow height of the snow patches (August 2013) and snow cornice (August 2012 and 2013) exceeds the isolation thresholds of 0.6 m (Hanson and Hoelzle, 2004) or 0.8 m (Keller and Gubler, 1993), respectively, established on Murtèl rock glacier. Density of snow cover is not measured during snow height measurements; however, the immense snow accumulation should isolate the underground even if snow is highly dense. Snow accumulation possesses the potential of preserving frozen underground or permafrost in the areas of snow patches and cornice. Snow remains longer in areas of high snow accumulation (Grünewald et al., 2010), thus, the patterns of snow cover in August should represent these areas of high snow accumulation.

7.5 Conclusion

The combination of temperature data loggers and photos of automatic cameras allows the temporal and spatial reconstruction of snow cover development. Avalanche probe measurements deliver spatial snow height data at the time of measurement. The snow stage model by Luetschg and Haeberli (2005) is applicable on steep rock walls. Stage IV in autumn or winter 2012 has a cooling effect on the underground. If Stage IV lasts into 2013, the warm air temperatures at the turn of the year result in a warming effect of Stage IV. The thin-snow cover stage (Stage I) affects the underground in a cooling way. If Stage II occurs after a warm period, it preserves warm underground temperatures and has a warming effect. Long-time Stage II possesses a cooling effect by preserving cold underground temperatures and delay warming. Stage III is dependent on aspect. Zero-curtain effects occur 1-4 weeks on north-facing slope and 1-3 months on south-facing slope. Stage IV in summer 2013 has a warming effect.

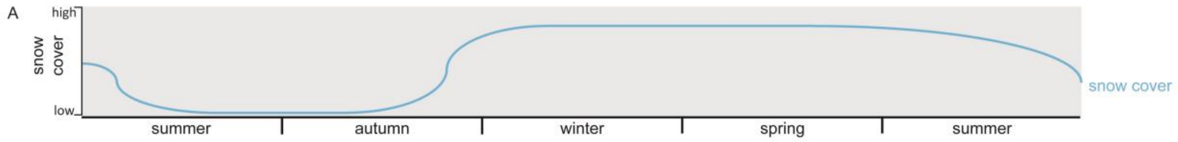

Fig. 7.9 Schematic illustration of snow cover development between summer 2012 and summer 2013.

During snow accumulation geomorphometric (slope angle), topographic (location on slope) and meteorological (snow redistribution by wind) factors are effective while during melting, aspect and slope angle are important control factors. Wind shows strong fluctuations and forms the snow patches and the snow cornice. Due to changing wind directions, the snow cornice cannot develop roll cavities. Snow height possesses the potential to preserve frozen underground or permafrost. Snow cover was long-lasting in 2013 and the length is incorporated in the conceptual approach of snow cover (Fig. 7.9).

8 Thermal regime

To monitor the thermal regime in rock walls is a difficult task. In the first Chapter 8.1 different possible methods to investigate the thermal regime, which are applied in the field, will be introduced with emphasis on electrical resistivity. Laboratory measurements of refraction seismics are presented in Chapter 8.2; the transfer of laboratory results to field applications is shown in Chapter 8.3. In Chapter 8.4, results of data measurements in 2012 and 2013 will be presented and discussed. Based on these results the conceptual approach (see Chapter 5.3) will be adapted in the conclusion (Chapter 8.5).

8.1 Methods to monitor thermal regimes of rock walls

In this chapter methods to monitor the thermal regime of rock walls are introduced; advantages and disadvantages of these methods are presented in Table 8.1. Temperature loggers are widely used to measure surface temperatures (Hoelzle et al., 1999). If adapted for rock walls (Gruber et al., 2003), temperature loggers can monitor daily rock surface temperatures. Measurements are used as input data for modelling or validation data for rock temperature models (Gruber et al., 2004b). However, temperature loggers only deliver data on a restricted spatial scale (rock sample/point scale) without information about the thermal regime in depth. Permafrost boreholes allow continuous monitoring of rock temperature at different depth, but boreholes are cost-intensive and information is restricted to a point scale. PERMOS (2013) gives an overview about 25 boreholes at 15 sites in Switzerland. Closest to our field site is the borehole at Stockhorn plateau 25 km away in the Matter Valley. The borehole shows topographic disturbance and is used for validation of permafrost modelling (Gruber et al., 2004c).

In general, models can be distinguished into statistical-empirical models and process-based models. Statistical-empirical permafrost models relate topoclimatic factors with permafrost occurrence based on simple statistical relationships (Hoelzle et al., 2001). No physical processes are included, but the models only require limited input data and are easily applicable. The statistical-empirical permafrost models allow the differentiation of probability of permafrost occurrence. They are applicable on local scales (e.g. catchment scale), regional or global scales and deliver reliable results if calibrated (Hoelzle et al., 2001). The BTS model by Haeberli (1973) is an example, other early approaches used in Engadin are PERMAKART (Keller, 1992) and PERMAMAP (Hoelzle, 1994). On regional scale, Gruber and Hoelzle (2001) used a statistical-empirical model to model the permafrost distribution in the Matter Valley. This model implies that the probability of permafrost occurrence in the Steintaelli is high. Boeckli et al. (2012a, 2012b) developed a permafrost model for the European Alps based on mean annual air temperature (MAAT), potential solar radiation as well underground material and calibrated the model with rock surface temperature data. Schrott et al. (2012) used PERMAKART combined with thresholds derived from BTS and geophysical measurements as well mapping of periglacial landforms to model permafrost distribution in the Hohe Tauern region, Austrian Alps. On global scale, Gruber (2012) established a relationship between MAAT and mean annual ground temperature (MAGT), used MAAT as a proxy for MAGT, incorporated topography and developed a global permafrost model.

Table 8.1 Advantages and disadvantages of temperature loggers, boreholes, statistical-empirical and process-based permafrost models, electric resistivity tomography (ERT) and seismic refraction tomography (SRT).

Method	Advantages	Disadvantages
Temperature data		
temperature loggers	continuous measurements	at the ground surface or in 10 cm depth
	cheap technique	information restricted to one point
boreholes with temperature loggers	continuous measurements	information restricted to one point
	information about thermal regime in depth	cost-intensive
Permafrost models		
statistical-empirical	local, regional scales	no physical processes
	limited data input	
process-based	detailed physical processes	data demanding
	longer time scales possible	
Geophysical techniques		
ERT	automatic monitoring possible	discontinuous, indirect method
	data processing less intensive	problematic in dry ground
	information on slope scale	
SRT	accurate detection of layer boundaries	discontinuous, indirect method
	information on slope scale	intensive data processing

Process-based models include detailed physical processes understanding and, thus, are data demanding (Hoelzle et al., 2001). The model PERMEBAL includes energy-balance processes and models surface temperatures (Mittaz et al., 2002; Stocker-Mittaz et al., 2002). Gruber et al. (2004b) extended PERMEBAL with a heat conduction model and adapting topography effects to a two-dimensional model called TEBAL. They use meteorological data as input data to simulate rock temperatures and validate the results with rock surface temperature measurements. Modelled results at Jungfraujoch and Corvatsch show both strong influences of topography and aspect. The influence of the heat summer 2003 on permafrost thaw was modelled with TEBAL, indicating that thaw exceeds maximum thaw depth of previous years and is considered as trigger for enhanced rockfall (Gruber et al., 2004a). Salzmann et al. (2007) downscaled Regional Climate Models (RCM) and used these models as input data for TEBAL to evaluate future development of permafrost in rock walls. Their results show that aspect is more important for rock surface temperature than slope as well as altitude and the influence of topography is weaker than the influence of emission scenarios. They argue that duration and thickness of snow will probably be the most important factor influencing the thermal regime. Noetzli et al. (2007) extended TEBAL to a third dimension and shows three-dimensional effects on heat transport and permafrost degradation in steep permafrost rock walls. Noetzli & Gruber (2009) used the 3D approach to show transient effects of Pleistocene Ice Age, Holocene Climate Optimum (HCO) and Little Ice Age (LIA) and show future scenarios of permafrost at Matterhorn. TEBAL and its extensions are based on conductive heat transport only; advective or convective heat transport along discontinuities or anisotropic conductive heat transport due to discontinuities are not included. Scherler et al. (2010) modelled influence of meltwater infiltration on active-layer thaw at Schilthorn by using the 1D heat transfer model COUP and validated the data with Electric Resistivity Tomographies (ERT). RCMs are used as input data for COUP to test sensitivity of permafrost to climate change (Engelhard et al., 2010; Marmy et al., 2013; Scherler et al., 2013). The COUP model incorporates soil in form of layers; however, infiltration and heat transport by water are highly anisotropic in rock walls due to discontinuities. Due to the anisotropic property of rock walls, COUP is not applicable to rock walls, but as shown by Scherler et al. (2010) the model deliver reasonable results for debris-covered slopes at Schilthorn.

An indirect method to monitor the thermal regime is the use of geophysical methods. Geophysical methods deliver no direct information about underground temperature but give information on physical changes possibly caused by temperature changes. Geophysical methods are widely applied in periglacial and permafrost studies. For a comprehensive overview see the book of Hauck and Kneisel (2008a) or review papers by Vonder Mühll et al. (2002), Hauck and Vonder Mühll (2003a), Kneisel et al. (2008) and recently by Supper et al. (2014) for periglacial studies as well as Schrott and Sass (2008) for geomorphological studies. In the framework of this dissertation geoelectrical and refraction seismic techniques are applied to monitor the thermal regime. Electrical resistivity technique is described in detail in the following passages while refraction seismics is introduced in Chapters 8.2 and 8.3.

Electrical resistivity tomography is successfully applied to map permafrost occurrence in different landforms e.g. rock glaciers (Hauck and Vonder Mühll, 2003b; Rosset et al., 2013), ice-cored moraines (Hauck and Vonder Mühll, 2003b), debris-covered slopes (Scherler et al., 2010; Otto et al., 2012; Rosset et al., 2013), talus slopes (Kneisel and Hauck, 2003; Rosset et al., 2013), bedrock (Hauck and Vonder Mühll, 2003b), arctic road embankments (Fortier et al., 2011), submarine arctic permafrost (Overduin et al., 2012), mudboils and ice wedges (Watanabe et al., 2012). Time-lapse ERT is used to monitor seasonal, annual and long-term variation of permafrost in landforms e.g. debris-covered rock slopes (Hilbich et al., 2008), talus slopes (Kneisel et al., 2014b), glacier forefields (Ottowitz et al., 2012; Kneisel et al., 2014b; Supper et al., 2014), rock glaciers (Hilbich et al., 2009; Kneisel et al., 2014b) and bedrock (Krautblatter and Hauck, 2007; Krautblatter, 2010; Krautblatter et al., 2010; Verleysdonk et al., 2011; Ottowitz et al., 2012; Supper et al., 2014); or to monitor processes such as snow melt infiltration in debris-covered slopes (Hilbich et al., 2011). Krautblatter et al. (2010) calibrated field measurements with laboratory-derived results and established a quantitative ERT to monitor temperature and permafrost in rock walls. Hauck and Vonder Mühll (2003a) and Hauck and Kneisel (2008b) advised the combined approach of electrical resistivity and refraction seismics which is applied to evaluate permafrost in rock glaciers (Ikeda and Matsuoka, 2002; Ikeda, 2006; Ikeda and Matsuoka, 2006; Springman et al., 2012; Schneider et al., 2013), ice-cored moraines (Hauck et al., 2007), strongly weathered bedrock (Hauck et al., 2004a), unweathered bedrock (Hauck et al., 2007), talus slopes (Kneisel and Hauck, 2003; Otto and Sass, 2006; Schneider et al., 2013) and pingos (Yoshikawa et al., 2006). Hauck et al. (2011) developed a method based on Electrical Resistivity Tomography (ERT) and Seismic Refraction Tomography (SRT) to quantify ice, water and air content in high-porosity landforms e.g. rock glaciers. Spatial scale is increased to 3D; 3D and pseudo 3D ERT is applied in glacier forefields (Rodder and Kneisel, 2012; Kneisel et al., 2014a), peat plateaus (Kneisel et al., 2014a) and bedrock (Krautblatter, 2009).

Resistivity of rock depends on water conditions (water saturation, chemical properties of pore water), lithological properties of the material (structure of pore volume) and thermal conditions (temperature) (Hauck and Kneisel, 2008b). Archie's (1942) law relates electrical resistivity of rocks to pore volume and saturation:

$$\rho_r = a\,\emptyset^{-m} S^{-n}\,\rho_w \tag{8.1}$$

where ρ_r is the resistivity of fluid saturated rock, φ is porosity of rock, S is water-saturated porosity, ρ_w is the resistivity of water and a, m, n are constants. If rock porosity is constant over short intervals, resistivity of porewater and saturation of pores determine resistivity of rock. McGinnis et al. (1973) postulated an exponential dependence of resistivity on temperature, however, Krautblatter (2009) demonstrated by laboratory measurements with high temperature resolution that resistivity depends linearly on positive temperatures and changes path to a new linear relationship for temperatures below the freezing point (Fig. 8.22). The relationship between resistivity and temperature is related to unfrozen water content which declines due to freezing. The unfrozen water content conducts electricity through ionic transport in the liquid phase (Hauck and Kneisel, 2008b). Coupling between electrodes and the surface is major challenge and can be resolved in bedrock by drilling screws enwrapped in conductive fluid into the rock surface (Hauck and Kneisel, 2008b). Despite the fact that geophysical methods are indirect methods, geophysical methods integrate anisotropy of the underground and can be used to validate permafrost models at slope scale.

8.2 Laboratory analysis of p-wave velocity changed in freezing rocks

This chapter is published under the title “P-wave velocity changes in freezing hard low-porosity rocks: a laboratory-based time-average model” by D. Draebing and M. Krautblatter in the Journal “The Cryosphere” in 2012. Formatting, pagination and numbering of equations and figures has been modified in context of this thesis. The paper presents laboratory data on p-wave velocity development of rock samples while freezing these samples. The rock samples are artificially frozen represent to permafrost conditions in mountains. The introduction (Chapter 8.2.2) defines permafrost and summarizes the state of the art on laboratory seismic measurements and seismic models. In Chapter 8.2.3, the authors describe the methodical procedure of the measurements and introduce the measured rock samples derived from Arctic and Alpine permafrost sites and former permafrost sites. The measurement results are described in Chapter 8.2.4. In the discussion (Chapter 8.2.5) the authors argue that p-wave velocity increase is caused not only by phase transition from water to ice and higher velocities of ice but also by developing ice pressure. A new p-wave velocity model is adapted based on the measurement results. The article shows the applicability of refraction seismics in low-porosity rock walls, highlights the feedbacks between the ice pressure and p-wave velocity increase. Chapter 8.2.6 concludes the main findings.

8.2.1 Abstract

P-wave refraction seismics is a key method in permafrost research but its applicability to low-porosity rocks, that constitute alpine rock walls, has been denied in prior studies. These explain p-wave velocity changes in freezing rocks exclusively due to changing velocities of pore infill, i.e. water, air and ice. In existing models, no significant velocity increase is expected for low-porosity bedrock. We postulate, that mixing laws apply for high-porosity rocks, but freezing in confined space in low-porosity bedrock also alters physical rock matrix properties. In the laboratory, we measured p-wave velocities of 22 decimetre-large low-porosity (<10%) metamorphic, magmatic and sedimentary rock samples from permafrost sites with a natural texture (>100 micro-fissures) from 25°C to –15°C in 0.3°C increments close to the freezing point. When freezing, p-wave velocity increases by 11-166 % perpendicular to cleavage/bedding and equivalent to a matrix velocity increase from 11-200 % coincident to an anisotropy decrease in most samples. The expansion of rigid bedrock upon freezing is restricted and ice pressure will increase matrix velocity and decrease anisotropy while changing velocities of the pore infill are insignificant. Here, we present a modified Timur’s two-phase-equation

implementing changes in matrix velocity dependent on lithology and demonstrate the general applicability of refraction seismics to differentiate frozen and unfrozen low-porosity bedrock.

8.2.2 Introduction

Most polar and many mountainous regions of the earth are underlain by permafrost, making them especially sensitive to Climate Change (Intergovernmental Panel on Climate Change, 2007; Nogués-Bravo et al., 2007). Permafrost is a thermally defined phenomenon referring to ground that remains below 0°C for at least two consecutive years (NRC-Permafrost-Subcommitee, 1988). Permafrost is not synonymous with perennially frozen underground due to freezing point depression resulting from solutes, pressure, pore diameter and pore material (Lock, 2005; Krautblatter et al., 2010). Ice develops in pores and cavities (Hallet et al., 1991) and affects the thermal, hydraulic and mechanical properties of the underground. Climate Change can degrade permafrost and, thus, alters permafrost distribution. In mountainous regions, rock walls with degrading permafrost are considered to be a major hazard due to rockfall activity and slow rock deformation (Gruber and Haeberli, 2007; Krautblatter et al., 2012).

Surface-based geophysical methods represent a cost-effective approach for permafrost characterization (Harris et al., 2001). The application of geophysical methods has a long tradition in permafrost studies (Barnes, 1963; Akimov et al., 1973; Ferrians and Hobson, 1973; Scott et al., 1990). Hauck and Kneisel (2008a) and Kneisel et al. (2008) provide an overview about geophysical methods suitable for permafrost monitoring in high-mountain environments. In contrast to direct temperature measurements in boreholes, geophysical methods provide only indirect information about permafrost occurrence. On the other hand, geophysical methods are non-invasive, provide spatial 2D/3D information and are also applicable in instable fractured rock. Frozen ground changes the properties of underground materials, the degree of change depends on water content, pore size, pore water chemistry, sub-surface temperature and material pressure (Scott et al., 1990). In field applications, the most prominent geophysical parameters for the differentiation between frozen and unfrozen underground are electrical resistivity and compressional wave velocity (Hauck, 2001). Alpine rock cliffs in permafrost regions mostly consist of hard low-porosity rocks (<10 %), according to Tiab and Donaldson’s (2004) definition, and the applicability of electrical and seismic methods to these is yet unclear. While the relationship between electrical resistivity and frozen low-porosity bedrock has been investigated by Krautblatter et al. (2010), this article will focus on the applicability of p-wave refraction seismics to low-porosity bedrock.

The p-wave velocity of freezing rocks was investigated in the laboratory mostly using polar high-porosity (>10 %) sedimentary rocks (Timur, 1968; Dzhurik and Leshchikov, 1973; King, 1977; Pandit and King, 1979; Pearson et al., 1986; Remy et al., 1994; Sondergeld and Rai, 2007). Only few studies included low-porosity (<10 %) sedimentary rocks (Timur, 1968; Pearson et al., 1986), igneous rocks (Takeuchi and Simmons, 1973; Toksöz et al., 1976) and metamorphic rocks (Bonner et al., 2009). Early laboratory studies demonstrated compressional and shear wave velocity increases in freezing bedrock (Timur, 1968; King, 1977). Seismic velocities increase at sub-zero temperatures until they reach a plateau when most of the pores are frozen and the unfrozen water content is negligible (Pandit and King, 1979; Pearson et al., 1986). P-wave velocity of freezing rocks is controlled by the original water-filled porosity, i.e. the velocity corresponds to the changing proportion of frozen and unfrozen pore water content (King et al., 1988). In that sense, saline pore water increases the unfrozen pore water content at a given temperature (Anderson and Morgenstern, 1973; Tice et al., 1978) and flattens the otherwise sharp p-wave velocity increase when freezing (Pandit and King, 1979). Some authors observed hysteresis effects between ascending and descending temperature runs and assumed supercooling of the pore water during the descending temperature run as a reason (Nakano et al., 1972; King, 1977).

These findings have been transferred to field applications of p-wave velocity refraction seismics to various sedimentary landforms in polar environments (Roethlisberger, 1960; Kurfurst and Hunter, 1977; King, 1984; Harris and Cook, 1986; Zimmerman and King, 1986; Bonner et al., 2009) and to rock glaciers (Barsch, 1973; Musil et al., 2002; Ikeda, 2006; Hausmann et al., 2007), to bedrock (Hauck et al., 2004b) and to talus slopes (Hilbich, 2010) in mountainous regions. Akimov et al. (1973) note the discrepancy between seismic laboratory and field investigations. Due to different ambient settings, the comparison of small-scale laboratory results to large-scale field applications is complicated. These include a high rate of cooling, a non-representation of the stressed state of material as found in field conditions, supercooling and the time required for transition into ice in laboratory studies.

Wyllie et al. (1956) developed a time-average equation

$$\frac{1}{v}=\frac{\Phi}{v_l}+\frac{1-\Phi}{v_m}\ , \qquad (8.2)$$

where v is the measured velocity, v_l is the velocity of the liquid inside the pore space, v_m is the matrix velocity and Φ is the porosity, based on measurements of sandstone ($0.02 < \Phi < 0.32$) and limestone samples ($0.001 < \Phi < 0.18$). The time-average equation requires a relative uniform mineralogy, fluid saturation and high effective pressure (Mavko et al., 2009). To fulfil the seismic ray assumption of the time-average equation the wavelength should be small compared with typical pore and grain size, respectively, and the pores and grains should be arranged as homogenous layers perpendicular to seismic ray path (Mavko et al., 2009). Due to larger size and more heterogeneous distribution of vugular, i.e. secondary solution-related, pores in carbonate rocks, p-wave velocities of carbonate rocks show less dependency on porosity and the time-average equation underestimates the p-wave velocities (Wyllie et al., 1958). The two-phase model of Timur (1968) modified the Eq. (8.2) to frozen states,

$$\frac{1}{v} = \frac{\Phi}{v_i} + \frac{1-\Phi}{v_m} \tag{8.3}$$

where v_i is the velocity of ice in the pore space. Timur (1968) extended Eq. (8.3) to a three-phase time-average equation:

$$\frac{1}{v} = \frac{(1-S_i)\Phi}{v_l} + \frac{S_i\Phi}{v_i} + \frac{1-\Phi}{v_m} \tag{8.4}$$

with S_i is the relative fraction of pore space occupied by ice. Equation (8.3) and Eq. (8.4) were tested for sandstone ($0.13 < \Phi < 0.42$), carbonate ($0.15 < \Phi < 0.47$) and shale samples ($0.04 < \Phi < 0.10$). McGinnis et al. (1973) deduced that the relative p-wave velocity increases upon freezing Δv_p [%] versus porosity is

$$\Delta v_p = \frac{\Phi - 0.0363}{0.0044} \tag{8.5}$$

based on a linear regression of Timur's (1968) measurements; a formula that implies that there are no p-wave velocity changes below 3.6 % porosity. This relation was only used as an interpretation tool for their field measurements and possesses no validity for low-porosity rocks. Hauck et al. (2011) extended Timur's (1968) equation to 4 phases and weighted the p-wave velocities of the components by their volumetric fractions:

$$\frac{1}{v} = \frac{f_l}{v_l} + \frac{f_m}{v_m} + \frac{f_i}{v_i} + \frac{f_a}{v_a} \tag{8.6}$$

$$f_l + f_m + f_i + f_a = 1 \text{ and } 0 \le f_l, f_m, f_i, f_a \le 1 \quad (8.7)$$

where v_a is the velocity of air, f_l is the volumetric fraction of liquid water, f_r is the volumetric fraction of rock, f_i is the volumetric fraction of ice and f_a is the volumetric fraction of air. Carcione et al. (1998) give an overview about existing modelling of permafrost based on seismic velocities mostly for unconsolidated porous media (Zimmerman and King, 1986; King et al., 1988; Leclaire et al., 1994).

The influence of pressure on seismic velocities (Nur and Simmons, 1969) and porosity (Takeuchi and Simmons, 1973; Toksöz et al., 1976) is observed by many researchers (King, 1966; Wang, 2001). Two pressures can be distinguished, the confining or overburden pressure of the rock mass and the pore pressure of the fluid. These can reinforce or compete with each other, which is expressed by different values of n (Wang, 2001). The effective pressure (P_e) is

$$P_e = P_c - nP_p, \quad (8.8)$$

where P_c is the confining pressure, P_p is the pore pressure and $n \le 1$. The net overburden pressure (P_d) is then described as

$$P_d = P_c - P_p. \quad (8.9)$$

Pores react to an increasing confining pressure according to their shape: spheroidal pores deform and become thinner while spherical pores decrease in volume (Takeuchi and Simmons, 1973; Toksöz et al., 1976). P-wave velocity will increase due to decreasing porosity if the confining pressure does not surpass the damage threshold and porosity increase due to microcracking (Wassermann et al., 2009; Eslami et al., 2010; Heap et al., 2010). In measurements with high confining pressures, the effect of pores is negligible but the effects of cracks become more important (Takeuchi and Simmons, 1973). In frozen rocks, the ice pressure effect is most pronounced for spheroidal “flat” pores or cracks (Toksöz et al., 1976).

Pore shape, cracks and fractures also determine seismic anisotropy next to anisotropic mineral components and textural-structural characteristics such as bedding and cleavage (Lo et al., 1986; Thomsen, 1986; Vernik and Nur, 1992; Wang, 2001; Barton, 2007). The two latter causes are referred to as intrinsic anisotropy and cannot decrease as a result of pressure (Lo et al., 1986; Thomsen, 1986; Barton, 2007). In contrast, “induced anisotropy” through pores, cracks and fractures corresponds to stress. Stress increase due to loading can preferentially close pre-existing microcracks perpendicular to stress direction and decreases anisotropy (Wassermann et al., 2009; Eslami et al., 2010; Heap et al., 2010). However, stress increase can also lead to preferential opening of axially orientated microcracks (Eslami et al., 2010) or microcrack generation due to threshold surpassing (Wassermann et al., 2009; Heap et al., 2010) which then enhances anisotropy. The anisotropy *A* is defined as

$$\mathrm{A} = \frac{v_{\max} - v_{\min}}{v_{\max}} , \qquad (8.10)$$

where v_{max} is the faster velocity of both compressional waves parallel and perpendicular to cleavage or bedding and v_{min} is the slower velocity (Johnston and Christensen, 1995).

We postulate that p-wave velocity measurements in low-porosity rocks could become an important method for the monitoring of Alpine rock wall permafrost. This study aims at (1) measuring the p-wave velocity increases in low-porosity rocks, (2) evaluating the increase of matrix velocity due to ice pressure, (3) describing the alteration of seismic anisotropy due to changes of induced pore pressure and (4) incorporating this matrix velocity increase in the time-average equation.

8.2.3 Methodology

We tested 20 Alpine and 2 Arctic rock specimens between 1.8 and 25 kg sampled from several permafrost sites (see Table 8.2 for details). We used large rock specimens with a statistical distribution of >100 fissures, cracks and cleavages in a sample to cope with natural bedrock heterogeneity (Akimov et al., 1973; Matsuoka and Murton, 2008; Jaeger, 2009). All samples were immersed in water under atmospheric conditions until full saturation indicated by a constant weight was achieved (W_s). The free saturation method resembles the field situation more closely than saturation under vacuum conditions (Krus, 1995; Sass, 2005a) but probably includes air bubbles and can complicate the interpretation. After that, the samples are dried at 105°C to a constant weight (W_d). The ratio of weight difference between saturated and dry weight is equal to moisture content in percentage by weight. This multiplied by the rock density is effective porosity Φ_{eff} and includes only hydraulically-linked pores (Sass, 2005a). Rock density is derived from Wohlenberg (2012).

Table 8.2 Rock samples, source, lithology, geologic description (fabric), porosity (Φ) and degree of saturation (S_r).

Sample	Location (Country)	Landform	Sort of sample	Lithology	Geological description (fabric)	Porosity		publ. data
						Φ [%]	S_r	
A5	Steintaelli/Mattervalley (CH)	Rock wall	Q	pyritic paragneiss	metamorphic lamination	1.04 ±0.14	0.99	1-4
H1	Matterhorn/Mattervalley (CH)	Roc wall	S	gneiss	metamorphic lamination	0.93 ±0.12	1.00	5-6
X5	Zastler/Black Forest (D)	Scree slope	S	gneiss	metamorphic lamination	0.95 ±0.12	1.00	7
				gneiss		*0.97 ±0.04*		
X2	Pasterze/Grossglockner (A)	Glacier forefield	S	serpentine	mixed fabric directions	1.27 ±0.16	1.00	8
H2	Matterhorn/Mattervalley (CH)	Rock wall	S	amphibolite	mixed fabric directions	1.31 ±0.08	0.96	5-6
				other metamorphic rocks		*1.14 ±0.13*		
S1	Steintaelli/Mattervalley (CH)	Rock wall	Q	schisty quartz slate	planar slaty cleavage	2.40 ±0.12	0.96	1-4
S4	Steintaelli/Mattervalley (CH)	Rock wall	Q	schisty quartz slate	planar slaty cleavage	1.94 ±0.10	0.94	1-4
S3	Steintaelli/Mattervalley (CH)	Rock wall	Q	quartz slate	planar schistosity	1.49 ±0.08	0.98	1-4
X8	Murtel/Upper Engadin (CH)	Rock glacier	S	greenschist	planar schistosity	1.86 ±0.13	0.97	9-10
A22	Bliggspitze/Kaunervalley (A)	Rock wall	Q	mica schist	planar schistosity	1.56 ±0.11	1.00	11
X13	Kitzsteinhorn (A)	Rock wall	S	mica schist	planar schistosity	0.83 ±0.06	0.91	12
D2	Muragl/Upper Engadin (CH)	Rock glacier	S	mica schist	planar schistosity	1.04 ±0.07	1.00	9-10, 13
C1	Corvatsch/Upper Engadin (CH)	Rock wall	Q	migmatic schist	planar schistosity	2.76 ±0.27	0.94	14
C2	Corvatsch/Upper Engadin (CH)	Rock wall	Q	migmatic schist	planar schistosity	1.56 ±0.15	0.99	14
				schists		*1.48 ±0.50*		
M1	Aiguille du Midi (F)	Rock wall	Q	granite	no pronounced fabric	1.31 ±0.07	1.00	15-16

X9	Gemsstock (CH)	Rock wall	Q	granodiorite	no pronounced fabric	2.25 ±0.05	0.99	17
				plutonic rocks		*1.43 ±0.55*		
X6	Präg/Black Forest (D)	Scree slope	S	andesite	no pronounced fabric	3.03 ±0.35	1.00	7
X7	Präg/Black Forest (D)	Scree slope	S	andesite	no pronounced fabric	3.45 ±0.40	1.00	7
				volcanic rocks		*3.24 ±0.21*		
L1	Longyeardalen/Svalbard (N)	Rock wall	Q	Endalen Sandstone	no pronounced fabric between bedding planes (sample size)	5.21 ±0.96	1.00	18
L2	Longyeardalen/Svalbard (N)	Talus slope	S	Endalen Sandstone	no pronounced fabric between bedding planes (sample size)	6.03 ±1.11	1.00	18
				clastic rocks		*5.62 ±0.41*		
A8	Zugspitze/Wettersteingebirge (D/A)	Rock wall	Q	Wetterstein Dolomite	no pronounced fabric between bedding planes (sample size)	1.91 ±0.16	1.00	19-20
K1	Saumur/Loire Valley (F)	Sedimentary bassin	Q	Tuffeau Limestone	no pronounced fabric between bedding planes (sample size)	45.16 ±5.96	0.95	21-23
				carbonate rocks		*23.54 ±21.63*		

Q = quarried out of rock wall , S = picked from the surface; 1 = Krautblatter & Hauck (2007) , 2 = Krautblatter (2008), 3 = Krautblatter (2009), 4 = Krautblatter (2010) , 5 = Hasler et al. (2011b), 6 = Hasler et al. (2012), 7 = Hauck & Kneisel (2008c), 8 = Geilhausen et al. (2012), 9 = Maurer & Hauck (2007), 10 = Hauck et al. (2011), 11 = Krautblatter et al. (2009) , 12 = Hartmeyer et al. (2012), 13 = Musil et al. (2002), 14 = Gubler et al. (2011), 15 = Ravanel & Deline (2010), 16 = Deline et al. (2009), 17 = Kenner et al. (2011), 18 = Siewert et al. (2012), 19 = Krautblatter et al. (2010), 20 = Verleysdonk et al. (2011), 21 = Murton et al. (2000), 22 = Murton et al. (2001), 23 = Murton et al. (2006).

To distinguish quantitatively connected and unconnected pores will help the interpretation but necessary methods were not available. In an earlier study by Krautblatter (2009), six plan-parallel cylindrical plugs were prepared with diameter and length of 30 mm from six of the 22 samples used in this study and porosity values were measured using a gas compression/expansion method in a Micromeritics Multivolume Pycnomter 1305. These absolute porosity values are used to estimate the quality of the effective porosity values.

All 22 samples were immersed again for 48 h under atmospheric conditions and the saturated weight W_{48h} was determined. To determine the moisture conditions we calculated the degree of saturation S_r

$$S_r = \frac{(W_{48h} - W_d)}{(W_s - W_d)} \quad . \tag{8.11}$$

Subsequently, samples were loosely coated with plastic film to protect them against drying and were cooled in a range of 25°C to -15°C in a WEISS WK 180/40 high-accuracy climate chamber (Fig. 8.1).

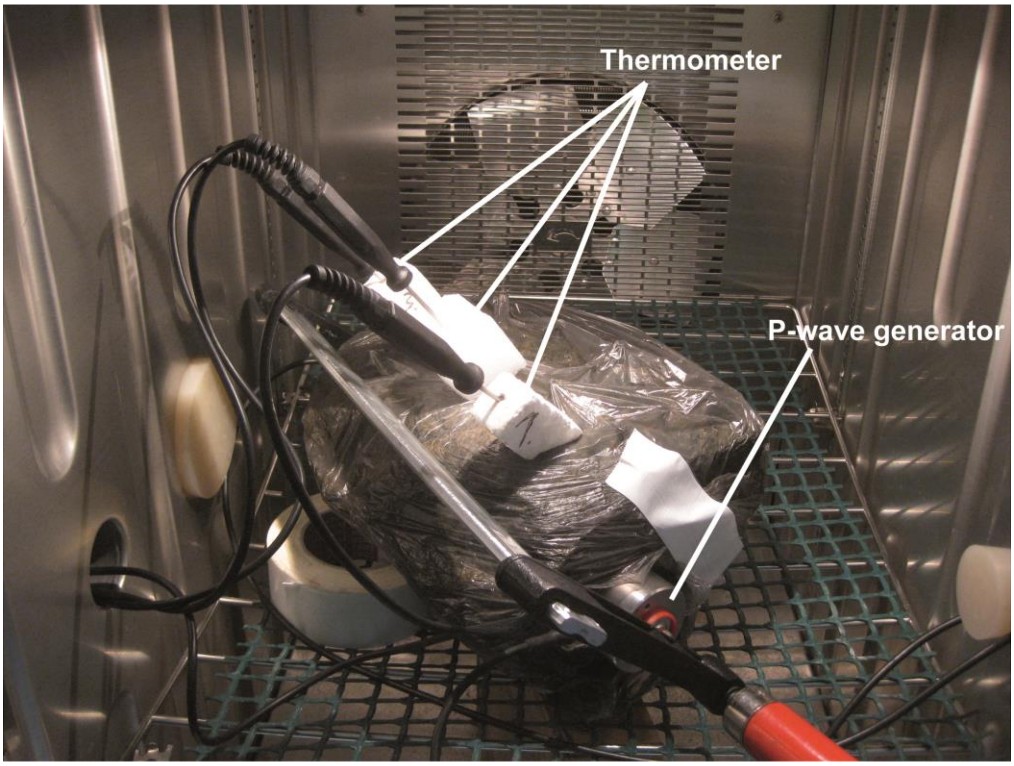

Fig. 8.1 Laboratory measurement set up of a p-wave velocity measurement of a schisty quartz slate sample (S1) in parallel direction to cleavage. Drilled into the rock sample are three thermometers to monitor rock temperature.

The cooling rate was first 7°C/h until sudden p-wave velocity increase due to freezing and was then decreased to 6°C/h (Matsuoka, 1990a). Ventilation was applied to avoid thermal layering. Two to three calibrated 0.03°C-accuracy thermometers were drilled into the rock samples to depths between 3 and 10 cm and a spacing of approximately up to 10 cm depending on sample size. Rock temperature at different depths and spacings were measured to account for temperature homogeneity in the sample (Krautblatter et al., 2010). The p-wave generator Geotron USG 40 and the receiver were placed on flattened or cut opposite sides of the cuboid samples. The wavelength of the generator was 20 kHz to fulfill requirements of the time-average equation; dispersion of p-wave velocities due to wavelengths are negligible (Winkler, 1983). The traveltime of the p-wave was picked using a Fluke Scopemeter 192B with an accuracy of $1\text{-}2*10^{-6}$ s. The internal deviation induced by the measurement procedure was assessed by conducting five subsequent traveltime measurements. To account for the anisotropy of the rock samples, we measured p-wave velocities in the same sample in the direction of cleavage/bedding and perpendicular to the cleavage/bedding direction. The matrix velocity v_m is calculated by solving Eq. (8.3). The velocity of the material in the pore space v_i is 1570 m/s for water in the unfrozen status and 3310 m/s for ice (Timur, 1968), we replaced porosity with effective porosity in the calculation. Matrix velocity is calculated for frozen (-15° C) and unfrozen status (mean value of v >0°C) both for parallel and perpendicular to cleavage/bedding measurements according to

$$v_m = \frac{1-\Phi}{\frac{1}{v}-\frac{\Phi}{v_i}} \tag{8.12}$$

The change of matrix velocity Δv_m due to freezing is calculated according to

$$\Delta v_m = \frac{v_{mf} - v_{ms}}{v_{ms}} \tag{8.13}$$

where v_{mf} is the matrix velocity in the frozen status and v_{ms} is the matrix velocity in the saturated status. The change of anisotropy ΔA due to freezing will be calculated according to:

$$\Delta A = A_s - A_f \tag{8.14}$$

where A_s is the anisotropy after 48h saturation and A_f is the anisotropy for frozen status.

8.2.4 Results

Table 8.2 and Table 8.3 give an overview about measured rock samples and their rock properties and seismic velocities. Figure 8.2 represents the evolution of p-wave velocities dependent on rock temperature of six selected rock samples from six different lithologies.

8.1.4.1 Porosities and degree of saturation

The absolute (vacuum) porosity values comprehending connected and non-connected porosity measured for 6 samples (A5, X2, S1, S3, X9, A8) by Krautblatter (2009) are compared with the effective (atmospheric pressure) porosity values comprehending only connected porosity. The absolute porosity (2.60 ±0.21 %) is on average 30% higher than the effective porosity (1.72 ±0.12 %), only in slate samples both were equivalent.

Rock samples are classified according to their lithology into three metamorphic, two igneous and two sedimentary rock clusters. Absolute deviations of porosity within the clusters are less than 1% except for carbonate rock samples. After 48h saturation, gneiss, plutonic rocks, volcanic rocks and clastic rocks show mean S_r of 1.00, other metamorphic rocks (mean S_r=0.98), schists (mean S_r=0,97) and carbonate rocks (mean S_r=0.98) are not fully saturated but all could possibly to develop cryostatic pressure upon the volumetric expansion of ice in more than 91% saturated pores (Walder and Hallet, 1986).

Table 8.3 Rock samples classified into lithological groups and seismic properties. The table shows p-wave velocity of a saturated unfrozen (v_{ps}) and a frozen (v_{pf}) sample, p-wave velocity increase due to freezing (Δv_p), matrix velocity of a saturated unfrozen (v_{ms}) and a frozen (v_{mf}) sample, matrix velocity increase due to freezing (Δv_m), anisotropy of a saturated (A_s) and a frozen (A_f) sample and the decrease of anisotropy due to freezing (ΔA).

Sample/	P-wave velocity						Matrix Velocity						Anisotropy		
Rock	parallel			perpendicular			parallel			perpendicular					
class	V_{ps} [ms^{-1}]	V_{pf} [ms^{-1}]	ΔV_p [ms^{-1}]	V_{ps} [ms^{-1}]	V_{pf} [ms^{-1}]	ΔV_p [ms^{-1}]	V_{ms} [ms^{-1}]	V_{mf} [ms^{-1}]	ΔV_m [ms^{-1}]	V_{ms} [ms^{-1}]	V_{mf} [ms^{-1}]	ΔV_m [ms^{-1}]	A_s [%]	A_f [%]	ΔA [%]
A5	6261	6689	428	4774	5474	700	6479	6749	270	4869	5481	612	23.75	18.16	5.59
H1	5401	6099	698	4933	5399	466	5529	6148	619	5034	5432	398	8.67	11.48	-2.81
X5	5699	5826	127	5007	5467	460	5858	5850	-8	5110	5480	370	12.14	6.16	5.98
gneiss			*418 ±194*			*542 ±105*			*294 ±217*			*460 ±101*			*2.92*
X2	5275	5873	598	4381	4672	291	5432	5923	491	4488	4687	199	16.95	20.45	-3.50
H2	4934	5929	995	4611	5356	745	5080	5992	912	4760	5401	641	6.55	9.66	-3.12
other metamorphic rocks			*797 ±199*			*518 ±227*			*702 ±211*			*420 ±221*			*-3.31*
S1	5249	5805*	556*	1953	4373*	2420*	5564	5906*	342*	1969	4400*	2431*	62.79	24.67*	38.12
S4	5236	5942*	706*	1667	4425*	2758*	5506	6037*	531*	1667	4455*	2788*	68.16	25.53*	42.63
S3	5116	6096	980	2615	3636	1021	5294	6165	871	2655	3631	976	48.89	40.35	8.53
X8	4682	5480	798	4504	5612	1108	4869	5540	671	4683	5687	1004	3.80	2.35	1.45
A22	4329	5833	1504	3882	5274	1392	4454	5904	1450	3942	5303	1361	10.33	9.58	0.74
X13	5740	6224	484	5263	5786	523	5868	6270	402	5395	5799	404	8.31	7.04	1.27
D2	5018	5373	355	4836	5355	519	5140	5408	340	4943	5352	409	3.63	0.34	3.29
C1	4030	5293	1263	2189	4356	2167	4249	5385	1136	2228	4395	2167	45.68	17.70	27.98
C2	5502	5978*	476*	1664	2595*	931*	5735	6051*	316*	1640	2579*	939*	69.76	56.59*	13.17
schists			*791 ±307*			*1427 ±681*			*673 ±319*			*1387 ±717*			*15.24*
M1	4228	5000	772	3583	4178	595	4332	5011	679	3663	4180	517	15.26	16.44	-1.18
X9	5191	6078	887	4039	4759	720	5471	6194	723	4181	4808	627	22.19	21.70	0.49
plutonic rocks			*830 ±58*			*658 ±63*			*701 ±22*			*572 ±55*			*-0.35*

X6	4345	6000	1655	4935	5538	603	4618	6129	1511	5286	5657	371	11.96	7.70	4.26
X7	4426	5541	1115	4317	5248	931	4730	5678	948	4597	5360	763	2.46	5.29	-2.83
volcanic rocks			*1385 ±270*			*767 ±164*			*1230 ±282*			*567 ±196*			*0.72*
L1	3422	5130	1708	5363	4904	1341	3652	5290	1638	3835	5031	1196	3.96	4.41	-0.45
L2	4521	5105	584	3989	4502	513	5139	5290	151	4440	4608	168	11.77	11.81	-0.04
clastic rocks			*1146 ±562*			*927 ±414*			*895 ±744*			*682 ±514*			*-0.25*
A8	3723	6383	2660	1879	6068	4189	3838	6500	2662	1864	6161	4297	49.53	4.93	44.59
K1	2247	4167	1920	2014	4211	2197	3566	5332	1766	2647	5467	2820	10.37	1.04	9.32
carbonate rocks			*2290 ±370*			*3193 ±996*									*26.96*

* indicates lowest sample temperatures above -10° C

8.2.4.2 P-wave velocities of frozen rock

P-wave velocity increases significantly as a result of freezing in all 22 samples. Supercooling causes hysteresis effects resulting in sudden latent heat release and rock temperature increase observed in 16 of 22 samples and indicated as p-wave velocity hysteresis of three rock samples (A5, X8, L2) in Fig. 8.2. Parallel to cleavage/bedding, p-wave velocity increase is highest in sedimentary (carbonate and clastic) rocks, followed by magmatic (volcanic and plutonic) rocks and lowest in metamorphic rocks (schists, other metamorphic rocks and gneiss) (Fig. 8.3A). The order remains the same perpendicular to cleavage/bedding except for schists (Fig. 8.3B).

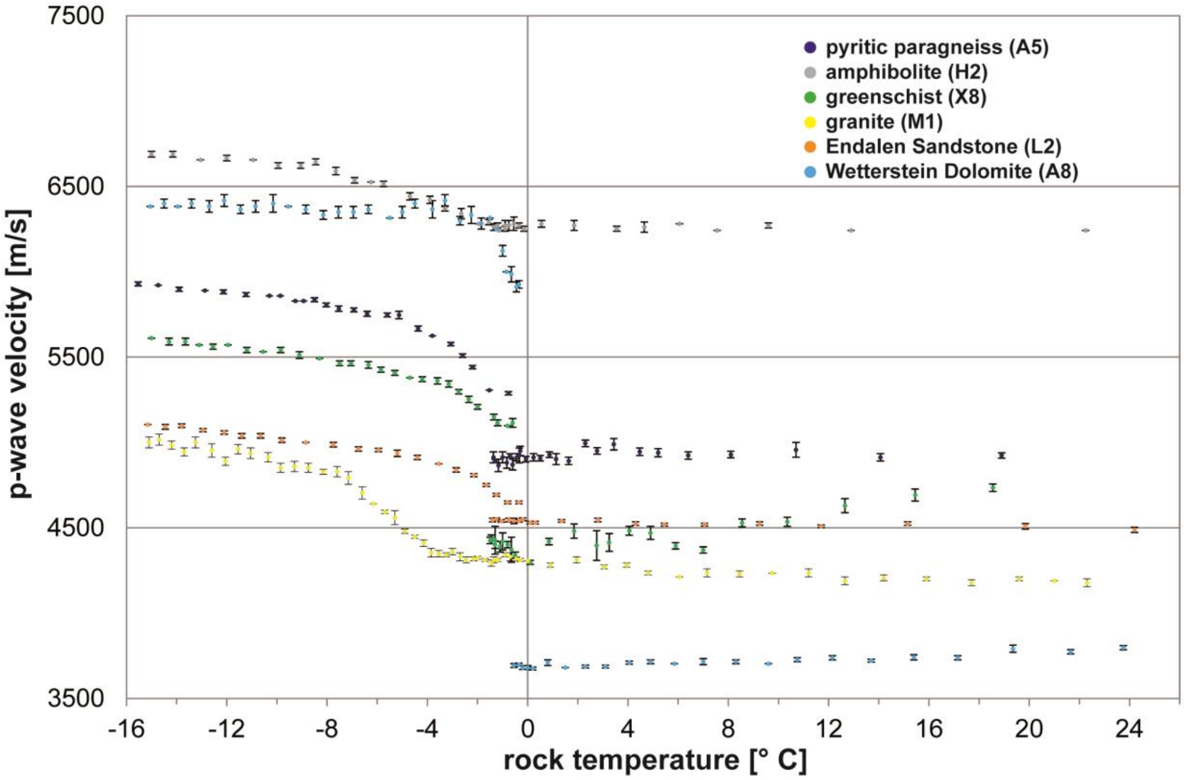

Fig. 8.2 P-wave velocity of several rock samples measures parallel to cleavage or bedding plotted against rock temperature; error bars indicate mean deviation of p-wave velocities.

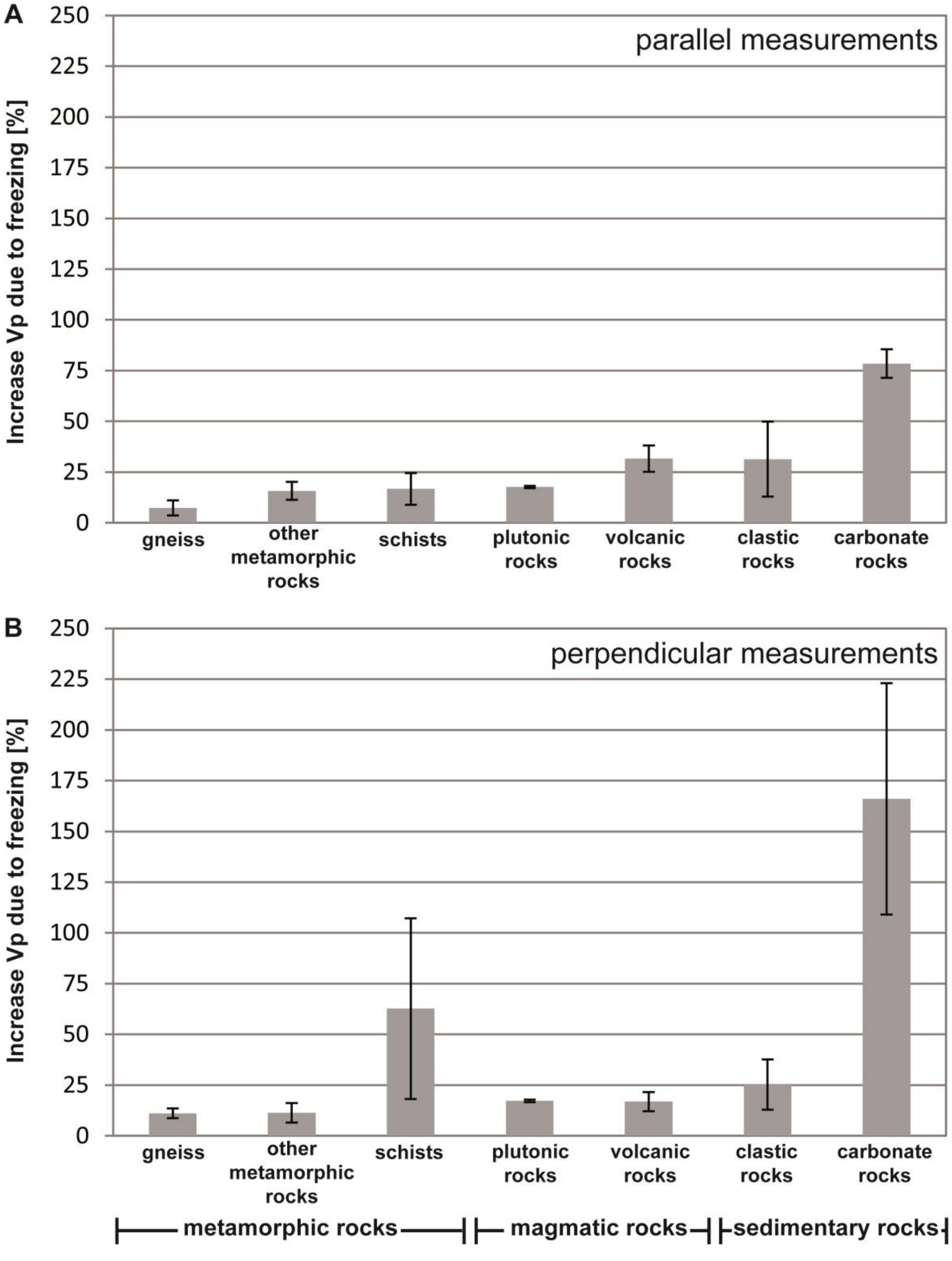

Fig. 8.3 P-wave velocity increase of samples in percent for rock groups classified based on lithology; A) parallel to cleavage/bedding and B) perpendicular to cleavage/bedding; error bars indicate mean deviation.

8.2.4.3 Porosity dependent change in p-wave velocities

Existing time-average models assume a dependence of p-wave velocity increase on porosity. We plotted the increase of p-wave velocity due to freezing measured and calculated with Eq. (8.3) against the mean effective porosity (Fig. 8.4 A and B). We excluded the carbonate rocks due to their vugular pores and the constrained applicability of the time-average equation (Wyllie et al., 1958). All measured p-wave velocity increases are much higher than calculated according to Eq. (8.3), expected as a result of phase transition from water (1570 m/s) to ice (3310 m/s) only. Parallel to cleavage or bedding, the offset between measured and calculated results is increasing from gneiss (296 ±205 m/s), schists (642 ±314 m/s), other metamorphic rocks (685 ±200 m/s), plutonic rocks (686 ±0 m/s), clastic rocks (815 ±683 m/s), to volcanic rocks (1158 ±278 m/s). Perpendicular to cleavage or bedding, the offset increases from other metamorphic rocks (414 ±210 m/s), gneiss (467 ±108 m/s), volcanic rocks (529 ±183 m/s), plutonic rocks (561 ±41 m/s), clastic rocks (626 ±474 m/s) to schists (1368 ±695 m/s).

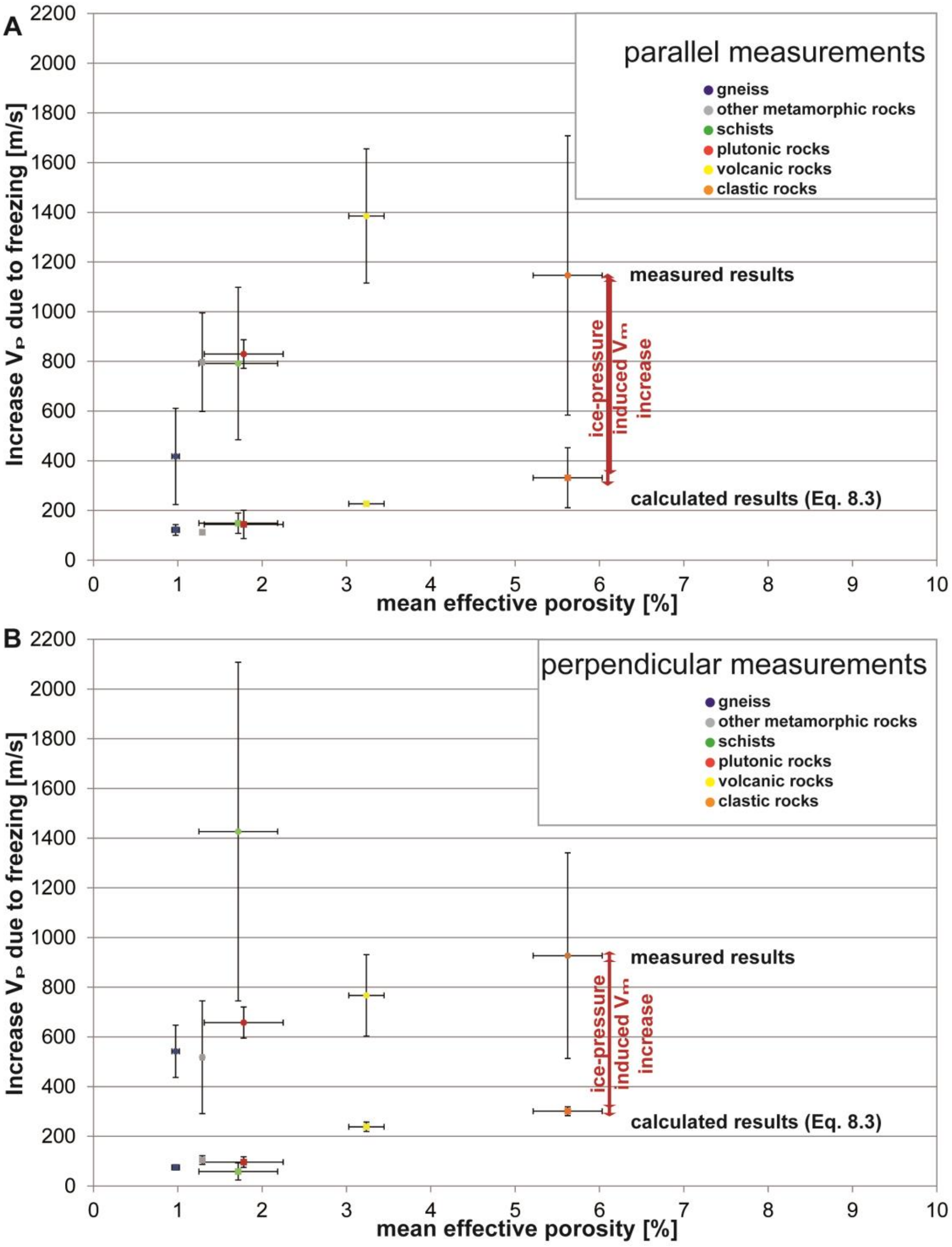

Fig. 8.4 P-wave velocity (v_p) increase due to freezing plotted against mean effective porosities for six different rock groups. P-wave velocity increases A) parallel to cleavage or bedding and B) perpendicular to cleavage/bedding, the dots are measured values and the quadrats are values calculated using Eq. (8.3).

8.2.4.4 Matrix Velocity

The increase in p-wave velocity is too high to be solely explained by changes of the p-wave velocity in the pore infill as is suggested by Timur (1968). Here, the additional change in p-wave velocity is explained by the increase in matrix velocity as shown in Eq. (8.12) and Eq. (8.13). All measured rock samples show significant matrix velocity increases v_m (see Table 8.3) due to freezing except one gneiss sample (X5). Timur (1968) expected no matrix velocity increase due to freezing. Figure 8.4 shows that Timur's Eq. (8.3) underestimates the measured p-wave velocity significantly.

8.2.4.5 Anisotropy

Anisotropy A is calculated according to Eq. (8.10) for conditions after 48h saturation (A_s) and frozen conditions at -15°C (A_f). Induced anisotropy due to pores, cracks and fractures can be reduced through pressure (Wang, 2001; Barton, 2007). Anisotropy alteration ΔA is calculated according to Eq. (8.14). In our experimental setup, pore ice pressure reduces induced anisotropy due to the closure of pores, cracks and fractures, while the confining (atmospheric) pressure remains constant. The pore pressure changes due to the phase transition from water to ice in saturated pores. Ice develops pressure through volumetric expansion and ice segregation (Matsuoka, 1990a; Matsuoka and Murton, 2008). 15 of 22 samples show an anisotropy reduction due to freezing (1-45 %), which is especially pronounced in slates, schists and carbonates. Seven samples show negligible (n=3, < 1.50 %) or small (n=4, ≤ 3.50 %) increases in anisotropy when freezing. Three samples (L1, L2, M1) show a low anisotropy increase, the anisotropy of four other samples (H1, H2, X2, X7) increases slightly.

8.2.5 Discussion

8.2.5.1 Model setup and representativeness

Previous studies (Timur, 1968; McGinnis et al., 1973) explained p-wave velocity increases exclusively as an effect of porosity and infill. We postulate, that these models apply well for soft high-porosity rocks but cannot be transferred to hard low-porosity rocks. This is due to the fact that the effects of freezing are determined by multiple effects including (i) porosity but also (ii) the pore form and the degree of fissuring and (iii) ice pressure development. Here, we try to derive a straightforward model that explains the effects of freezing in low-porosity rocks on p-wave velocity.

(i) We have tested 7 clusters or 22 specimens of low-porosity rocks. These indicate p-wave velocity increases from 518 ±227 m/s (other metamorphic rocks), 542 ±105 m/s (gneiss), 658 ±63 m/s (plutonic rocks), 767 ±164 m/s (volcanic rocks), 927 ±414 m/s (clastic rocks), 1427 ±681 m/s (schists) to 3193 ±996 m/s (carbonate rocks) perpendicular to cleavage or bedding. Timur's (1968) model would, respectively, anticipate p-wave velocity changes from 104 ±17 m/s (other metamorphic rocks), 75 ±2 m/s (gneiss), 96 ±21 m/s (plutonic rocks), 238 ±19 m/s (volcanic rocks), 301 ±60 m/s (clastic rocks) to 58 ±34 m/s (schists) and underestimates strongly p-wave velocity increases in low-porosity bedrock (Fig. 8.4B). Due to vugular pores, the time-average equation and Eq. (8.3) are not applicable to carbonate rocks (Wyllie et al., 1958) and we excluded them from further calculations. The offset between measured velocities and calculated velocities shows that porosity is not the dominant determinant of p-wave velocity changes in low-porosity bedrock. Calculations of p-wave velocities parallel to cleavage or bedding reflect this offset trend but are violating the seismic ray assumptions of the time-average equation and should be used with caution for parallel velocities.

(ii) Pore form is among the most important factors for seismic properties (Nur and Simmons, 1969; Toksöz et al., 1976; Wang, 2001) and the most difficult one to quantify (Wang, 2001). Pore form determines pressure susceptibility (Takeuchi and Simmons, 1973; Toksöz et al., 1976) and ice effects (Toksöz et al., 1976) while pore linkage affects the saturation. Water-saturated porosity controls p-wave velocity (King, 1977; King et al., 1988) and frost weathering (Matsuoka, 1990a; Sass, 2005a; Matsuoka and Murton, 2008). We assume no influence of salinity due to low solubility of rock minerals in the used specimens (Krautblatter, 2009). Hydraulically linked porosity is best described by effective porosity (Sass, 2005a) and we replace porosity in Eq. (8.3) with effective porosity. In future studies, the pore form could be assessed by porosimetric analyses and, thus, the differentiation of connected and non-connected porosity would facilitate a quantitative interpretation. However, calculating matrix velocity with absolute porosity values would change matrix velocity only by 2 ±2 %, which is well below the accuracy within the clusters. The weathering history determines the enlargement of pores, fissures and fractures in permafrost and non-permafrost samples, and we assume that the long periglacial weathering history of high-alpine and arctic samples affects pore shape and connectivity. Previous mentioned studies mostly used high-porosity arctic specimens from Mesozoic sedimentary rocks and frost susceptibility in these low-strength rocks operates at a millimeter- to centimeter-scale (Matsuoka and Murton, 2008). We choose decimeter-large rock samples from several Alpine and one Arctic permafrost sites instead of standard bore cores. These are derived from the surface or quarried out of rock walls, are affected by permafrost in their history, include hundreds of micro-fissures, and represent the natural texture of permafrost-affected bedrock. This reflects, that properties like pore distribution, texture, fissures and fractures provide the space and determine the effects of confined ice growth in hard rock samples (Matsuoka and Murton, 2008). In hard rocks, volumetric expansion and ice segregation is restricted by the rigid matrix and ice growth in pores and fissures causes high levels of stress inside the samples.

(iii) The variation of confining pressure related to rock overburden is a long-lasting process on a millennium scale, whereas pore pressure changes steadily (Matsuoka and Murton, 2008). Frequent daily freeze-thaw-cycles reach a depth of approximately 30 cm (Matsuoka and Murton, 2008) while annual cycles often reach up to 5 m and more (Matsuoka et al., 1998). In our experiment the change in matrix velocity in combination with reduced anisotropy points towards “induced anisotropy” (Wang, 2001) in pores that reflects intrinsic stress generation. The pore pressure in the connected pores presumably increases due to ice-stress applied on the matrix and probably closes non-connected porosity embedded in the matrix which results in decreasing anisotropy. A surpassing damage threshold or opening of microcracks could explain anisotropy increase. The pore pressure can be generated by the ice pressure building (Matsuoka, 1990a; Vlahou and Worster, 2010) due to volumetric expansion of in situ water (Hall et al., 2002; Matsuoka and Murton, 2008) and ice segregation (Walder and Hallet, 1985; Hallet, 2006; Murton et al., 2006). In the laboratory, any open system allows water migration and enables ice segregation while closed systems with water-saturated samples favour volumetric expansion (Matsuoka, 1990a). Our experimental setup is a quasi-closed system; water is only in situ available due to saturation and ice can leave through pores and joints. Due to 48h saturation, the degree of saturation reaches at least 0.91 in all samples and the threshold for frost cracking as a result of volumetric expansion is fulfilled (Walder and Hallet, 1986). According to Sass (Sass, 2005a) and Matsuoka (1990a) our quasi-closed system and fully saturated samples could be a good analogue to natural conditions.

Cooling rates of 6°C/h have been used by Matsuoka (1990a) before and produce high expansion and freezing strain. Sass (2005a) assumes high saturation of alpine rocks below the upper 10 cm. This is due to the fact that ice pressure is relaxed through ice deformation and ice expansion into free spaces (Tharp, 1987), ice extrusion (Davidson and Nye, 1985) and the contraction of samples was observed in the long-term due to ice creep (Matsuoka, 1990a). In our system, samples cool from all outer faces which presumably act to seal the sample with ice. On the other hand, ice segregation along temperature gradients in fissured natural bedrock will cause suction up to several MPa (Walder and Hallet, 1985; Murton et al., 2006) and ice growth, and presumably cause a persistent elevated level of cryostatic stress similar to our laboratory setup.

8.2.5.2 A time-average model for low-porosity rock

Fig. 8.4 A and B show an offset which is not explainable by Eq. (8.3). This offset is induced by ice-pressure. The way ice-pressure is effective depends on the pore form of connected and non-connected pores. A quantitative analysis needs to distinguish between connected and non-connected pores. We use lithology as a proxy for pore form in our model and we assume an elevated level of stress in cryostatic systems. The pressure-induced variable *m* depends on lithology and is introduced as an extension of Eq. (8.3):

$$\frac{1}{v}=\frac{\Phi}{v_i}+\frac{1-\Phi}{v_m}*\frac{1}{m} \tag{8.15}$$

where $m=1+\Delta v_m$; (8.16)

Δv_m is the increase of matrix velocity empirically derived from our measurements. These general conclusion referenced by rock type are preliminary and should be applied with caution since we used a restricted number of samples. For our rock samples, we propose values of *m* of 1.09 ±0.02 for gneiss, 1.09 ±0.05 for other metamorphic rocks, 1.62 ±0.45 for schists, 1.15 ±0.00 for plutonic rocks, 1.12 ±0.05 for volcanic rocks and 1.17 ±0.13 for clastic rocks or, alternatively a general *m* of 1.34 ±0.31 (Table 8.3). The use of Eq. (8.15) enhances to differentiate between frozen and unfrozen status of low-porosity rocks and can facilitate interpretation of field data.

8.2.6 Conclusion

Here, we propose to incorporate the physical concept of freezing in confined space into empirical mixing rules of p-wave velocities and present data (1) of p-wave measurements of 22 different alpine rocks, (2) evaluate the influence of ice pressure on seismic velocities, (3) determine anisotropic decrease due to ice pressure and (4) extend Timur's (1968) 2-phase model for alpine rocks:

(1) All tested rock samples show a p-wave velocity increase dependent on lithology due to freezing. P-wave velocity increases from 418 ±194 m/s for gneiss to 2290 ±370 m/s for carbonate rocks parallel to cleavage/bedding; perpendicular measurements show an acceleration ranging from 414 ±210 m/s for other metamorphic rocks to 2745 ±1444 m/s for carbonate rocks.

(2) P-wave velocity increases due to freezing are dominated by an increase of the velocity of the rock matrix while changes in pore-infill velocities are insignificant. Matrix velocity increases perpendicular to cleavage/bedding from 420 ±221 m/s for other metamorphic rocks to 1387 ±717 m/s for schists; parallel measurements reflect the matrix velocity increases perpendicular to cleavage but should be treated with caution.

(3) Anisotropy decreases by up to 45 % as a result of crack closure due to ice pressure in 15 of 22 rock samples. This effect is observed especially in all samples containing planar slaty cleavage or planar schistosity.

(4) We developed a novel time-average equation based on Timur's (1968) 2-phase equation with a lithology dependent variable to increase the matrix velocity responding to developing ice pressure while freezing.

This study provides the physical basis for the applicability of refraction seismics in low-porosity permafrost rocks. Due to their rigidity low-porosity bedrock cannot expand freely in response to ice pressure and, thus, matrix velocity increases. P-wave velocity increases predominantly as a result of ice pressure and to a lesser extent as a result of the higher velocity of ice than water in pores. The extension of the time average equation provides a more realistic calculation of the rock velocity and facilitates the interpretation of field data and possible permafrost distribution in alpine rock walls.

Acknowledgements

The authors thank G. Nover, J. Ritter and W. Scherer for equipment support to enable this study. Thanks to D. Amitrano and the anonymous reviewer for their extensive remarks and suggestions that helped a lot to improve the final paper. Also thanks to D. Funk for critical discussions, S. Verleysdonk for measurements, C. Hauck, C. Hilbich, L. Ravanel, A. Hasler, M. Siewert and P. Deline and M. Geilhausen for providing samples and all other involved persons.

8.3 Field monitoring of permafrost in the Steintaelli 2006 and 2007

This chapter is published by M. Krautblatter and D. Draebing under the title "Pseudo 3D - P-wave refraction seismic monitoring of permafrost in steep unstable bedrock" in the "Journal of Geophysical Research – Earth Surface" in 2014. Formatting, pagination and numbering of equations and figures has been modified for production of this thesis. The article is written in American English which is preserved. This paper transfers the findings of Draebing and Krautblatter (2012) from laboratory to field conditions. Chapter 8.3.2 introduces the importance of permafrost research, overviews geophysical methods and shows the potentials of refraction seismics to monitor permafrost in steep rock walls. The geologic conditions as well climatic conditions in 2006/07 in the study site Steintaelli are described in Chapter 8.3.3. Chapter 8.3.4 describes laboratory and field data appraisal and data processing. Results (Chapter 8.3.6) are presented and discussed (Chapter 8.3.6). The conclusion (Chapter 8.3.7) summarizes the main findings of the paper. The methodical findings are the base for data analysis of seismic field data from 2012 and 2013.

8.3.1 Abstract

Degrading permafrost in steep rock walls can cause hazardous rock creep and rock slope failure. Spatial and temporal patterns of permafrost degradation that operate at the scale of instability are complex and poorly understood. For the first time, we used p-wave seismic refraction tomography (SRT) to monitor the degradation of permafrost in steep rock walls. A 2.5D survey with five 80 m long parallel transects was installed across an unstable steep NE-SW-facing crestline in the Matter Valley, Switzerland. P-wave velocity was calibrated in the laboratory for water-saturated low-porosity paragneiss samples between 20° and -5° C and increases significantly along and perpendicular to the cleavage by 0.55-0.66 km/s (10-13 %) and 2.4-2.7 km/s (>100 %) respectively, when freezing. Seismic refraction is, thus, technically feasible to detect permafrost in low-porosity rocks that constitute steep rock walls. Ray densities up to 100 and more delimit the boundary between unfrozen and frozen bedrock and facilitate accurate active-layer positioning. SRT shows monthly (Aug. and Sep. 2006) and annual active-layer dynamics (Aug. 2006 and 2007) and reveals a contiguous permafrost body below the NE-face with annual changes of active-layer depth from 2-10 m. Large ice-filled fractures, lateral onfreezing of glacierets and a persistent snow cornice cause previously unreported permafrost patterns close to the surface and along the crestline which correspond to active seasonal

rock displacements up to several mm/a. SRT provides a geometrically highly-resolved subsurface monitoring of active-layer dynamics in steep permafrost rocks at the scale of instability.

8.3.2 Introduction

Degrading permafrost in rock walls is a major hazard due to both, rockfall activity and slow rock deformation that endanger infrastructure and can cause casualties (Harris et al., 2009; Bommer et al., 2010). Enhanced tourism-related use (Messerli, 2006) and the revival of hydro-power generation and storage in high-topography Alpine settings require an enhanced assessment of the rockfall hazard from permafrost rock walls, as much of the infrastructure was designed at a time when thawing permafrost was not taken into consideration (Haeberli et al., 2010). Rock permafrost is not synonymous with perennially frozen rock as intact rock often only freezes significantly below the datum freezing point T_0 (0° C), due to the effects of solutes, pressure, pore diameter and pore material (Lock, 2005; Krautblatter et al., 2010). However, below 0°C ice develops in cavities such as fractures and fissures in the rock mass (Hallet et al., 1991) and, thus, the perennial presence of ice has serious implications on the thermal, hydraulic and mechanical properties of the system. Two lines of evidence support the hypothesis of increasing instability in thawing permafrost rock walls: Rockfall inventories point towards an increasing frequency and magnitude of rockfalls from permafrost –affected rock walls (Noetzli et al., 2003; Schoeneich et al., 2004; Ravanel and Deline, 2008), and, from a geotechnical point of view, mechanical properties of water-saturated rock and ice are highly susceptible to temperature changes close to the thawing point (Krautblatter et al., 2013). Slope instability in thawing permafrost bedrock is affected by (i) temperature change, (ii) altered hydrostatic pressure, (iii) ice segregation and (iv) loading. (i) Temperature changes control ice-mechanical properties (Davies et al., 2000; Guenzel, 2008) and rock-mechanical properties (Mellor, 1973; Inada and Yokota, 1984; Krautblatter et al., 2013) of permafrost rocks. (ii) permafrost can influence the hydrostatic pressure in rock walls due to water seepage from decaying permafrost and due to perched water levels in rock masses with ice-sealed rock (Pogrebiskiy and Chernyshev, 1977; Harris and Murton, 2005; Fischer et al., 2007). Elevated hydrostatic pressure promotes the creep of ice (Weertman, 1973), increases lateral shear stress on the rock mass, and reduces friction by lowered effective normal stress. (iii) Ice segregation acts to prepare and enlarge existing planes of weakness and to abolish the effects of surface roughness along these (Murton et al., 2006; Gruber and Haeberli, 2007). (iv) Temperature cycles can lead to cyclic loading due to the volumetric expansion of warming ice (Davies et al., 2000). These destabilization processes occur below the active-layer in several to tens of meters depth and cannot be observed at the surface. Subsurface methods to temporally and spatially monitor stability-relevant parameters in permafrost rocks are crucial to understand involved processes at relevant depths and will gain increasing importance in the foreseeable future.

Hauck and Kneisel (2008a) provide an overview of geophysical methods for permafrost monitoring in loose materials and underlying bedrock in high-mountain environments. Hereby, tomographies are a common geophysical display tool for imaging spatial changes in physical parameters such as p-wave velocity, electrical resistivity and others in 2D and 3D sections. Tomographies are solved as an inverse problem based on systematic spatial measurements of electrical, seismic and other properties like for instance electrical resistance and seismic wave traveltimes. Significant freezing-induced changes in these physical properties have been observed in laboratory studies and these support the interpretation of tomographies in terms of permafrost occurrence and change. The use of repeated electrical resistivity and seismic refraction tomography for active-layer monitoring along fixed transects in unconsolidated permafrost materials has been shown by several authors (Hilbich et al., 2008; Kneisel et al., 2008; Hilbich, 2010; Hilbich et al., 2011). However, few geophysical studies exist on the applicability of geophysical methods in steep low-porosity bedrock. Sass (1998) showed that electrical resistivity tomography (ERT) is capable of measuring temporal and spatial variations of the freezing front on a centimeter- to decimeter-scale in solid rock faces. Krautblatter and Hauck (2007) extended this method to a decameter-scale and applied it to the investigation of active-layer processes in steep permafrost rock walls. A first attempt for the quantitative application of ERT in rock walls, in particular to image the temperature distribution inside rock walls, has been demonstrated by Krautblatter et al. (2010). However, the resolution of ERT is limited to the detection of bulk resistivity properties of usually decimeter to meter-thick layers and their change with increasing investigation depth, whereas seismic methods are predestined to resolve sharp boundaries and discontinuities with higher geometric accuracy. Seismic refraction tomography (SRT) and ground penetrating radar (GPR) have been applied to determine 2D and 3D rock mass properties and potential instabilities in unfrozen rocks (Heincke et al., 2006a; 2006b). Significant correlations between p-wave velocity and joint spacing were demonstrated in seismic refraction surveys for the upper 25 to 30 meters (Sjogren et al., 1979; Sjogren, 1984; Barton, 2007). The application of SRT in steep permafrost rock walls has not been demonstrated yet, probably due to the challenges in field surveying, laboratory analysis and the misconception that P-wave velocity would not increase significantly upon freezing in low porosity rocks.

Refraction seismics is based on the interpretation of refracted headwaves that indicate the transition of a slower unfrozen top layer to a frozen layer with faster p-wave propagation below (King et al., 1988). McGinnis et al. (1973) explain the relative increase in p-wave velocity Δv_p [%] of frozen rocks

$$\Delta v_p = \frac{p - 3.63}{0.44} \tag{8.16}$$

as a result of porosity p [%]. Bedrock with porosities below 3.6 % would not cause any p-wave acceleration in the laboratory; bedrock with porosities below 5% would cause an acceleration <6%, hardly detectable in field surveys. Timur (1968) suggested a three-phase time-average equation to estimate compressional wave velocities v_p

$$v_p = \frac{(1 - S_i)\varphi}{v_l} + \frac{S_i \varphi}{v_i} + \frac{1 - \varphi}{v_m} \tag{8.17}$$

where φ is pore space, and S_i is the fraction of pore space occupied by ice, (1-S_i) is the pore space filled by water under the assumption that air is absent, and v_m, v_i and v_l and are p-wave velocities of the rock matrix, interstitial ice (3.31 km/s) and water (1.57 km/s). However, both studies rely on the Timur’s (1968) laboratory testing, where only 2 samples had less than 10% porosity. These water-saturated shale samples with 3.5 and 9.6 % porosity had shown p-wave velocity increases of 8 and 36 % that significantly exceed estimates of equation (8.16) and are not explainable with equation (8.17). Thus, for consolidated samples (i.e. bedrock), Carcione and Seriani (1998) introduced the “cementation effect.” For this they used the Leclaire et al. (1994) model with a logistic growth function of p-wave velocity due to freezing but performed slowness averaging of ice and solid phases when computing average moduli. Comparing models that average bulk modulus (Voigt), compressibility (Reuss/Wood), slowness (Wyllie et al., 1956) and 2/3-phase models (Zimmerman and King, 1986; Minshull et al., 1994), Carcione and Seriani (1998) concluded that the considered cementation effect best explains experimental data from high-porosity bedrock samples where the proportion of supercooled unfrozen water in pores controls wave propagation. In low-porosity bedrock, the expansion of rigid rock is restricted and ice pressure controls wave propagation; Draebing and Krautblatter (2012) tested 22 low-porosity and almost fully-saturated rock samples and incorporated the results in a modification of Timur’s (1968) 2-phase equation

$$v_p = \frac{\varphi}{v_i} + \frac{1 - \varphi}{v_m} * \frac{1}{m} \tag{8.18}$$

where *m* is the lithology-dependent p-wave velocity increase of the rock matrix due to developing ice pressure (Draebing and Krautblatter, 2012). P-wave velocity in low-porosity bedrock types increases by 11–166 % when freezing and should be detectable in field surveys.

The present knowledge of permafrost distribution at the meter and decameter scale, at which instability develops, is restricted. This is due to the complex interplay of topographic, hydrologic, climatic and long-lasting transient thermal influences and due to the lack of appropriate monitoring techniques (Harris et al., 2009). Coupled glacier-permafrost systems develop complex behavior due to hydrological interconnectivity between glaciers and permafrost systems, the impact of hanging glaciers, the onfreezing of glacierets, and enhanced heat transfer along ice-filled fractures (Haeberli, 2005; Harris and Murton, 2005; Moorman, 2005; Krautblatter, 2010). Spatial and temporal effects of snow cover, the onfreezing of glacierets and ice-filled fractures on steep permafrost rocks have not been monitored yet with sufficient resolution. Snow cover influences permafrost distribution by insulating or cooling the subsurface, altering the albedo and influencing water availability (Gruber, 2005; Gruber and Haeberli, 2007). Snow warming or cooling effects depend on season, quantity and thermal characteristics (Phillips, 2000; Ishikawa, 2003; Luetschg et al., 2008). Climate Change scenarios of the IPCC (2007) point towards decreasing snow depth at lower altitudes and a reducing of the snow season (Bavay et al., 2009). Luetschg et al. (2008) postulate amplified effects of temperature rise for regions with thin snow cover and where the snowmelt is preponed. Ice-filled rock crevices act as efficient semiconductors. Cold thermal impulses propagate instantaneously, as no active-layer has to be frozen, and effectively, with the high thermal conductivity of ice of 2.2 W/mK along ice-filled fractures. Warm thermal impulses are buffered by the latent heat capacity of ice. Conduction of cold thermal impulses along ice-filled fractures operates effectively during a much higher number of days compared to snow-free rock surfaces. The reaction of high-alpine permafrost rock walls to climate change will additionally be orchestrated by changes in permafrost-glacier interconnectivity and snow cover depth and duration. Detailed insights into the thermal control exerted by snow cover, onfreezing and ice in fractures are essential to anticipate the impact of climate change on permafrost rocks.

In this paper, we use laboratory calibration (8.3.4.1) to establish a p-wave velocity vs. temperature relation (8.3.5.1). This helps to accurately interpret permafrost distribution scenarios observed in field measurements (8.3.5.3). In the field, we appraise data on steep rock faces and process these data (8.3.4.2), analyze raw data (8.3.4.3) and use up-to-date inversion methods to create tomographies. We test the sensitivity of the tomographies to initial settings like velocity (8.3.4.4) and ray propagation (8.3.4.5). We use a 1D-conduction model (8.3.4.6) to link seismic results with modeled permafrost development during the year (8.3.6.4).

This article aims to show (i) that, in contradiction to the McGinnis et al. (1973) hypothesis, low-porosity rocks show significant p-wave acceleration when freezing; (ii) that the increase of p-wave velocity is accurately detectable in high-resolution field surveys, that (iii) p-wave SRT delivers a geometrically precise delineation of active-layer depth in steep unstable permafrost rock walls including complex effects exerted by lateral onfreezing, persistent snow cover and ice in fractures.

8.3.3 Study area

The study site close to the crestline between Matter and Turtmann Valleys (3070 to 3150 m a.s.l., Valais, Switzerland) consists of slaty paragneiss which slightly dips (10-20°) towards the NE slope. Several rock bars dissect the Rothorn-NE-Glacier into small glacierets. The mean annual air temperature (MAAT) inferred from measurements in the Matter Valley from 1962 to 1990 is –3.5°C. Since 2002, climatological data have been recorded close to the study site at a meteorological station at 2770 m a.s.l. and were corrected 0.6°C per 100 m.

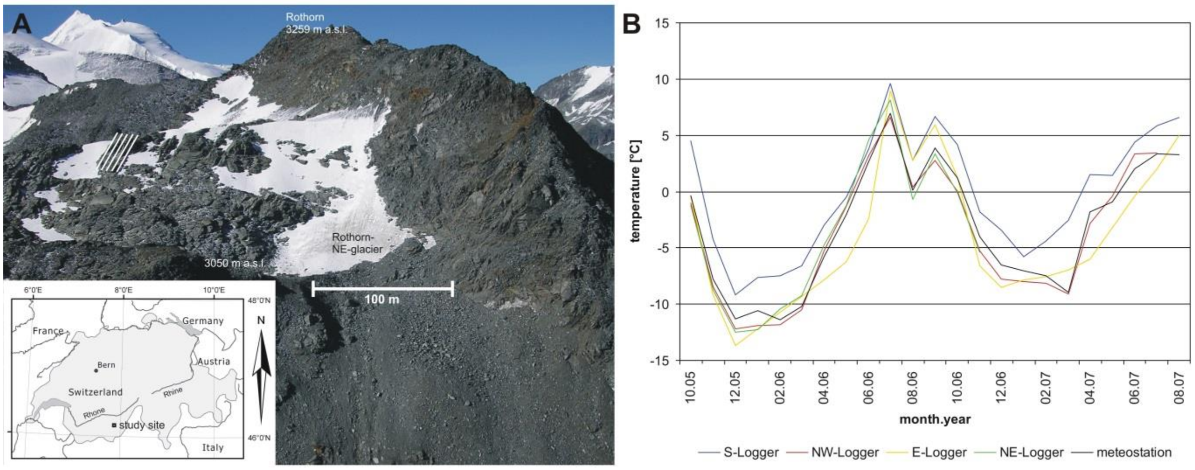

Fig. 8.5 A: The study site “Steintaelli” at the crestline between Matter and Turtmann Valleys, Valais, Switzerland; the white lines indicate the 5 seismic arrays that collate into the 2.5D tomography displayed in Figure 2 (left side). B: Monthly air and rock temperatures indicate a several degrees colder winter period in 2005/2006 than in 2006/2007.

In 2005, four rock temperature loggers were installed at 10 cm depth and in four aspects according to the design suggested by Gruber et al. (2003). Mean rock near surface temperatures in winter

2005/2006 were on average 5.5°C degrees lower than in 2006/2007 (Fig. 8.5 B). The relatively cool August 2006 (mean air temperature (MAT) 0.0°C), when seismic monitoring began, interrupted the warmer July and September (MAT 7.0°C and 3.9°C) periods in 2006. In summer 2007, temperatures rose continuously until July/August (MAT 3.3°C). The crestline of the Steintaelli is most of the time covered by a 2-3 meters thick and wide snow cornice. In August 2007, the north facing slope also hosted snow/firn patches and the advancing glacier extended onto Transect 1 and froze onto the rock wall (Fig. 8.6 C). Persistent ice also exists in decimeter wide rock fractures along the crestline that are created by the diverging rock block creep with crack opening of several millimeters per month in late summer (Krautblatter, 2009).

8.3.4 Methods

8.3.4.1. Laboratory work

P-wave velocity at different rock temperatures was measured using two 30x20x15 cm large cuboid paragneiss samples taken from Steintaelli rock crest. These large rock samples incorporate dozens of cleavages to cope with their natural heterogeneity of schistosity. Porosity ranges between 1.94 ±0.10 % (Sample S4) and 2.40 ±0.12 % (Sample S1). Samples were submerged in low conductive 0.032 (±0.002) S/m water in an undisturbed closed basin to approach their chemical equilibrium. Pore space was fully saturated under atmospheric pressure, as free saturation resembles the field situation more closely than saturation under vacuum conditions (Krus, 1995; Sass, 2005a). Samples were cooled in a range of 20 to -5°C in a WEISS WK 180/40 high-accuracy climate chamber. Ventilation was applied to avoid thermal layering. Samples were loosely coated with plastic film to protect them against drying. Three calibrated 0.03°C-accuracy thermometers measured rock temperature at different depths to account for temperature heterogeneity in the sample. The mean deviation of measured temperature heterogeneity in the sample is indicated by error bars in Fig. 8.12. The p-wave generator and the receiver were place on flattened opposite sides of the cuboid samples. The traveltime of the p-wave was picked using a Fluke Scopemeter with an accuracy of 1-2*10^{-6} s. The internal deviation induced by the measurement procedure was assessed by conducting five subsequent traveltime measurements. We measured p-wave velocities in the direction of cleavage and perpendicular to the cleavage to quantify anisotropy.

8.3.4.2 Data appraisal

In 2006, 5 parallel transects with 24 drilled geophone positions each (total 120) were installed across the NE and SW-facing steep crestline. We applied 2 m geophone spacing along the transects and the five parallel transects are separated by a 4 m spacing. Exact geophone x, y and z positions were measured using a Leica TCA 1800L tachymeter with an accuracy of ca. 1 cm (Fig. 8.6).

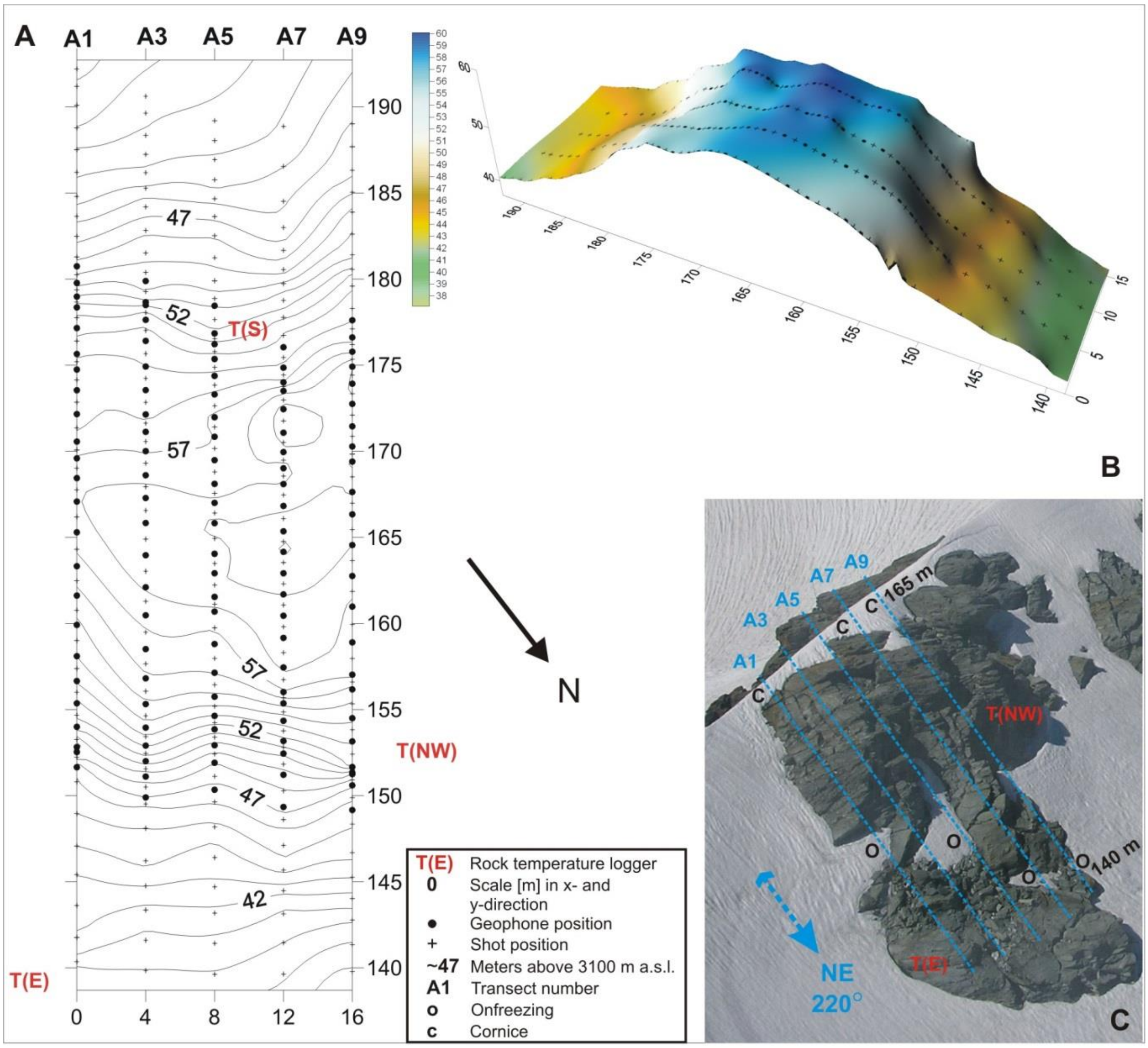

Fig. 8.6 Geometry of the 2.5D transect consisting of five parallel monitoring transects with 120 geophones and 200 shot positions across the instable Steintaelli crestline. Contour lines in Fig. 2 A and color scale in Fig. 2 B indicate altitude above 3100 m a.s.l..

40 shot positions with 2 m spacing along each transect start 13 m north of first geophone and end 19 m south of the last geophone. Shot positions were marked for repeated measurements with

identical geometries. The resulting pseudo 3D array comprises 78*16 m and consists of 200 shot positions arranged around 120 geophone positions. Enhanced coupling of the geophones was accomplished by firmly fixing geophones in 10 mm holes drilled in the rock face. We recorded seismic data with a 24 channel seismograph (Geode, Geometrics Inc.) with 4.5 Hz geophones in August and September 2006 as well as in August 2007. A 5 kg sledgehammer was used as a source; for signal improvement and noise reduction multiple shots were stacked. To cope with short traveltimes, the record interval was set to 63 µs which corresponds to a 0.25 m propagation of a 4.0 k m/s p-wave. The first arrival was amplified by 36 dB to better show first arrivals of remote shots. We used the software package ReflexW 5.5.2 for processing and interpretation of refraction seismic data. The reconstruction of the subsurface velocities in ReflexW is based on the adaptation of synthetic traveltimes calculated by forward modeling to observed traveltimes. The tomographic algorithm applies the Simultaneous Iterative Construction Technique (Sandmeier, 2008), i.e. the iteratitive process ends if a stopping criterion is fulfilled (modeling parameter settings and stopping criteria see Table 8.4) and displays the best model result. First arrivals of seismic waves are picked manually and topography is readily implemented in the traveltime analysis.

Table 8.4 Adjusted parameters for Reflex W tomography modeling.

Modeling parameter	value/active
space increment [m]	0.5
maximum number of iterations	50
maximum CPU-time [s]	1000
threshold	0.001
def. data variance	0.1
model change A	1
model change B	0.1
convergence search	10
max def. change [%]	50
max. beam width	10
started curved ray	1
average x	2
average z	2
min. velocity	0
max. velocity	6000
statistical criterium	active
check no ray area	active
curved ray	active
force 1st iteration	active

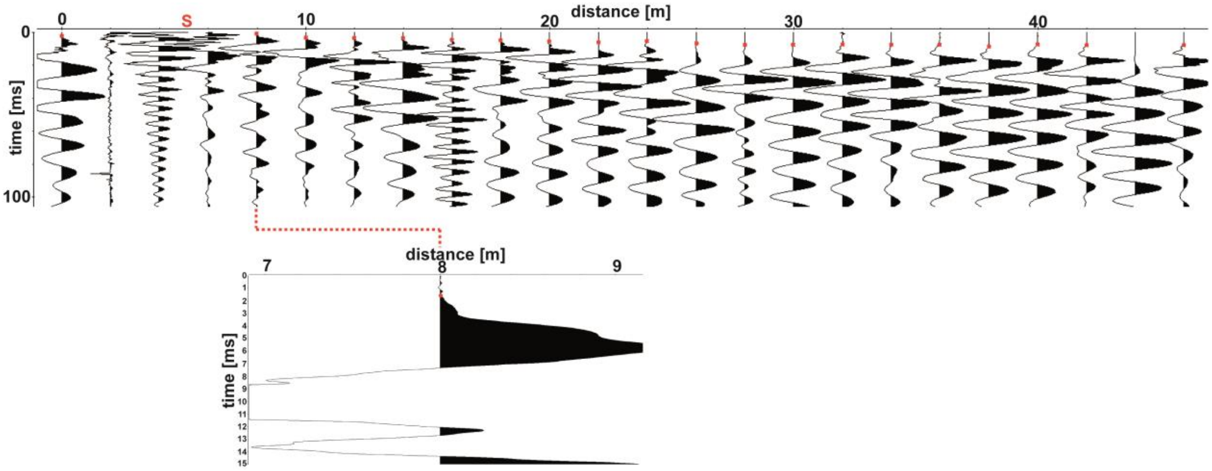

Fig. 8.7 Picked first arrivals of a shot at 5 m in Transect 1 in September 2006; the plotscale is 60 (upper image). One single first arrival at 8 m with a plotscale of 1866 (bottom image).

First arrivals of shots are picked at high plotscales (>1500); higher plotscales increase the amplitude without altering the wavelength. This picking mode allows a precise picking with picking errors ranging from 0.25 ms for first arrival close to the shot and up to 1 ms for first arrivals far from the shot. As a result the p-wave velocity can differ up to ± 300 m/s but typically less.

The quality of tomographies is assessed in terms of Root Mean Square (RMS) and total absolute time difference. The latter sums up absolute time differences between calculated and measured travel times independently and evaluates the overall adaptation (Sandmeier, 2008). For this, we used a position bin size that is a quarter of the model block size of 0.5 m (K.-J. Sandmeier, personal communication, 2011).

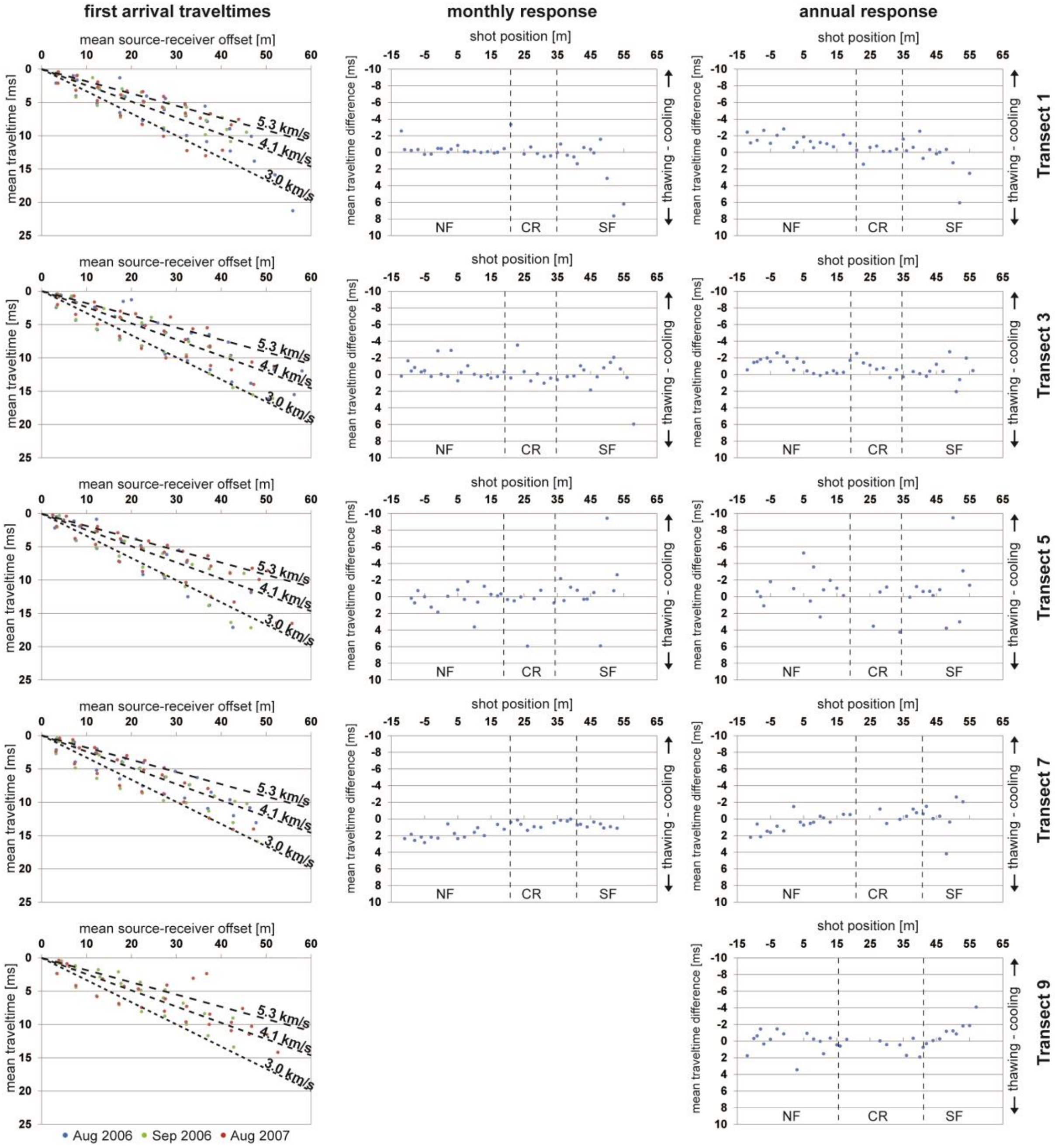

Fig. 8.8 Mean traveltimes are plotted against mean source-receiver offset for every 5 m source-receiver offset and indicate p-wave velocities below 3.0 km/s, above 4.1 km/s and above 5.3 km/s. Mean traveltime differences are plotted against shot position for subsequent measurements (NF = north face, SF = south face and CR = crestline) and indicate tendency of thawing or cooling as monthly and annual response, respectively.

8.3.4.3 Raw data analysis

Mean first arrival traveltimes of August and September 2006 as well as August 2007 are plotted against the mean source-receiver offset of every 5 m source-receiver offset (Fig. 8.8) (Hausmann et al., 2007; Hilbich, 2010). The dotted lines indicate velocities above 4.1 km/s and 5.3 km/s, respectively. All transects show existence of low p-wave velocities below 3.0 km/s. Mean monthly (2006) and annual (2006/2007) traveltime differences were plotted against the shot position. Negative values indicate a mean traveltime decrease, i.e. a p-wave velocity increase. The raw data provides valuable information for the preprocessing of tomography modeling and the evaluation of model quality.

8.3.4.4. Initial model optimization and data quality

Initial model velocity and gradient influence ray path propagation of seismic waves. Hauck (2001) and Lanz et al. (1998) recommend adjusting initial velocities to representative p-wave velocities for the research area if a priori information is available or, alternatively, to overestimate initial velocity gradients to ensure sufficient ray coverage. We tested different start models with initial velocities ranging from 2.0 to 5.5 km/s and gradients of 0, 0.2 and 0.6 km/s; best results in terms of RMS and total absolute time difference were gained without a predefined gradient. We tested initial model velocities between 2.0 and 5.5 km/s using data sets of Transects 1, 5 and 9. Total absolute time difference decreases with increasing initial velocity and reaches a minimum at 4.0 km/s in Transects 1 and at 3.5 km/s in Transects 5 and 9 (Fig. 8.9). The RMS minima in Transects 1, 9 and Transect 5 at initial p-wave velocities of 3.5 km/s and 2.5 km/s are only slightly below RMS values at 4.0 km/s.

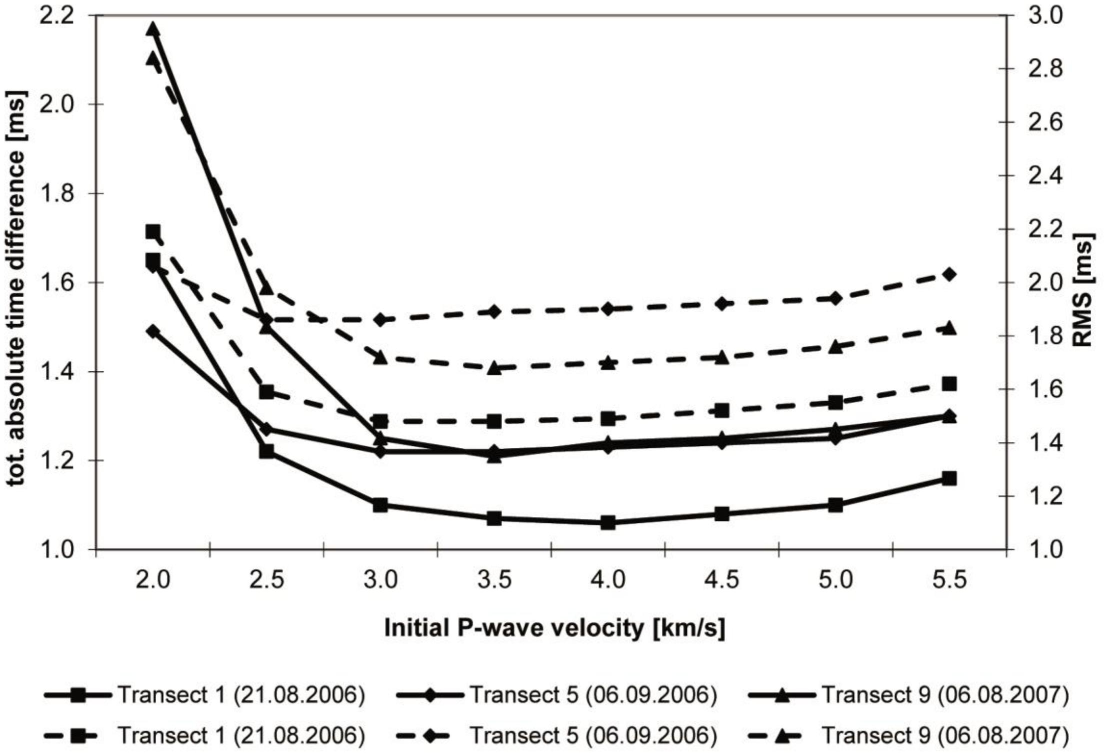

Fig. 8.9 Total absolute time difference (lines) and RMS (dotted lines) for different initial p-wave velocities implemented in ReflexW-modeling.

According to RMS error and total absolute time difference, initial velocities of 3.5 and 4.0 km/s show best results (Fig. 8.9). Raw data analysis shows the existence of p-wave velocities ≥5.3 km/s and ≤2.5 km/s, which correspond to laboratory values for paragneiss samples. Initial velocities lower than 4.0 km/s would exclude higher velocities in the final tomographies (Fig. 8.10). Tomographies based on initial velocities faster than 4.5 km/s exclude velocities lower than 3.0 km/s. We decide to choose initial velocity of 4.0 km/s to combine best fit in terms of RMS error and total absolute time difference with the most appropriate representation of raw data lower than 2.5 km/s and faster than 5.3 km/s in the final tomographies.

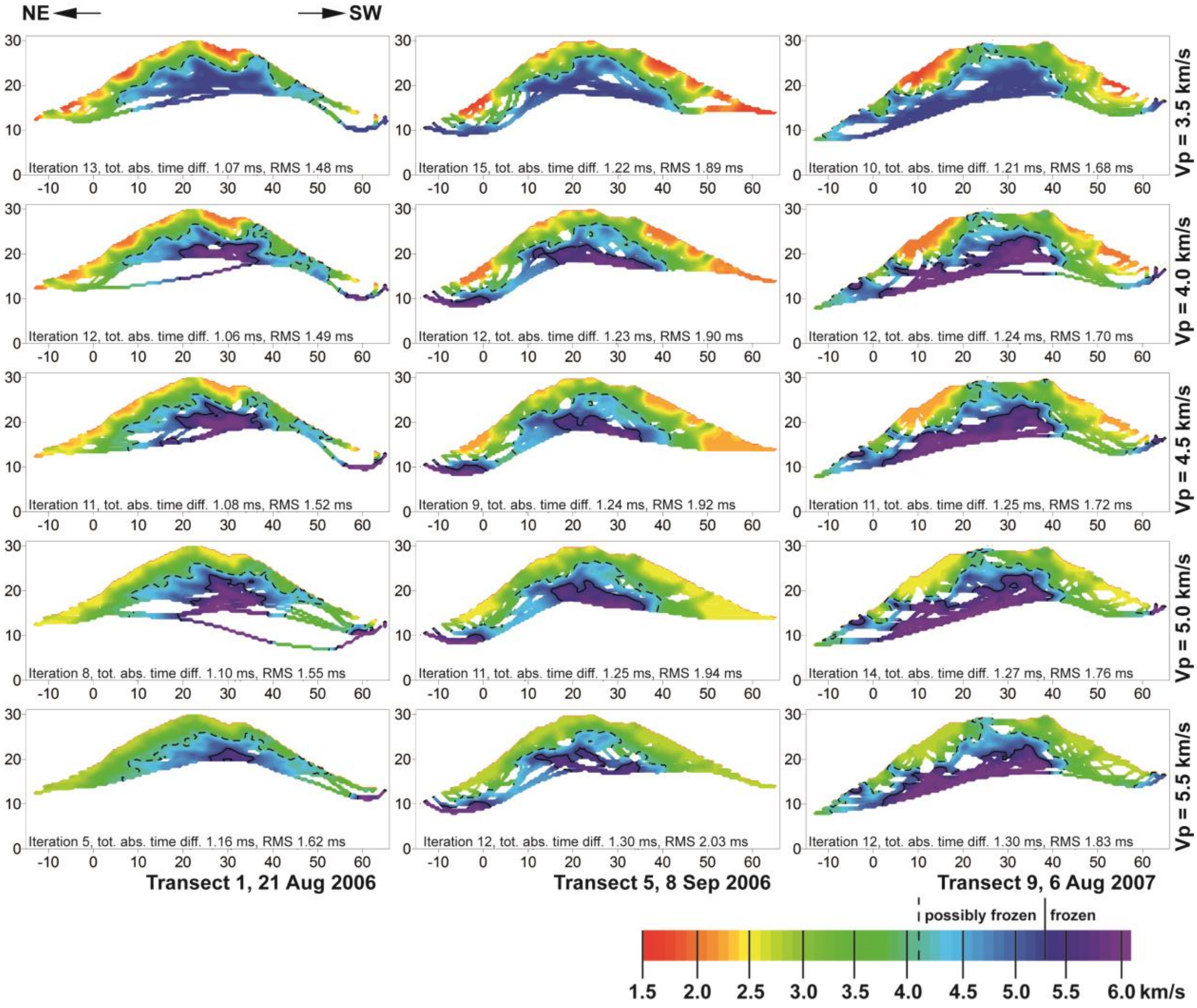

Fig. 8.10 Response of transects 1, 5 and 9 to different initial velocities (Vp) for the inversion modeling process.

8.3.4.5 Model sensitivity

Model resolution and accuracy are influenced by the number of model blocks and should correspond to the density of ray paths (Hauck and Vonder Mühll, 2003a). An increasing number of model blocks enhance model resolution but decreases model accuracy. Ray density and the number of rays crossing a cell generally decrease with increasing depth (Lanz et al., 1998). Due to the shallow thawing depth we define 0.5 m as the minimum acceptable resolution. ReflexW displays ray density as the number of rays crossing a model block divided by the total number of rays (Fig. 8.11) (Sandmeier, 2008).

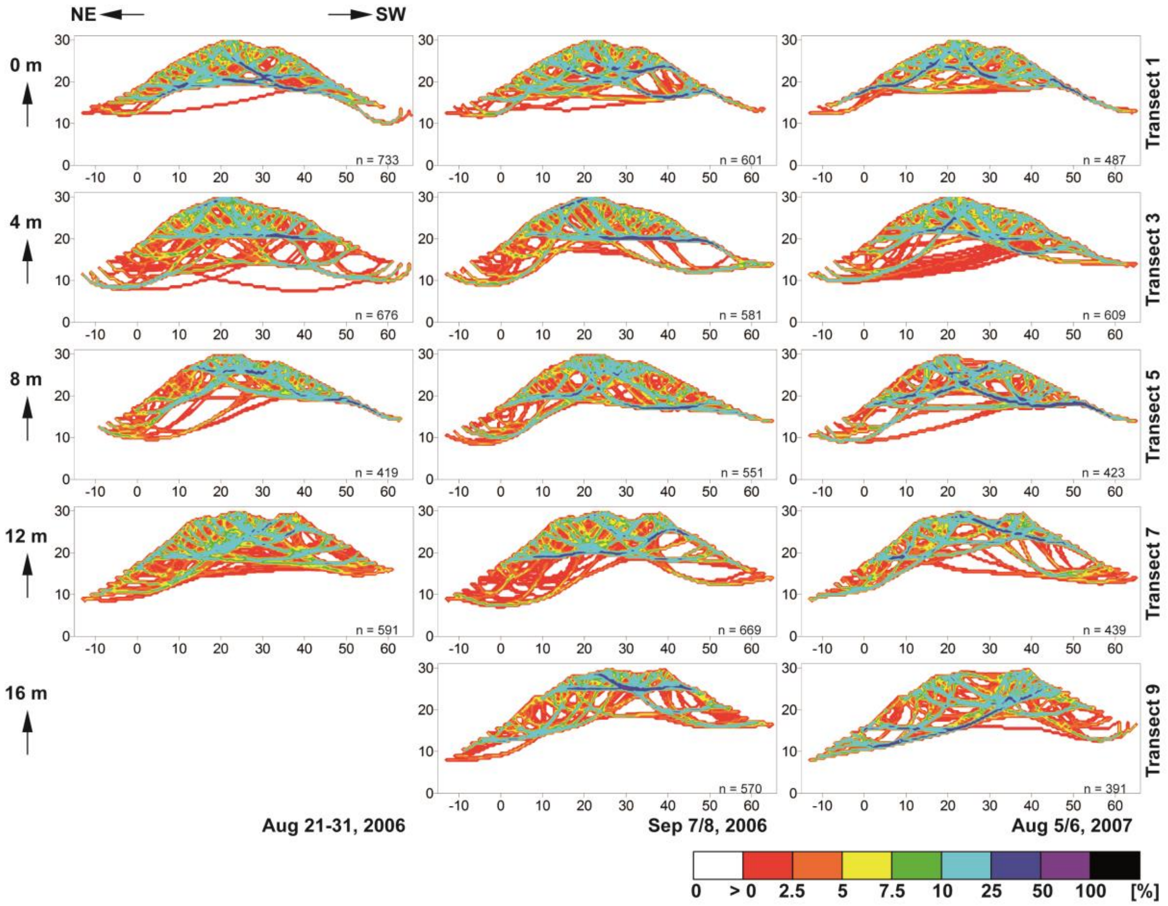

Fig. 8.11 Ray density in the 5 transects with n is giving the total number of rays in each transect and ranges between 391 and 733. The maximum ray density of 100 % equals the total number of rays n.

Model regions with ray densities close to 25 % indicate subparallel movement of up to 100 rays and more and indicate high accuracy while ray densities close to 0 indicate low accuracy. In the resulting tomographies we blanked out sections of the tomographies that are not sufficiently covered by rays.

8.3.4.6 Thermal modeling

To justify our interpretations (8.3.6.4) we try to link seismic data from the different times and years with thermal modeling of 2006. We use the data from NW- and S-exposed temperature loggers (Fig. 8.6) as input data for a thermal underground model. The simplest way to analyze the thermal variation in depth in time is the use of a one-dimensional heat conduction given by a sinusoidal temperature variation:

$$T(z,t) = MART + Tae^{-z\sqrt{\frac{\omega}{2\kappa}}} \sin\left(\omega t - z\sqrt{\frac{\omega}{2\kappa}}\right), \tag{8.19}$$

where T is temperature [°C], t is time, z is depth of rock, MART is mean annual rock temperature, Ta is the half amplitude of the sinusoidal variation, ω is the frequency of sinusoid (in our case one year) and κ is the thermal diffusivity (Carslaw and Jaeger, 1986; Williams and Smith, 1989). In 2006, MART is -3.4°C for NE-Logger and -0.3°C for S-Logger, Ta is 9.3 K and 8.6 K, respectively.

Thermal conductivity of alpine metamorphic approaches values between 1.5 and 3.5 W $m^{-1} K^{-1}$ and specific heat capacity between 0.75-0.8 kJ $kg^{-1} K^{-1}$ (Vosteen and Schellschmidt, 2003). We use a thermal conductivity of 2.5 W $m^{-1} K^{-1}$, a specific heat capacity of 0.8 kJ $kg^{-1} K^{-1}$ and a density of 2600 kg m^{-3} for slaty paragneiss. The calculated volumetric heat capacity is 2.08 x 10^{6} J $m^{-3} K^{-1}$ and thermal diffusivity 1.2 x 10^{-6} m^2 s^{-1}. The assumed geothermal gradient is 0.05 W m^{-2}. This model is purely conductive and does not account for discontinuities in the rock mass, multidirectional heat flow due to topography (Noetzli et al., 2007), advective (Hasler et al., 2011a; Hasler et al., 2011b) or conductive processes (Hasler et al., 2011b).

8.3.5 Results

8.3.5.1 Laboratory results

P-wave velocities parallel and perpendicular to the cleavage increase by 10-13 % (550-660 m/s) and more than 100 % (2400-2700 m/s) subsequent to freezing (Fig. 8.12).

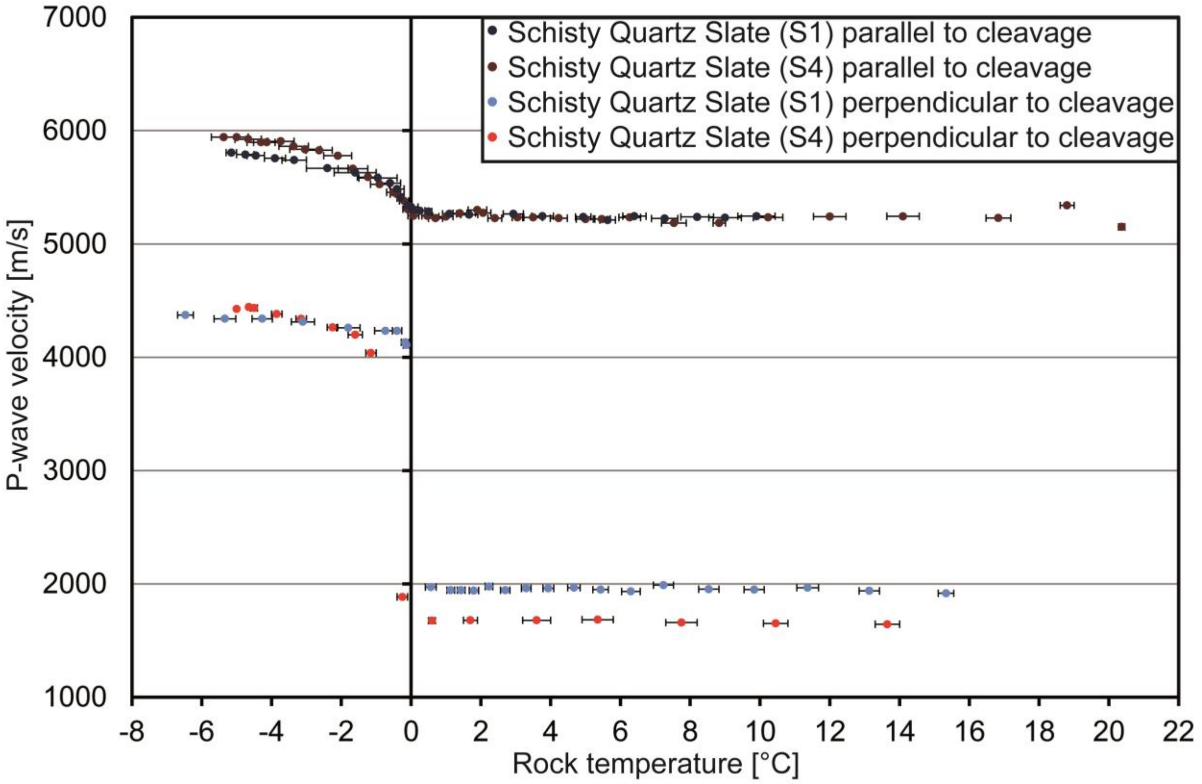

Fig. 8.12 P-wave velocity of frozen and unfrozen Steintaelli paragneiss samples in the direction of the cleavage and perpendicular to the cleavage.

Otherwise, p-wave velocities parallel to the cleavage direction stay constant above (S1: 5228 ±25 m/s and S4: 5239 ±19 m/s) and significantly below freezing point (5774 ±21 m/s (S1) and 5895 ±27 m/s (S4)) at relevant temperatures of –3°C to –5°C. Correspondingly, p-wave velocities perpendicular to the cleavage direction stay constant (S1: 1953 ±15 m/s and S4: 1667 ±14 m/s) above the freezing point and respond with a sudden increase below the freezing point to values of 4331 ±12 m/s (S1) and 4404 ±36 m/s (S4) between –3°C and –5°C. Supercooled conditions were possibly observed between 0°C and –0.25 ±0.15 °C (S4).

8.3.5.2 Raw data

The raw data show mean traveltimes in the range of frozen p-wave velocities perpendicular (≥4.1 km/s) and parallel to cleavage (≥5.3 km/s) in all transects (Fig. 8.8). Thawing or drying of rocks increase traveltimes, freezing and wetting reduce traveltimes. From August to September 2006, Transect 7 shows a remarkable increase of traveltimes while other transects show diverse traveltime changes. From August 2006 to August 2007, traveltimes predominantly decreases in Transects 1 and 3, while the remaining transects show more differentiated patterns.

8.3.5.3 Scenario building

Laboratory results were used to reference field values. In the field, ray paths combine vertical (perpendicular to cleavage) and horizontal (parallel to cleavage) directions (Fig. 8.11). As we pick first arrivals, faster ray paths along the cleavage will outpace slower ray paths perpendicular to cleavage for longer distances. Seismic waves perpendicular to cleavage are only recognized near to the surface. For higher depths, the critical distance is exceeded and first arrivals filter fast parallel p-waves.

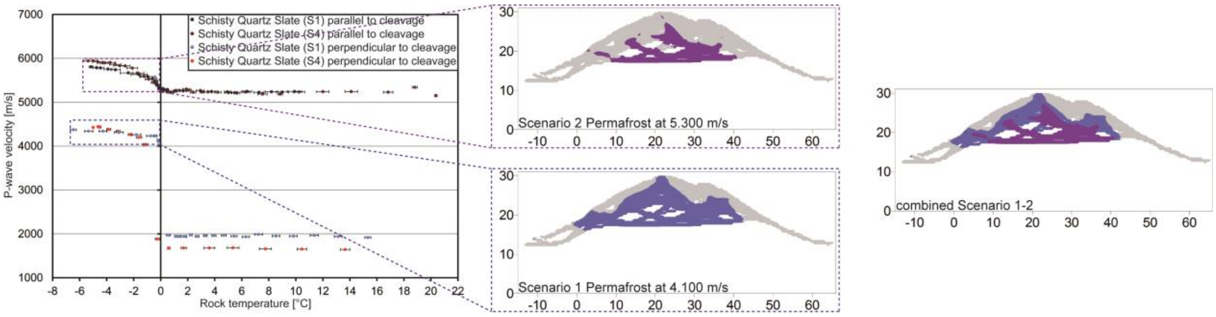

Fig. 8.13 Scenario development demonstrated for the measurement of Transect 1 on Aug 5, 2007 based on laboratory measurements. Scenario 1 (Permafrost at 4.1 km/s; blue area), the maximum permafrost distribution, is based on perpendicular laboratory measurements; scenario 2 (Permafrost at 5.3 km/s; violet area), the minimum permafrost distribution, is based on measurements parallel to cleavage direction (see text).

Thus, the laboratory p-wave velocity of frozen rock perpendicular to cleavage (≥4.1 km/s) represents the maximum permafrost distribution and Scenario 1 is valid close to the surface. Scenario 2 (≥5.3 km/s) based on laboratory measurements parallel to cleavage is the minimum scenario for permafrost distribution and is increasingly valid for greater depths but will overestimate the p-wave velocity of the complete ray path. Therefore, the reality will be best displayed in a combination of scenario 1 and 2. The scenarios are implemented in the tomographies in the terms of dotted lines for scenario 1 (possibly frozen) and continuous lines for scenario 2 (frozen). P-wave velocities in Figures 8.10 and 8.14 are classified according to laboratory results as “unfrozen”, “possibly frozen” and “definitely frozen” with p-wave velocities from 1.5 to 4.1 km/s, 4.1 to 5.3 km/s and 5.3 to 6.0 km/s.

8.3.6 Discussion

8.3.6.1 Laboratory

The laboratory calibration of p-wave velocities of frozen and unfrozen samples appears to be a necessary and helpful tool for both, accurate preprocessing of the tomographic inversion and the interpretation of tomographies. The laboratory values show that (i) low-porosity metamorphic rocks show significant increases in p-wave velocity when freezing and (ii) that velocities parallel and perpendicular to the cleavage tend to differ by a factor of 2 when unfrozen but assimilate when freezing. Thus, seismic refraction is generally capable of detecting permafrost in low-porosity rocks that constitute steep rock walls. P-wave velocities between 1.5 and 4.1 km/s can be defined as definitely unfrozen rock and velocities between 5.3 and 6.0 km/s refer to definitely frozen conditions. However, transitional velocities between 4.2 and 5.2 km/s cannot be assigned to either frozen or unfrozen rock due to the effect of anisotropy. As has been demonstrated in Fig. 8.10, the range of laboratory p-wave velocities in combination with raw data analysis is an important quality check for tomographies and helps to choose appropriate initial velocities. This is increasingly true as rock samples show significant anisotropic behavior and mixing laws do not apply well to low-porosity rocks (Draebing and Krautblatter, 2012). While the p-wave velocity of ice (ca. 3.3 km/s) is an important indicator for the occurrence of frozen ice-rich sediment (Hilbich, 2010), this benchmark is not applicable to frozen bedrock. The anisotropic behavior of rocks also requires the use of two scenarios for minimum (≥4.1 km/s, freezing velocity perpendicular to cleavage) and maximum extend (≥5.3 km/s, frozen velocity parallel to cleavage) of frozen rock in SRT.

8.3.6.2 Field methodology

The field appraisal with small geophone and shot position spacings of 2 m and several offset shot positions appears to deliver appropriate ray coverage for active-layer detection (Vonder Mühll et al., 2001). Short travel distances and high p-wave velocities require highly resolved (here 63 µs) recording of traveltimes. As refracted waves travel along boundaries of material with different elastic properties, layer boundaries can be sharply delineated with high accuracy (Hauck and Vonder Mühll, 2003a). Layer boundaries with high velocity differences result from the large seismic velocity contrast between the active-layer and the permafrost body (Hauck and Vonder Mühll, 2003a) or anisotropies corresponding to macroscopic ice-filled faults and joints (Heincke et al., 2006b). According to the laboratory results, the transition from frozen to unfrozen bedrock is a good target because of the sharp gradient in p-wave velocity and elastic properties. The concentrated travel of seismic rays along the refractor at the transition between unfrozen and frozen rock presumably provides a more accurate detection of depth by SRT in comparison to ERT. In ERT, bulk apparent resistance measurements with half-space geometries covering volumes of several cubic meters at relevant depths will smooth the transition from unfrozen to frozen bedrock. According to the high ray coverage at the transition layer in SRT and the reduced smoothing of an ERT bulk effect, we assume that SRT can provide a more accurate estimate of active-layer depth.

8.3.6.3 Raw data analysis and inversion

We introduced several quality criteria for SRT to address the inverse problem: (i) RMS and absolute time difference should be at a reasonably low level, but the lowest level might not necessarily indicate the best model fit. RMS and absolute time difference approach their minima between 2.5-4 km/s and 3.5-4 km/s, while higher initial p-wave velocities cause increasing errors. Predefined gradients generally caused higher errors. (ii) The coincidence of laboratory p-wave velocity values for paragneiss samples and p-wave velocities derived from traveltime analysis provides a quality criterion for tomographies. Tomographies should roughly cover the entire spectrum of p-wave velocities from 1.7 (S4, perpendicular) to 5.9 (S1, parallel) km/s. In reality, this means that velocities ≥6 km/s are improbable, velocities ≥4.1 km/s must be expected for longer ray paths in frozen rocks, and velocities ≤1.7 km/s are only possible for dry rocks at the surface (Sass, 2005a). Mean traveltimes indicating p-wave velocities ≥5.3 km/s would only occur for a ray movement predominantly parallel to cleavage over most of the travel distance. Thus, we assume that appropriate SRT would simultaneously (i) indicate low RMS and absolute time differences (valid for initial velocities 3.5-4 km/s) and (ii) cover the spectrum of velocities predefined by laboratory and raw data analysis (valid for initial velocities 4-4.5 km/s) and, thus, initial velocities of 4 km/s fulfill both quality criteria.

To avoid misinterpretations of SRT, we blanked out areas that are not determined by seismic waves. Because of subparallel movement of seismic rays resulting from high velocity gradients, ray coverage and ray density provide only partial information about the spatial resolution and some studies used ray density tensors (Heincke et al., 2006b). Here, we used the ray density to define well-covered and non-covered parts of SRT and displayed only the well-constrained parts in final SRT (Fig. 8.14).

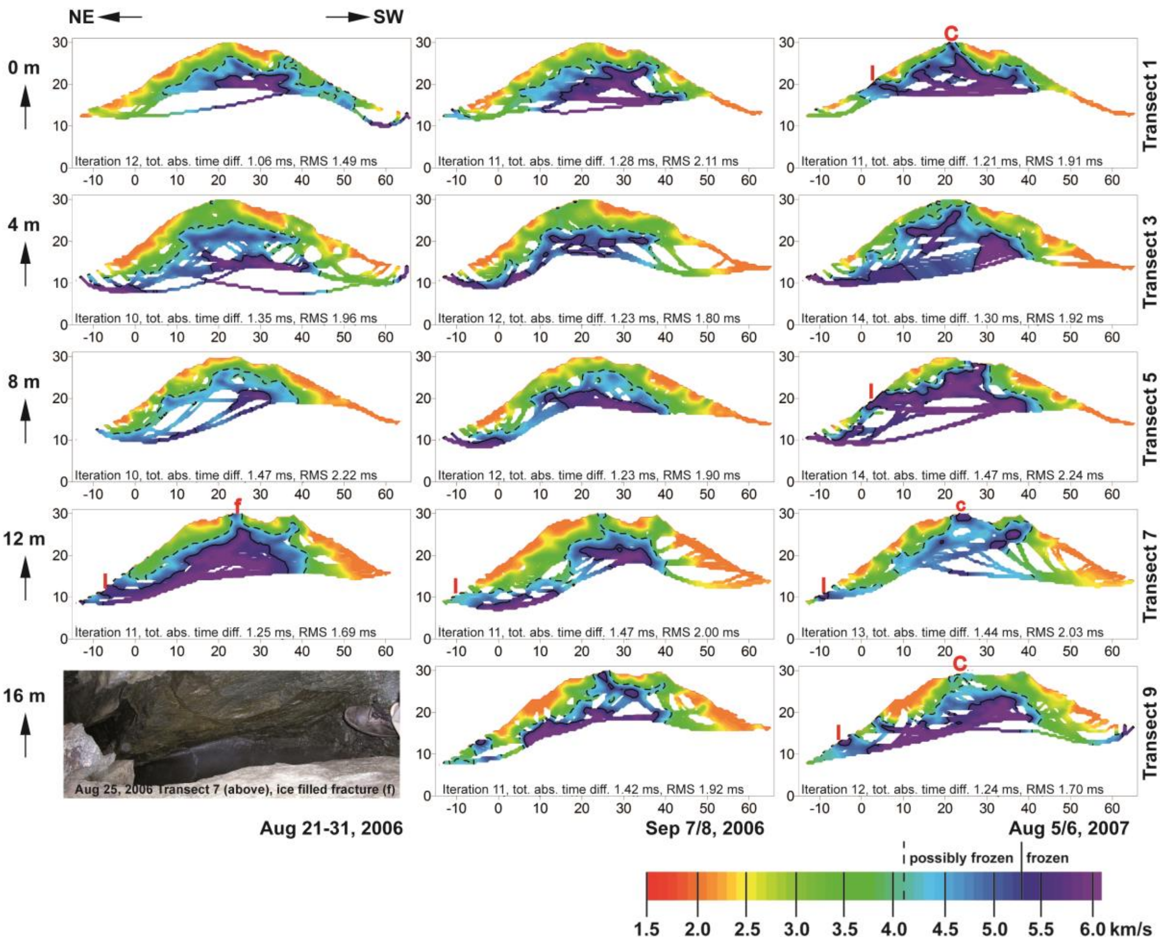

Fig. 8.14 Seismic Refraction Tomographies for Steintaelli study site. Tomographies show effects of onfreezing (I), persistent cornice development (C) and ice-filled fractures (f). Areas with low ray densities are blanked out. For the definition of "possibly frozen" and "definitely frozen" see Figure 8.13.

8.3.6.4 Permafrost interpretation

The late summer distribution of definitely frozen rock at depth (i.e. permafrost) is governed by aspect. Permafrost is omnipresent below the NW-facing slope and along the crestline (0-40 m), mostly present at the NW-foot of the slope (-13 to 0 m) and virtually absent on the SW-facing rock slope (40 to 65 m). Lateral onfreezing (I) of the glacieret and firn/ice remnants below snow patches at the NW-foot (-13 to 0 m), corresponds to definitely frozen rock at the surface and lowest recorded rock temperatures from spring to early summer (Logger E in Fig. 8.5). Surface permafrost is also found below the combination of the virtually persistent snow cornice (C) and decimeter-wide ice-filled fractures (f) (see Fig. 10). Active-layer depth in undisturbed NW-facing rock slopes approaches 4-10 m in September 2006, after a considerable propagation of the thawing front from August to September. Thermal modeling of 2006 data assumes active-layer depth of 3.75 m on the NE-facing slope (based on NW-Logger) and 8 to 9.25 m on the SW-facing slope (based on S-Logger). The modeled active-layer depth underestimates the active-layer depth resulting from lack of anisotropic heat transfer due to discontinuities, advective processes due to percolating melt water (Hasler et al., 2011a) and possible convective processes (Hasler et al., 2011b). There is no up-to-date model taking account of these processes and rock mass properties. Active-layer depth in August 2007 reaches 2-5 m.

Raw data shows remarkable monthly thawing processes on SW facing slopes of Transects 1 and 3 and on the NE-facing slope of Transect 7. Shorter traveltimes on the crestline can be interpreted as impacts of onfreezing and cornice development resulting in snow cover isolation (Keller and Gubler, 1993) preventing thawing in 2007 in Transect 1, 3 and 5. The onfreezing in Transect 7 and 9 and cornice in Transect 9 persists and responds with only small traveltime differences.

Linear features like fractures will affect tomographies in different ways. Air-filled fractures at the surface will significantly reduce the bulk p-wave velocity of the surrounding rock mass according to fracture density, dimensions and orientation of fractures (Sjogren et al., 1979; Barton, 2007). Ice-filled fractures could be either resolved or not resolved according to their size with respect to SRT resolution. They could act as a blind layer or be detected according to their ambient influences on the neighboring rock mass. Assuming that ice-filled fractures only exist in frozen rock, ice in fractures (3.3 km/s) will act as a blind layer. The rock mass surrounding an ice-filled fracture is often cooler than the surrounding due to the high thermal conductivity of ice and its semiconductor performance. In that case, rather the indirect effect on the frozen rock mass is detected. The permafrost distribution at the crestline is obviously heavily influenced by the centimeter to decimeter wide ice-filled fractures.

Only few studies have focused on the snow on alpine permafrost terrain (Keller and Gubler, 1993; Hanson and Hoelzle, 2004; Schmidt, 2010). Steep rock walls (>45°) in high alpine terrain tend to have a much thinner and more heterogeneously distributed snow cover than is found in flatter terrain (Seligman, 1980; Lapen and Martz, 1996; Wirz et al., 2011). Spatial and temporal distribution of snow in structured rock faces are increasingly controlled by wind, local topography and radiation patters

(Winstral et al., 2002). The SRTs display surficial frozen bedrock in late summer under snow cornices along the crestline and under persistent snow patches in the north face. Snow cover is among the most important influences on permafrost distribution in alpine rock walls that can yet not be sufficiently modeled (Gruber and Haeberli, 2007; Krautblatter et al., 2012). The SRT technique developed in this paper could, thus, significantly contribute to the understanding of snow, ice and water influence on local permafrost evolution and the resulting impacts on stability.

8.3.7 Conclusion

- Refraction seismic in steep permafrost rock walls is a non-trivial task due to high topography, anisotropic seismic behavior of rocks, an unknown range of subsurface velocities and a curved ray penetration that is difficult to judge.
- We have installed a 2.5D p-wave refraction seismic array across the instable Steintaelli crestline, Matter Valley, Switzerland, at 3070-3150 m a.s.l.. It comprises 78*16 m, consists of 200 shot positions arranged around 120 geophone positions and was measured repeatedly in 2006 and 2007.
- Laboratory measurements of p-wave velocity of decimeter large cuboid water-saturated paragneiss samples was performed at temperature from 20° to -5°C at small increments in a laboratory cooling device.
- These show that parallel to cleavage velocity increases from 5228 ±25 m/s (sample S1) and 5239 ±19 m/s (S4) to values of 5774 ±21 m/s (S1) and 5895 ±27 m/s (S4) upon freezing. Perpendicular to the cleavage, p-wave velocity increases from 1953 ±15 m/s (S1) and 1667 ±14 m/s (S4) to values of 4331 ±12 m/s (S1) and 4404 ±36 m/s (S4), respectively.
- We argue that (i) a priori information on p-wave velocity behavior from laboratory testing, (ii) traveltime raw data analysis, (iii) initial model evaluation with different initial velocities and gradients are needed to create reliable SR tomographies in steep fractured bedrock.
- Glacier onfreezing, the position of snow accumulations and deep-reaching ice-filled fractures seem to have a systemic and locally dominant impact on spatial and temporal permafrost development.

- Glacier onfreezing can cause permafrost up to the surface without active-layer below the ice; deep ice-filled fractures and persistent snow patches can generate extended permafrost in positions that would otherwise have no permafrost – these features correspond with the highest measured rock displacement activity.
- Here we show for the first time, that calibrated seismic refraction tomography provides a geometrically highly-resolved subsurface detection of active-layer and permafrost dynamics in steep permafrost rock walls at the scale of instability.

Acknowledgments

This study was supported by the DFG-Research Training Group "Landform (GRK 437)", by the DFG research project "Sensitivity of rock permafrost to regional climate change scenarios and implications for rock wall instability" and the DACH (DFG/SNF) project "ISPR Influences of snow cover on thermal and mechanical processes in steep permafrost rock walls." The authors acknowledge G. Nover and J. Ritter for infrastructural support and S. Verleysdonk, D. Funk, P. Oberender, S. Wolf for the field work.

8.4 Thermal Regime of the Steintaelli in 2012 and 2013

Potential methods to monitor the thermal regime were introduced in Chapter 8.1. The basis of the applicability of seismic refraction was demonstrated in the laboratory (Chapter 8.2) and in the field (Chapter 8.3). In the following chapter, the results from thermal modelling, electric resistivity tomography (ERT) and seismic refraction tomography (SRT) are used to describe the thermal regime of the Steintaelli in 2012 and 2013.

8.4.1 Climatic situation

The mean monthly air temperatures of Steintaelli between 2002 and 2013 are presented in Fig. 8.20. The data is derived from a meteo station in the Hungerli Valley at 2.770 m a.s.l. at a horizontal distance of approximately 500 m to the Steintaelli. Data is adapted to the Steintaelli using a thermal gradient of 0.6°C/100 m for 330 m altitudinal difference. The months August and September 2006, August 2007, August 2012 and August 2013, in which geophysical measurement were conducted, are emphasized in Fig. 8.20.

The heat summer of 2003 is highlighted by three warm summer months with mean monthly air temperatures between 5.1 and 7.4°C, thus all mean values are higher than the average air temperature in July (4.1°C). The occurrence of such an extreme event is statistically unlikely (Schär et al., 2004) and resulted in an increased activity of landslide events from permafrost-affected rock walls due to increased active-layer thaw depth (Gruber et al., 2004a). Warm conditions in 2006 and 2007 are described in more detail in chapter 8.3.3. In 2012, the meteo station measured no data in the first half of the year. July 2012 (4.0°C) was as warm as July averages between 2002 and 2013, however, August 2012 was the second warmest measured August (6.4°C) and only 1°C colder than August 2003 (7.4°C). The warm summer of 2012 is followed by the coldest winter 2012/2013 in the measurement period between 2002 and 2013 (Fig. 8.20). July 2013 was 1.9°C warmer (6°C) than July 2012 or July averages (4.1°C); August 2013 was 1.3°C colder (5.1°C) than August 2012. As response to the warm summer active-layer thaw should reflect the warm conditions.

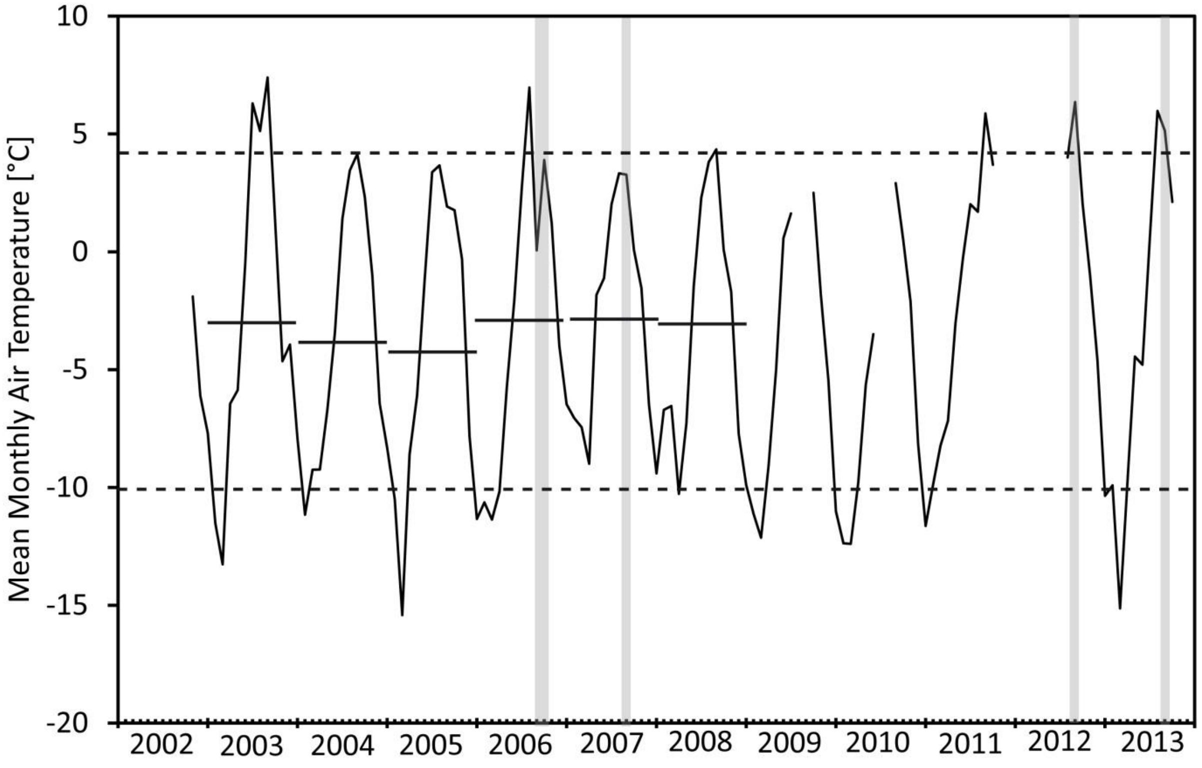

Fig. 8.20 Mean monthly air temperatures at Steintaelli between 2002 and 2013. Grey bars indicate the months August and September 2006, August 2007, August 2012 and August 2013, in which geophysical measurements were conducted. The upper dotted line represents the mean monthly air temperature of July, while the lower dotted line indicates the mean air temperature of January. Mean annual air temperature are calculated for years with complete temperature record (2003-2008) and are presented as black lines.

8.4.2 Methods

8.4.2.1 Thermal modelling

To estimate the seasonal variations of rock temperature between August 2012 and 2013, a simple 1D process-based approach of thermal conductivity is used. Temperature, thermal conductivity and ground thermal heat flow act over a long time and control the position of the permafrost base, in contrast seasonal fluctuations about the mean annual value and the warmest temperature of the year control the position of the top of the permafrost and the depth of the active-layer (Williams and Smith, 1989). Solar radiation and air temperature fluctuate seasonally and generate a temperature wave into the underground. The temperatures at depth fluctuate with the same frequency but with lower amplitude and lag in phase (Williams and Smith, 1989). The attenuation of temperature and the phase lag can be incorporated and rock temperatures in depth can be expressed according to Eq. 8.19:

$$T(z,t) = MAGST + Tae^{-z\sqrt{\frac{\omega}{2\kappa}}} \sin\left(\omega t - z\sqrt{\frac{\omega}{2\kappa}}\right), \tag{8.20}$$

where T is temperature [°C], t is time, z is depth of rock, MAGST is mean annual rock temperature, Ta is the half amplitude of the sinusoidal variation, ω is the frequency of sinusoid (in our case one year) and κ is the thermal diffusivity (Carslaw and Jaeger, 1986; Williams and Smith, 1989). MAGST (MART was equivalently used in Chapter 8.3.4.6) and T_a are calculated from the temperature logger data for the period between September 2012 and August 2013 (Table 8.5). Long snow cover decreased the half amplitude T_a. Only temperature data is used, if the logger records during the measurement period were complete. To calculate the volumetric heat capacity of 2.08×10^6 J m^{-3} K^{-1} and the thermal diffusivity of 1.2×10^{-6} m^2 s^{-1}, a thermal conductivity of 2.5 W m^{-1} K^{-1}, a specific heat capacity of 0.8 kJ kg^{-1} K^{-1} and a density of 2600 kg m^{-3} for slaty paragneiss was used.

Table 8.5 MAGST and T_a of the rock temperature loggers.

Logger	MAGST [°C]	T_a [°C]
N6	-2.5	2.7
N5	-2.9	4.1
N4	-3.5	6.9
N3	-3.7	8.3
N2	-2.2	11.3
N1	-1.7	6.9
C1	-1.6	10.1
C2	0.0	10.2
C3	1.2	11.4
C4	0.8	9.1
S3	0.5	9.6
S4	1.3	10.3
S5	1.4	4.9

8.4.2.1 Data acquisition and processing of geoelectrical data

To monitor inter-annual and intra-annual changes of frozen underground, we conducted geoelectrical measurements along five parallel transects in the Steintaelli on August 8th and 18th 2012 as well as on July 31st and August 2nd 2013, respectively. In 2013, at Transect 9 no geophysical measurements were conducted due to immense snow cover. The geophysical transects were installed by M. Krautblatter in the framework of his dissertation. For location of transects see Fig. 7.2. Location of the electrodes were measured with a tachymeter by Krautblatter (2009) to incorporate the complex topography into the inversion, which is in important factor in mountain terrain (Hauck and Kneisel, 2008b). For data acquisition a Wenner array with up to 190 measurements is used which yields lowest signal to noise ratio (Krautblatter, 2009). Penetration depth (*d*) depends on measurement topography and the distance between the outermost current electrodes (*L*). Using the formula by Barker (1989):

$$d = 0.17\,L; \qquad (8.21)$$

the penetration depth is approximately 13.25 m. The same set-up was successfully used by Krautblatter (2009). Finite-element ERT-Grids adjusted to individual topography for each transect were constructed by Adrian Flores-Orozco (Fig. 8.21). Unfortunately, mesh size of a grid element was chosen to large resulting in an error of 0.25 m for each 2 m and an overestimation of the horizontal distance of 10 m.

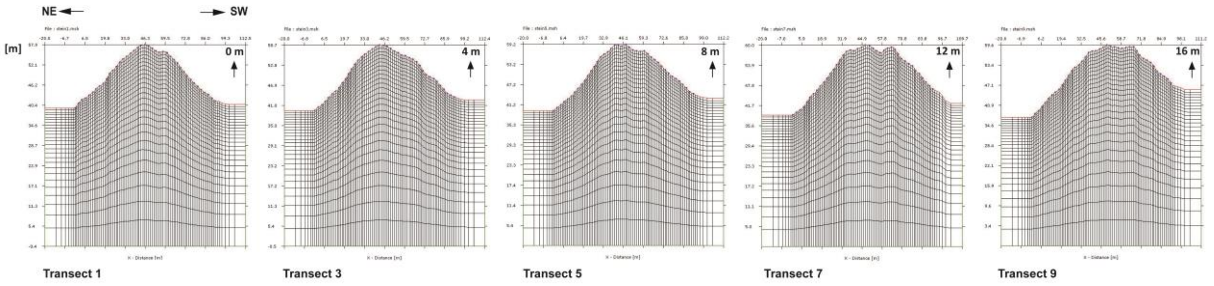

Fig. 8.21 Finite-element ERT-grids for the five transects in the Steintaelli (A. Flores-Orozco).

Overestimation of transect length resulted in slightly smoothing of topography by 0.25 m but should not significantly affect tomography results. ERT is processed using 2D smoothness-constrained inversion algorithm CRTomo developed by Kemna (2000). CRTomo was successfully used for ERT inversion of data from Steintaelli (Krautblatter, 2009) and Zugspitze (Krautblatter et al., 2010). Operation mode of the CRTomo algorithm in permafrost terrain is well described by Krautblatter et al. (2010). In CRTomo, model roughness is minimized by fitting of data to a predefined degree to avoid overfitting of data. Errors in the ERT data can be distinguished into systematic and random errors. Malfunction of the used measurement equipment, bad galvanic contact of electrodes and misplaced or misconnected electrodes can cause systematic errors. Systematic errors should be corrected or rejected before the inversion. Stochastic fluctuations in the contact between the electrodes with the ground, in the current injected and pathway changes of the current cause random errors (Slater et al., 2000). Random errors are uncorrelated and are assumed to be normal distributed. Normal and reciprocal measurements are used to characterize random errors (Binley et al., 1995; LaBrecque et al., 1996; Slater et al., 2000; Koestel et al., 2008), Krautblatter (2009) used the model by Slater (2000) and the procedure by Koestel et al. (2008) to describe data errors at Steintaelli in measurements in 2008. Error contribution is expressed in an absolute resistance term *a* and a relative resistance term *b* (Table 8.6). Table 8.7 presents the number of iterations of the inversion until the predefined degree (term *b* in Table 8.6) is reached.

Table 8.6 Error model parameters for the different 2.5D ERT measurements in the Steintaelli calculated by Krautblatter (2009).

Parameter	Transect 1	Transect 3	Transect 5	Transect 7	Transect 9
a [Ω]	23.19	47.5	32.33	35.01	66.82
b [%]	8.42	8.33	9.13	9.29	9.34

Table 8.7 Number of iterations until predefined degree is reached.

Date	Transect 1	Transect 3	Transect 5	Transect 7	Transect 9
Aug 8th 2012	4	3	3	5	4
Aug 18th 2012	4	4	3	4	3
Jul 31st/Aug 2nd 2013	4	2	9	9	-

An overestimation of the error lead to a smooth and low-resolution image due to underfitting of data while underestimation of error results in overfitting and artefact generation (Krautblatter et al., 2010). Random errors range between 23.19 to 66.82 Ω in absolute terms and between 8 to 9 % in a reasonable value according to errors obtained in permafrost terrain at Zugspitze by Krautblatter et al. (2010). The results of CRTomo inversion are imported into SURFER 8.05, interpolated using Nearest Neighbour Algorithm and graphically represented (Fig. 8.24).

Krautblatter (2009) measured electric resistivity during freezing in the laboratory using two rock samples from Steintaelli (Fig. 8.22). For detailed description of measurement set up and petrophysical characterization of rock samples see Krautblatter (2009).

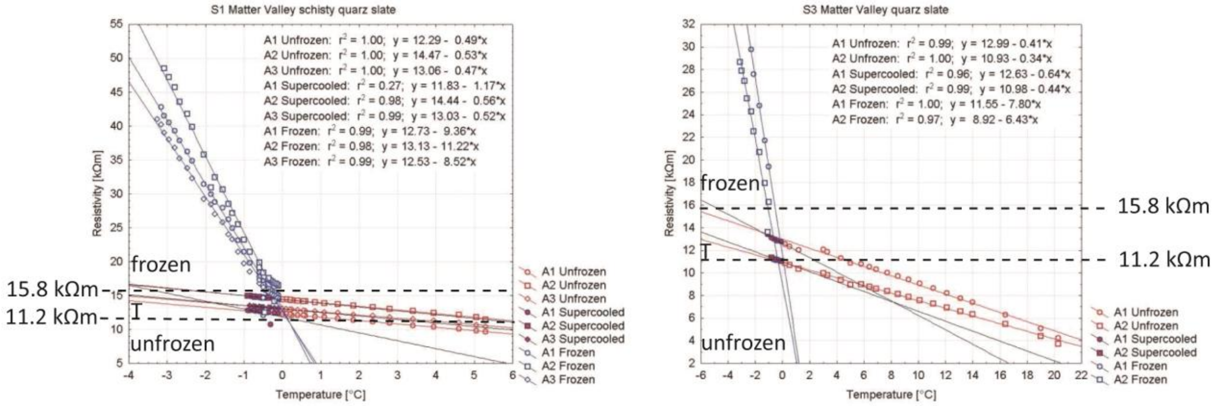

Fig. 8.22 Temperature-resistivity paths of two rock samples with linear approximation of two and three arrays, respectively (Krautblatter, 2009). Boundaries are adapted by the author with T is transition zone.

Krautblatter (2009) shows that resistivity values below 11.2 kΩm ($10^{4.05}$ Ωm) indicate unfrozen rock conditions, values between 11.2 kΩm ($10^{4.05}$ Ωm) and 15.8 kΩm ($10^{4.2}$ Ωm) indicate freezing transition (T) and above 15.8 kΩm ($10^{4.2}$ Ωm) indicate frozen rock conditions.

8.4.2.2 Data acquisition and processing refraction seismic data

Refraction seismic measurements were conducted along the transects described in Chapter 8.3.4.2 on August 15th and 17th 2012 and August 1st and 3rd 2013. Data was processed using the developed method by Krautblatter & Draebing (2014). Additionally p-wave velocity changes between the two measurements are calculated and presented in Fig. 8.25.

8.4.2 Results

8.4.2.1 Thermal modelling

Modelling results are shown in Fig. 8.23. North-facing loggers on the NE-Slope and the crestline showed permafrost and active-layer thaw depth ranged between 0 m (N6) and 6.5 m (C1). South-facing loggers showed no permanent frozen underground. Underground froze from October 2012 on down to depths from 4 m (S5) to 12.5 m (C2).

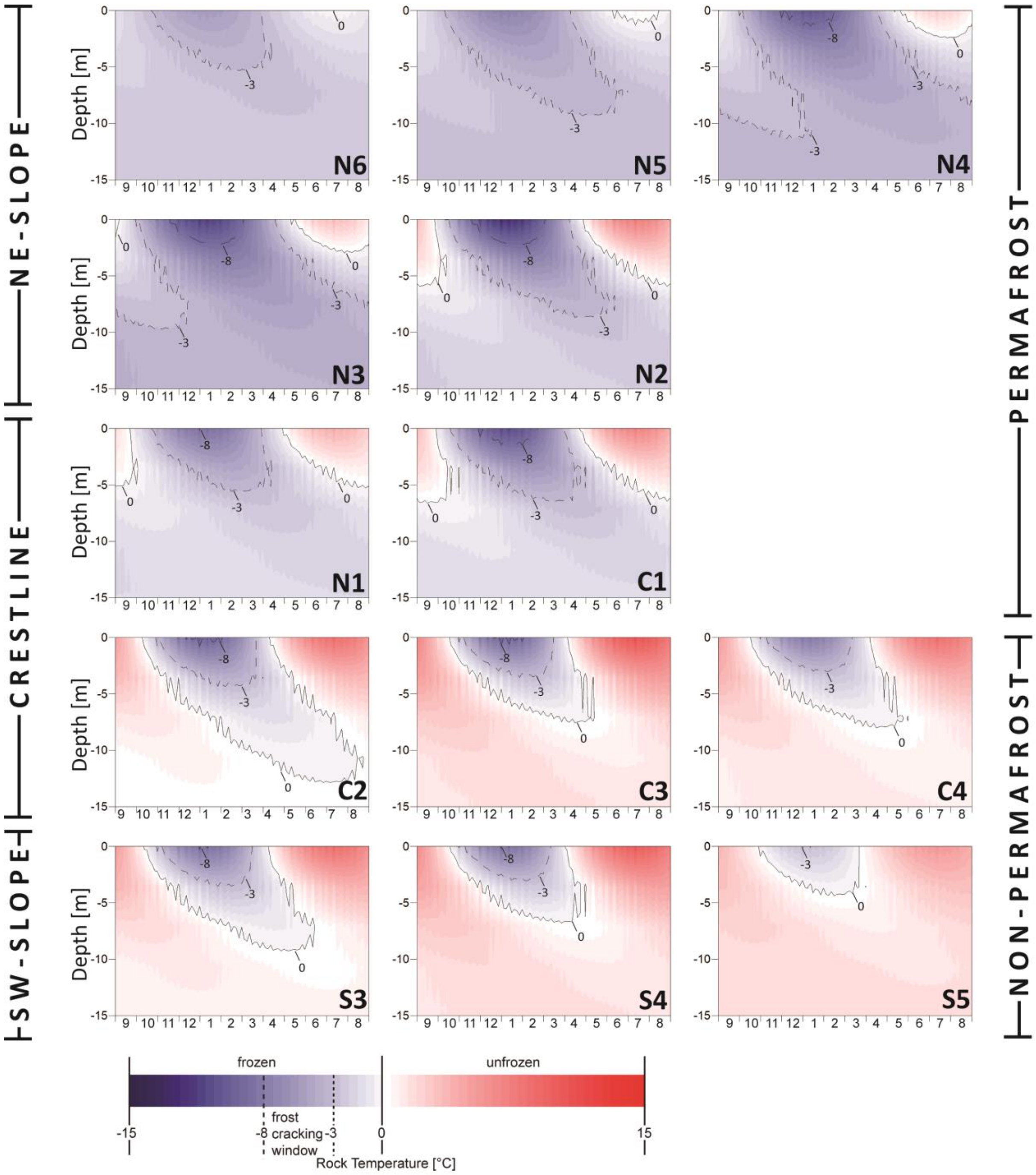

Fig. 8.23 Rock temperatures between 0 and 15 m depth of the rock wall for the period September 2012 until August 2013; for logger positions see Fig. 7.2.

8.4.2.2 Results of Electrical Resistivity Tomography (ERT)

Table 8.8 presents the extent of NE-slope, crestline and SW-slope of each transect in the geophysical tomographies. Due to smoothing by ReflexW, the extent of slopes and crestline differs slightly between ERT and SRT.

Table 8.8 Extent of NE-slope, crestline and SW-slope of each transects in SRT and ERT tomographies.

Transect	NE-slope		crestline		SW-slope	
	SRT	ERT	SRT	ERT	SRT	ERT
T1	-14 to 20 m	0 to 40 m	20 to 35 m	40 to 57 m	35 to 66 m	57 to 90 m
T3	-14 to 18 m	0 to 38 m	18 to 35 m	38 to 57 m	35 to 66 m	57 to 90 m
T5	-14 to 18 m	0 to 38 m	18 to 35 m	38 to 57 m	35 to 66 m	57 to 90 m
T7	-14 to 20 m	0 to 40 m	20 to 40 m	40 to 69 m	40 to 66 m	69 to 90 m
T9	-14 to 15 m	0 to 35 m	15 to 40 m	40 to 69 m	40 to 66 m	69 to 90 m

Results of the electric resistivity tomographies (Fig. 8.24) are presented from left (NE-slope) to the middle (crestline) to the right side (SW-slope). On August 8th 2012, ERT-Transects showed resistivities larger than $10^{4.2}$ Ωm, indicating frozen conditions according to laboratory measurements by Krautblatter (2009), from the surface downwards at the lower part of the NE-slope (0-15 m; T1-T5), at the lower and middle part of the NE-slope (0-25 m; T7) or on the whole NE-slope (0-35 m; T9), respectively. Areas with resistivities below $10^{4.05}$ and $10^{4.2}$ Ωm indicating unfrozen and transient conditions, respectively, were located at the middle and upper part of NE-slope of Transects 1 to 5 down to depth of 5 m. Below 5 m depth, tomographies showed resistivities in the range of frozen conditions. In Transect 7, cells of resistivities in the range of unfrozen conditions existed at the upper part of NE-slope (25-40 m) down to 2 m depth, cells of resistivities in the range of transient conditions existed down to depths of 3 m. Below 3 m and isolated at the surface, Transect 7 showed resistivities in the range of frozen conditions in this area. In Transect 9 was an isolated lens from top to 10 m depth visible at 34 m with resistivities in the range of transient conditions at depth and in the range of unfrozen conditions close to the surface. The crestline of all transects showed high resistivities (frozen rock) with isolated lenses of low resistivities (unfrozen rock) close to the surface. On the SW-slope, areas of high resistivities (frozen rock) were located in the upper part, while lower parts showed low resistivities (unfrozen rock) down to depths of maximum penetration depth. On August 18th 2012, the observed pattern from 10 days before was preserved and slightly changes occurred locally and reduced isolated cells from very high (>$10^{5.0}$ Ωm) to high resistivities (>$10^{4.2}$ Ωm).

On July 31st and August 2nd 2013, respectively, the lower parts of the NE-slope showed areas of high resistivity (frozen rock) in all transects and in Transect 3 and 7 additionally patches of very high resistivities indicating ice-intercalations. In the upper parts of the NE-slope of Transect 1 to 5, low resistivities in the range of unfrozen underground were located down to 3 or 5 m depth. An extensive 10 m depth lens of resistivities in the range of unfrozen rock was visible at 30 m transect length in Transect 5. Transect 7 showed resistivities in the range of frozen rock at the upper part of the NE-slope with isolated unfrozen rock cells at the surface and in 5 m depth. The crestline of all transects showed resistivities in the range of frozen rock from surface to bottom. Only on the edges of the crestline of Transect 1 and 3 small cells of low resistivities in the range of unfrozen rock and the transition zone were located. In Transect 1 and 3, the SW-slope showed high resistivities in the upper part, while the lower parts showed resistivities in the range of transition and unfrozen underground. Transect 5 showed high resistivities with a small cell of resistivities in the range of the transition zone in the upper part and resistivities in the range of frozen rock in the lower part. In Transect 7, in the whole SW-slope resistivities in the range of frozen rock were visible.

8.4.3.3 Results of Seismic Refraction Tomography (SRT)

Results of the seismic refraction tomographies (Fig. 8.25) are presented from left (NE-slope) to the middle (crestline) to the right side (SW-slope). On August 15th/17th 2012, the NE-slope of all transects showed low p-wave velocities (< 4.1 km/s) in the range of unfrozen rock to depth of 7 to 10 m. Small cells of high p-wave velocities (> 5.3 km/s) in the range of frozen rock were visible at the toe of the NE-slope. Transect 9 showed high p-wave velocities in 7 m depth.

Below the crestline, from the surface down to depths of 5-10 m were patches of low p-wave velocity located. Below this layer of low p-wave velocities, p-wave velocities in the range of possible frozen rock (4.1 to 5.3 km/s) were visible in Transect 3 to 9 or in the range of frozen rock in Transect 1, respectively. On the SW-slope, rock subsurface showed low p-wave velocities down to 10 m depth. In the upper part of Transects 1 to 5 in 3-5 m depth are sporadic cells of p-wave velocities in the range of possibly frozen or frozen rock, respectively.

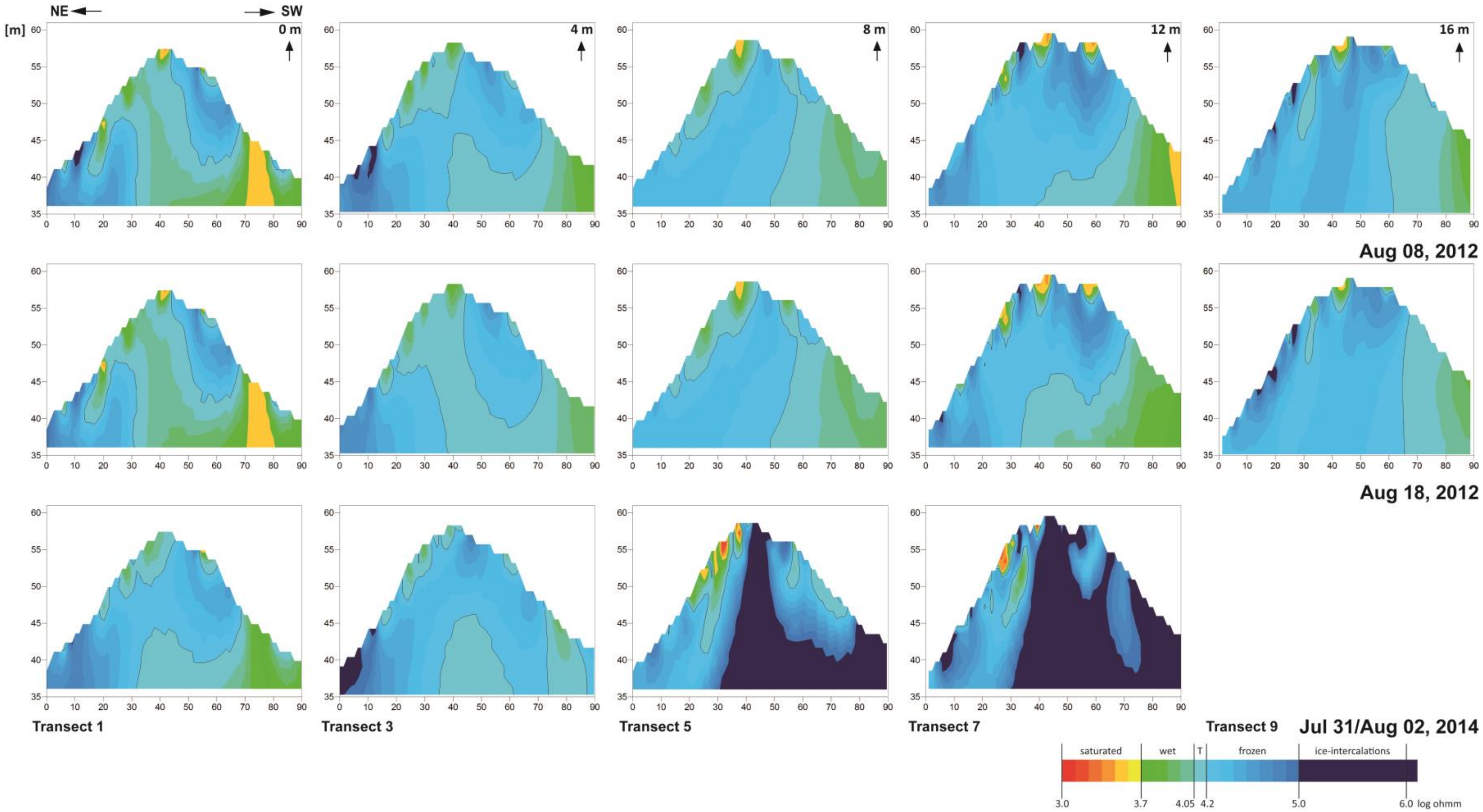

Fig. 8.24 ERT Tomographies of five transect in the Steintaelli in August 8th 2012 (top row), August 18th 2012 (middle row) and July 31th or August 2nd 2013 (bottom row), respectively. T indicates the transition zone between unfrozen and frozen underground.

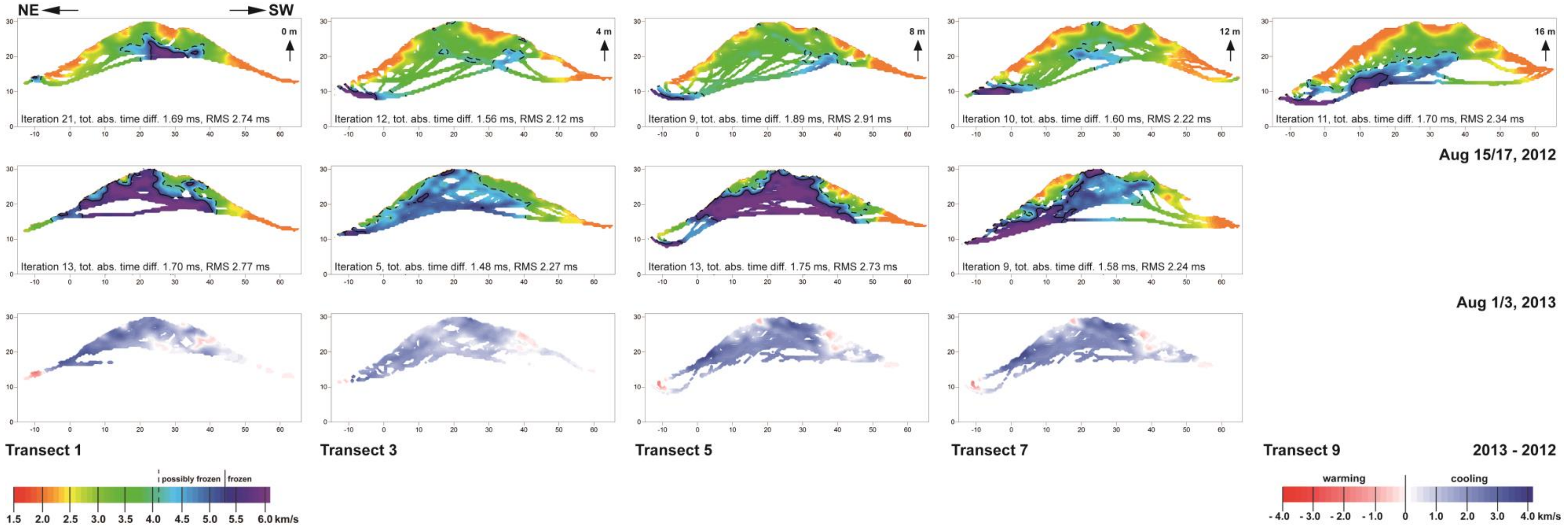

Fig. 8.25 Seismic Refraction Tomographies for Steintaelli in August 2012 (top row) and August 2013 (middle row). Difference tomography between 2012 and 2013 shows warming or cooling areas (bottom row).

On August 1st and 3rd 2013, the NE-slope showed areas in the range of possibly frozen and frozen rock from the surface downwards. Small cells in the p-wave velocity range of unfrozen rock were located at the toe or lower part of the slope in Transect 1 and 5 as well as at the upper part from the surface down to 3-5 m depth in Transect 3 to 7. On the crestline, subsurface areas were in the p-wave velocity range of possibly frozen rock in Transect 3 and in the p-wave velocity range of frozen rock in the other transects. However, the south-exposed parts of the crestline showed p-wave velocities in the range of unfrozen rock down to 3-5 m depth. On the SW-slope, areas in the p-wave velocity range of unfrozen rock were located from the surface to 5-10 m depth.

The time-lapse tomography showed an overall p-wave velocity increase of all transects in August 2013 compared to August 2012. Only isolated cells at the toe of all transects, at the north-exposed face of the crestline in Transect 5 and 7 and the middle part of the SW-slope of all transects showed a slight p-wave velocity decrease.

8.4.3 Discussion

8.4.3.1 Thermal modelling

Thermal modelling can give valuable information about variations of thermal regime on a seasonal scale (Williams and Smith, 1989). The model excludes latent heat processes and non-conductive heat transfer. Latent heat processes prolong the response time of active-layer thaw, due to higher amount of energy needed for melting, and response time of freezing due to latent heat release. Excluding latent heat leads to an overestimation of the active-layer thaw depth and the freezing penetration depth. Non-conductive heat transfer can amplify warming processes in discontinuities (Hasler et al., 2011a) and results in an earlier development of a thick active-layer (Gruber and Haeberli, 2007). The model underestimates active-layer depth by excluding non-conductive processes. The model assumes a 1D-solution of conductive heat transfer in an infinite expanded medium (Wegmann, 1998). Geometry of the Steintaelli is more complicated, thus, to include topography, topographic-induced heat transfer (Noetzli et al., 2007) and latent heat transport by using Neumann's resolution of the Stefan-problem (Wegmann, 1998) would give more realistic model results. However, despite model limitations model results can be used analytically to enhance process understanding and understand topographic or snow effects. More realistic models require input data e.g. high-resolution terrain model and especially a discontinuity model which is not available. Non-conductive heat transfer models including the influences of discontinuities are non-existent for high-alpine rock walls.

Due to topography and aspect, permafrost is abundant in north-facing slopes (Gruber et al., 2004b) while south-facing slopes are warmer resulting from increased insolation (Noetzli et al., 2007). The rock temperature models indicated permafrost occurrence on the NE-slope and north-facing areas of the crestline while the SW-slope and south-facing areas of the crestline showed only seasonal freezing. Active-layer thaw reached depth up to 6.5 m. Snow cover reduced the annual temperature amplitude and decreased modelled active-layer thaw depths. Due to use temperature data beginning in September 2012 and the seasonal response time of thawing, modelled results are only comparable to SRT and ERT results in August 2013. The model showed active-layer depth increasing from zero thawing at Logger N6 to 6m thawing at Logger N2. SRT results can confirm modelled active-layer depths (Transect 5 in Fig. 8.25), however, the ERT results (Transect 5 in Fig. 8.24) indicated 2-3 m lower active-layer depths. The modelled active-layer depth of Loggers N1 and C1 on the crestline reached 5 to 7.5 m depths, respectively. ERT and SRT results confirm the active-layer depth at Logger N1, unfortunately at position of Logger C1 ERT and SRT deliver contrasting result. The ERT showed an active-layer depth of 5 m, 2.5 m lower than modelled active-layer depth, while SRT showed no active-layer thawing. The Loggers C3, C4, S3 to S5 showed only seasonal freezing and positive rock temperature down to 15 m depths, however, the SRT showed possible frozen or frozen areas in 10 m depth in August 2013. These areas were unfrozen in August 2012 according to SRT results. These deep-laying frozen areas might be affected by neighbouring frozen areas, 2D-effects, which cannot be included in the 1D-model. Despite limitations of the model, the results fit really well. Model results are incorporated in the frost cracking model by Hales and Roering (2007) presented in Chapter 9.4.

8.4.3.2 Geophysical Methods

Bad electrode contacts can significantly influence the inversion results and are characterized by highly fluctuations of high- and low-anomalous apparent resistivities (Hauck and Kneisel, 2008b), thus, tomographies should reflect fluctuations of high- and low-anomalous resistivities. However, resistivity pattern between the two measurements in August 2012 is consistent suggesting no disturbance of bad electrode contacts in the data. To avoid systematic error of bad electrode contacts, electrodes with bad contact were removed before the measurement by the geoelectrical system (ABEM Terrameter LS or AEBM SAS 1000). Resistivity contrast between air and ice is low because the ERT depends on unfrozen water content (Hauck and Kneisel, 2008b). Due to lower insolation, north-facing slopes contain more moisture near the surface than south-facing slopes (Sass, 2005a), thus, south-facing rocks dry-out easier and problems distinguishing between resistivities of air and ice occur more frequently on south-facing slopes. Unusual areas with high resistivity reflect this problem especially in August 2012 (Fig. 8.24). To avoid this problem, Hauck and Kneisel (2008b) advice to use complementary refraction seismic because contrast between ice (3500 m/s) and air (300 m/s) is large. In low-porosity bedrock of Steintaelli laboratory measurements show a high contrast between frozen rock (4.1 km/s perpendicular to cleavage or 5.3 km/s parallel to cleavage) and unfrozen air-filled rock (1.064 to 1.578 km/s perpendicular to cleavage or 4.819 to 4.914 km/s parallel to cleavage) (Draebing and Krautblatter, 2012; Krautblatter and Draebing, 2014). Areas with p-wave velocities in the range of very dry rocks (< 2.0 km/s) showed resistivities in the range of ice-intercalations (>5.0 log ohm) while areas with p-wave velocities in the range of dry rocks (2.0 -2.5 km/s) showed resistivities in the frozen range (4.2 – 5.0 log ohm). These areas were unfrozen and occurred on north-facing and south-facing rock walls in 2012 (Fig. 8.24) but with a deeper extent on south-facing slopes. Sectors with resistivities in the range of unfrozen rock possessed p-wave-velocities confirming the unfrozen state. In 2013, the rock wall was wetter and areas with resistivities indicating frozen rock correspond to areas possessing p-wave velocities indicting also frozen rock. The only exceptions could be observed on the south-facing slope, where the absence of moisture resulted in high resistivities indicating frozen rock which went along with low p-wave velocities indicating unfrozen rock.

Seismic waves travel along boundaries of material with different elastic properties (e.g. unfrozen and frozen rock), thus, refraction seismics can outline boundaries (e.g. active-layer or discontinuities) more accurate. The used resolution of 0.25 m seems to overestimate discontinuity size in the tomography. To estimate a delineation threshold of discontinuities in tomographies would be eligible. Refraction seismics cannot resolve layers with low elastic properties (hidden layers) below layers of high elastic properties e.g. taliks below permafrost. ERT provides an independent method to evaluate SRT. If the rock wall does not contain sufficient moisture, resistivities indicate misleadingly frozen conditions, while SRT shows unfrozen conditions. Due to this limitation of ERT, if contrary results indicate dry rock wall situation, results from calibrated SRT should be preferred. In all other cases the ERT and SRT deliver corresponding results and represent a tool to identify permafrost or frozen ground occurrence.

8.4.3.3 Combined ERT and SRT interpretation and discussion

Permafrost distribution is affected by climate, topography and ground material (Gruber, 2005). Climatic factors like air temperature, precipitation and radiation are affected by global atmospheric circulation and regional orographic conditions (Gruber, 2005). Air temperature was similar between 2012 and 2013 (Chapter 8.4.1) while snow conditions differed significantly. Topography modifies short-wave solar irradiation, heat transport, sky-view factor, snow distribution by avalanche and wind, etc. (Gruber, 2005). For instance, south-facing slopes were warmer than north-facing slopes, thus, south-facing slopes show no permafrost or frozen ground occurrence in the Steintaelli (Fig. 8.24 and 8.25).

At slope scale, complex heat transfer in the snow cover and the bedrock determines temperature and active-layer thaw (Gruber, 2005). Snow height distribution at the times of geophysical measurements are described in Chapter 7.3.4 and visualized in Fig. 7.8. Thresholds for isolating snow height were determined at Murtèl rock glacier and were between 0.6 m (Hanson and Hoelzle, 2004) and 0.8 m (Keller and Gubler, 1993). The snow height of the snow cornices in 2012 and 2013 as well of the snow patch in 2013 exceeded the snow height thresholds for isolation obtained at Murtèl rock glacier. In 2012, active-layer depths was slightly reduced below the snow cornice (8-10 m) according to SRT (Fig. 8.25), while snow-free areas showed active-layer depths down to 15 m. Snow prevented active-layer thawing in 2013 in the areas below the snow patch on the NE-slope and below the cornice on the crestline (Fig. 8.24 and 8.25). Time-Lapse SRT reflected the overall cooling effect of the snow cover (Fig. 8.25). Active-layer thawed between 5 and 10 m in snow-free areas. Snow remains longer in areas of high snow accumulation (Grünewald et al., 2010), thus, areas of high snow accumulation are conserved and are reflected by the patterns of snow cover in August 2013. The length of snow cover influences the thickness and intensity of active-layer thaw (Luetschg et al., 2008). Snow stage II lasted long in 2013 and prevented active-layer thaw (Chapter 7), thus, near-surface frozen underground existed below snow-covered areas. Snow melting depends on aspect and slope angle (Chapter 7), thus, high-inclined south-facing rock walls melted earlier than low-inclined south facing rock walls and south-facing rock walls melted earlier than north-facing rock walls due to higher insolation, respectively, resulting in deeper active-layer thaw. Snow cover influences underground temperatures and, thus, frozen state, and underground temperatures determine snow cover length (Phillips, 2000). The data demonstrated interaction between snow cover and frozen ground in 2013. However, on the SW-slope a small snow patch without underlying permafrost or frozen ground existed. Despite the interaction of frozen ground and snow cover, there are influences of solar radiation, topography by shading which also influences snow distribution. Snow preserves permafrost and plays a key control on evolution of permafrost and frozen ground.

Blocky surface modifies heat transfer on the ground scale (Gruber, 2005) due to Balch effect, chimney effect, summer evaporation/sublimation of water/ice or continuous air exchange with the atmosphere (Harris and Pedersen, 1998; Juliussen and Humlum, 2008). Blocks accumulated as a result of rockfall and probably change microclimate due to cooling effects of blocky surface (Gruber and Hoelzle, 2008). In the Steintaelli large blocks accumulated at the toe of the NE-slope (Fig. 9.3 A), while smaller plates of schist accumulated on the SW-slope (Fig. 9.3 B). ERT and SRT showed permafrost conditions at the toe of the NE-slope which can be a result of cooling effects by the blocky surface.

Active-layer thawing depths observed in ERT and SRT reflect heat transport by conduction, advection and convection. To distinguish different heat transports and their influence on thawing is not possible on this temporal scale. An increased measuring frequency, e.g. daily measurements, has the potential to analyze the influence of individual heat transfer and fast-response as demonstrated by Hilbich et al. (2011) for advective thawing during snowmelt. In 2012, ERT patterns were similar between August 8th and August 18th, thus, intra-annual response of active-layer thaw was not significant in this short period of ten days. Most of the snow cover except the cornice was already melted and heat transfer predominantly occurred in a conductive and convective way with slower speed and resulting in longer response time of thawing. Inter-annual response reflects climatic conditions, snow conditions and heat transfer. In August 2012, snow was already melted and advective heat transfer along discontinuities with fast responding active-layer thaw (Gruber and Haeberli, 2007; Hasler et al., 2011a) already occurred. In July/August 2013, snow cover decreased conductive and convective heat transfer. Snow cover still stored water and reduced advective heat transfer which leads to a less thick active-layer and frozen ground close to the surface.

The combined use of SRT and ERT enable differentiation between frozen and unfrozen ground. All rock temperature data loggers classified to Ishikawa's (2003) regime type (iii) showed BTS values in late winter indicating permafrost occurrence (Chapter 7.3.2). South-facing loggers C4 and S1-S4 are located in permafrost-free locations according to SRT, thus, the application of BTS method is limited in bedrock. The use of GST from rock data loggers and calculation of MAGST provide a better temperature-dependent technique to evaluate permafrost or frozen ground distribution. The modelled thermal regime based on MAGST of temperature loggers was not significantly different on permafrost-affected north face of the rock wall (see Chapter 8.4.3.1 for detailed discussion).

8.5 Conclusion

Permafrost distribution is affected by climate, topography and ground material (Gruber, 2005). When rocks freeze, ice pressure develops and increases the matrix velocity of rocks which presents the dominant influence on p-wave velocity increase (Draebing and Krautblatter, 2012). Due to this increase, refraction seismics allow the differentiation between frozen and unfrozen rock as shown by Krautblatter and Draebing (2014).

Air temperature in the summers 2012 and 2013 were comparable but snow cover differed significantly. Thermal modelling can differentiate permafrost and no-permafrost areas. Despite limitations or simplifications of physical processes, the modelled active-layer depth in permafrost areas could be confirmed by geophysical methods and deviations are smaller than expected. In non-permafrost areas, the modelled results cannot resolve seasonal frozen conditions in depth.

ERT and SRT can resolve active-layer depth. Contrary results between both methods exist, if near-surface areas are dry, which results in high resistivities and low p-wave velocities. SRT are not sensitive to near-surface moisture conditions and should be used for analysis instead of ERT.

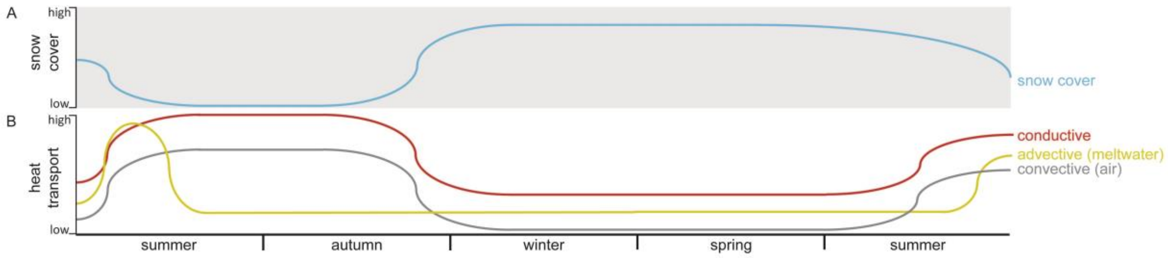

Fig. 8.26 Conceptual approach of snow cover and depending heat transport processes.

Topography leads to deeper thawing on south-facing slopes. Blocky material seems to produce a permafrost-favouring microclimate on the toe of NE-slope. Snow cover plays a key role of permafrost evolution on slope facet scale. Long lasting snow cover in 2013 delayed heat transport processes by insulating the underground or storing water as snow (Fig. 8.26) and influenced thickness of active-layer thaw.

9 Mechanical regime

9.1 Geomorphological and geological conditions at Steintaelli

The southern Valais is part of the Penninikum and determined by Bernhard/Monte Rosa nappe. Several nappes are layered slightly inclined in southerly direction. The Steintaelli lies in the Siviez-Mischabel nappe, in the geological map (Fig. 9.1 A-B) called Mischabel-Kristallin (Bearth, 1980). The Siviez-Mischabel nappe is a Palaeozoic, polymetamorph complex consisting of different paragneiss, schists, amphibolites and orthogneiss. In Jung valley and Turtmann valley, Chlorite-Muscovite-Schists and mica gneiss are dominating including layers of amphibolites (Bearth, 1980). Geologic folds are common in the Siviez-Mischabel nappe inclining 10-30° in W or SW direction.

In-situ rock in the investigated Steintaelli rock wall consists of quartz slate with planar schistosity and schisty quartz slate with planar slaty cleavage. Two rock samples were analysed with petrophysical methods, results show high quartz contents of 46.6 % for quartz slate and 35.9 % for schisty quartz slate (Krautblatter, 2009). High mica content of 40.0 % (schisty quartz slate) and 27.5 % (quartz slate) (Krautblatter, 2009) in combination with schistosity allow high fissionability in direction of foliation. Further mineral contents are feldspar (15.9 %, schisty quartz slate; 15.5 %, quartz slate), glaucophane (4.4 %, schisty quartz slate) and chlorite (3.8 %, schisty quartz slate; 10,4 %, quartz slate) (Krautblatter, 2009).

Halla (2013) mapped discontinuities and discontinuity properties (orientation, spacing, persistence, roughness, wall strength, aperture, filling, seepage) according to the classification of ISRM (1978) using scanline measurements (Hencher, 1987) along the geophysical Transects 1, 5 and 9. The most important discontinuities are visualized in Fig. 9.4. He found 6 sets of discontinuities (Fig. 9.4). The orientation of Set 1 (31°/223°) along the direction of foliation conforms to the inclination of the Siviez-Mischabel nappe (Fig. 9.3 B) (Halla, 2013). The other 5 sets are typical for the regional geology and are from tectonic origin (Halla, 2013).

Glacial history and paraglacial adjustment influence rock stability. According to the model by Kelly et al. (2004) the ice-surface of the Matter Valley glacial system during the last glacial maximum (LGM) extended lower than the Steintaelli (Fig. 9.2). Probably, the NE-Rothorn Glacier (Fig. 8.5) overlaid the Steintaelli during LGM and little ice age (LIA). No photo proof of LIA extent exists but a photo by Jules Beck in 1882 shows the large LIA extent of the NW-Rothorn Glacier, thus, the photo suggests a larger extent of the NE-Rothorn Glacier and coverage of the near-by Steintaelli. The rock wall in the

Steintaelli is probably ice-free since approximately 100 years and paraglacial adjustment is occurring since glacier retreat.

Mass movements are abundant in the Steintaelli. Mass movements are processes without transport medium (water, ice, air) and synonymously called landslides (Dikau, 2004b). Landslides can be distinguished according to morphology, mechanism, type of material and rate of movement (Dikau, 2004b). Fall is free movement of material from steep slopes (Dikau, 2004b) and can be classified according to their specific volume (Whalley, 1984). Rock flows are rock deformations of creep-flow type, affecting homogenous rock masses of high volume and are characterised by small displacement rates (Dikau, 2004b) below 1.5 mm/a (Varnes, 1978). The terms deep-seated gravitational slope deformation (DSGSD), “Bergzereißung”, “Sackung” and “Talzuschub” are used synonymously by several authors. DSGSD can be classified into the two main types sackung and lateral spreading (Soldati, 2004). The term “Talzuschub” is common in Austria while in Switzerland “Sackung” is used to describe the same phenomenon (Bayerisches Landesamt für Umwelt, 2010). Rock flow causes typical structures and landforms at different locations. Upper parts of the deforming slope are characterised by graben-like depressions, double ridges, ridge depressions and troughs (Dikau, 2004b). This upper part is called in German “Bergzereißung” which describes the rupture of the mountain top (Ward, 2004). The middle part of the deforming slope shows sagging of the rock mass and development of crevasses, this part is called “Sackung” in German. The toe of the slope is characterized by compressional features like bulging (Dikau, 2004b) and is called “Talzuschub” in German (Ward, 2004). In this dissertation the term rock flow is used to describe the process. Rock flows are found in four different locations in the Turtmann valley and form multiple ridges or terrace-like steps on the trough slopes (Otto and Dikau, 2004).

The rock wall at Steintaelli is assumed to be a rock flow. Double ridges are recognizable on the crestline. The almost vertical inclining discontinuity Set 3 (84°/041°) strike parallel to the crestline and Halla (2013) assumes that fluctuations of inclinations between NE and SW indicate a graben structure. Sagging or bulging features are obviously absent in the Steintaelli. In the lower lying valley Rinderälpi, bulging features are absent (Krautblatter, pers. Communication), thus, the rock wall in the Steintaelli may be not part of a larger scale rock flow. Accordingly, the slope height in the GSI analysis by Halla (2013) is assumed 40 m equivalent to the rock wall height.

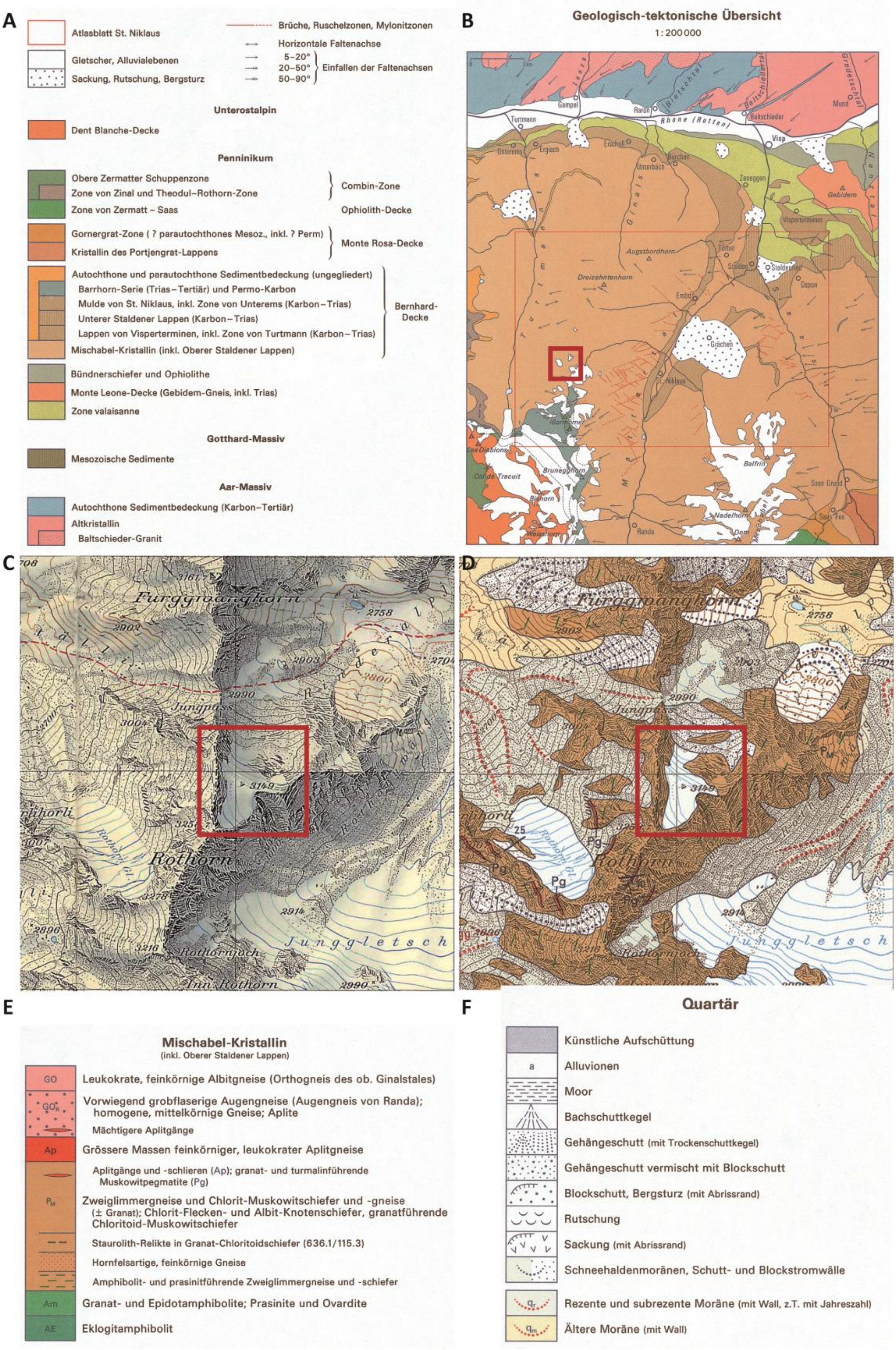

Fig. 9.1 A-B: Geological-tectonic map of St. Niklaus (Bearth, 1980) with Steintaelli (red rectangle); C: Topographic map of the Steintaelli (red rectangle); D: Geologic map of the Steintaelli (red rectangle) (excerpt from geologic map by Bearth (1980)); E-F: Legend of geologic map (Bearth, 1980).

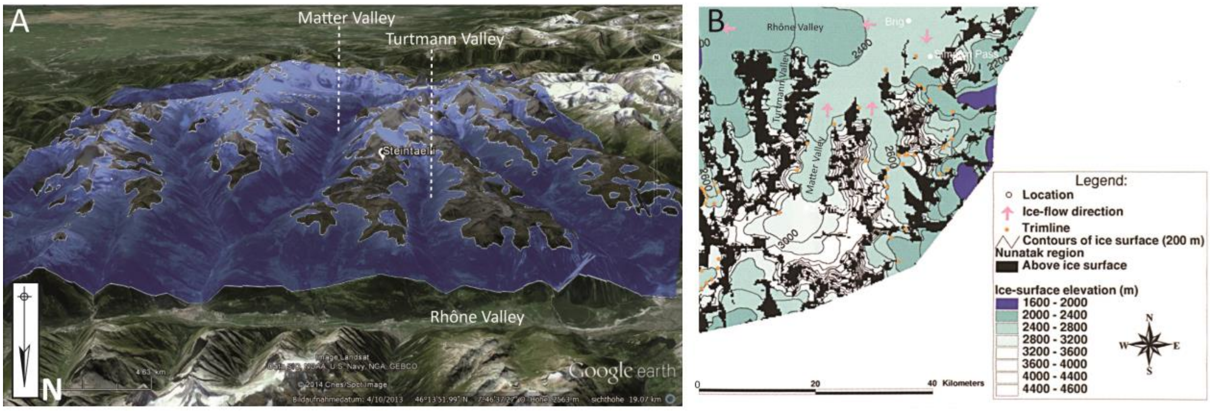

Fig. 9.2 A: Glacier extent during the LGM based on the model by Kelly et al. (2004) spatially referenced by K. Leith; B: Ice-surface elevation during LGM (adapted from Kelly et al., 2004).

Block size of the rock wall results from number of discontinuities, spacing and persistence and was analysed using the volumetric joint count method by Palmström (1982). The NE-slope possesses the highest number of joints each volume (J_V) (2.2 joints each m^3) followed by the crestline (1.3) and the SW-slope (1.2) (Halla, 2013). Depending on assumed width-to-height-ratio for quadratic and laminatic blocks, block size varies between 2-5 m^3 on NE-slope (Fig. 9.3 A), 25-30 m^3 on the crestline and 20-40 m^3 on the SW-slope (Fig.9.3 B) which is in accordance to field observations (Halla, 2013). Block failures can occur on the NE-slope (Fig. 9.3 A). On the SW-slope (Fig. 9.3 B), high volume-blocks in combination with discontinuity Set 1 in the range of middle slope inclination can fail in a sliding or shearing way (Halla, 2013).

Halla (2013) used the JRC-method by Barton and Choubey (1977) to estimate shear strength of the discontinuity sets with scenarios for profile length of 0.25 m and 2 m. The friction angle is minimum 43° (Set 1 in scenario 2 m profile length) and exceeds mean slope angles of 36-40° resulting in stable discontinuity conditions (Halla, 2013). Aperture of discontinuities ranges from very wide (1-10 cm) for 43 % of discontinuities on SW-slope and 44 % of discontinuities on the NE-slope to extremely wide (10-100 cm) for 83 % of the discontinuities on the crestline (Halla, 2013). In August 2012, two discontinuities on the NE-slope and nine discontinuities on the crestline were ice-filled (see Fig. 9.4 for location) (Halla, 2013). The rock mass was analysed using the GSI method by Hoek and Brown (1997). GSI was estimated to be 52 ±4 on the NE-slope indicating a very blocky structure and 40 ±3 on the SW-slope indicating a blocky structure, respectively (Halla, 2013). The Mohr-Coulomb failure criterion is calculated from the Hoek-Brown criterion showing higher cohesion on NE-slope (528 kPa) than SW-slope (285 kPa) and a higher friction angle on NE-slope (46.2°) than SW-slope

(39.4°) (Halla, 2013). Minimum friction angles are higher than average slope angles indicating rock mas stability (Halla, 2013).

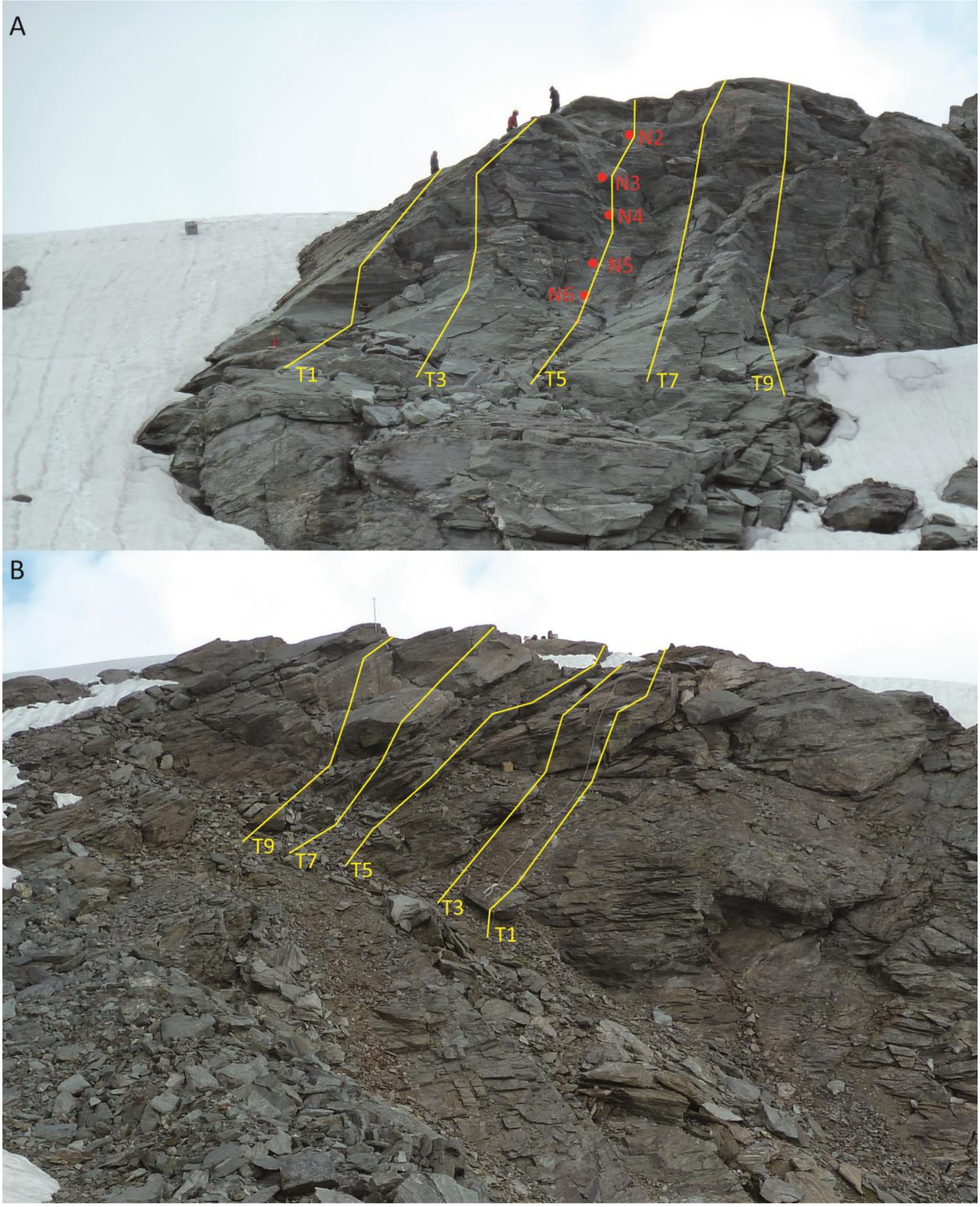

Fig. 9.3 Steintaelli rock wall with geophysical Transects (yellow) on August 14th 2012; A: NE-slope with logger positions (red), see persons for scale; B: SW-slope.

9.2 Inter-annual dynamics of discontinuity movements

Zangerl et al. (2008) give an overview about possibilities to measure dynamics of mass movements. They distinguish point measurements, measurements along transects and spatial measurements. Tachymeters (Willenberg et al., 2008), GPS (Strozzi et al., 2010; Wirz et al., 2014), crackmeters (Matsuoka et al., 1997; Matsuoka and Murton, 2008; Willenberg et al., 2008) and distometers enable point measurements (Zangerl et al., 2008). Inclinometers (Willenberg et al., 2008) and Tape-Extensometers (Willenberg et al., 2008) can measure movements along transects (Zangerl et al., 2008). InSar (Strozzi et al., 2010; Strozzi et al., 2013) and ground-based InSar (Gischig et al., 2009; Kos et al., 2011; Caduff et al., 2014), aerial (Fischer et al., 2011; Fischer et al., 2013) and terrestrial laserscanning (Oppikofer et al., 2008; Oppikofer et al., 2012; Ravanel et al., 2013) and digital photogrammetry (Fischer et al., 2006; Ravanel and Deline, 2010; Strozzi et al., 2010; Fischer et al., 2011; Strozzi et al., 2013) enable a spatial measurement of movement (Zangerl et al., 2008). For a detailed overview of remote sensing techniques see Kääb et al. (2005). To measure rock flow activity extensometer measurements are a common technique (Amann, 2006; Moser et al., 2009).

9.2.1 Data appraisal and processing

Five extensometer transects were installed in August 2005 and extended to 18 transects in August/September 2006 by Krautblatter (2009) (Fig. 9.4). Due to anchor failure two transects were renewed in 2013.

Measurements were conducted by different persons between 2005 and 2013 (Table 9.1) Oertel (2009) used the extensometer with a slightly higher tension, which resulted in an increased inaccuracy. Results by Ortlieb (2012) show unusual convergence and divergence of transect in the range up to 2 cm. Measurements by Halla (2013) show a decline of movement in the exactly same range suggesting a misapplication of the extensometer before. Therefore, data by Ortlieb (2012) and Oertel (2009) was excluded from further analysis. Transects are composed of two anchors, which allow measurements between the exact two points. Measurements were conducted using the analog tape extensometer provided by M. Moser from the manufactory itmsoil between 2005 and 2012. From 2013 on we used the digital version of the tape extensometer provided by M. Krautblatter. The accuracy of meter reading is 0.01 mm for the digital tape extensometer (itmsoil, 2014a, 2014b) and analog extensometer (Amann, 2006).

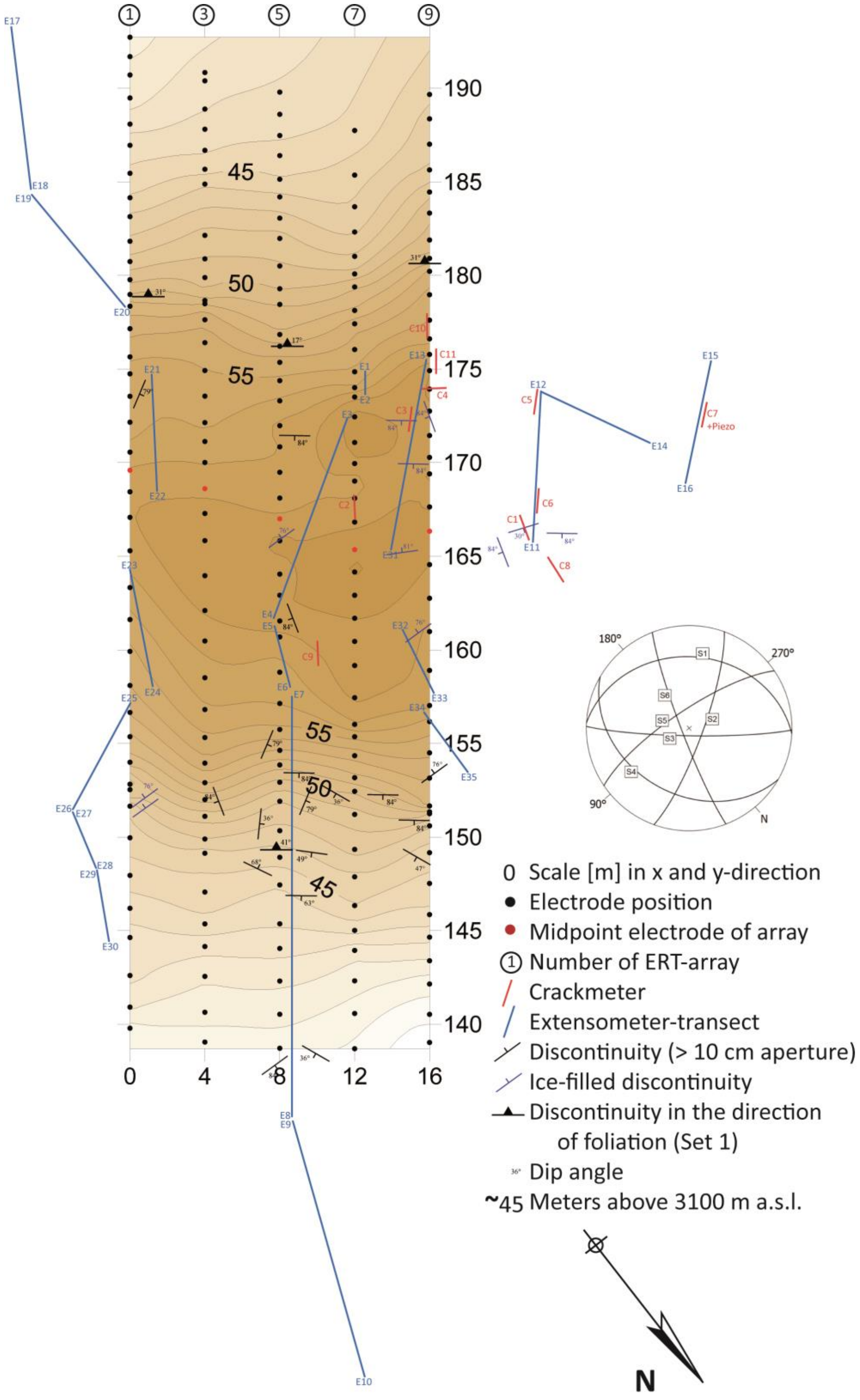

Fig. 9.4 Map of extensometer transects, crackmeters, discontinuities. Electrode position and extensometer transect position are sketched according to Krautblatter (2009). Discontinuity positions and infill in 2012, dip and Schmidt net is mapped and created by Halla (2013).

Table 9.1 Extensometer measurements in the Steintaelli.

Date	Measured by
Aug 20th, 2005	Krautblatter (2009)
Sep 23rd, 2005	Krautblatter (2009)
Aug 2nd, 2006	Krautblatter (2009)
Aug 15th, 2006	Krautblatter (2009)
Sep 5th, 2006	Krautblatter (2009)
Sep 21st, 2006	Krautblatter (2009)
Aug 11th, 2007	Oertel (2009)
Aug 19th, 2007	Oertel (2009)
Sep 11th, 2007	Oertel (2009)
Sept 2nd, 2008	Krautblatter (2009)
July 11th, 2011	Ortlieb (2012)
Aug 24th, 2011	Ortlieb (2012)
Aug 8th, 2012	Halla (2013)
Aug 19th, 2012	Halla (2013)
Aug 3rd, 2013	Halla
Sep 14th, 2013	Krautblatter

Temperature was measured alongside the extensometer measurements with a 0.03°C-accurate thermometer to correct thermal expansion of the extensometer. Temperature correction is conducted using the correction factor α provided by itmsoil (2014b)

$$\alpha = L * 11.6 * 10^{-6}\, T + 8.33 * 10^{-6}\, T \tag{9.1}$$

where L is tape length of the extensometer and T is air temperature. The left-hand side of the equation is the correction for the stainless steel tape and the right-hand side of the equation for the instrument itself. All extensometer measurements are corrected to $T_{0°}$ to exclude the effects of thermal expansion. The digital extensometer is modified with an adapter. Differences between analog and digital extensometer are evaluated by Petschik (2014). According to Petschik (2014:47) a correction factor of 8.77 mm has to be added to the digital extensometer length.

9.2.2 Evaluation of uncertainties

The accuracy of the extensometer is 0.01 mm (itmsoil, 2014a). All measurements are repeated between 3 and 5 times for each transect and mean values are calculated. Repeatability depends on the experience of the operator and is given by itmsoil as 0.1 mm for the digital (itmsoil, 2014a) and analog extensometer (Amann, 2006). Measurements conducted in 2012 and 2013 show higher standard deviations than 0.1 mm for few measurements conducted by Halla (Table 9.2).

Table 9.2 The table shows extensometer transects and extensometer measurements. Transect, length of transect, accuracy of itmsoil extensometer A_{soil} (itmsoil, 2014a), standard deviation of repeated measurements of itmsoil extensometer (itmsoil, 2014a), standard deviation of measurements on August 8th 2012 R_1, August 19th 2012 R_2, August 3rd 2013 R_3 and September 14th 2013 R_4, error resulted from accuracy of thermometer A_{therm} and error resulted of air temperature change during measurement T_{ac}.

Transect	Length [m]	A_{soil} [mm]	Repeatability						A_{therm} [10^{-3} mm]		T_{ac}
			R_{soil} [mm]	R_1 * [mm]	R_2 * [mm]	R_3 * [mm]	R_4 ** [mm]				
E1 -E2	2.0	±0.01	±0.1	±0.06	±0.06	±0.07	±0.01		±0.95		
E3 - E4	13.6	±0.01	±0.1	±0.09	±0.17		±0.06		±4.97		
E5 - E6	3.8	±0.01	±0.1	±0.04	±0.05	±0.03	±0.01		±1.57		
E7 - E8	27.9	±0.01	±0.1	±0.30	±0.35	±0.28	±0.05		±9.96		
E9 -E10	14.3	±0.01	±0.1	±0.07	±0.36						
E9-E10_2	14.1	±0.01	±0.1			±0.17	±0.01		±5.16		
E11 - E12	8.1	±0.01	±0.1	±0.10	±0.12						
E12 - E14	7.0	±0.01	±0.1	±0.07	±0.19		±0.04		±2.67		
E13 - E31	10.0	±0.01	±0.1	±0.16	±0.22		±0.06		±3.74		
E15 - E16	7.4	±0.01	±0.1	±0.17	±0.17		±0.02	+	±2.82	+	Fig. 9.5
E17 - E18	14.4	±0.01	±0.1	±0.17	±0.63	±0.16	±0.02		±5.25		
E19 - E20	10.7	±0.01	±0.1	±0.13	±0.13	±0.09	±0.09		±3.97		
E21 - E22	8.4	±0.01	±0.1	±0.10	±0.30		±0.09		±3.16		
E23 - E24	6.9	±0.01	±0.1								
E23-E24_2	6.9	±0.01	±0.1		±0.35		±0.04		±2.65		
E25 - E26	6.9	±0.01	±0.1	±0.04	±0.46		±0.03		±2.66		
E27 - E28	2.6	±0.01	±0.1	±0.10	±0.23		±0.02		±1.15		
E29 - E30	5.4	±0.01	±0.1	±0.10	±0.25						
E32 - E33	4.6	±0.01	±0.1	±0.09	±0.14	±0.01	±0.06		±1.85		
E34 - E35	4.4	±0.01	±0.1	±0.08	±0.11	±0.02	±0.09		±1.77		

measurements conducted by *Halla and **Krautblatter

Raw data of measurements before 2012 are not available for error estimation and are assumed in the same range as the measurement conducted by Krautblatter in September 2013. The accuracy of the thermometer could result in an error of temperature correction, however, the high accuracy of 0.03°C result in an error of correction in September 2013 between 0.95 and 9.96 x 10^{-3} mm. The low error due to thermometer accuracy is negligible. If temperature changes during the repeated measurements the extensometer will expand or contract dependent on extensometer tape length (Fig. 9.5). Temperature changes can result in significant errors and can lead to high standard deviation. Measurements last only a few minutes and high temperature changes with resulting extensometer tape length change during this short period are unlikely but possible.

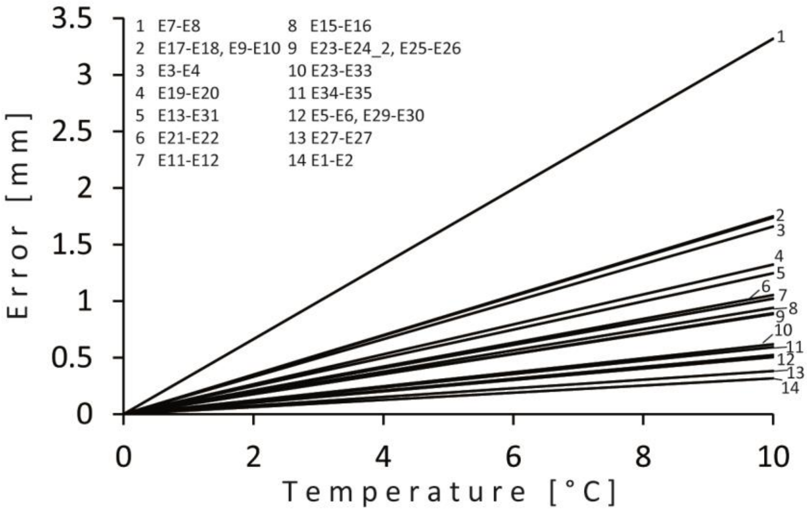

Fig. 9.5 Relationship between the error of extensometer measurement and the temperature for each transect.

To avoid errors air temperature is measured alongside each measurement and extensometer values are corrected with the temperature at the time of measurement.

9.2.3 Results

Extensometer measurements provide information about convergent or divergent movements between two anchors. None anchor is installed in potential not moving and stable terrain. Thus, extensometer measurements provide information about relative and absolute displacement (Amann, 2006). Extensometer transects expand over several discontinuities, thus, measured displacement results from a combination of potential divergent and convergent alteration of discontinuity aperture. Long transects usually expand over more discontinuities. Discontinuity spacing is comparable low on NE-slope resulting in a joint volume of 2.2 joints each cubic metre and block sizes of 2-5 m³ (Halla, 2013). Larger spacing on the crestline and SW-slope lead to joint volumes of 1.3 and 1.3 joints each cubic meter and block sizes ranging from 20 to 40 m³ or from 25 to 30 m³ (Halla, 2013), respectively. Discontinuity aperture is predominantly wide on NE-slope or SW-slope and very wide on the crestline (Halla, 2013). Transects on NE-slope incorporate more discontinuities each transect. Nine ice-filled discontinuities are mapped on the crestline and only two on the NE-slope (Halla, 2013). Extensometer measurements on the crestline are potentially affected by ice-filled discontinuities. Permafrost conditions are present below the crestline and on the NE-slope with annual differing active-layer depth. Permafrost conditions alter rock stability and shear strength properties of discontinuities (Krautblatter et al., 2013).

To allow differentiation of potential influencing factors, extensometer transects are classified depending on location on the rock wall. All transects independent on location show convergent and divergent displacement (Fig. 9.6). A typical dependency of displacement on location is not visible. Between August 20th and September 23rd 2005 three extensometer transects converge while two transects diverge, respectively. The periods between September 23rd 2005 and August 2nd 2006 show predominantly divergent displacement. In August 2006 displacement behaves predominantly in a convergent manner followed by a predominantly divergent displacement in September 2006 and between September 2006 and 2008. The period between September 2008 and August 2012 as well the period from August 8th to August 19th 2012 show predominantly convergent behaviour. In the following periods no displacement type is predominant.

In total only four transects show an overall divergent behaviour between the first and the last measurement. Total divergent displacement (Fig. 9.7 A) ranges from 0.29 to 14.07 mm and convergent ranges from 1.53 to 6.79 mm, respectively. Mean annual displacement (Fig. 9.7 B) is between 0.05 and 2.00 mm a^{-1} for converging transects and between 0.20 and 1.13 mm a^{-1} for diverging transects. The measurement period of Transect E9-10_2 was too short to calculate a mean annual displacement rate. Observed rates are in the range of rock flow rates suggested by Varnes (1978). Inter-annual rates are calculated for periods C, E and G (see Table 9.3 for period description). The calculated rates for period C, E and G are slightly higher than the total average emphasizing unusual large displacements in short periods (Fig. 9.7 C, E, G). Three intra-annual rates of mean annual displacement are calculated for Periods D, F and H (see Table. 9.3 for period description); two rates in summer 2006 and one rate in summer 2012. Intra-annual rates (Fig. 9.7 D, F, H) are 1 to 2 magnitudes higher than inter-annual rates indicating a relative large displacement in a relative short period in summer. Period D and H are measured in late summer and show high rates of predominant converging displacement while Period F is measured in early autumn and show predominantly diverging displacement.

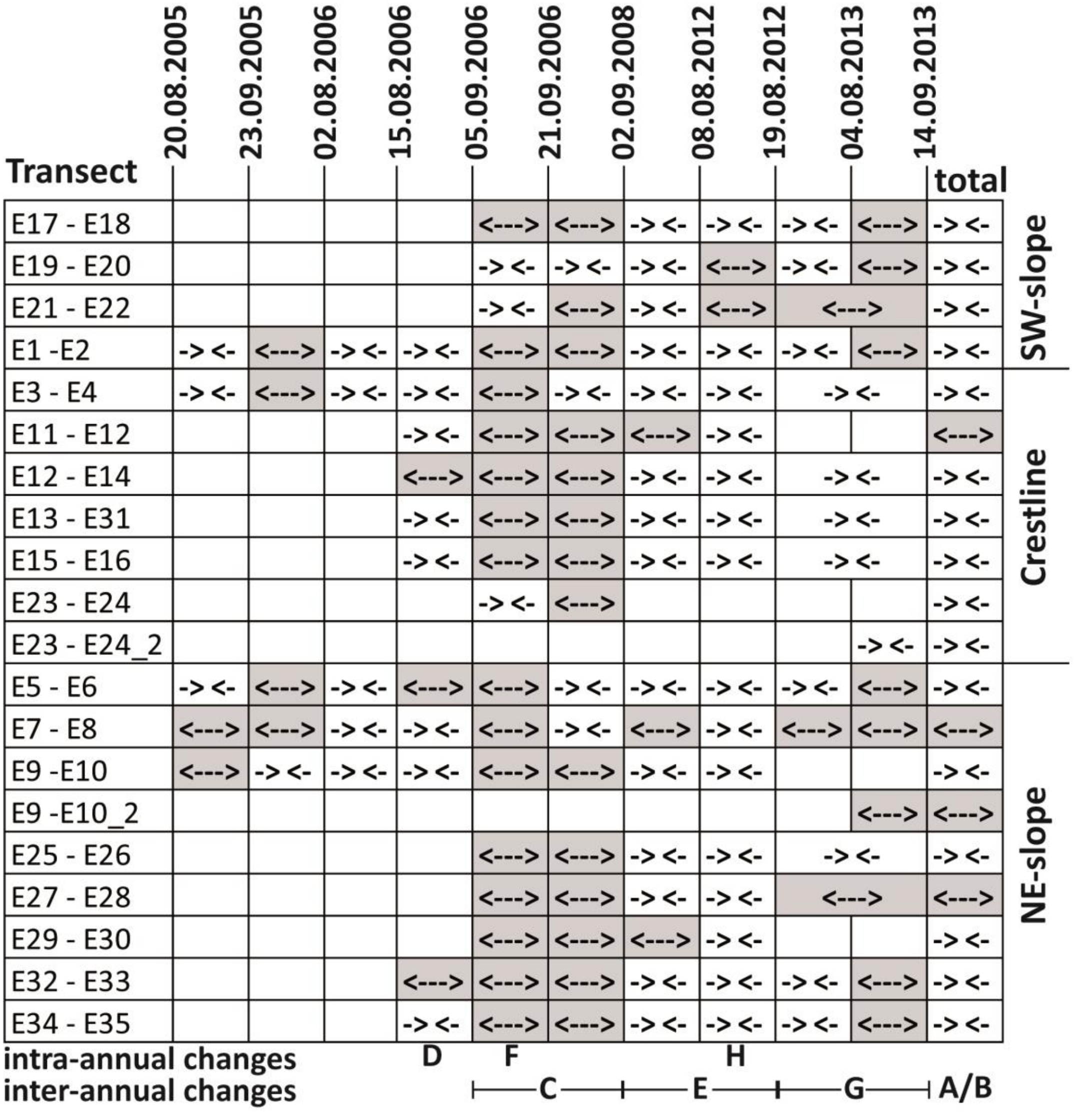

Transect	20.08.2005–23.09.2005	23.09.2005–02.08.2006	02.08.2006–15.08.2006	15.08.2006–05.09.2006	05.09.2006–21.09.2006	21.09.2006–02.09.2008	02.09.2008–08.08.2012	08.08.2012–19.08.2012	19.08.2012–04.08.2013	04.08.2013–14.09.2013	total	
E17 - E18					<--->	<--->	-> <-	-> <-	-> <-	<--->	-> <-	SW-slope
E19 - E20					-> <-	-> <-	-> <-	<--->	-> <-	<--->	-> <-	
E21 - E22					-> <-	<--->	-> <-	<--->	<--->		-> <-	
E1 -E2	-> <-	<--->	-> <-	-> <-	<--->	<--->	-> <-	-> <-	-> <-	<--->	-> <-	
E3 - E4	-> <-	<--->	-> <-	-> <-	<--->	-> <-	-> <-	-> <-	-> <-		-> <-	Crestline
E11 - E12				-> <-	<--->	<--->	<--->	-> <-			<--->	
E12 - E14				<--->	<--->	<--->	-> <-	-> <-	-> <-		-> <-	
E13 - E31				-> <-	<--->	<--->	-> <-	-> <-	-> <-		-> <-	
E15 - E16				-> <-	<--->	<--->	-> <-	-> <-	-> <-		-> <-	
E23 - E24					-> <-	<--->					-> <-	
E23 - E24_2										-> <-	-> <-	
E5 - E6	-> <-	<--->	-> <-	<--->	<--->	-> <-	-> <-	-> <-	-> <-	<--->	-> <-	NE-slope
E7 - E8	<--->	<--->	-> <-	-> <-	<--->	-> <-	<--->	-> <-	<--->	<--->	<--->	
E9 -E10	<--->	-> <-	-> <-	-> <-	<--->	<--->	-> <-	-> <-			-> <-	
E9 -E10_2										<--->	<--->	
E25 - E26					<--->	<--->	-> <-	-> <-	-> <-		-> <-	
E27 - E28					<--->	<--->	-> <-	-> <-	<--->		<--->	
E29 - E30					<--->	<--->	<--->	-> <-			-> <-	
E32 - E33				<--->	<--->	<--->	-> <-	-> <-	-> <-	<--->	-> <-	
E34 - E35				-> <-	<--->	<--->	-> <-	-> <-	-> <-	<--->	-> <-	
intra-annual changes				D	F			H				
inter-annual changes					C		E		G		A/B	

Fig. 9.6 Movement classified into divergent (<--->) and convergent (-> <-) for every period. For Period A total displacement and for Periods B-H mean annual displacement is shown in Fig. 9.7.

Table 9.3 Inter-annual and intra-annual periods

Abr.	Period	
A	first to last measurement	inter-annual
B	first to last measurement	
C	05.09.2006 to 02.09.2008	
E	02.09.2008 to 19.08.2012	
G	19.08.2012 to 14.09.2012	
D	15.8.2006 to 05.09.2006	intra-annual
F	05.09.2006 to 21.09.2006	
H	08.08.2012 to 19.08.2012	

Cumulative deformation along extensometer transects are shown in Fig. 9.8. Errors are assumed to be lower than 0.1 mm for measurements before 2012 or given in Table. 9.2 (R_1–R_4). All extensometer transects show a sequence of convergent and divergent displacements. Displacement varies highly between individual transects e.g. Transect E29-E30 displacement is in the range of 3 mm compared to displacement up to 15 mm of Transect E17-E19. Most transects show an increase of convergent displacement from 2012 on. Transect E17-E18 and E13-E31 enlarge between 2006 and 2008 up to 15 mm and 10 mm, respectively, and reducing by the same amount between 2008 and 2012.

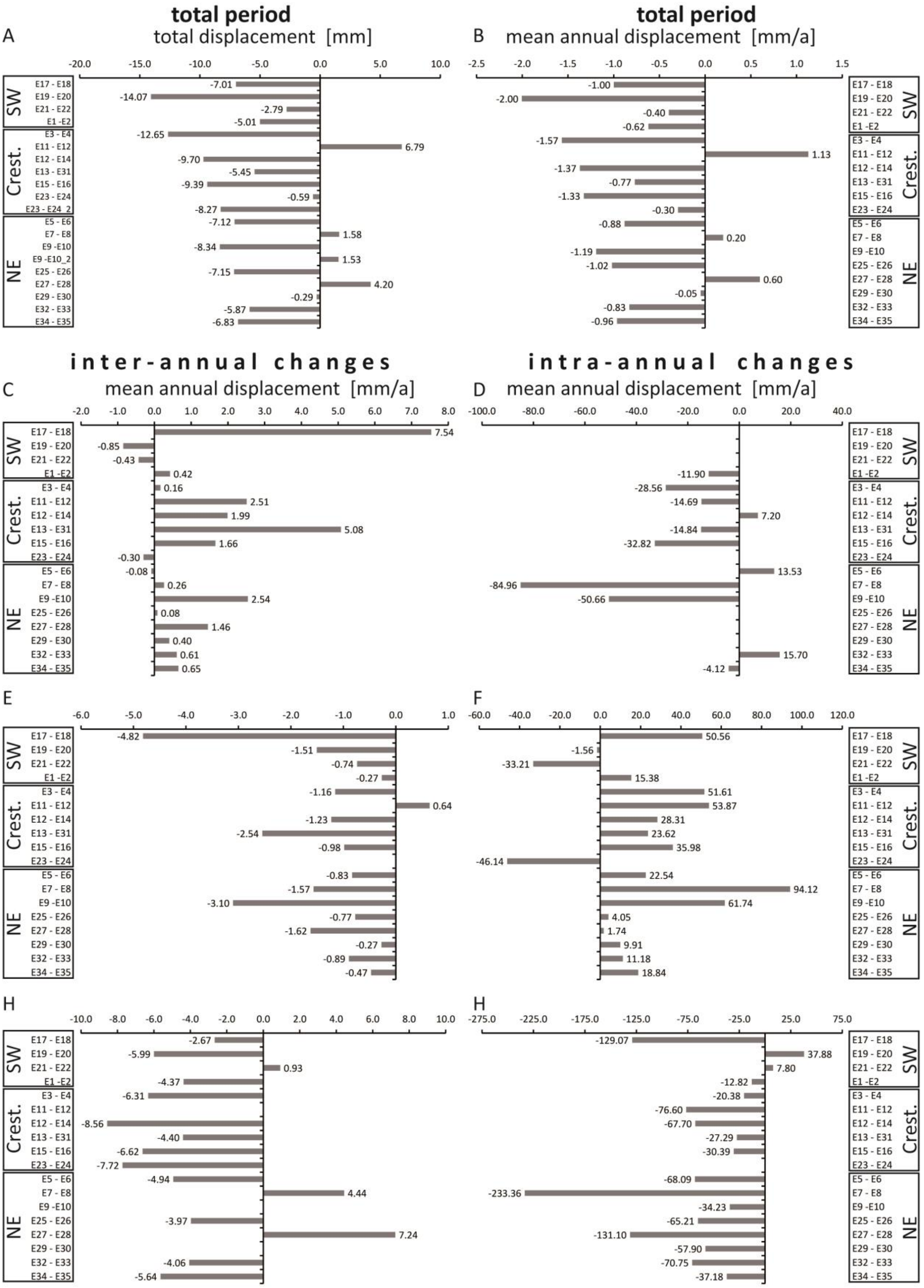

Fig. 9.7 Total displacement and inter-annual as well intra-annual displacement rates. For period details see Table 9.3.

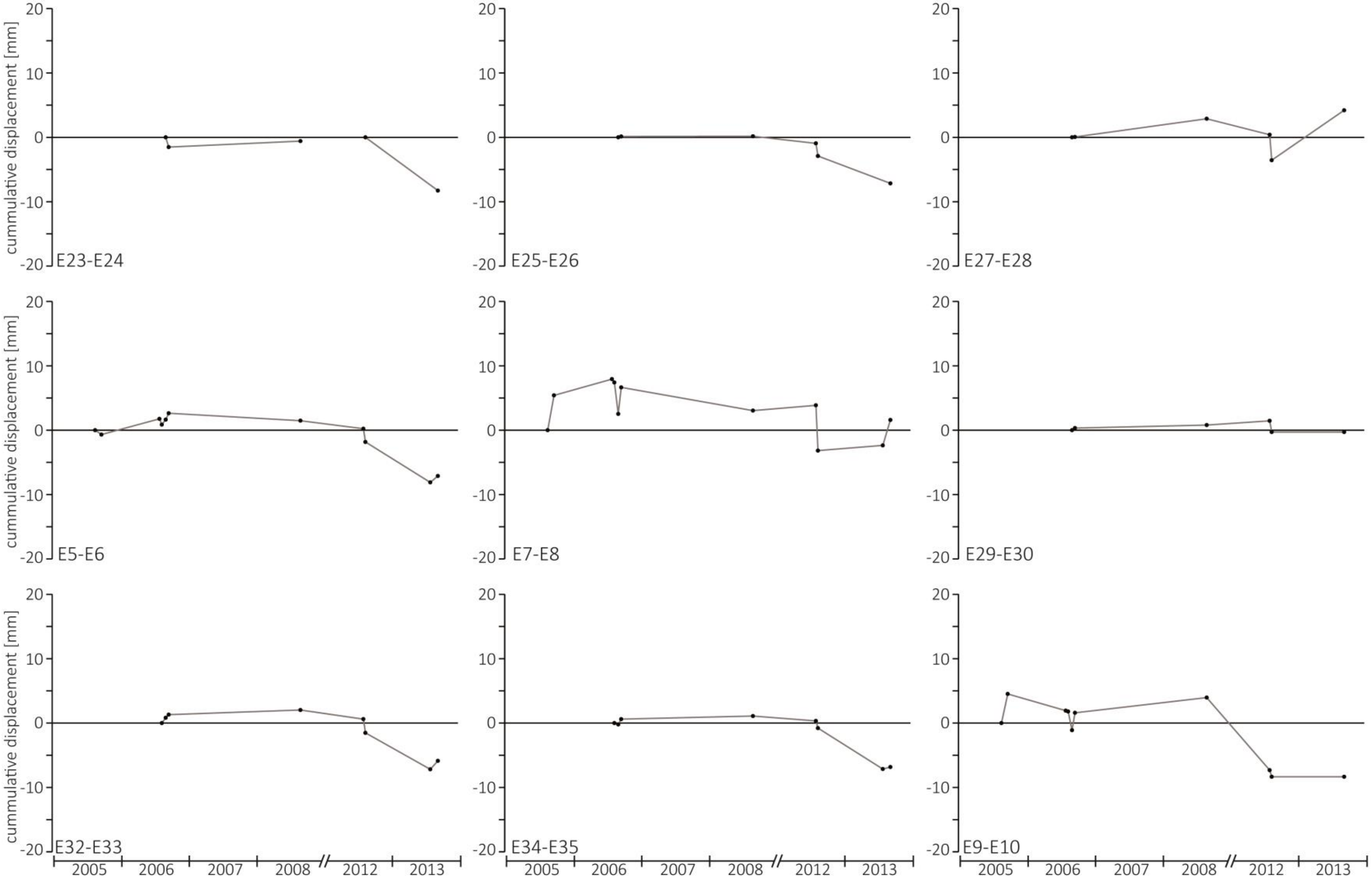

Fig. 9.8 Development of displacement between 2005 and 2012. Error bars are not shown due to low visibility of small errors.

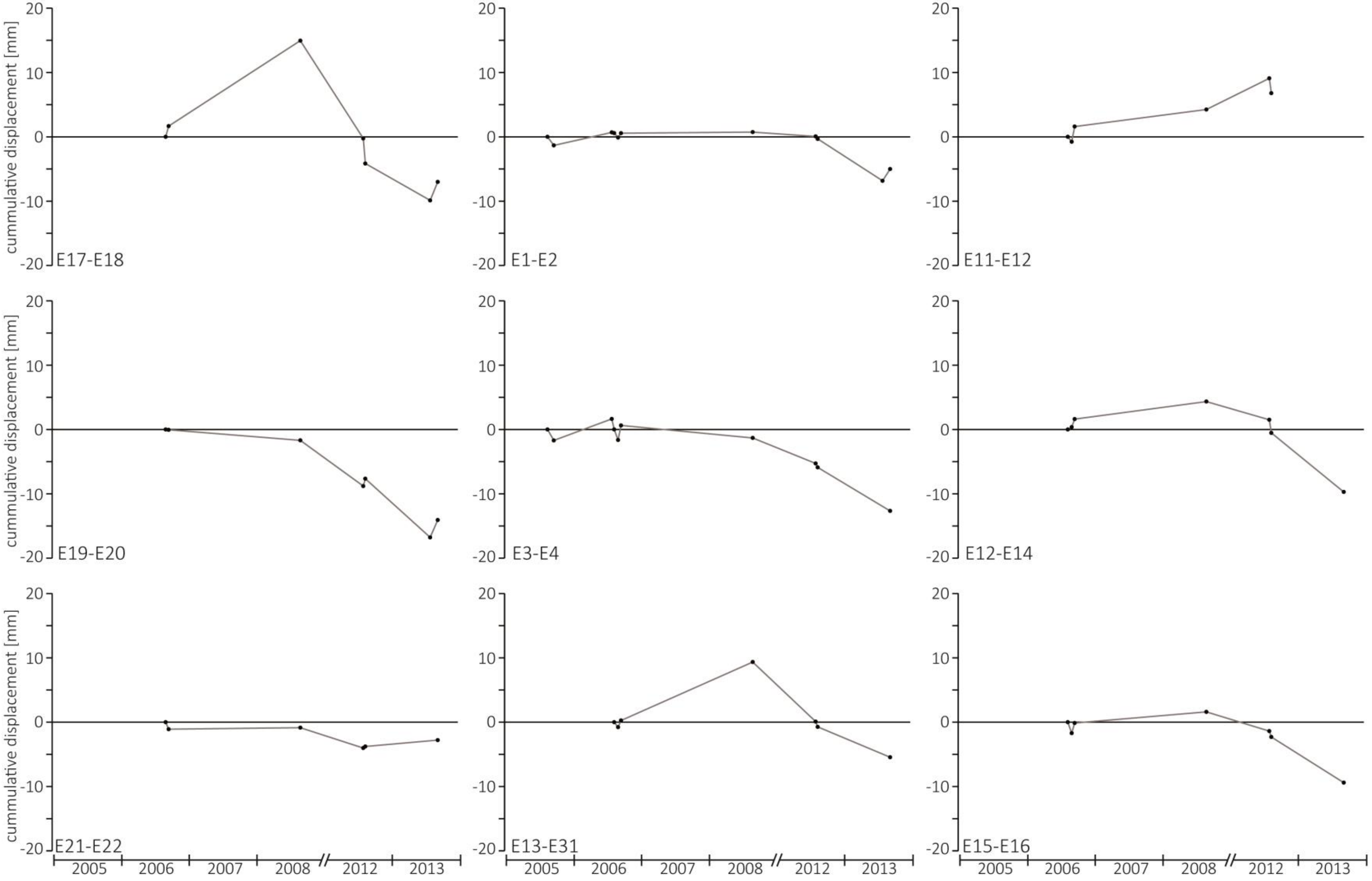

Fig. 9.8 Continued.

9.2.4 Interpretation and discussion

Four potential mechanisms for discontinuity movements are conceivable: (1) purely gravitative movement, (2) thermal expansion, (3) movement caused by hydrostatic pressure or (4) movement resulting from ice changes in discontinuities.

Case (1) is rock flow as a consequence of mechanical properties and their change. Rock flow can be caused by deglaciation and resulting debuttressing (Ballantyne, 2002; McColl, 2012). However, McColl and Davies (2013) showed the possibility of larger rock flow occurrence in contact with a glacier in New Zealand. The Steintaelli as a part of a much larger rock flow is excluded due to missing bulging toe (Talzuschub) at Rinderälpi or sacking features (Sackung). Halla (2013) used the JRC method to analyse discontinuities and the GSI to analyse rock mass stability; both methods suggest stable conditions. The geotechnical methods are based on geotechnical properties of the rock without involving ice or permafrost, thus, a purely gravitative movement can be excluded. However, the shearing plane could be deep-seated resulting in a multi-block failure with internal shearing (see Fig. 5.4 D right bottom column) (Eberhardt et al., 2004). Small block size especially on the NE-slope (2-5 m^3) (Halla, 2013) show the existence of multiple blocks. The observed sequence of divergent and convergent displacement can be a result of a multi-block failure. On the SW-slope block size of 20-40 m and the dominant discontinuity Set 1 (31°/223°) oriented along the direction of foliation (Halla, 2013) induce sequenced failure with internal shearing (Fig. 5.4 D middle right column) (Eberhardt et al., 2004). Thus, sequenced failure can cause observed sequence of divergent and convergent displacement. However, Halla (2013) concluded that the discontinuity Set 1 is the lowest friction but still sufficient to stabilize the SW-slope. The crestline shows graben-like features and would be the Bergzereißung-part of the rock flow. The observed divergent and convergent displacement would be logical consequence of Bergzereißung-processes.

Rock expands or contracts as a result of temperature changes (Case 2) (Moore et al., 2011); these thermal induced expansions can be effective even in high depths (Gischig et al., 2011a, 2011b). Measured displacement exceeds thermal expansion of the rock by far. In August 2012 and 2013 mean monthly air temperatures are high (Fig. 8.20) and thermal expansion is expected resulting in divergent behaviour. However, extensometer displacements show a reverse convergent behaviour (Fig. 9.6 and Fig. 9.8). Hydrostatic pressure (Case 3) can be developed due to summer rainstorms or snow melt. The discontinuous measurement with a monthly or annual resolution cannot resolve such events occurring in small periods. A cryostatic pressure increase (Case 4) due to ice segregation (Murton et al., 2006) or volumetric expansion (Matsuoka, 2001a) can result in diverging displacement. Otherwise, seasonal thawing or warming of permafrost rock walls can decrease cryostatic pressure and reduce shear resistances (Krautblatter et al., 2013), thus can cause a convergent displacement.

High intra-annual displacement rates in summer suggest ice melting or freezing involved in displacement. In 2012, active-layer reached high depth (Fig. 8.24 and 8.25) and this can explain convergent behaviour observed at 16 of 18 extensometers. However, divergent behaviour continues between 2012 and 2013 observed at 11 of 18 extensometers while active-layer depth reached minimum depth due to snow isolation.

9.2.5 Conclusion

Based on extensometer data and findings by Halla (2013) a purely gravitative movement can be excluded. However, a rock flow with deep-seated shear plane is still a reasonable explanation. Cryostatic and hydrostatic pressures are possible causes of discontinuity movements and cannot be resolved on an annual or weekly resolution. To analyse the effects of cryostatic pressure on displacement, a higher temporal resolution is necessary. To obtain this temporal resolution, ten crackmeters were installed in 2012 to monitor continuously discontinuity movements. A continuous monitoring of permafrost conditions is necessary, but can only be achieved by drilling a permafrost borehole to monitor rock temperatures at point scale. The inaccessibility of the site hinders monitoring with continuous ERT, which requires maintenance.

9.3 Seasonal dynamics of discontinuity movements

9.3.1 Introduction

The following chapter is actually a paper in preparation by Draebing, D., Krautblatter M. and T. Hoffmann. The statistical calculations, originally calculated by Draebing using Microsoft Excel, were transferred by Hoffmann into statistical software R in form of a R-script. The idea to use Equation 9.2 to quantify thermal expression coefficient α was originally by T. Hoffmann after the author found a strong relationship between temperature und discontinuity expansions (Fig. 9.21 and Table 9.5). Actually, Krautblatter plans to measure thermal expansion coefficient α of rock samples from Steintaelli in the freezing laboratory at TU München to calibrate the field data.

The factor of safety expresses stability as the sum of resisting forces (shear strength) divided by sum of driving forces (shear forces). If the factor of safety is one or close to one failure can occur (Dikau, 2004a), which Bovis (2004) describes as dislocation within material or movement. Instability can occur if shear forces increase and/or shear strengths decrease. In the Steintaelli, six potential causes of seasonal discontinuity movements have to be taken into account (Fig. 9.9):

(1) Gravity is constant over time (Fig. 5.10 C). If shear strength is reduced gravity could lead to opening of discontinuities (Fig. 9.9 A). (2) Hydrostatic pressure changes seasonally due to snowmelt and daily due to rainfall events. If water infiltrates into discontinuities and is retained, e.g. due to permafrost or other impermeable layers (Fig. 9.9 B), water causes a hydrostatic pressure potentially sufficient to open discontinuities (Fig. 9.9 C). (3) Insolation is the driving force of thermal changes (Hall and André, 2001). On daily or shorter scale, warming of rock mass results in expansion of rock (Fig. 9.9 E) and cooling causes contraction (Fig. 9.9 D), respectively. Expansion of rocks decreases aperture of discontinuity due to expansion into fractures (Cooper and Simmons, 1977), while contraction is associated with dilatation of fractures. (4) If the saturation of discontinuities is sufficient high (Walder and Hallet, 1986) (Fig. 9.9 F) freezing of water to ice leads to volumetric expansion up to 9 % and ice pressures develop up to 207 MPa (Matsuoka and Murton, 2008). As a result, discontinuities open (Fig. 9.9 G). The snowmelt infiltrates into discontinuities and transports advective heat, which results in ice erosion (Hasler et al., 2011a), decrease of cryostatic pressure and potential closing of discontinuity (Fig. 9.9 H). (5) If ice is present in the discontinuities, the ice develops a cryosuction of 1.2 MPA for a temperature drop of 1°C (Williams and Smith, 1989).

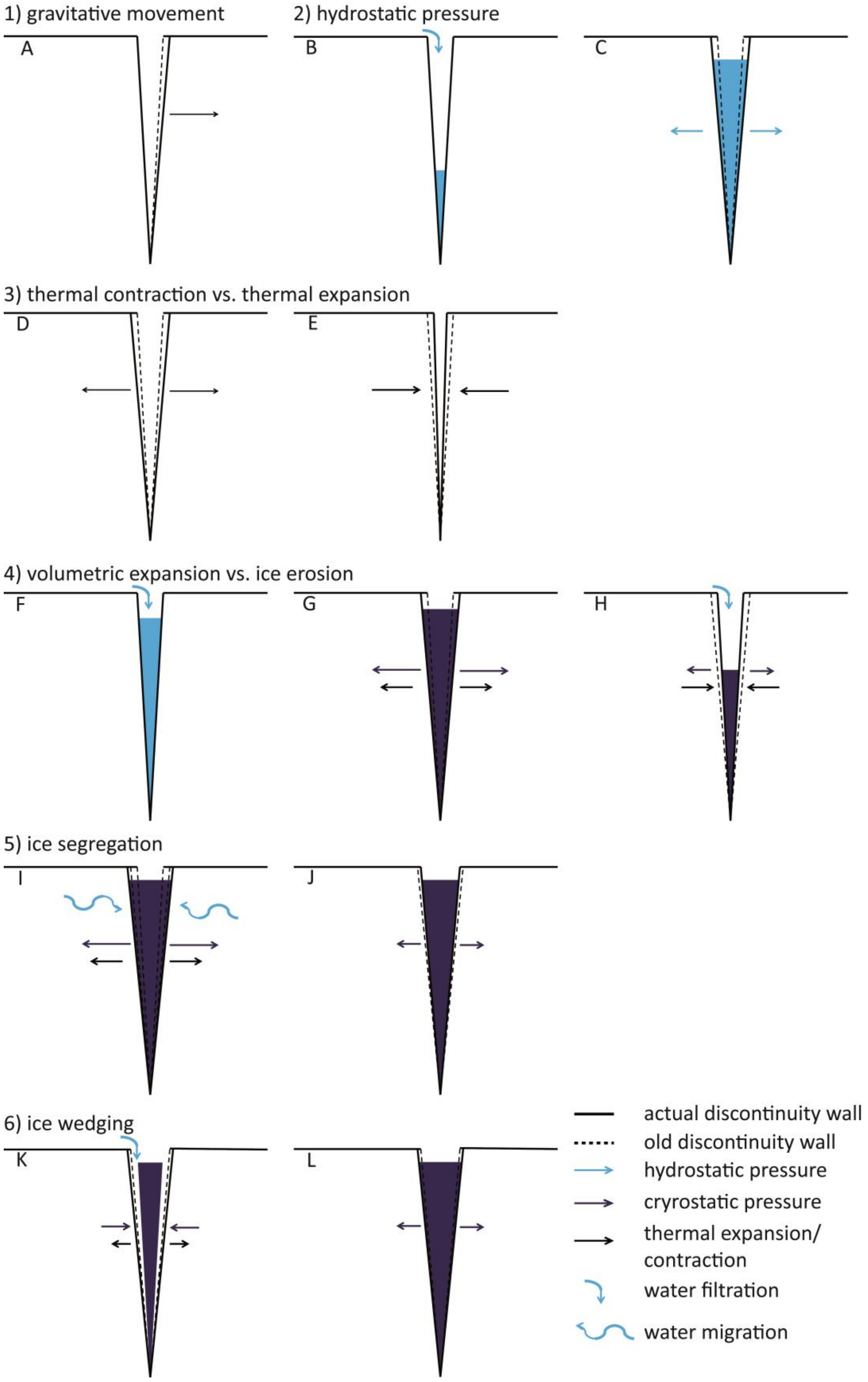

Fig. 9.9 Potential cause of discontinuity movements at Steintaelli; 1) purely gravitative movement (A), 2) hydrostatic pressure (B, C), 3) thermal contraction and expansion (D, E), 4) volumetric expansion (F, G) and ice erosion (H), 5) ice segregation (I, J) and 6) ice wedging (K, L).

Unfrozen water can migrate along the grain boundaries towards the ice body within the discontinuity (Fig. 9.9 I) (Walder and Hallet, 1985). As soon as water reaches the ice body surface forces decrease, water can freeze, which results in a further increase of the ice body. Due to ice body growth, cryostatic pressure coincidently increases and has the potential to open the discontinuity (Fig. 9.9 J).

(6) Ice possesses a thermal expansion coefficient ($\alpha_i = 6 \times 10^{-5}$°$C^{-1}$) of a magnitude higher than rocks. Wegmann (1998) assumes that an intense cooling in winter results in stronger contraction of the ice body in the discontinuity than contraction of the frozen discontinuity wall. As a result, a small gap between the ice body and the discontinuity wall develops. In spring meltwater can infiltrate in this gap (Fig. 9.9 K), freezes to ice and enlarge the ice body (Fig. 9.9 L). This process is comparable to ice wedging in the arctic.

9.3.2 Methods

To monitor movements of discontinuities, we installed ten 40 cm-long Geokon Vibrating Wire Crackmeter 4420-1-50 with thermistors (Fig. 9.10) across approximately 30 cm wide discontinuities in a permafrost rock wall (Fig. 9.4). One piezometer (P) was installed below Crackmeter 7 in an ice-filled discontinuity in approximately 2 m depth by laying the piezometer on the ice (Fig. 9.19 C). Groutable anchors fixed the crackmeters, half tubes protected crackmeters from snow load and a 16-Channel Geokon data logger Lc2x16 record the rock surface temperature (RST) and fracture movement data or pressure data in 3hr intervals from Sep 1st 2012 to Aug 31st 2013. Temperature correction of vibrating wire was automatically conducted and of pressure transducer was manually (piezometer) conducted using the linear gage factor provided by Geokon for each crackmeter or piezometer, respectively. A standard deviation of RST lower than 0.3 K for 24 h points to the existence of snow cover (Schmidt et al., 2009). The measurement period is divided into a “cooling” period ranging from Sept 1st 2012 until snow cover insulation starts, a snow cover period, a zero-curtain period and a “warming” period. We calculated 3hr fracture movement change and RST change for each period and performed a regression analysis using a 90 hour-window to show r^2 development. Additionally, we correlated the fracture movement change and the RST change for the measurement period and each seasonal period. Table 9.4 shows the block length and discontinuity aperture (crack length) at all crackmeters. The block size and the crack length are derived from geotechnical mapping by Halla (2013) or estimated from crackmeter photos (Fig. 9.10).

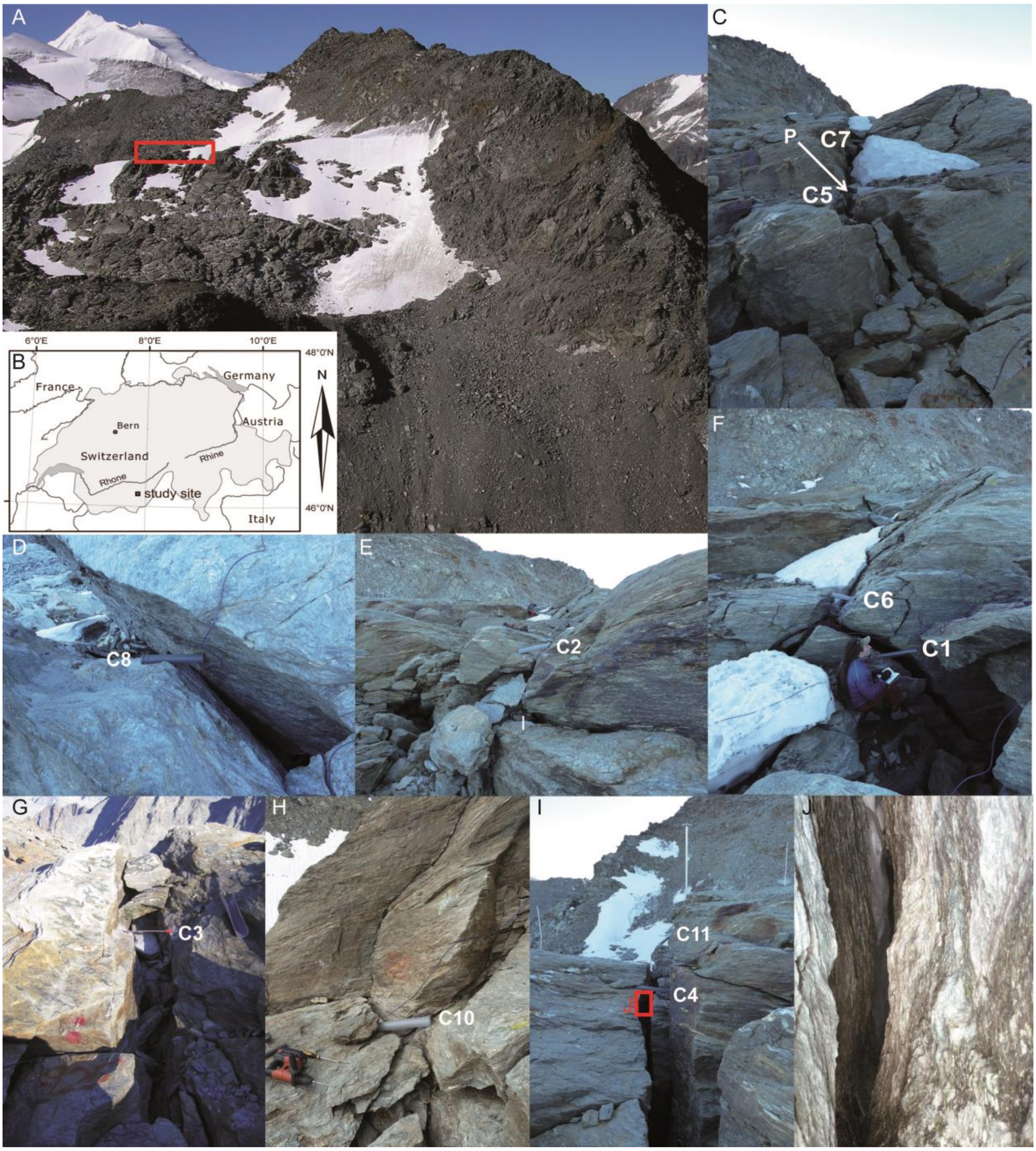

Fig. 9.10 A: View to Steintaelli catchment area located on crestline between Matter and Turtmann Valley, the red square shows the location of crackmeters on the crestline of the rock wall; B: study area location in Switzerland; C-I: Location of crackmeters (C1-C11) and piezometer (P) (F: see person for scale), red square shows location of an exemplary ice-filled fracture (J).

Thermal expansion can be calculated according to Equation 5.18. Since rock expands in all direction equivalently, Equation 5.18 can be transferred to express changes of length:

$$\alpha = \frac{\Delta L/\overline{L_b}}{\Delta RST} \quad (9.2)$$

where $\overline{L_b}$ is mean block length, ΔRST is change of rock surface temperature and ΔL is change of expansion (crack length). The mean block length at Steintaelli is shown in Table 9.4.

Table 9.4 Block length (L_b) and crack length (L_c) at crackmeter positions.

Crackmeter	Block length [m]			Crack length [m]
	south of crack	north of crack	mean	
C1	1.0 – 2.0	4.0 – 6.0	3.3	0.25
C2	1.5	6.0	3.8	0.1 – 0.2
C3	3.4	7.2	5.3	0.25
C4	3.0	5.0 – 6.0	4.3	0.3
C5	2.0	4.0	3.0	0.3
C6	1.0	2.0	1.5	0.3
C7	4.0 - 5.0	2.0	3.3	0.3
C8	5.0 - 6.0	3.0	4.3	0.1
C10	1.7	1.7	1.7	0.1
C11	1.0	3.0 – 4.0	2.3	0.2

9.3.3 Results

Figures 9.11 to 9.20 show measurements of rock surface temperature (RST), change of rock surface temperature (ΔRST), expansion, change of expansion (ΔExpansion) in 3h-intervalls and the correlation between ΔRST and ΔExpansion between Sep 1st 2012 and Aug 31st 2013. The mean annual rock surface temperature (MARST) ranged between -0.52°C (Crackmeter C10) and -4.47°C (Crackmeter C8) (Table 9.5). The snow-covered period is highlighted as light grey rectangle and the zero-curtain period as dark grey rectangle. The sum of both periods is the number of snow-covered days and ranged between 119 days for south-facing Crackmeter C11 and 312 days for Crackmeter C6. Except for the south-facing Crackmeter C11, all crackmeters recorded more than 250 snow-covered days larger than 250 and three crackmeters were covered more than 300 days by snow. This high number of snow-covered days results from the location of the crackmeters. All crackmeters were installed on the crestline and were affected by the massive snow cornice (Fig. 7.7 C-D).

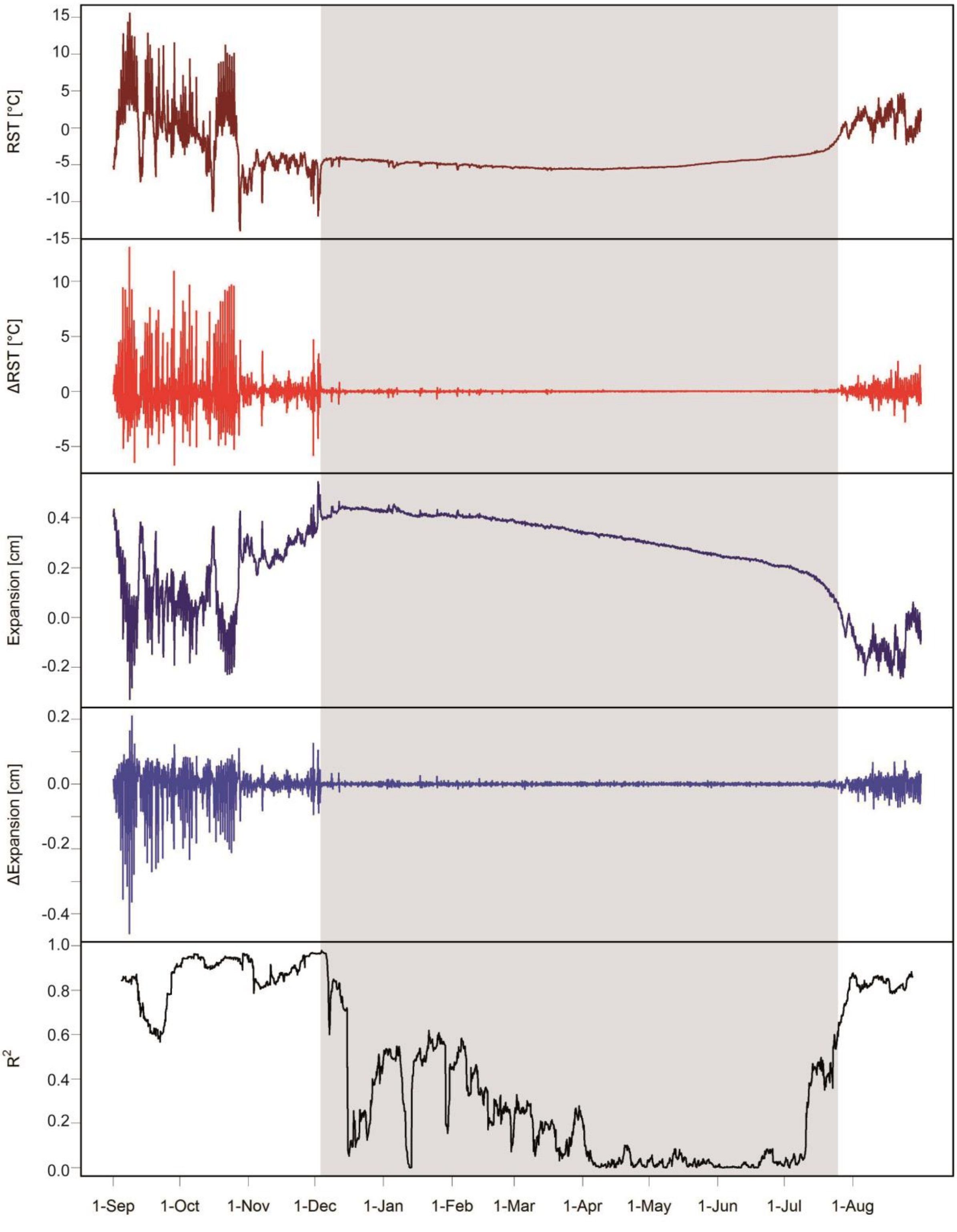

Fig. 9.11 Rock surface temperature (RST), change of rock surface temperature (ΔRST), expansion, change of expansion (ΔExpansion) in 3h-intervalls and the correlation between ΔRST and ΔExpansion between Sep 1st 2012 and Aug 31st 2013 measured at Crackmeter C1.

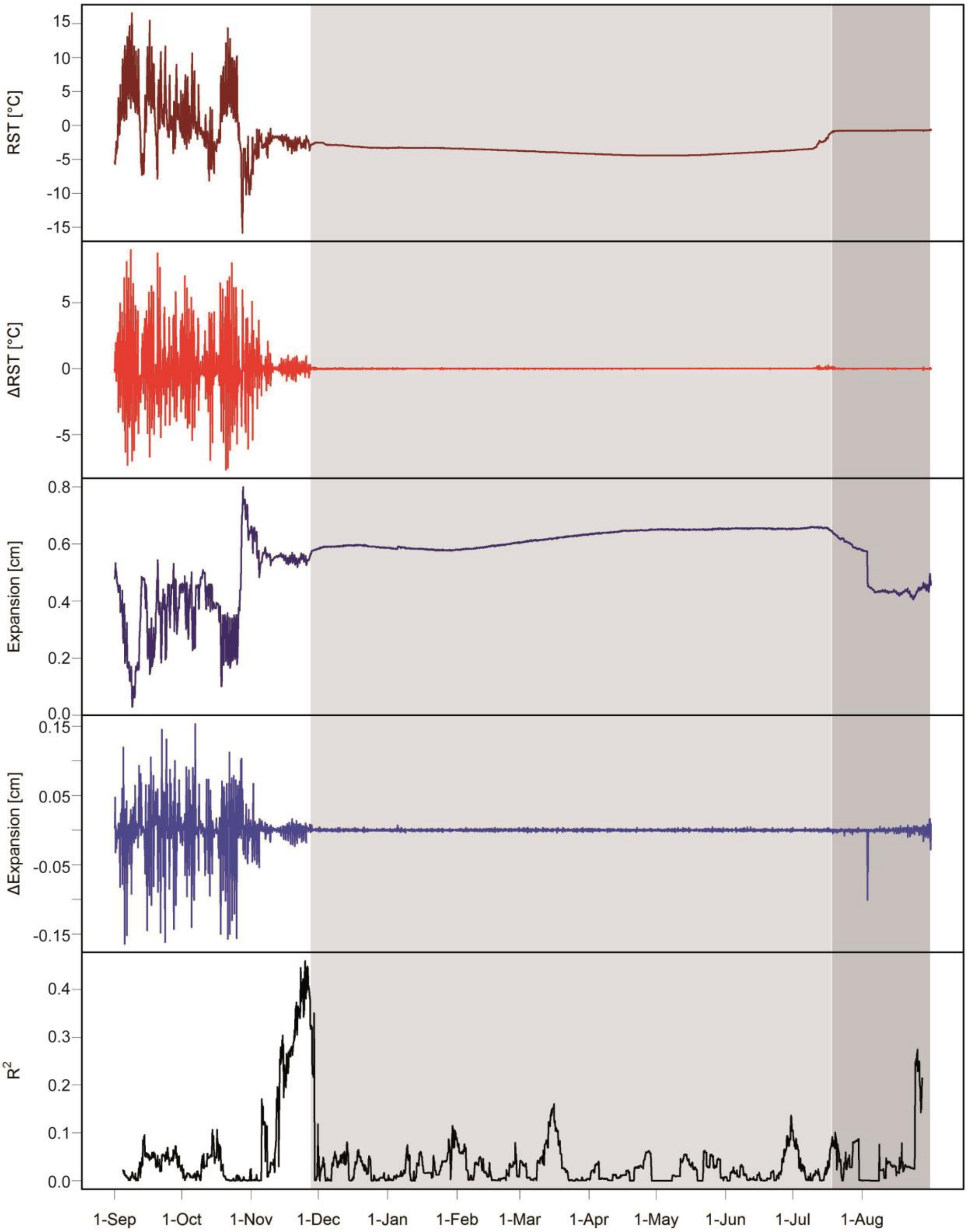

Fig. 9.12 Rock surface temperature (RST), change of rock surface temperature (ΔRST), expansion, change of expansion (ΔExpansion) in 3h-intervalls and the correlation between ΔRST and ΔExpansion between Sep 1st 2012 and Aug 31st 2013 measured at Crackmeter C2.

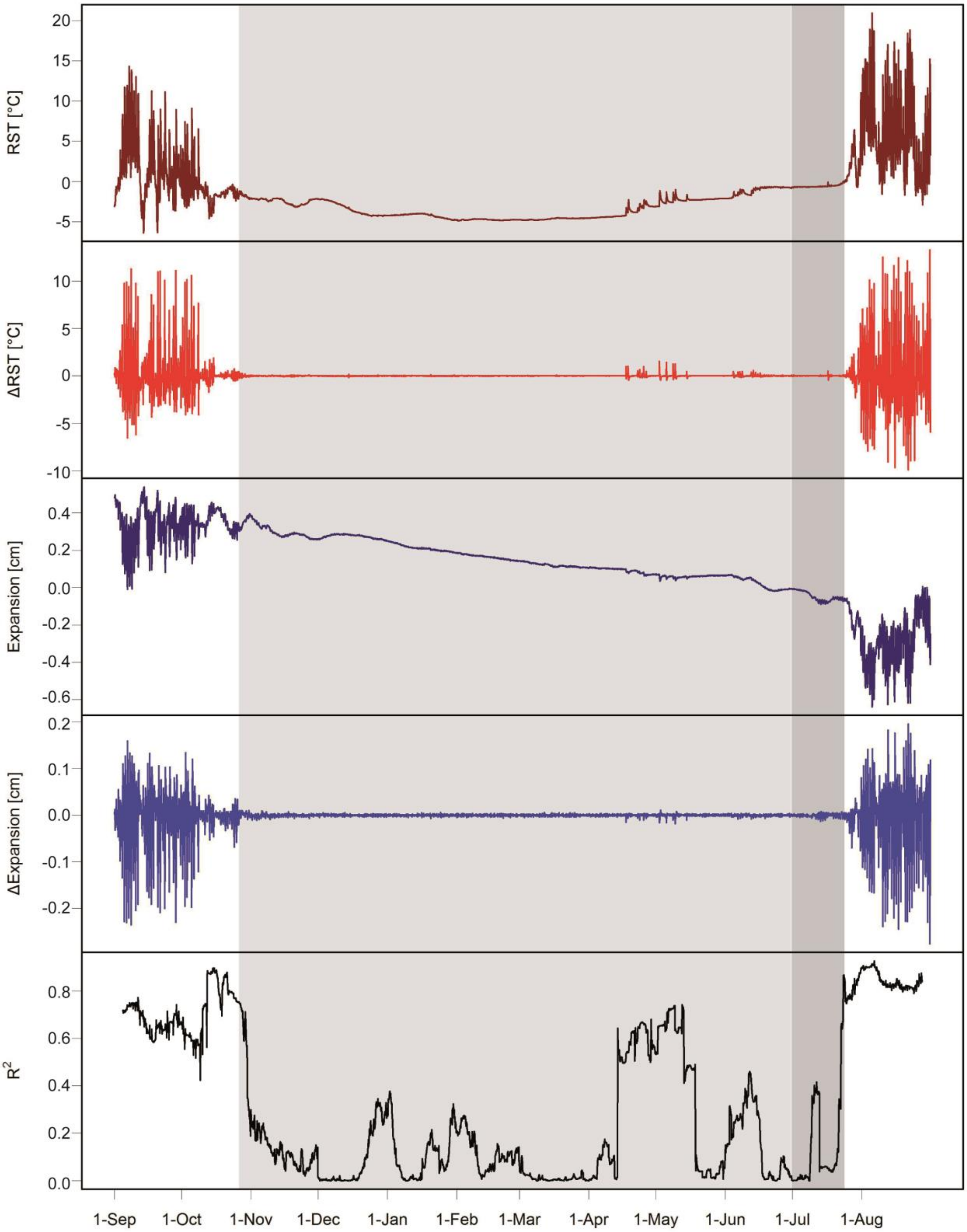

Fig. 9.13 Rock surface temperature (RST), change of rock surface temperature (ΔRST), expansion, change of expansion (ΔExpansion) in 3h-intervalls and the correlation between ΔRST and ΔExpansion between Sep 1st 2012 and Aug 31st 2013 measured at Crackmeter C3.

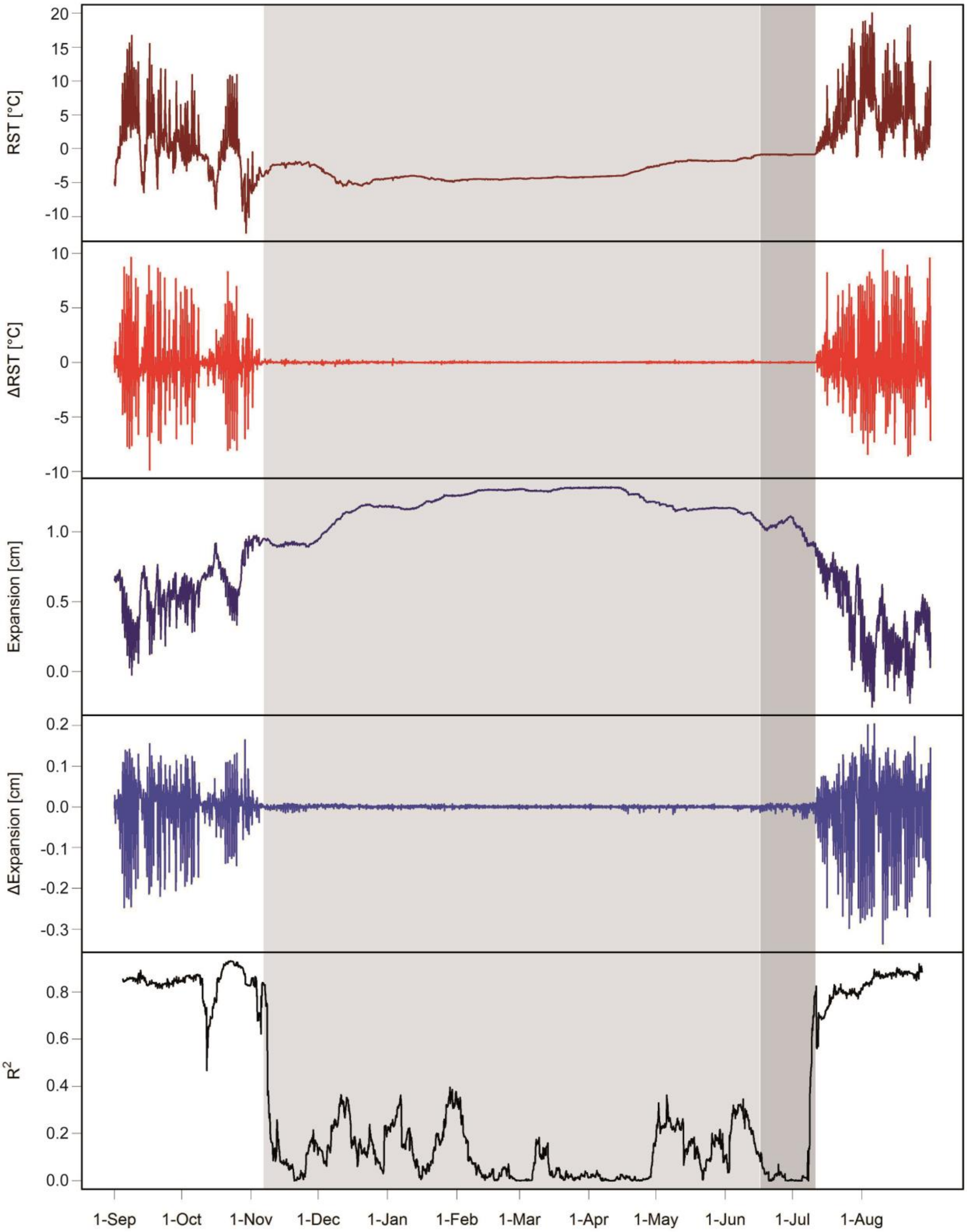

Fig. 9.14 Rock surface temperature (RST), change of rock surface temperature (ΔRST), expansion, change of expansion (ΔExpansion) in 3h-intervalls and the correlation between ΔRST and ΔExpansion between Sep 1st 2012 and Aug 31st 2013 measured at Crackmeter C4.

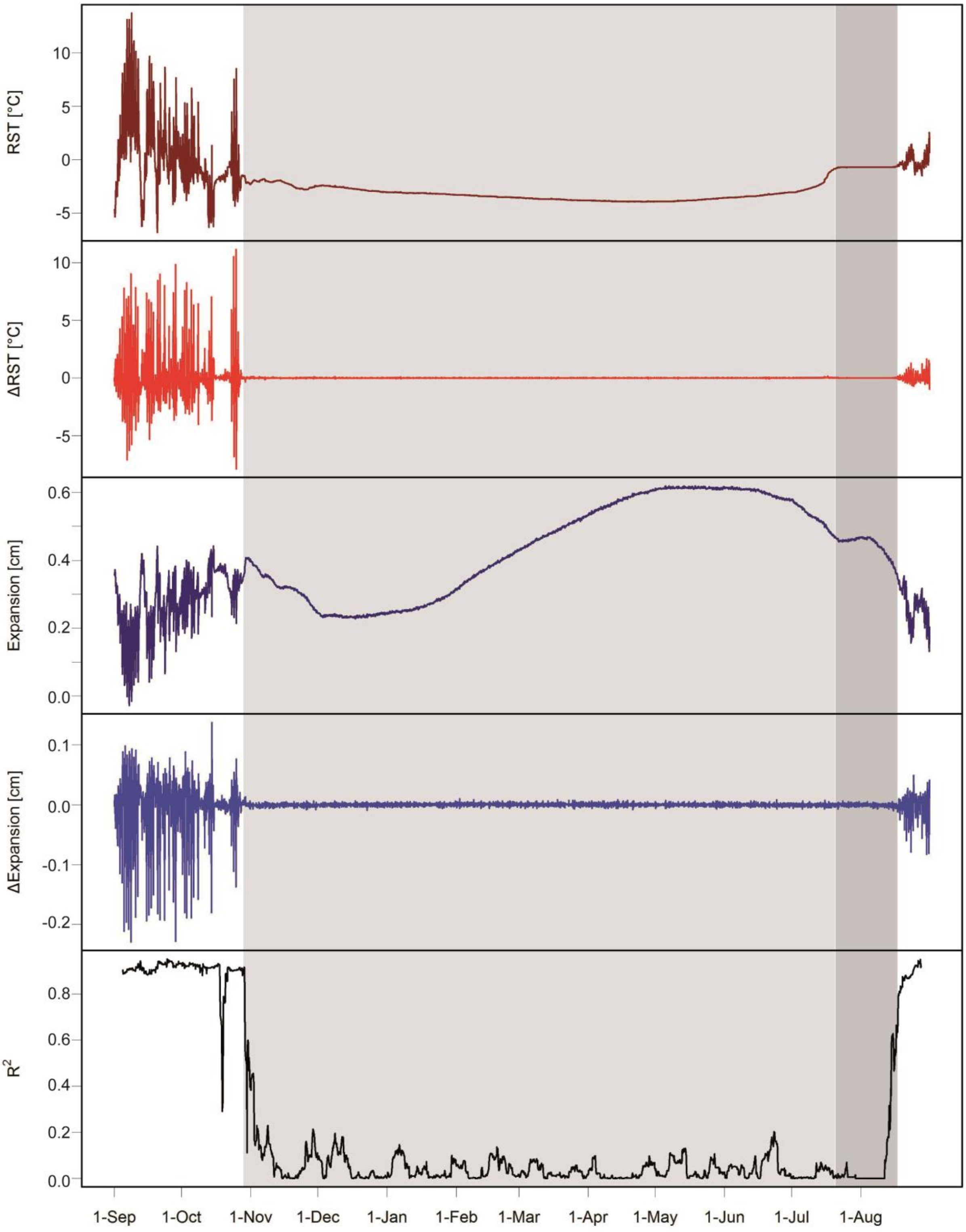

Fig. 9.15 Rock surface temperature (RST), change of rock surface temperature (ΔRST), expansion, change of expansion (ΔExpansion) in 3h-intervalls and the correlation between ΔRST and ΔExpansion between Sep 1st 2012 and Aug 31st 2013 measured at Crackmeter C5.

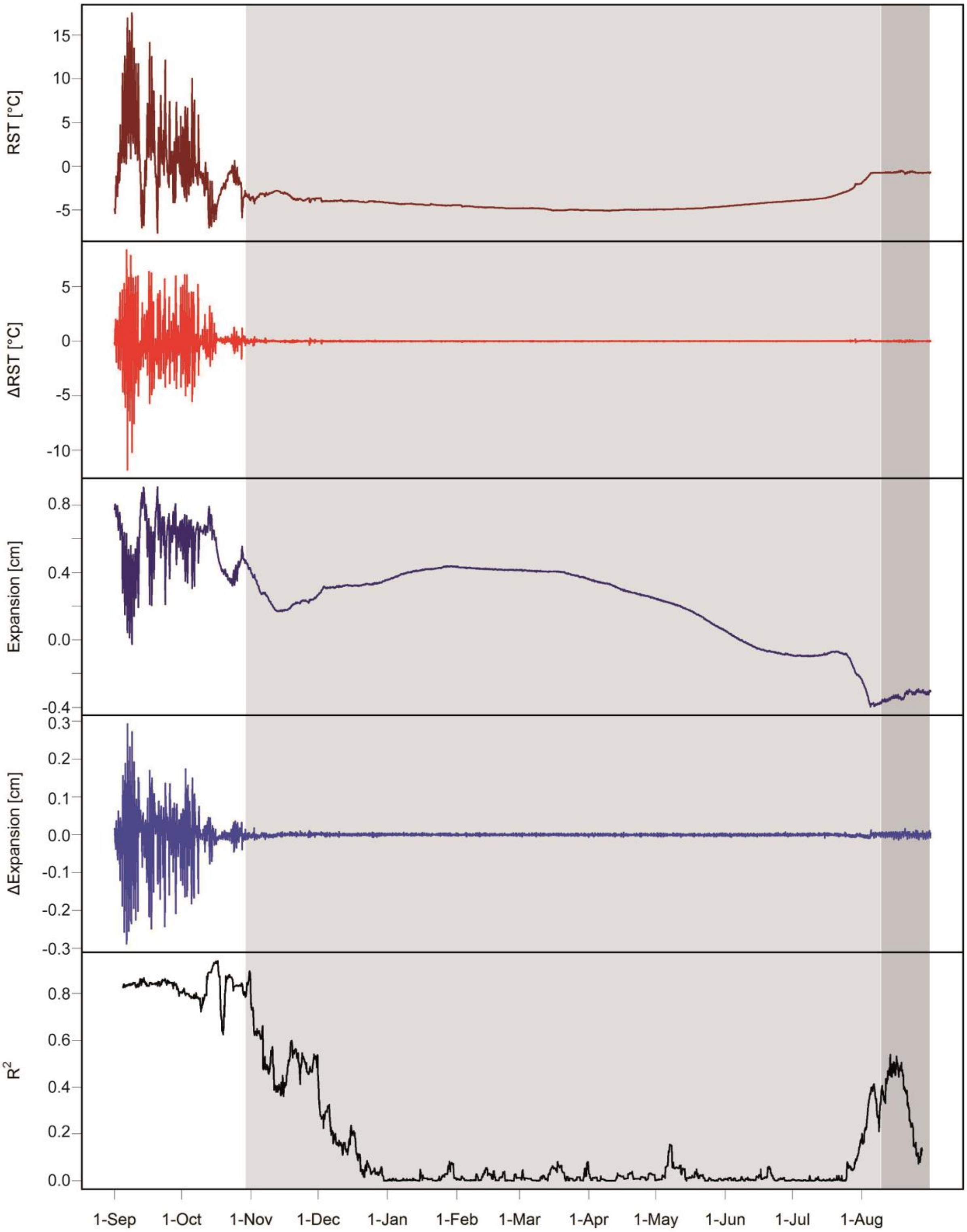

Fig. 9.16 Rock surface temperature (RST), change of rock surface temperature (ΔRST), expansion, change of expansion (ΔExpansion) in 3h-intervalls and the correlation between ΔRST and ΔExpansion between Sep 1st 2012 and Aug 31st 2013 measured at Crackmeter C6.

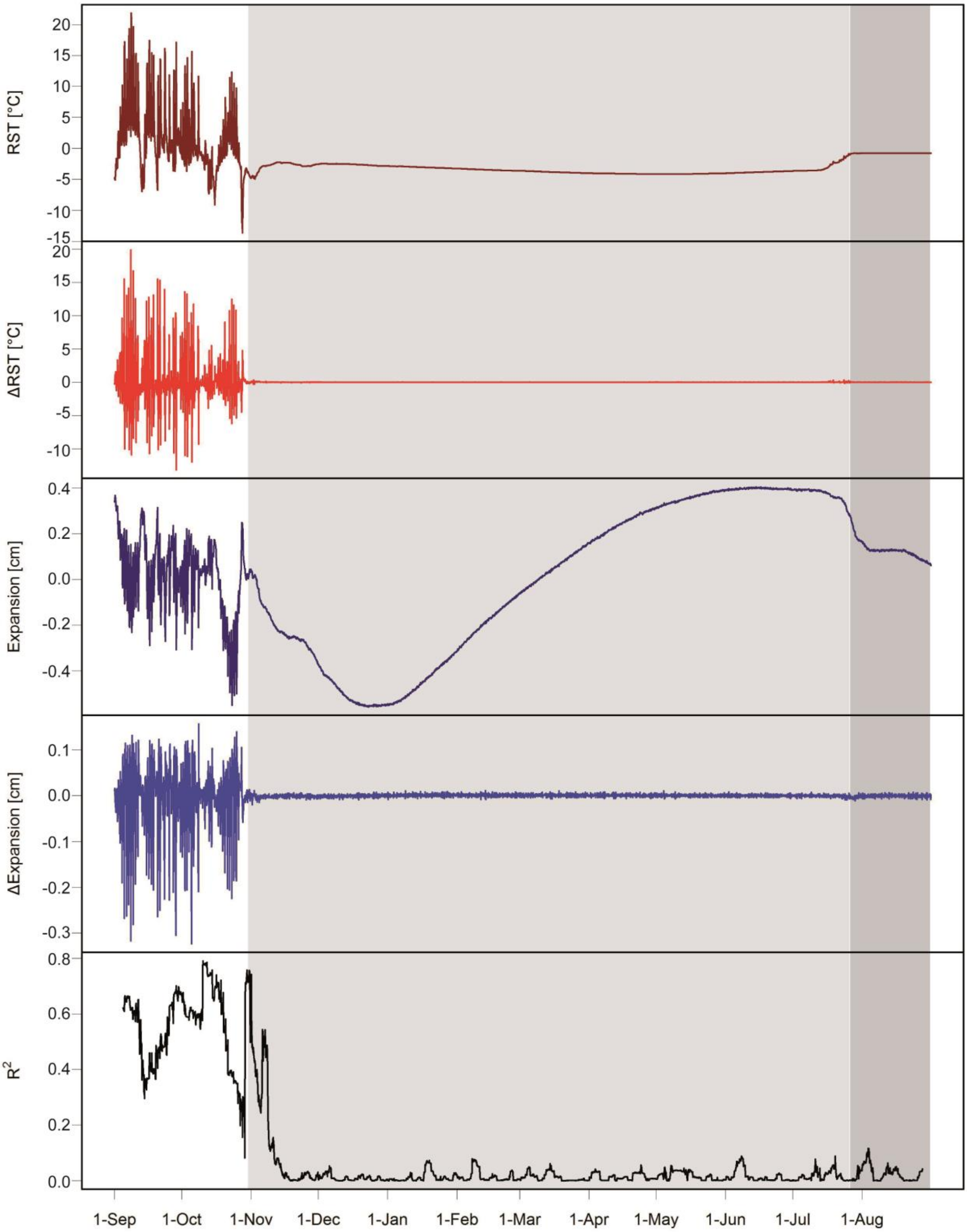

Fig. 9.17 Rock surface temperature (RST), change of rock surface temperature (ΔRST), expansion, change of expansion (ΔExpansion) in 3h-intervalls and the correlation between ΔRST and ΔExpansion between Sep 1st 2012 and Aug 31st 2013 measured at Crackmeter C7.

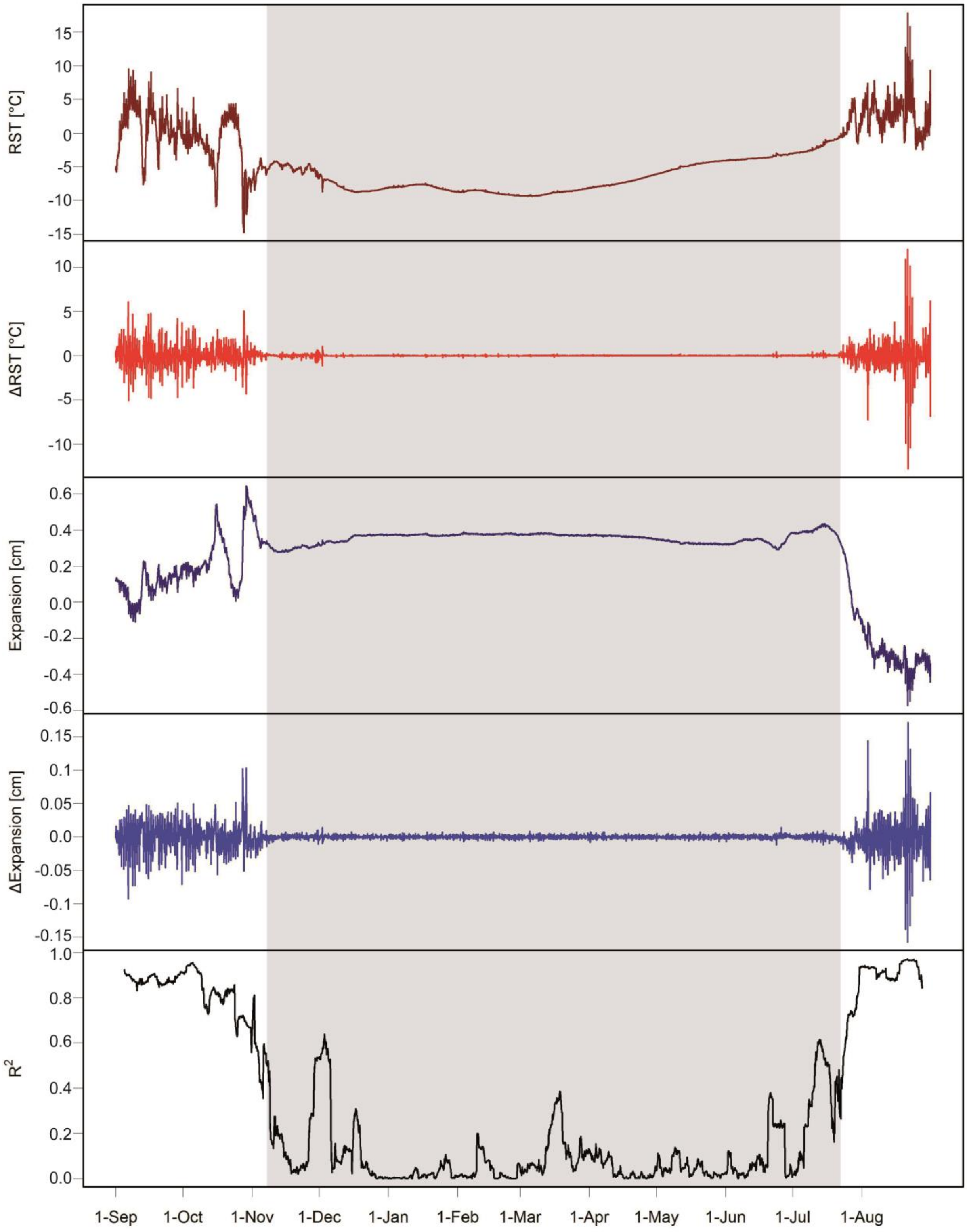

Fig. 9.18 Rock surface temperature (RST), change of rock surface temperature (ΔRST), expansion, change of expansion (ΔExpansion) in 3h-intervalls and the correlation between ΔRST and ΔExpansion between Sep 1st 2012 and Aug 31st 2013 measured at Crackmeter C8.

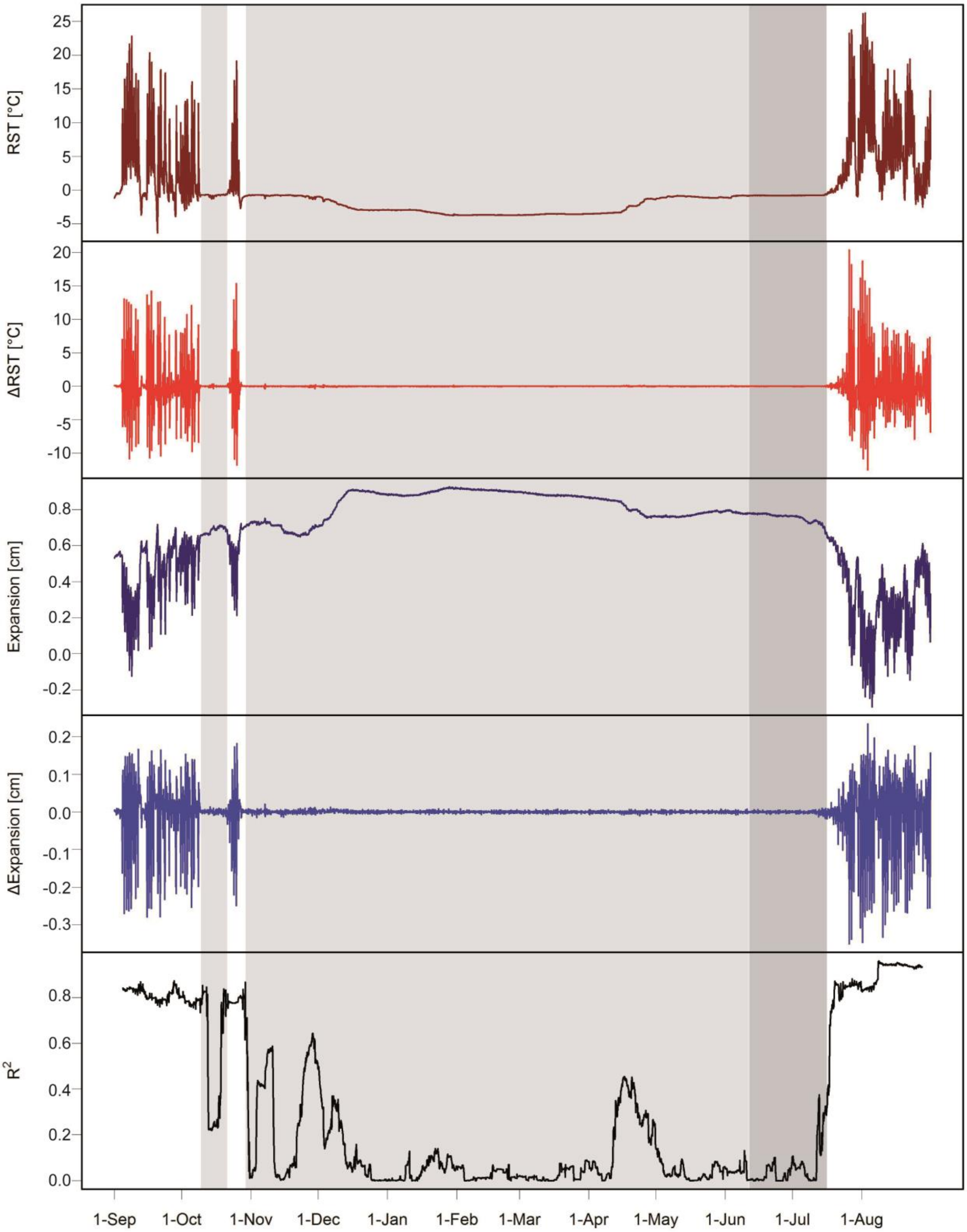

Fig. 9.19 Rock surface temperature (RST), change of rock surface temperature (ΔRST), expansion, change of expansion (ΔExpansion) in 3h-intervalls and the correlation between ΔRST and ΔExpansion between Sep 1st 2012 and Aug 31st 2013 measured at Crackmeter C10.

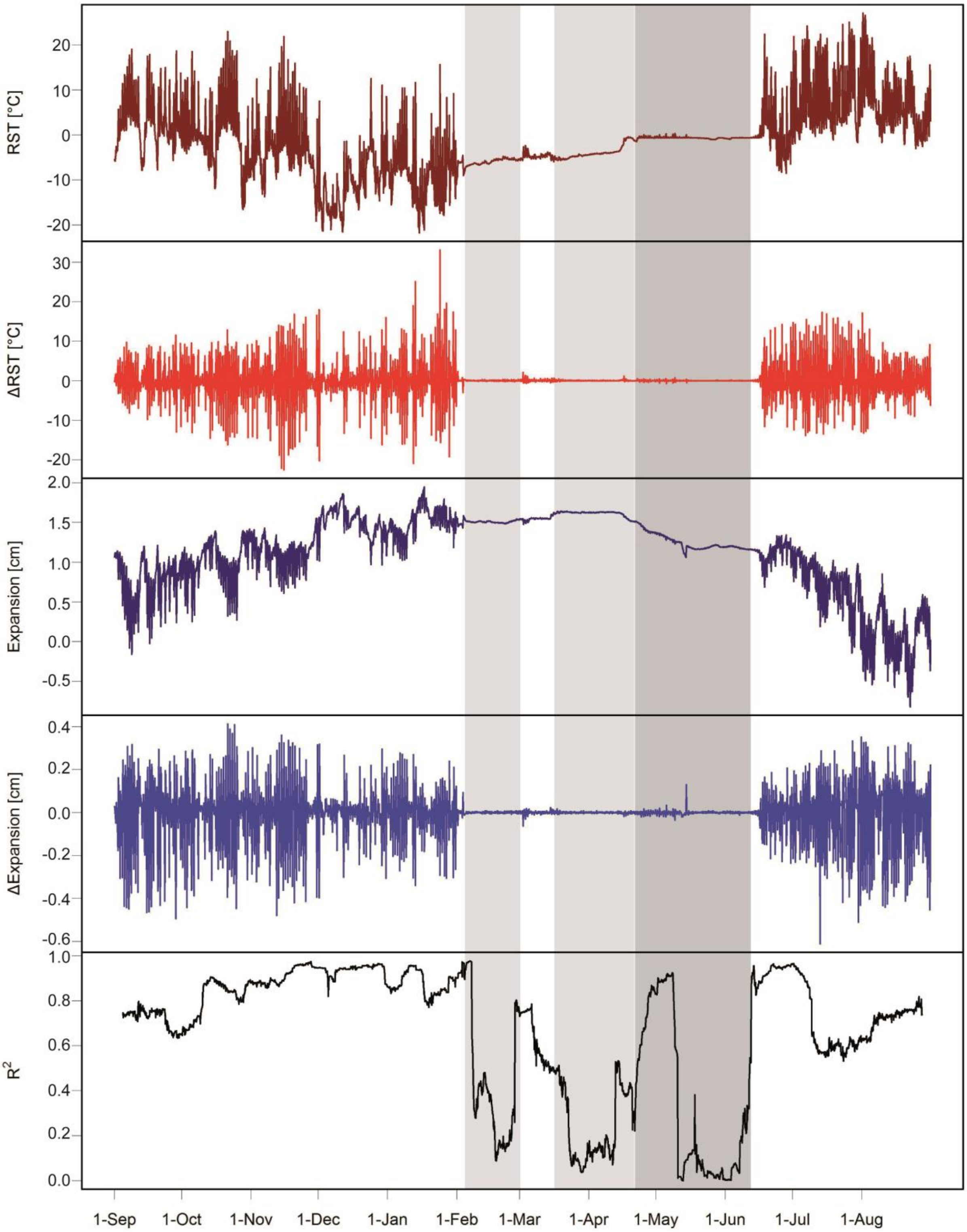

Fig. 9.20 Rock surface temperature (RST), change of rock surface temperature (ΔRST), expansion, change of expansion (ΔExpansion) in 3h-intervalls and the correlation between ΔRST and ΔExpansion between Sep 1st 2012 and Aug 31st 2013 measured at Crackmeter C11.

The snow-free period lasted until the end of October and the beginning of November 2012. Crackmeter C1 and C2 showed a snow cover period starting in December 2012. During the snow-free period high amplitudes of ΔRST and of ΔExpansion were observable at all crackmeters. Rock surface temperature ranged between 20°C and -15°C, except for south-facing Crackmeter C11, which was snow-free for more than 200 days and showed RST down to -20°C. Discontinuity expanded up to 2 cm (Crackmeter C11). At the end of October, five crackmeters (C1, C2, C4, C7, C8) measured a temperature decrease of up to -15°C and a coincident discontinuity opening of up to 0.7 cm. After this temperature drop, temperature increased again and discontinuities closed partially.

Table 9.5 Mean annual rock surface temperature (MARST), number of snow-covered days and correlation for whole measurement period, "cooling" period, snow-covered period, zero-curtain period and "warming" period for each crackmeter.

Crackmeter	MARST [°C]	Snow-covered days	R^2 of Δ Temperature and Δ Crack Movement				
			09/2012-08/2013	cooling	snow cover	zero curtain	warming
C1	-3.40	238	0.80	0.81	0.25		0.83
C2	-2.48	287	0.02	0.02	0.00	0.02	
C3	-1.69	270	0.75	0.66	0.22	0.05	0.84
C4	-1.52	250	0.83	0.84	0.11	0.01	0.84
C5	-2.40	305	0.85	0.88	0.04	0.02	0.88
C6	-3.27	312	0.82	0.83	0.17	0.27	
C7	-2.43	307	0.54	0.54	0.04	0.00	
C8	-4.47	257	0.84	0.82	0.11		0.90
C10	-0.52	283	0.82	0.80	0.17	0.19	0.86
C11	-1.48	119	0.64	0.73	0.30	0.17	0.54

During the snow-covered period RST remained continuously below 0°C due to snow isolation and remained in the frost-cracking window by Anderson (1998) or Hallet et al. (1991). The crackmeters showed no ΔRST and ΔExpansion. All discontinuities opened and/or closed during snow cover but the changes are slow; reflected by the 3h-resolution of ΔExpansion of crackmeters, which showed no changes. The opening of discontinuities was pronounced at Crackmeters C5 and C7 which opened up to 0.9 cm.

Eight crackmeters showed a zero-curtain period due to melting processes between two weeks (C4) and 2 months (C11). During the zero-curtain period Crackmeters C2, C4, C5, C7 and C11 showed a closing trend. The change of the expansion obtained in 3h-intervalls was close to zero, thus, discontinuities closed slowly. Only Crackmeter C2 recorded an abrupt discontinuity closing and Crackmeter C11 an abrupt discontinuity opening, which results in a sudden decreased or increased ΔExpansion, respectively.

Seven crackmeters were snow-free in the late summer 2013 and recorded a direct decrease of expansion after the end of the snow-covered period. The temperature increased as a result of missing snow cover isolation, this goes along with high amplitudes of both ΔRST and ΔExpansion.

Temperature changes caused thermal expansion and, if it occurs repeatedly, thermal expansion results in thermal fatigue (Hall and Thorn, 2014). To test the influence of thermal expansion, ΔRST and ΔExpansion are plotted for the whole period that comprises the “cooling” period ranging from September 1st 2012 to the beginning of snow cover, the snow cover period, the zero-curtain period and the “warming” period ranging from the end of snow cover or zero-curtain to the end of August 2013 (Fig. 9.21 and Table 9.5). The whole period show high ($r^2 > 0.5$) or very high ($r^2 > 0.75$) correlation except for Crackmeter C2 ($r^2 = 0.02$). During “cooling” and “warming” periods temperature changes are highly correlated with discontinuity opening or closing. No correlation between ΔRST and ΔExpansion exists during snow-cover period and zero-curtain period (Table 9.5).

The thermal expansion coefficient α is calculated using Equation 9.2 and plotted against RST (Fig. 9.22). In the whole RST range α is between 0 (Crackmeter 2) and -200×10^{-6}°C^{-1} (Crackmeter 11). Unusual positive and negative α are clustered at -1°C and between -3 and -6°C.

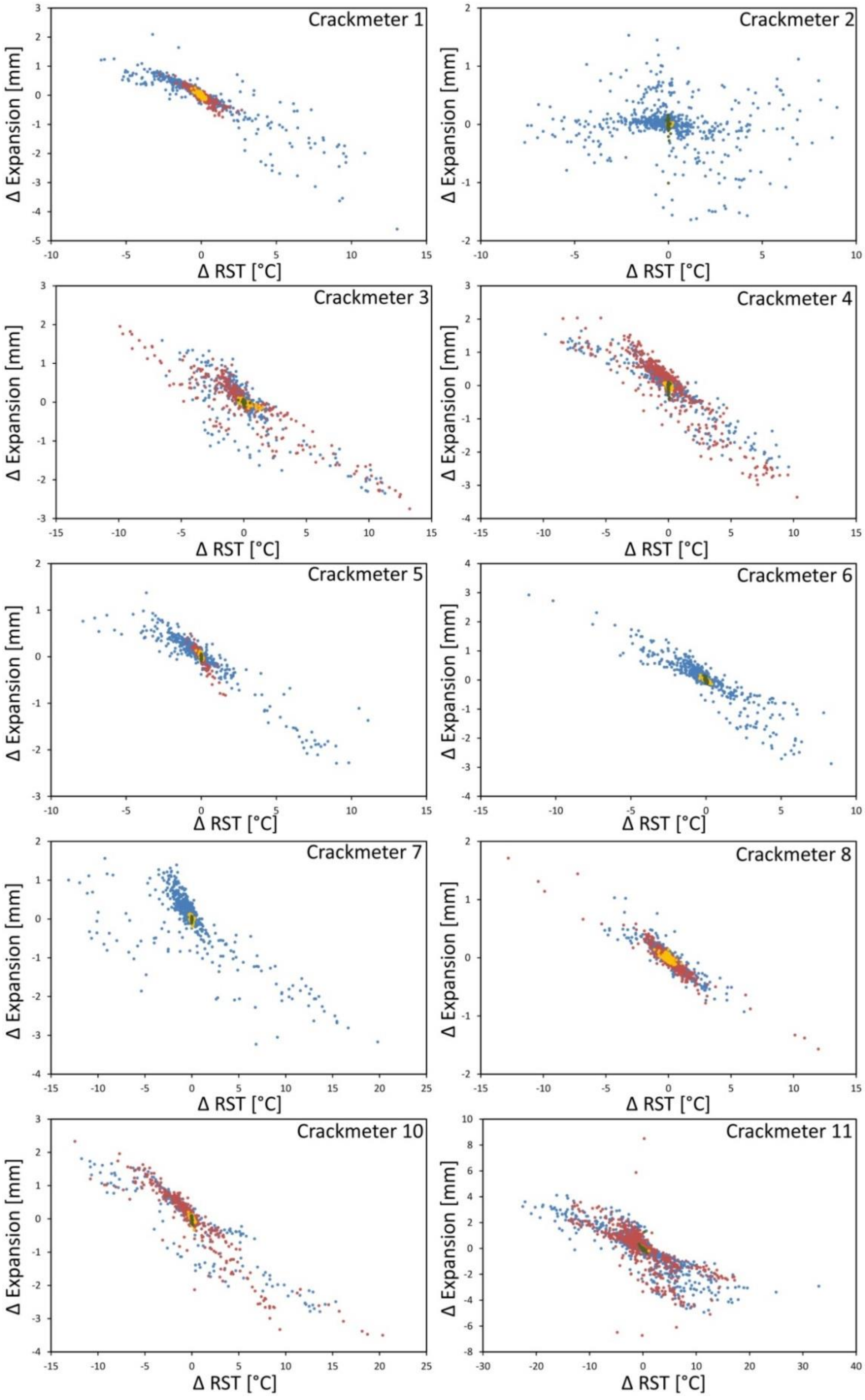

Fig. 9.21 Change of expansion plotted against change of rock surface temperature for “cooling” period (blue dots), snow-covered period (yellow dots), zero-curtain period (green dots) and “warming” period (red dots). The figure shows a negative correlation during the “warming” and “cooling” period.

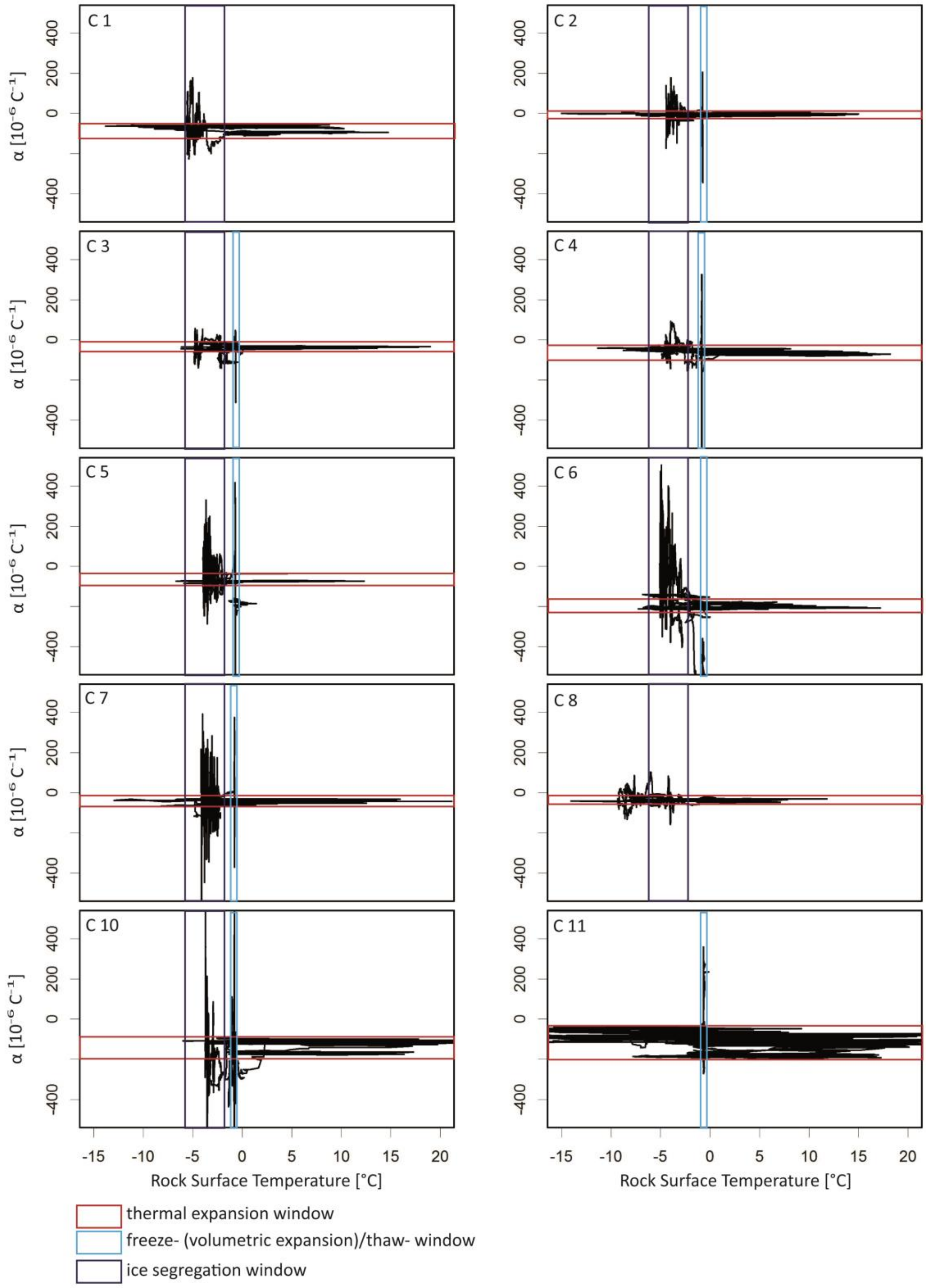

Fig. 9.22 Thermal expansion coefficient *α* plotted against rock surface temperature. The figure shows the thermal expansion window (red rectangle), freeze-thaw-window (light blue rectangle) and ice segregation window (dark blue rectangle).

9.3.4 Interpretation

Six different processes can cause discontinuity movements (Fig. 9.9). Given a constant gravity over time, a decrease of shear strength can result in movement of discontinuity (Fig. 9.9 A). In permafrost rock walls, a decrease of shear strength may have several reasons and can be attributed to ice creep and ice fracture, fracture of rock-ice contacts, reduced friction of rock-rock contacts and rock fracturing (Fig. 5.7) all sensitive to warming or thawing (Krautblatter et al., 2013). The differences of discontinuity aperture between Sep 1st 2012 and Aug 31st 2013 are low, whereas on daily scale, high-frequent opening and closings are currently much higher. As indicated by Krautblatter et al. (2013) shear strengths decrease due to warming or active-layer thawing which is a seasonal process. Therefore, discontinuity movement due to gravity and shear strength decrease is supposed to show a seasonal pattern with maximum movements during active-layer thawing period.

On the other hand, instability can be result of increasing shear forces. Cryostatic and hydrostatic pressure can vary on a seasonal and shorter time scale (Fig. 5.10 C). Hydrostatic pressure develops due to retaining of water (Fig. 9.9 B) in the discontinuities caused by an impermeable layer, e.g. permafrost. Snowmelt or summer rainfalls can deliver water and increase hydrostatic pressure. Since there is no data on summer rainfall, rainfall cannot be included in the analysis. In the future, rainfall measurements would be reasonable. An increase of hydrostatic pressure due to meltwater infiltration occurs when snow melts and snow melt is indicated as a zero-curtain effect. However, only Crackmeter C4 showed a minor opening of 0.1 cm during the zero-curtain period, which might be associated with a hydrostatic pressure increase. All other discontinuities installed with crackmeters closed during zero-curtain or at the beginning of the snow-free period. Even though hydrostatic pressure has the potential to cause discontinuity movement, as shown by as shown by Blikra and Christiansen (2014) at Jettan rockslide in Norway, in the Steintaelli hydrostatic pressure was likely not a driving factor for slope instability.

Thermal contraction and expansion occurs only during snow-free periods, when the isolating properties of the snow cover are absent. Thermal changes can result in ΔExpansion up to 0.7 cm within a 3hr-resolution, thus, the response time is fast. The change of expansion is higher at crackmeters with high ΔRST (C11) and high ΔRST is more pronounced at south-facing slopes, thus, thermal contraction and expansion occur with higher magnitudes on south-facing rock walls. Thermal expansion coefficients (Fig. 9.22) are negative because expansion is measured as a decrease of discontinuity aperture. Due to the use of Equation 9.2, thermal expansion coefficients are twice higher than α of rocks because the expansion or contraction of two blocks expressed as mean block length decrease or increase discontinuity aperture. Calculated α is one magnitude higher than observations in laboratory (Wegmann, 1998; Hall et al., 2008; Siegesmund et al., 2008) and needs to be calibrated on a laboratory scale. Mineral anisotropy results in different thermal contraction and expansion along c-axis of crystals, but the observed higher magnitude cannot be explained by mineral anisotropy alone. Pores of rocks in the Steintaelli can be filled by air, water and/or ice, but the effects of pore infill on thermal expansion are not yet investigated. Despite these shortcomings, the qualitative tendencies of the results are not affected. In order to use α quantitatively, a more accurate measurement of block size and laboratory calibration with different pore infills are necessary. Actually, the calculated values of α cannot be used in quantitative physical modelling, but the unusual increases of α can be used to show activity of processes as freeze-thaw processes and ice segregation.

Freeze-thaw processes can result in discontinuity movement (Fig. 9.9 F-H). A temperature decrease below the freezing point (freezing) or an increase above the freezing point (thawing) is necessary to freeze water or melt ice, respectively. The data of 8 out of 10 crackmeters demonstrates significant outliers of unlikely positive and negative thermal expansion coefficients at approximately -1°C (Fig. 9.22). Krautblatter (2009) observed a freezing point depression to -1°C at two rock samples from Steintaelli, thus, the outliers of unlikely positive and negative thermal expansion coefficients occur at the freezing point. Walder and Hallet (1986) assume that a high degree of saturation (>91 %) is necessary (Fig. 9.9 F) to build-up effective pressure due to volumetric expansion of ice (Fig. 9.9 G), however, Jia et al. (2014) demonstrated significant discontinuity opening at sandstone samples even with lower saturation. In mountain rock walls, Sass (2005) showed that rock moisture fluctuates between 0 and 100 % in the uppermost 15 cm in the pores. However, since there exists no comparable work on the fluctuation of water in discontinuities up to now, it can only be assumed that moisture fluctuates more frequently and to higher depths in discontinuities. High freezing rates are required to generate high cryostatic pressure, because they can prevent a cryostatic pressure decrease due to evaporation and ice extrusion (Davidson and Nye, 1985), ice expansion into free spaces or ice relaxation with time (Tharp, 1987). The crackmeter data demonstrated a fast temperature decrease down to -15°C (C1, C2, C4, C7, C8) in late October 2012, which went along with a coincident discontinuity opening. Since the correlation between ΔRST and ΔExpansion decreases at the timing of freezing point crossing at -1°C, the expansion might be caused by ice. The subsequent correlation increase indicates the occurrence of thermal contraction due to the temperature decrease which amplified the discontinuity opening.

The opposing process to freezing is thawing, which occurs at the freezing or thawing point. Snowmelt can transport advective heat into discontinuities and can erode rapidly ice, if the amount of heat is sufficient (Hasler et al., 2011a). As a result of ice erosion, cryostatic pressure decreases and discontinuity closes (Fig. 9.9 H). During zero-curtain effects, a slow closing of the discontinuities occurred, which might be consequence of slow occurring ice erosion and, thus, slow decreasing cryostatic pressure. Due to the slow response, thawing of ice due to conductive heat transport needs to be considered as a possible cause. Crackmeter 2 showed a sudden closing of discontinuities during snowmelt implying a fast acting process like ice-erosion.

Ice segregation is investigated on microcracks in the laboratory (Hallet et al., 1991; Murton et al., 2000; Murton et al., 2001; Murton et al., 2006) and can cause discontinuity movement in discontinuities with higher aperture (Fig. 9.9 I-J). The data demonstrates significant outliers of unlikely positive and negative thermal expansion coefficients in the temperature range between approximately -3°C and -6°C at nine out of ten crackmeters (Fig. 9.22). Discontinuity opened 0.4 cm and 0.9 cm at Crackmeters C5 (Fig. 9.15) and C7 (Fig. 9.17), respectively. In this same temperature range Hallet et al. (1991) observed 90 % of cracking events due to ice segregation on Berea Sandstone samples. Preconditions for ice segregation are sub-zero temperature gradient to cause a thermomolecular pressure gradient (Murton et al., 2006) and a unfrozen liquid water migration. RST ranged continuously between -3 and -6°C during the snow-covered period, thus, snow cover isolation enables the development of a relatively constant sub-zero temperature gradient. Unfrozen water exists at temperatures down to -10°C (Mellor, 1970) and negative temperature before snow isolation should led to development or growth of ice-filling in discontinuities. The ice develops cryostatic suction resulting in unfrozen water migration towards the ice body. Murton et al. (2000) observed negative pressure values (tension) during heaving periods as a result of ice segregation. The piezometer in the discontinuity below Crackmeter C7 observed a decreasing discontinuity pressure with decreasing discontinuity temperature (Fig. 9.23). In the middle of December 2012, the discontinuity pressure values turned negative at a discontinuity temperature of -1.5°C. The negative pressure values went along with the start of discontinuity opening observed at the crackmeter. The discontinuity temperature and the pressure measured by the piezometer decreased further down to -3.7°C and -1.25 kPa, while discontinuity opened 0.7 cm. With decreasing discontinuity temperature cryostatic suction increased, which resulted in negative discontinuity pressure. As a consequence water moved towards the ice body within the discontinuity, the ice body grew and, thus, the ice body developed an increasing cryostatic pressure. This increased cryostatic pressure was associated with the discontinuity opening.

In July 2013, the discontinuity temperature increased rapidly by 2°C from -3.5°C to -1.5°C (Fig. 9.23) while RST at C7 showed a zero-curtain effect (Fig. 9.17). Coincidently, piezometer pressure increased as a result of increasing discontinuity temperature. Cryosuction was reduced but still active, which is indicted by remained negative discontinuity pressure. The discontinuity closed rapidly (0.2 cm) during zero-curtain (Fig. 9.17) maybe due to ice relaxation and cryostatic pressure decrease (Fig. 9.9 J) as result of ice warming.

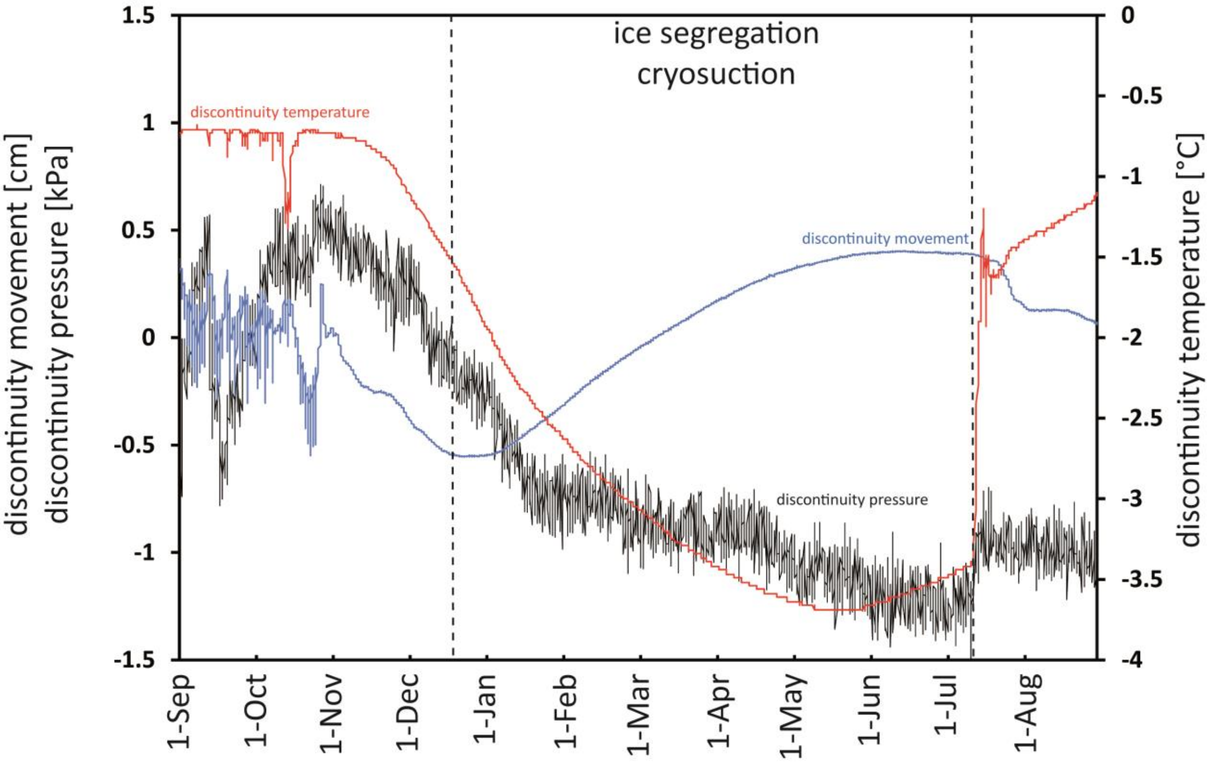

Fig. 9.23 Discontinuity movement of Crackmeter 7, discontinuity pressure and discontinuity temperature of the piezometer inside the discontinuity below Crackmeter 7 plotted against time for the period Sep 1st 2012 until Aug 31st 2013.

Wegmann (1998) introduced an ice-wedge process capable to open discontinuities (Fig. 9.9 K-L). During cold temperature periods, ice contracts more than rock due to higher thermal expansion coefficients, which results in a gap between ice and discontinuity wall. As a consequence, meltwater can infiltrate into this gap (Fig. 9.9 K), refreezes and enlarges the ice body. Therefore, this process is temporarily restricted to melting periods or rainfall events. During melting indicated by zero-curtain, Crackmeter C11 showed a sudden discontinuity opening up to 0.2 cm (Fig. 9.20) which might be implicated by ice-wedging.

9.3.5 Conclusion

Six different processes can cause discontinuity movements. There are evidences that might indicate movements as a result of gravitation, hydrostatic pressure and ice-wedging. More systematically, the data demonstrates three processes responsible for discontinuity movements. During snow-free periods, thermal expansion and contraction result in closing and opening of discontinuities up to 0.7 cm. This process is rapidly responding and highly dependent on ΔRST, which is more pronounced on south-facing rock walls due aspect and solar radiation. When temperature crosses the freezing point and the discontinuity is sufficiently water-saturated, volumetric expansion leads to an opening of discontinuities up to 0.6 cm. Volumetric expansion is rapidly responding and only effective in late autumn when no snow cover exists. Ice erosion is the rapidly responding counterpart to volumetric expansion, where ice is eroded by water and the melt energy of heat is transported by water. Ice segregation is a slowly running process, which is only active if temperatures are constantly below zero during snow cover. Cryosuction leads to migration of unfrozen water towards the ice infill inside the discontinuity. Ice segregation resulted in discontinuity opening of up to 0.9 cm and acts on a seasonal scale.

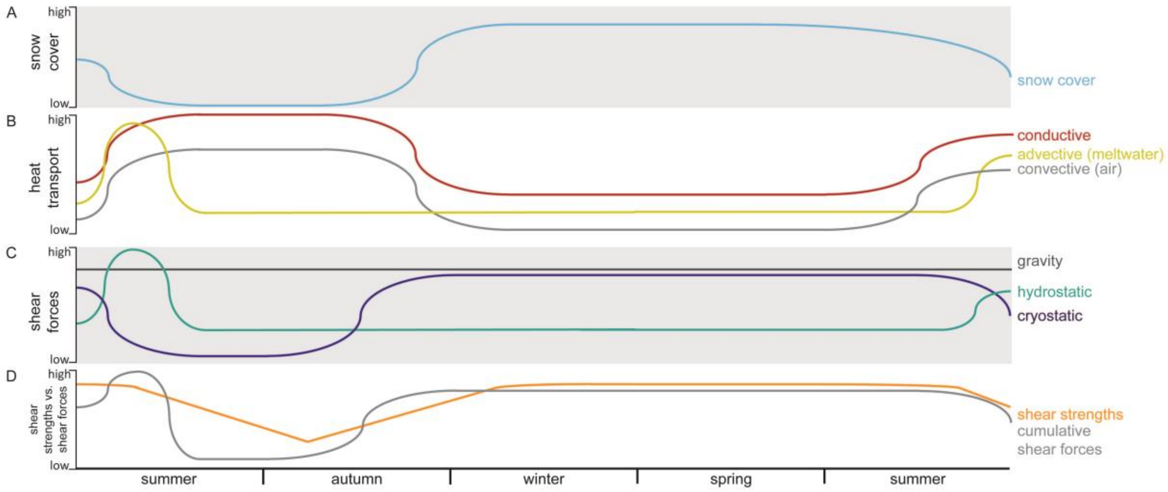

Fig. 9.24 Schematic illustration of development of A) snow cover, B) heat transport processes, C) shear forces, D) cumulative shear forces and shear strengths between summer 2012 and summer 2013.

Two critical time windows of instability can be identified (Fig. 9.24). In late autumn cryostatic pressure increases faster than shear strength due to freezing. Data confirmed this time window, five crackmeters show sudden opening of discontinuities due to volumetric expansion with coincident thermal contraction and this opening mostly preserved during winter.

The second time window occurs in early summer during snow melt. In 2013, this time window was delayed due to prolonged snow period. Cryostatic pressure and shear strengths decreases due to thawing and warming while hydrostatic pressure increases and lead to instability. Even though the data cannot confirm this time window at Steintaelli in 2013, Blikra and Christiansen (2014) observed a discontinuity opening due to hydrostatic pressure increase during snow melt at Jettan rockslide in Norway.

Due to ice segregation, cryostatic pressure increases and opens the discontinuities slowly, but continuously, despite coincidently high shear strengths exist due to frozen active-layer. Therefore, ice segregation has the potential to cause instabilities during winter.

9.4 Seasonal dynamics of rock decay

Weathering associated with freeze-thaw action and thermal changes are analysed in the following chapter. Frost weathering is distinguished into ice segregation and volumetric expansion. Frost cracking is synonymously used for ice segregation.

9.4.1 Methods

9.4.1.1 Volumetric expansion

Volumetric expansion of in situ water requires a high-saturated (> 91 %) rock (Walder and Hallet, 1986) and a high freezing rate (Matsuoka, 1990a) to avoid ice extrusion (Davidson and Nye, 1985; Tharp, 1987). Matsuoka (1990b, 2008) used the frequency of freeze-thaw cycles defined as cycle oscillating above and below 0°C to analyse the effect of volumetric expansion. This threshold was used to analyse rock temperature logger data. For logger location see Fig. 7.2.

9.4.1.2 Ice segregation

Ice segregation is analysed using a frost cracking model developed by Hales and Roering (2007). This model uses the mean annual air temperature (MAAT) and the annual temperature amplitude to calculate the location and the efficacy of segregation ice. The authors modelled the frost cracking activity and evaluated their model with location of scree slopes in the Southern Alps in New Zealand (Hales and Roering, 2005, 2009). MAAT was used as a proxy for MAGST. Krautblatter and Draebing (2014) replaced mean annual air temperature with MAGST (synonymously MART) in Eq. 8.20 (Eq. 8.19 herein). The model calculates rock temperature in a 1 cm-resolution in depths down to 20 m based on conductive heat transfer. Hales and Roering (2007) assume three criteria for ice segregation. (1) A temperature window with enhanced frost cracking ranging from -3°C to -8°C was observed by Hallet et al. (1991) using acoustic emission measurements in the laboratory on Berea Sandstone samples. (2) Water availability is given in a temperature range larger than 0°C, potential water sources are from the surface (top) by percolating meltwater or from aquifers (bottom) by ascending groundwater. Hales and Roering (2007) defined water availability by groundwater if temperature in 20 m depth is positive. Ice segregation occurs if a negative temperature gradient occurs (Hales and Roering, 2007). In theory, the growth of segregation ice is controlled by temperature and water availability. A steeper negative temperature gradient increases water transfer towards the freezing front (Worster and Wettlaufer, 1999) while the amount of available water influences ice lens growth (Wettlaufer and Worster, 1995). Walder and Hallet (1985) assume a strong relationship between growth rate of ice and frost cracking intensity, thus, Hales and Roering (2007) used the annual sum of the temperature gradient as a proxy for frost cracking intensity. Temperature logger data is used as model input (Table 8.4). To analyse frost cracking activity, days spend in the frost cracking window are calculated according to Anderson (1998).

9.4.1.3 Thermal stresses

Hall and Thorn (2014) distinguish thermal weathering into thermal shock and thermal fatigue. To analyse thermal shock, a high temporal resolution (one minute or lower) of temperature is necessary to evaluate crossing of the threshold of ≥2°C min^{-1} suggested by Richter and Simmons (1974). The data loggers record temperature with a temporal resolution of 2 h, thus, the resolution is insufficient to analyse thermal shocks. Thermal fatigue is produced by repeated temperature changes and subsequent stresses (Hall and Thorn, 2014) and is evaluated qualitatively based on temperature logger records.

9.4.1.4 Efficacy of weathering on rock strength

Weathering affects the strength of rock. To analyse the efficacy of near surface weathering caused by thermal stresses or freeze-thaw processes, rock strength is measured with a Schmidt hammer (L-type). The use of Schmidt hammer is common in studies focusing on rock strength and weathering (Goudie, 2006; Viles et al., 2011). Schmidt hammer results are incorporated in rock mass strength classification systems (Barton and Choubey, 1977; Selby, 1980; Bieniawski, 1987). Rock strength was measured along the geophysical Transects T1, T5 and T9 by Halla (2013) in 2012 and along Transects T1 and T3 by the author in 2013. Data by Halla (2013) is reanalysed; rebound values (R-values) of the Schmidt hammer are analysed according to the method by Barton and Choubey (1977). From the five highest R-values of 10 Schmidt hammer measurements at each measuring point R-values are corrected according to Schmidt hammer angle (Barton and Choubey, 1977); mean value and standard deviation are calculated. Uniaxial compressive strength σ_c (UCS) is calculated using the formulae by Deere and Miller (1966):

$$\sigma_c = 9.97\ e^{0.02*R*\rho} \tag{9.3}$$

where R is the rebound value of the Schmidt hammer and ρ is the density of the rock. The density for Schisty quartz slate and Quartz slate is assumed to be 2600 kg m^{-3} according to Wohlenberg (2012).

9.4.2 Results of rock decay

9.4.2.1 Volumetric expansion

Table 9.6 and Fig. 7.5 present the number of freeze-thaw cycles of temperature loggers. For loggers with a complete data set, number of freeze-thaw cycles ranges from 8 (Logger S5) to 159 (Logger C3).

Table 9.6 Number of frost cycles of all loggers between September 2012 and August 2013.

Month/ Logger	2012				2013								total
	Sep	Oct	Nov	Dec	Jan	Feb	Mar	Apr	May	Jun	Jul	Aug	
N8	NA	NA	0	0	0	0	0	0	0	0	0	4	4
N7	NA	NA	0	0	0	0	0	0	0	0	0	13	13
N6	15	4	0	0	0	0	0	0	0	0	0	16	35
N5	17	17	0	0	0	0	0	0	0	0	4	13	51
N4	11	17	0	0	0	0	0	0	0	0	1	10	39
N3	11	19	0	0	0	0	0	0	0	3	1	3	37
N2	9	21	0	0	0	0	1	21	0	6	1	0	59
N1	8	19	0	0	0	0	0	0	0	0	1	0	28
C1	8	19	13	0	0	0	0	0	0	0	0	0	40
C2	4	8	18	4	10	0	0	0	0	2	0	0	46
C3	6	15	24	6	15	7	20	23	26	15	0	2	159
C4	5	9	18	6	1	0	0	0	0	2	1	0	42
S1	4	7	13	0	0	0	0	0	0	7	NA	NA	31
S3	6	12	25	1	0	0	0	0	0	7	0	1	52
S4	7	14	24	1	0	0	0	0		3	1	2	52
S5	2	4	0	2	0	0	0	0	0	0	0	0	8

Matsuoka (2008) measured 10 to 50 frost cycles at north-facing and up to 150 frost cycles at south-facing rock walls in the Corvatsch area in comparable altitude between 1994 and 2006. In Steintaelli, two peaks of freeze-thaw cycles are visible; one peak in autumn 2012 and one in summer 2013; thus, freeze-thaw cycles are short-term and occur with high frequency two times a year. Between the two peaks most loggers are covered by snow. Logger C3 is snow-free the whole period and 159 freeze-thaw cycles are counted. In spring 2013, only the Loggers C3 and N2 are snow-free and showing an additional peak of frost-cycles (Fig. 7.5). Snow cover and temperature amplitude seem to control the amount of number of freeze-thaw cycles (Matsuoka et al., 1997). The amount of snow-covered days restricts the number of freeze-thaw cycles. At north-facing loggers temperature amplitude is smaller than at south-facing loggers resulting in lesser freeze-thaw cycles due to a longer period without positive temperatures in autumn and winter 2012 (Fig. 7.4). Temperature drops seldom from positive GST to GST lower than -3°C and these drops occur 2 or 3 times in September and October 2012.

9.4.2.2 Ice segregation

Inside the temperature window ranging from -3 to -8°C frost cracking is enhanced. The result of the heat transfer model is shown in Fig. 8.23 and in Fig. 9.25. The frost cracking window is emphasised by dotted lines or grey rectangles, respectively. The analytical model based on conductive heat transfer suggests permafrost existence on the north-facing crestline and the NE-slope and, in contrast, non-permafrost areas on the south-facing crestline and SW-slope. Loggers in permafrost rock walls (Fig. 9.26 B) show a higher number of days spend in the frost cracking window than logger in permafrost-free rock wall (Fig. 926 D). The frost cracking window reaches higher depths (more than 5.5 m) in permafrost rock walls than in permafrost-free rock wall (less than 4.5 m). From October 2012 to March 2013 the frost cracking window is present at all loggers. Loggers N3 and N4 show a year-long frost cracking window below 9.5 m or 11 m depth, respectively.

Water availability and a negative temperature gradient restrict ice growth. In permafrost areas of the rock wall, water is only available from the top during thawing of the active-layer in summer (Fig. 8.23). The temperature at 20 m depth is always below 0°C preventing water transfer according to the model (Fig. 9.25). The water restriction results in low frost cracking activity (less than 2.3°C/cm; Fig. 9.26 A). Peaks of frost cracking activity lie in depth between the surface (Logger N5 and N6) and 2.5 m (Logger N2 and N3). In permafrost-free parts of the rock wall, water is available from the surface when the surface is unfrozen from spring to the end of summer (Fig. 8.23). Freezing penetrates to depth between 4 and 13 m between October and March (Logger S5), May (C3, C4, S4), June (S3) or August (C2) (Fig. 8.23). Due to the non-existence of permafrost, water is available from groundwater at 20 m depth the whole year (Fig. 9.25). Negative temperature gradients exist only during the time of freezing. From April on during the freezing period water is available from the top by melting of snow or frozen rock and from the groundwater (Fig. 8.23). The high water availability results in high cracking intensity up to 2.75°C/cm (Fig. 9.26 C). Peaks of high frost cracking intensity are located near the surface between surface and 1 m depth.

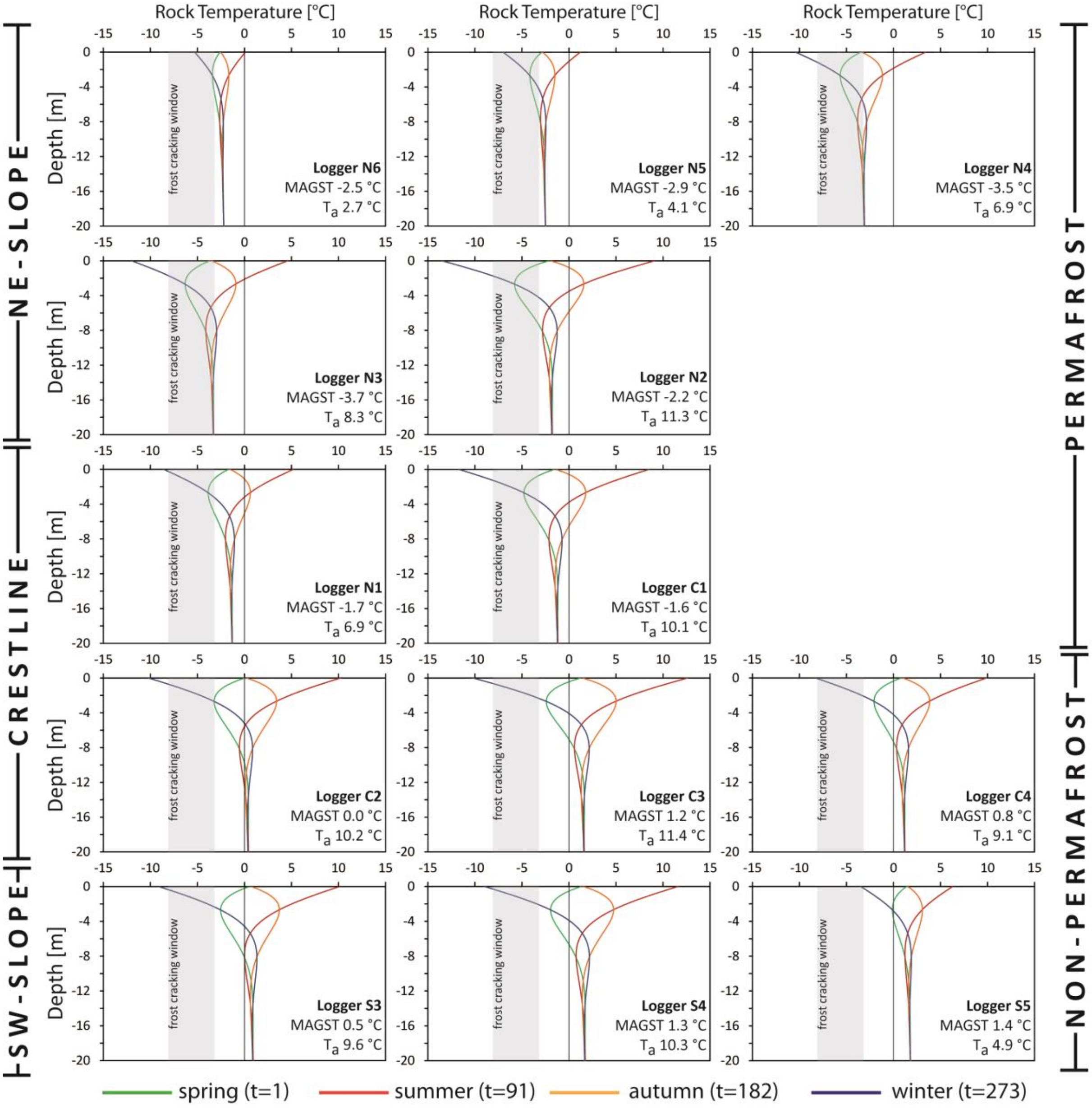

Fig. 9.25 Temperature profiles derived from conductive heat transfer-model in spring, summer, autumn and winter. Frost cracking window is indicated by a grey rectangle.

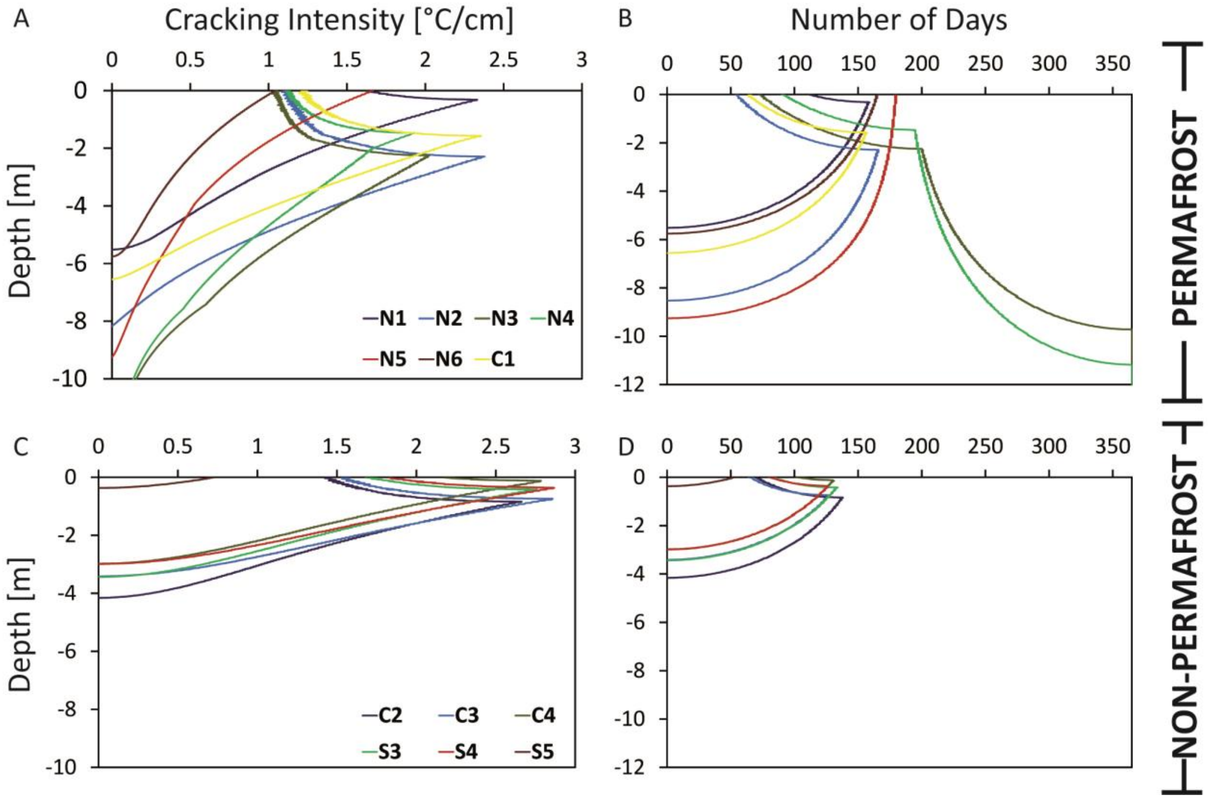

Fig. 9.26 Cracking intensity plotted against depth for logger in permafrost rock wall (A) and non-permafrost rock wall (C). Number of days spend in the frost cracking window for logger in permafrost rock wall (B) and permafrost-free rock wall (D).

9.4.2.3 Thermal fatigue

Thermal fatigue results from repeated temperature changes and subsequent stresses (Hall and Thorn, 2014). Daily temperature changes are high-frequent during snow-free periods (Stage IV) and are “switched-off” by snow cover (Stage I-III; Fig. 7.4). South-exposed loggers show higher temperature amplitude reflecting higher temperature changes than north-facing loggers.

9.4.2.4 Rock strength

Mean R-values and calculated mean UCS-values are presented in Fig. 9.27. On the NE-slope, most R-values range between 30 and 60. The crestline shows slightly higher R-values. On the SW-slope, R-values range between 18 and 40, except Transect 9, which shows no R-value decrease. Standard deviation is between 0.64 and 6.48; positive and negative least standard deviation (LSD) is presented as an error bar in Fig. 9.27. UCS values range from 50 to 200 MPa on the NE-slope. On the crestline, UCS-values are slightly higher. On the SW-slope, UCS-values range from 25 to 80 MPa except in Transect 9 which shows no UCS-value decrease. Standard deviation is between 1.4 and 58.0 MPa; positive and negative LSD is presented as an error bar.

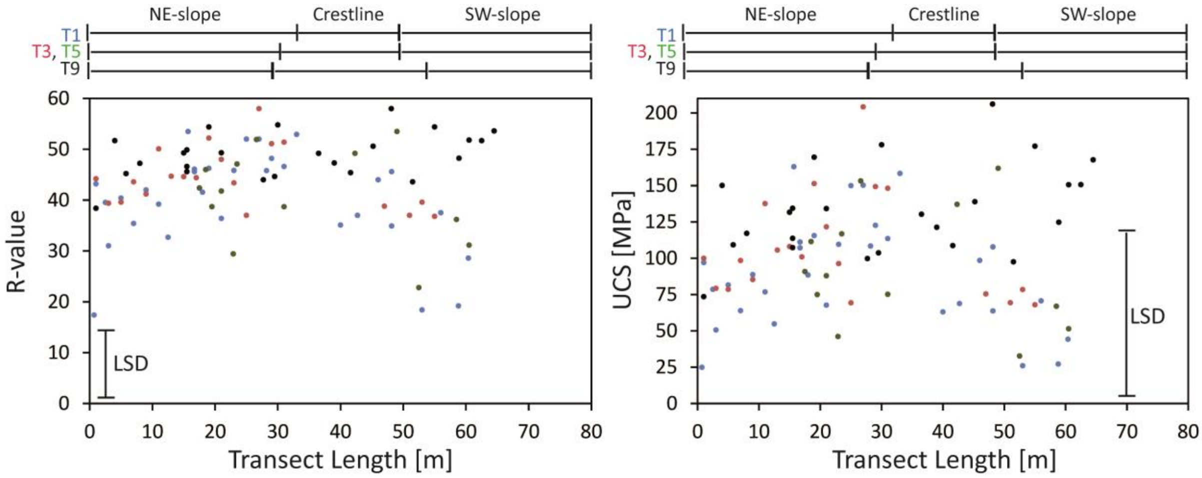

Fig. 9.27 Mean R-values and mean uniaxial compressive strength (UCS) plotted against transect length for Transect 1 (blue dots), Transect 3 (red dots), Transect 5 (green dots) and Transect 9 (black dots). LSD indicates least standard deviation.

9.4.3 Discussion

9.4.3.1 Volumetric expansion

Rock temperature is measured at 10 cm depth, thus, the number of freeze-thaw cycles is lower than at the surface. Matsuoka (2008) observed a reduction of approximately 30 % of freeze-thaw cycles in 10 cm depth compared to the surface in different rock walls of comparable altitude and different lithologies in the Corvatsch area between 1994 and 2006. It can be assumed that the number of frost cycles in the Steintaelli may be underestimated by 30 %. The freeze-thaw cycle definition used here does not incorporate freezing point depressions because not all rock freezes at 0°C. Krautblatter (2009) observed a freezing temperature depression of 0.9 to 1.1°C at rock samples from Steintaelli. Matsuoka (1990b; 1991) introduced an effective freeze-thaw cycle where temperature has to drop below a threshold of -2°C and increase above +2°C. The number of effective freeze-thaw cycles is only two third of the freeze-thaw cycles (Matsuoka, 1990b; Matsuoka, 1991), thus, the number of frost cycles in the Steintaelli might be overestimated. McGreevy and Whalley (1982) introduced a thermal threshold of -3°C and argued about the significance of moisture content (McGreevy and Whalley, 1985). The threshold of -3°C is crossed 2-3 times in September and October 2012. High freezing rates are required to induce high pressures. Short-term freeze-thaw cycles seldom penetrate 15 cm depth to high-saturated areas (Sass, 2003) and rock moisture fluctuates between 0 and 100 % in the uppermost 15 cm (Sass, 2005a), consequently, preconditions for volumetric expansion are seldom fulfilled. If preconditions are fulfilled, volumetric expansion possesses the potential to release low-volumetric rock particles. Water, which not freezes instantaneously, is pushed away from the freezing front (Sass, 2004). As shown by Sass (2005a) rocks are wetter in summer than in winter, thus, freeze-thaw events during winter are probably ineffective. South-exposed loggers in Steintaelli show more freeze-thaw cycles. South-facing rocks are generally less moist than north-facing rocks (Sass, 2005a), thus, higher frequent freeze-thaw cycles may not result in higher frequent volumetric expansion. Matsuoka et al. (1997) and Matsuoka (2008) measured short-term freeze-thaw penetration up to 50 cm depth, thus, volumetric expansion only detaches rock volume in the size of debris (< 50 cm). To evaluate the efficacy of volumetric expansion, rock temperature and moisture monitoring as well as geotechnical investigations of rock strength are required.

9.4.3.2 Frost cracking intensity by ice segregation

The used model only includes conductive heat transfer and no latent heat processes. Excluding convective and advective heat transport may lead on one hand to underestimation of active-layer depth and cooler rock temperatures with increasing depths. Latent heat processes while freezing or melting slow down the heat transfer, thus, on the other hand the model overestimates active-layer depth and rock temperatures.

The results using the model of Hales and Roering (2007) show a higher frost cracking intensity of permafrost-free rock walls than permafrost-affected rock walls. Peaks of the frost cracking intensity are located in higher depths in permafrost-affected than permafrost-free rock walls. The frost cracking window is based on laboratory acoustic emission measurements on Berea Sandstone (Hallet et al., 1991). Anderson (1998) established the term frost cracking window for the temperature range between -3 and -8°C. Hallet et al. (1991) observed 90 % of events in the temperature range between -3 and -6°C. Berea Sandstone is a porous sedimentary rock with a porosity of approximate 20 %, a uniaxial compressive strength of 67.6 MPa at 0°C and up to 96.5 MPa at -7°C and a tensile strength of

8.3 MPA at 0°C up to 12.4 MPa at -8°C (Fig. 5.6 A, B) (Mellor, 1971, 1973). Walder and Hallet (1985) modelled ice segregation in high-strength St. Pons Marble and Westerly Granite and calculated highest crack growth between -2 and -3°C at a 5 mm long crack and -10 and -15°C at a 0.5 mm long crack in St. Pons Marble as well as between -4 to -7°C at a 50 mm long cracks and -11 to -16°C at a 5 mm long crack in Westerly Granite. Murton et al. (2001) observed ice segregation between -0.2 and -2.5°C at high-porosity low-strength Tuffeau limestone. Thus, ice segregation depends not only on a temperature range but also on rock strength and crack geometry. Krautblatter (2009) observed freezing point depression of 0.9 and 1.1° C in Schisty quartz slate with 2.35 ±0.15 % porosity and Quartz slate with 1.52 ±0.09 % porosity, respectively. Laboratory and theoretical finding suggest that the upper boundary of frost cracking may be somewhere between the freezing point and -3°C.

Water availability in the model is defined by temperature above 0°C (Hales and Roering, 2007). However, unfrozen water can exist at temperatures up to -10°C (Mellor, 1970) and could migrate towards the freezing front. Thus, the model probably underestimates frost cracking intensity in permafrost-affected rocks. The use of temperature gradient as a proxy of ice segregation is solely based on theoretical concepts (Wettlaufer and Worster, 1995; Worster and Wettlaufer, 1999) and needs to be verified by measurements.

Murton et al. (2006) measured by laboratory experiments higher efficacy of ice segregation at permafrost-affected rock samples (bi-directional freezing) than at permafrost-free rock samples (uni-directional freezing) (Fig. 5.8 C). Timing of ice-segregation is observed especially during active-layer thawing (Murton et al., 2006). Transferring Murton et al. (2006) findings into the model by Hales and Roering (2007), the crack intensity is expected to increase during active-layer thaw in summer and the largest peak of cracking intensity is expected to occur at lower boundary of the active-layer between 2 m (Logger N4) and 7 m depth (Logger C1). According to the tomographies of geophysical measurements (Fig. 8.24 and 8.25) the model probably overestimates the thawing depths, thus, peaks should be estimated in slightly lower depths.

Concerning the efficacy of ice segregation for rock decay, the findings reveal ice segregation can detach blocks up to 6.5 m size or equivalent to active-layer thaw depth in permafrost-affected rock walls, whereas permafrost-free rock walls are only prone to detachment of small blocks up to 1.5 m.

9.4.3.3 Thermal fatigue

Rock temperature was measured in 10 cm depth and probably underestimates number of thermal changes at the rock surface. Rock surfaces heat non-uniformly due to orientation and albedo (Anderson and Anderson, 2012). In Steintaelli, lithology is relatively uniform in terms of albedo, thus, temperature amplitude differences between north- and south-facing rocks are aspect-related. Snow cover controls the frequency of thermal fatigue (Matsuoka and Sakai, 1999) due isolating property of snow cover switching of temperature changes. Snow cover lasts longer on north-facing rocks due to higher snow depths (Schmidt, 2009), interaction with permafrost (Phillips, 2000) and reduced solar radiation (Keller, 1994; Phillips, 2000); as a consequence the frequency of temperature changes decreases. Anisotropic behaviour of minerals leads to non-uniform rock expansion (Hall et al., 2008; Siegesmund et al., 2008); thermal fatigue exploits pre-existing planes of weakness e.g. mineral surfaces, bedding planes and schistosity (Richter and Simmons, 1974; Mahmutoglu, 1998). Given the schistosity parallel to the surface on the south-facing rock wall in the Steintaelli (Fig. 9.3), thermal fatigue may cause failure along this pre-existing line of weakness. According to measurements by Gunzberger and Merrien-Soukatchoff (2011) daily penetration of temperature cycles down to 50 cm depth in a gneiss outcrop, thermal fatigue might be restricted to the near surface area and weathering products should reflect the penetration depth.

9.4.3.4 Rock strength results

Schmidt hammer values are measured along scanlines at discontinuities by Halla (2013) and on the rock surface by the author. In contrast to south-facing slope or crestline, the north-facing slopes are related to a higher number of discontinuities, and therefore, a smaller block size. Due to scanline method more discontinuities imply a change in stability and results in more Schmidt hammer tests at discontinuity walls. Weathering affects discontinuities as well as the surface, thus, rebound values of the Schmidt hammer and the compressive strength of the discontinuity walls are reduced in the same amount as at the rock surface. Despite the lower number of measurements, the results of the rebound values and the compressive strength are as representative on the SE-slope as on the NE-slope, thus, scanline methods measure changes in terms of discontinuity. A lot of changes in terms of discontinuity results in an increased number of measurements. The scanline method can lead to significant differences, if small-scale rock surface strength differs between discontinuities. Standard deviations of R-values are low and, except Transect 9, a decrease of R-values is observed in the data.

The SW-slope of Transect 9 is covered by debris and maybe protected from weathering processes (Fig. 9.3).

9.4.4 Implications for rock decay

Beside the thermally defined frost cracking window, the data demonstrates the existence of temporal and spatial windows for each weathering process (Fig. 9.28). Short term freeze-thaw cycles associated with volumetric expansion occur before snow cover in autumn and after the end of snow cover. In 2013, Snow lasted long and the peak should occur in spring suggested by snow-free loggers C3 and N2. Fast freezing rates occur only in autumn 2012 and findings by Sass (2005a) suggest higher moisture content at this time of year. Spatially the crestline shows the most freeze-thaw cycles due to possible wind redistribution of snow and less snow accumulation caused by steep topography.

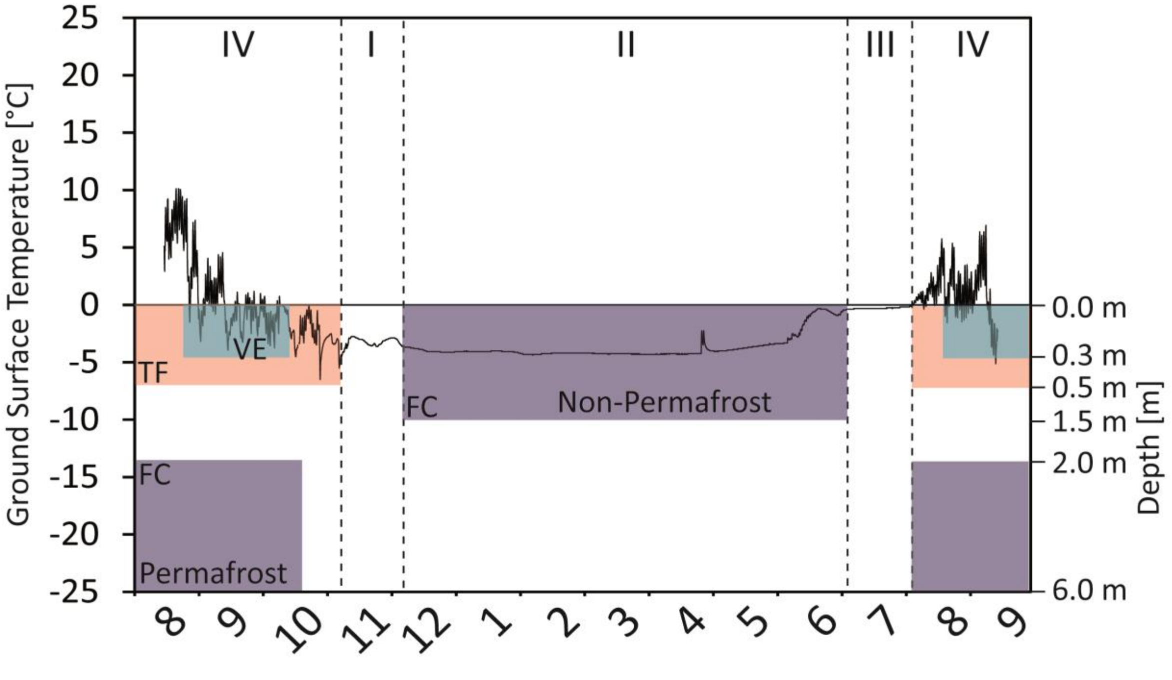

Fig. 9.28 Ground surface temperature plotted against time. Roman letters indicate snow cover stage according to Luetschg (2005). Rectangles present spatial and temporal extent of weathering windows; TF is thermal fatigue window (red), VE is volumetric expansion window (light blue); FC is frost cracking/ice segregation window (violet).

South exposed slopes contain lesser moisture close to the surface than north-facing slopes (Sass, 2005a), suggesting lesser efficacy of volumetric expansion on south-facing slopes. The lower boundary of spatial volumetric expansion window is determined by the penetration depth of frost cycles and ranges between 15 cm (Sass, 2005a), 30 cm (Matsuoka and Murton, 2008) and 50 cm (Matsuoka et al., 1997; Matsuoka, 2008).

The spatial extent of ice segregation depends on permafrost occurrence and snow isolation. If permafrost is present, e.g. on NE-slope, ice segregation occurs during active-layer thawing at the boundary between active-layer and permafrost table (Murton et al., 2006). In the Steintaelli this boundary probably ranges between 2 m and 6 m according to conductive modelling (Fig. 8.23) and geophysical tomographies (Fig. 8.24 and Fig. 8.25). If permafrost is not present, e.g. on SW-slope, ice segregation occurs during snow Stage II. Isolating snow cover preserves continuous negative temperature and enables negative temperature gradients for a long period. Water can migrate upwards towards the freezing front between surface and 1.5 m depth (Fig. 9.26 C) based on the frost cracking model by Hales and Roering (2007). Rock detachment size caused by ice segregation is in the range of active-layer depth in permafrost-affected NE-slope and maximum up to 1.5 m on non-permafrost SW-slope.

Thermal changes only occur during snow-free period (Stage IV) and are effective to depth down to approximately 50 cm (Gunzburger and Merrien-Soukatchoff, 2011). Amplitude of thermal changes is higher on south-facing slopes due to increased solar radiation. Rock decay due to thermal changes is expected to be effective up to 50 cm in intact rock and much deeper in discontinuities (Gischig et al., 2011a, 2011b). Blocks detached by thermal fatigue are restricted in size to effective depth of 50 cm.

Chemical and biological weathering processes are excluded in this study, however, these processes are active in the Steintaelli and may lead to synergetic effects (Viles, 2013a) existing between the described weathering processes.

9.4.5. Evidences of weathering

Efficacy of weathering depends on rock strength and lithological structures, e.g. schistosity. The Schmidt hammer values reflect near-surface weathering. The R-values suggest a decrease of rock strength on the south-facing slope in contrast to north-facing slope. The SW-slope is permafrost-free and weathering processes are restricted to the upper 1.5 m. The inclination of the SW-slope parallel to schistosity (Fig. 9.3 B) indicates sheeting. Platy debris on the SW-slope supports this theory (Fig. 9.3 B).

On the crestline, snow lasts long in form of the snow cornice. Long snow periods prevent thermal changes and, thus, thermal expansion and volumetric expansion, but provide ice segregation. Near-surface rock shows a high rock strength suggesting low efficacy of near-surface occurring thermal expansion and volumetric expansion.

On the NE-slope, permafrost is present and schists are less dominant. Permafrost occurrence implies frost cracking/ice segregation between the boundary of active-layer and permafrost table. Block sizes are between 2 and 5 m³ on the NE-slope (Halla, 2013) and of a more cubic form (Fig. 9.3 A). Repeated frost cracking could destroy rock bridges (Krautblatter et al., 2013) and lead to instabilities of block sizes of maximum the permafrost table depth. Frost cracking processes involved in the detachment of the blocks are possible. High Schmidt hammer values reflect low-effective near-surface thermal fatigue or volumetric expansion. Additionally, the absence of planes of weakness restricts the efficacy of these processes.

On permafrost-affected Ne- slope, rock decay is less effective near the surface due to deeper reaching ice segregation, less thermal expansion/contraction and volumetric expansion due to longer snow cover period and, thus, longer isolation by snow cover.

9.5 Conclusion

Inter-annual extensometer measurements show divergent and convergent displacement despite the rock wall should be stable according to geotechnical investigations by Halla (2013). Intra-annual extensometer rates are 1-2 magnitudes higher than inter-annual rates suggesting short-term displacement in summer. Active-layer thaw and freezing are potential causes of displacement and changes seasonally rock stability (Fig. 9.29).

Snow cover is a main controlling factor of discontinuity movement and rock decay by controlling the occurrence of thermal expansion and volumetric expansion and by preventing these processes while favouring ice segregation due to isolation. Volumetric expansion increases short-term cryostatic pressure, whereas ice segregation leads to seasonal cryostatic pressure. Active-layer thaw decreases shear strengths during summer (Krautblatter et al., 2013) and increases instability seasonally (4 in Fig. 9.29).

Thermal expansion and volumetric expansion are active close to the surface while ice segregation occurs near-surficial predominantly in permafrost-free areas and in 2-5 m depth in permafrost rock walls.

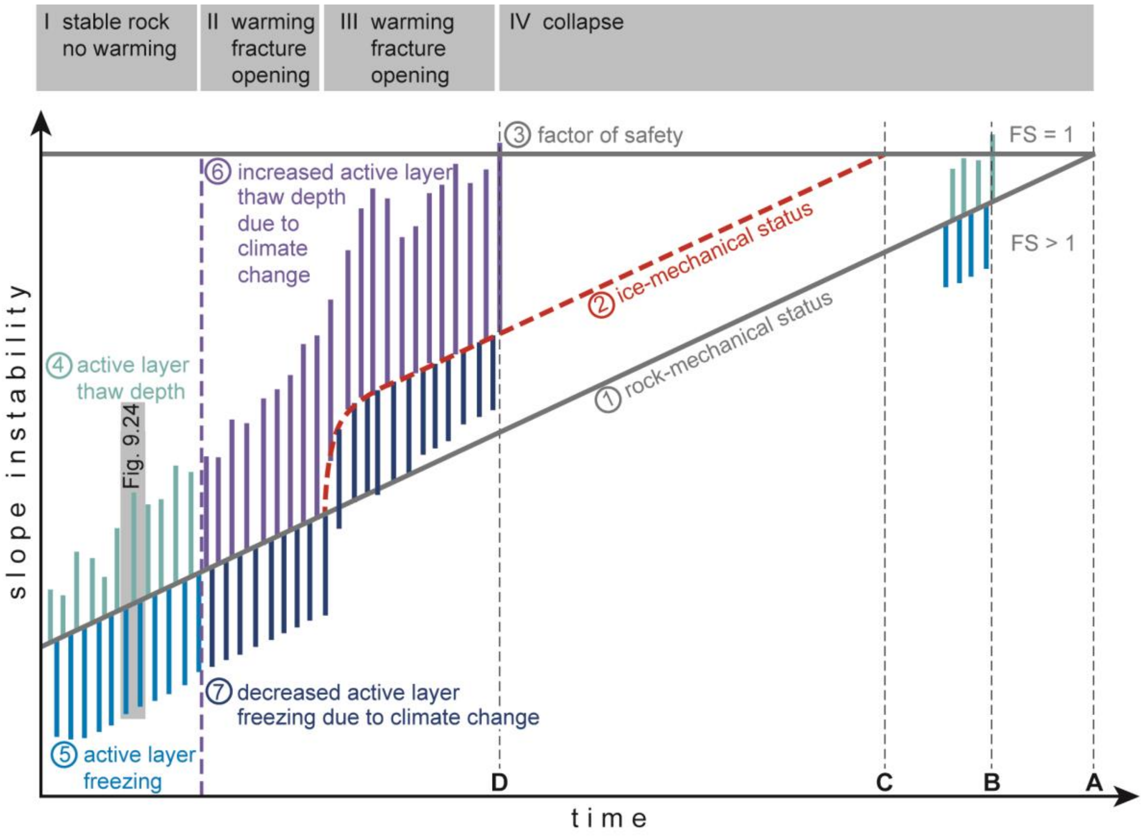

Fig. 9.29 Development of slope instability through time of a permafrost rock system. In longer time scales the rock-mechanical instability (1) increases in time and is amplified by the influences of the ice-mechanical system status (2). Failure occurs when the factor of safety (3) equals 1. On an annual time scale active-layer thaw (4) and active-layer freezing (5) seasonally change the instability of the rock-mechanical system. If the rock system is significantly affected by cleft ice rise of air temperature leads to active-layer thaw (6) increase and active-layer freezing decrease (7) (after Schumm (1973)). Seasonal scale of Fig. 9.24 is denoted by a grey rectangle.

Based on geotechnical mapping without including ice or permafrost the rock wall is stable (Halla, 2013) and should be currently in phase I (Fig. 9.29). Active-layer thawing and freezing decreases and increases shear strengths seasonally (Krautblatter et al., 2013). In combination with cryostatic and hydrostatic pressure changes, windows of instabilities exist temporarily at the beginning of active-layer thaw and at the beginning of active-layer freezing. Intra-annually instabilities vary seasonally due to active-layer activity. Inter-annual discontinuity movements are small but significant indicating that the rock wall moved into phase II (Fig. 9.29). Ice segregation can crack rock bridges and can change the system status from rock-mechanical to more sensitive ice-mechanical status (2 in Fig. 9.29). Climate change can increase active-layer thaw (6 in Fig. 9.29) that and, thus, seasonal sensitivity to rock wall failure. Path-dependent system change and increased seasonal instability both will increase sensitivity to instability in the future.

10 Synoptic discussion

10.1 Theory

1) Snow is a major control of permafrost evolution on a slope facet scale.

In previous research, the controlling influence of snow cover on permafrost evolution was identified and quantified on low inclined terrain (Keller and Gubler, 1993; Hanson and Hoelzle, 2004; Luetschg and Haeberli, 2005). Salzmann et al. (2007) assume that seasonal snow cover will probably be the most important factor influencing the thermal regime of rock walls, however, snow cover was previously neglected due to steep (> 50°) inclination of rock walls (Salzmann et al., 2007). As snow accumulates on small ledges even in steep rock walls, in form of cornices on crestline and snow patches at the toe of rock walls, this a priori neglection of snow cover is not justified. In this study, temperature loggers validated the seasonal influence of snow cover, indicating isolation due to snow cover and isothermal status (zero-curtain) during snow melt. Geophysical tomographies showed the spatial influence of snow cover on active-layer thaw and indicate no or low active-layer thaw in snow-covered areas in August 2006 and 2007 (Krautblatter and Draebing, 2014) as well as in August 2012 and 2013. The importance of snow cover as major control of permafrost evolution is therefore significantly proven.

2) Snow is a key control of rock decay and the near-surface mechanical regime.

The influence of snow cover on rock decay by freeze-thaw processes was described by Matsuoka et al. (1997), but the influence on ice segregation or thermal fatigue was not investigated systematically. Short-term freeze-thaw processes, including volumetric expansion, are controlled by snow cover, as snow cover isolates the underground and thereby prevents the short-term occurrence of freeze-thaw-cycles. This study shows that freeze-thaw processes are temporally restricted to snow-free periods, where freezing point-crossings occur. Snow melt can deliver water and increase moisture and saturation of rocks, which is an important requirement for the efficacy of volumetric expansion. On the one hand, snow cover prevents daily underground temperature changes due to the isolation property and, thus, prevents thermal fatigue and restricts the occurrence of thermal fatigue to snow-free periods. On the other hand, snow cover enhances the occurrence of ice-segregation due to its isolation property. This study shows that continuous low temperatures in the range of the frost cracking window (Hallet et al., 1991; Anderson, 1998) enable the development of continuous temperature gradients and development of cryosuction.

3) Slope instability occurs in critical time windows.

On a seasonal scale, shear strengths decrease due to active-layer thaw (Krautblatter et al., 2013). Shear forces vary seasonally and the proportion of shear forces and shear strengths results in the occurrence of critical time windows of instability (Fig. 5.10). These windows occur (1) at the beginning of active-layer thaw during snowmelt, mostly in early summer, and (2) at the beginning of active-layer freezing before snow isolation in late autumn. Crackmeter data in this study validates the (2) critical time window of instability in autumn, which results from fast freezing and cryostatic pressure increase, while shear strengths are still reduced due to active-layer thaw. During the melting and thawing period in early summer, hydrostatic pressure can compensate cryostatic pressure decrease, while shear strengths decrease due to thawing. The (1) critical time window cannot be validated at Steintaelli, but the investigation by Blikra and Christiansen (2014) at Jettan rockslide shows the potential of this mechanism. This thesis shows that the consideration of active-layer thaw and shear strength reduction alone without considering shear forces cannot explain the timing and the occurrence of rockfall events. The conceptual approach presented in the study can explain the temporal occurrence of rock wall instability. Therefore, more research is necessary to quantify the conceptualised processes, e.g. advective heat transport.

10.2 Methodology

4) P-wave velocity is highly sensitive to freezing in rocks.

Timur (1968) explained p-wave velocity increase in rocks as a result of phase transition from water to ice and higher p-wave velocity of ice compared to water. As a consequence, low-porosity rocks will show a low increase of p-wave velocity and, thus, the differentiation of frozen or unfrozen status based on p-wave velocity would not be possible as argued by McGinnis et al. (1973). In previous studies, the influence of overburden pressure on increasing p-wave velocity was detected (King, 1966; Nur and Simmons, 1969; Takeuchi and Simmons, 1973; Toksöz et al., 1976). When water freezes to ice, cryostatic pressure develops and, thus, this pressure increases the p-wave velocity of low-porosity rocks (Draebing and Krautblatter, 2012). The detected pressure-induced p-wave velocity increase reveals the possibility to apply refraction seismics in low-porosity rock walls.

5) P-wave velocity can be used for high-resolution active-layer monitoring in steep rock walls.

Based on the findings on the applicability of refraction seismics in low-porosity rocks, Krautblatter and Draebing (2014) could show that refraction seismics enable the monitoring of active-layer thaw in high resolution. Seismic waves travel along underground boundaries (Hauck and Vonder Mühll, 2003a), e.g. the boundary between frozen and unfrozen rock, and, thus, refraction seismics allow a more accurate delineation of active-layer depth than ERT. Macroscopic ice-filled joints and faults are detectable by refraction seismics (Heincke et al., 2006b) and deliver valuable information on the mechanical regime of the rock wall. In contrast, active-layer depth detection by using electrical resistivity tomography is based on the resistivity contrast between active-layer and permafrost. This precondition is not given, if the rock wall and, thus, the active-layer dries out. As a consequence, the resistivity contrast between air (active-layer) and ice (permafrost) is too low to differentiate both material properties. Therefore, ERT is not always a suitable method, while refraction seismics are not sensitive to drying of rock walls and, thus, still enable active-layer and permafrost differentiation.

6) Combined kinematics, piezometric measurements and thermal observation allow for an attribution of discontinuity displacements to different forcing processes.

Kinematic measurements were applied by several authors to monitor discontinuity movements (Matsuoka, 2008; Hasler et al., 2012; Blikra and Christiansen, 2014), however, a systematic analysis of forcing processes and their differentiation was not conducted. The combination of kinematic, piezometric and thermal measurements allow the differentiation of forcing processes as thermal expansion/contraction, freeze-thaw processes (volumetric expansion and ice erosion) and ice segregation. Thermal expansion/contraction depends on high-frequent temperature changes and are active both at positive and negative temperatures and need no freezing point crossing. Freeze-thaw processes only occur in a small window at the freezing point, which is crossed on a low frequency during a short time window. This time window only exists in snow-free periods. Ice segregation is a very slowly acting process, which temporarily occurs in a temperature range between -3° and -6°C (Hallet et al., 1991; Anderson, 1998). This study shows that continuously measuring crackmeters enable the recording of high-frequent, low-frequent and as well slow-running processes. In combination with thermal measurements, it is possible to differentiate these processes. Piezometric measurements showed for the first time the existence of cryosuction in field conditions and validated the existence of ice-segregation outside of laboratory conditions.

10.3 System understanding

7) Insights gained by p-wave velocity measurements help to assess and anticipate critical stages of permafrost degradation in steep rock walls.

Active-layer thawing decreases shear strengths seasonally (Krautblatter et al., 2013). The accurate identification of active-layer depth and temporal changes are provided by seismic refraction tomography (SRT). Identification of amplified active-layer thaw due to climate change will be enabled by time-lapse SRT. Geotechnical mapping allows the appraisal of spatial distribution of discontinuities, while the distribution in depth is only assumed. Thus, SRT delivers valuable information on discontinuity distribution and discontinuity infill inside the rock wall, which are required for stability analysis and as input data for stability models.

8) In critical stages, snow and ice distribution have a high impact on the spatial and temporal pattern of degradation.

As thawing of active-layer decreases shear strengths (Krautblatter et al., 2013), it was assumed that instability will be lowest when active-layer thaw reaches the seasonal maximum. However, rockfall occurred before reaching this maximum thawing depth (Gruber et al., 2004a). Warmer air temperatures imply deeper active-layer thaw and, thus, higher volumetric rockfall (Ravanel and Deline, 2008). On the one hand, snow cover can damp the influence of high air temperatures and prevent active-layer thaw. On the other hand, snow cover delivers water during snowmelt, which can increase hydrostatic pressure in early summer and possesses the potential to destabilize rock walls (critical time window 1). Freezing in late autumn increases cryostatic pressure during a period of deep reaching active-layer thaw, which can result in critical instability (critical time window 2). Ice segregation slowly increases cryostatic pressure during snow-covered periods and can destabilize rock walls on a system scale by cracking rock bridges and on a seasonal scale, if cryostatic pressure exceeds rock strengths. In conclusion, critical stages exist on a seasonal scale, but the efficacy of these critical stages depends on system state.

9) These insights can be used to understand thresholds for critical system changes.

The sensitivity of a system to changes, e.g. collapse, depends on system state. This also applies for the efficacy of events of a certain magnitude. Therefore, the use of system theory and the sensitivity concept delivers insights on how the system, in our case permafrost rock wall, works. Sensitivity of this system can be increased by system state changes, which can occur continuously and lead to collapse (A in Fig. 5.12) or suddenly increases sensitivity (path-dependent system change; C in Fig. 5.12). Magnitude of events can change the sensitivity on a seasonal scale (climate change; 6 in Fig. 5.12). Depending on system state, these magnitudes can lead to a collapse of the whole system (D in Fig. 5.12). Thus, the conceptual approach helps to understand how external and internal thresholds work for critical system changes.

11 Conclusion

Rockfalls from permafrost-affected rock walls present an important natural hazard in high-mountain areas. Snow cover influences thermal and mechanical processes in steep rock walls. To investigate these influences the DFG/SNF financed project ISPR (Influences of snow cover on thermal and mechanical processes in steep permafrost rock walls) was started. Information on snow cover in steep terrain is low and will be investigated in detail in the thesis of our Swiss project partners. This thesis aims to diminish the knowledge gaps on thermal and mechanical response. To achieve this aim, on the one hand geophysical methods to monitor thermal regime of rock walls are combined with temperature measurements. On the other hand, geotechnical methods are used to describe the mechanical regime. This two side way and the fundamental conceptual approach allowed discovering the preserving property of isolating snow cover, the complex thermal response to snow accumulation or ablation and the complex mechanical response of discontinuities.

The differentiation of thermal heat transport processes was not possible, however, this differentiation should be a main goal of future permafrost research. Advective and convective heat transport can change the thermal regime and mechanical regime with a faster than previously assumed response time. Climate change will probably alter active-layer thawing and amplify heat transport processes. Without a profound process understanding and knowledge about system state of the rock wall, a prediction of what can happen and when will never be possible, and, this prediction is highly necessary in natural hazard management.

Index of Tables

Index of Figures

Acknowledgements

This dissertation was made possible by the DACH (DFG/SNF) project "ISPR Influences of snow cover on thermal and mechanical processes in steep permafrost rock walls". The fieldwork in 2006/06 was financed by DFG research project "Sensitivity of rock permafrost to regional climate change scenarios and implications for rock wall instability". The laboratory work of the Cryosphere-Paper was "financed" by Agentur für Arbeit Bonn.

Richard Dikau and Michael Krautblatter were my main supervisors. I am grateful that I could continue the PhD project of Michael Krautblatter in the Steintaelli and I owe him thanks for enhancing my interest in rock permafrost and the fantastic teamwork in the last 8 years. A lot of thanks to Richard Dikau for increasing my interests in geomorphology, system theory and for mentoring support especially when I can't see the wood for the trees. This dissertation would be not possible without our Swiss project partners Marcia Phillips, Anna Haberkorn (both SLF), Martin Hoelzle and Stephan Gruber. Special thanks to the SLF team for providing a lot of data used in this work. For field assistance I like to thank Natalie Gorus, Chris Halla, Claudia Bierbaum, Christian Querner and Hermann Reinartz.

This dissertation would not be possible without the support from my working group: Jana Eichel, Karoline Meßenzehl, Thomas Hoffmann, Manuela Schlummer, Sarah Verleysdonk as well as former member Daniel Funk. I like to thank them for their critical discussions and encouragements.

I also owe thanks to G. Nover, J. Ritter and W. Scherer for equipment support to enable parts of this dissertation and to C. Hauck, C. Hilbich, L. Ravanel, A. Hasler, M. Siewert and P. Deline and M. Geilhausen for providing rock samples.

Last but not least I like to thank my family for all their support even if some of them still believe that I spend every summer two months on vacations in Switzerland.

References

Akimov, A.T., Dostovalov, B.N., Yakupov, V.S., 1973. Geophysical methods of studying permafrost. In: F. Sanger (Ed.), 2nd International Conference on Permafrost. USSR Contribution, Yakutsk, USSR, pp. 767-777.

Amann, F., 2006. Großhangbewegung Cuolm Da Vi (Graubünden, Schweiz) - Geologisch-geotechnische Befunde und numerische Untersuchungen zur Klärung des Phänomens, University of Erlangen-Nürnberg.

Anderson, D.M., Morgenstern, N.R., 1973. Physics, chemistry, and mechanics of frozen ground: A review. In: F. Sanger (Ed.), 2nd International Conference on Permafrost. Northamerican Contribution, Yakutsk, USSR, pp. 257-288.

Anderson, R.S., 1998. Near-surface thermal profiles in alpine bedrock: Implications for the frost weathering of rock. Arctic and Alpine Research 30, 362-372.

Anderson, R.S., Anderson, S.P., 2012. Geomorphology. The Mechanics and Chemistryof Landscapes. Cambridge University Press, Cambridge.

Anderton, S.P., White, S.M., Alvera, B., 2002. Micro-scale spatial variability and the timing of snow melt runoff in a high mountain catchment. Journal of Hydrology 268, 158-176.

Anderton, S.P., White, S.M., Alvera, B., 2004. Evaluation of spatial variability in snow water equivalent for a high mountain catchment. Hydrological Processes 18, 435-453.

Archie, G.E., 1942. The electric resistivity log as an aid in determining some reservoir characteristics. Trans. AIME 146, 54-62.

Aschenwald, J., Leichter, K., Tasser, E., Tappeiner, U., 2001. Spatio-temporal landscape analysis in mountainous terrain by meansof small format photography: a methodological approach. IEEE transactions on geoscience and remote sensing 39, 885-893.

Ballantyne, C.K., 2002. Paraglacial geomorphology. Quaternary Science Reviews 21, 1935–2017.

Barker, R.D., 1989. Depth of investigation of collinear symetrical 4-electrode arrays. Geophysics 54, 1031-1037.

Barnes, D.F., 1963. Geophysical methods for delineating permafrost, 1st International Conference on Permafrost, LaFayette, Indiana, pp. 349-355.

Barsch, D., 1973. Refraktionsseismische Bestimmung der Obergrenze des gefrorenen Schuttkörpers in verschiedenen Blockgletschern Graubündens, Schweizer Alpen. Zeitschrift für Gletscherkunde und Glazialgeologie 9, 143-167.

Bartelt, P., Lehning, M., 2002. A physical SNOWPACK model for the Swiss avalanche warning Part I: numerical model. Cold Regions Science and Technology 35, 123-145.

Barton, N., 2007. Rock quality, seismic velocity, attenuation and anisotropy. Routledge, London, Leiden, New York.

Barton, N., Choubey, V., 1977. The shear strength of rock joints in theory and practice. Rock Mechanics 10, 1-54.

Bavay, M., Lehning, M., Jonas, T., Löwe, H., 2009. Simulations of future snow cover and discharge in Alpine headwater catchments. Hydro. Proc. 23, 95-108.

Bayerisches Landesamt für Umwelt, 2010. Talzuschub/Sackung, Augsburg.

Bear, J., 1972. Dynamics of Fluids in Porous Media. Environmental Science Series. Elsevier, New York.

Bearth, P., 1980. Geologischer Atlas der Schweiz 1:25000. In: S.G. Kommision (Ed.), pp. Erläuterungen zum Atlasblatt 71 (1308 St. Niklaus).

Berkowitz, B., 2002. Characterizing flow and transport in fractured geological media: A review. Advances in Water Resources 25, 861-884.

Berthling, I., Melvold, K., 2008. Ground Pentrating Radar. In: C. Hauck, C. Kneisel (Eds.), Applied Geophysics in Periglacial Environments. Cambridge University Press, pp. 81-97.

Beven, K., Germann, P., 1982. Macropores and water flow in soils. Water Resources Research 18, 1311-1325.

Bieniawski, Z.T., 1987. Engineering Rock Mass Classsifications. Wiley & Sons, New York.

Bierbaum, C., 2013. Variabilität der Schneebedeckung in steilen alpinen Felswänden. Master Thesis, unpublished, Universität Wien.

Binley, A., Ramiraz, A., Daily, W., 1995. Regularised image reconstruction of noisy electrical resistance tomography data, 4th Workshop of the European Concerted Action on Process Tomography, Univ. of Bergen, Bergen, Norway.

Blikra, L.H., Christiansen, H.H., 2014. A field-based model of permafrost-controlled rockslide deformation in northern Norway. Geomorphology 208, 34-49.

Boeckli, L., Brenning, A., Gruber, S., Noetzli, J., 2012a. Permafrost distribution in the European Alps: calculation and evaluation of an index map and summary statistics. Cryosphere 6, 807-820.

Boeckli, L., Brenning, A., Gruber, S., Noetzli, J., 2012b. A statistical approach to modelling permafrost distribution in the European Alps or similar mountain ranges. Cryosphere 6, 125-140.

Bommer, C., Phillips, M., Arenson, L.U., 2010. Practical Recommendations for Planning, Constructing and Maintaining Infrastructure in Mountain Permafrost. Permafrost Periglac. 21, 97-104.

Bonner, J.L., Leidig, M.R., Sammis, C., Martin, R.J., 2009. Explosion Coupling in Frozen and Unfrozen Rock: Experimental Data Collection and Analysis. B Seismol Soc Am 99, 830-851.

Bottino, G., Chiarle, M., Joly, A., Mortara, G., 2002. Modelling rock avalanches and their relation to permafrost degradation in glacial environments. Permafrost and Periglacial Processes 13, 283-288.

Bovis, M.J., 2004. Failure. In: A. Goudie (Ed.), Encyclopedia of Geomorphology. Routledge, London, pp. 360-361.

Bradford, J.H., Harper, J.T., Brown, J., 2009. Complex dielectric permittivity measurements from ground-penetrating radar data to estimate snow liquid water content in the pendular regime. Water Resources Research 45, W08403.

Brunsden, D., 1996. Geomorphological events and landform change - The Centenary Lecture to the Department of Geography, University of Heidelberg. Zeitschrift Fur Geomorphologie 40, 273-288.

Brunsden, D., Thornes, J.B., 1979. Landscape sensitivity and change. Transactions of the Institute of British Geographers 4, 463-484.

Caduff, R., Kos, A., Schlunegger, F., McArdell, B.W., Wiesmann, A., 2014. Terrestrial Radar Interferometric Measurement of Hillslope Deformation and Atmospheric Disturbances in the Illgraben Debris-Flow Catchment, Switzerland. Ieee Geoscience and Remote Sensing Letters 11, 434-438.

Carcione, J.M., Seriani, G., 1998. Seismic and ultrasonic velocities in permafrost. Geophys. Prospec. 46, 441-454.

Carslaw, H.S., Jaeger, J.C., 1986. Conduction of heat in solids. Clarendon Press, Oxford.

Chang, S.-H., Lee, C.-I., Jeon, S., 2002. Measurement of rock fracture toughness under modes I and II and mixed-mode conditions by using disc-type specimens. Engineering Geology 66, 79-97.

Chorley, R.J., Schumm, S.A., Sugden, D.E., 1984. Geomorphology. Methuen, London.

Christiansen, H.H., 2001. Snow-cover depth, distribution and duration data from northeast Greenland obtained by continuous automatic digital photography. In: K. Hutter (Ed.), Annals of Glaciology, Vol 32, 2001. Annals of Glaciology. Int Glaciological Soc, Cambridge, pp. 102-108.

Christiansen, H.H., 2005. Thermal regime of ice-wedge cracking in adventdalen, Svalbard. Permafrost and Periglacial Processes 16, 87-98.

Church, M., 1996. Space time and the mountain - How do we order what we see? In: B.L. Rhoads, C. Thorn (Eds.), The scientific nature of geomorphology. Wiley & Sons, Chichester, pp. 147-170.

Church, M., Ryder, J.M., 1972. Paraglacial sedimentation: a consideration of fluvial processes conditioned by glaciation. GSA Bulletin 83, 3059-3071.

Clark, J., Phillips, R., 2003. Centrifuge modelling of frost heave of arctic gas pipelines. In: M. Phillips, S. Springman, L. Arenson (Eds.), 8th International Conference on Permafrost, Zurich, Switzerland, pp. 151-156.

Cooper, H.W., Simmons, G., 1977. The effect of cracks on the thermal expansion of rocks. Earth Planet. Sci. Lett. 36, 404-412.

Corripio, J.G., 2004. Snow surface albedo estimation using terrestrial photography. International Journal of Remote Sensing 25, 5705-5729.

Corripio, J.G., Durand, Y., Guyomarc'h, G., Merindol, L., Lecorps, D., Pugliese, P., 2004. Land-based remote sensing of snow for the validation of a snow transport model. Cold Regions Science and Technology 39, 93-104.

Danby, R.K., Hik, D.S., 2007. Responses of white spruce (Picea glauca) to experimental warming at a subarctic alpine treeline. Glob. Change Biol. 13, 437-451.

Davidson, G.P., Nye, J.F., 1985. A Photoelastic Study of Ice Pressure in Rock Cracks. Cold Reg Sci Technol 11, 141-153.

Davies, M.C.R., Hamza, O., Harris, C., 2001. The effect of rise in mean annual temperature on the stability of rock slopes containing ice-filled discontinuities. Permafrost and Periglacial Processes 12, 137-144.

Davies, M.C.R., Hamza, O., Harris, C., 2003. Physical modelling of permafrost warming in rock slopes. In: M. Phillips, S. Springman, L. Arenson (Eds.), 8th International Conference on Permafrost, Zurich, pp. 169-174.

Davies, M.C.R., Hamza, O., Lumsden, B.W., Harris, C., 2000. Laboratory measurement of the shear strength of ice-filled rock joints. Ann. Glac. 31, 463-467.

de Boer, D.H., 1992. Hierarchies and spatial scale in process geomorphology: a review. Geomorphology 4, 303-318.

Deere, D.U., Miller, R.P., 1966. Engineering classification and index properties for intact rock.

Deline, P., 2009. Interactions between rock avalanches and glaciers in the Mont Blanc massif during the late Holocene. Quaternary Science Reviews 28, 1070-1083.

Deline, P., Coviello, V., Cremonese, E., Gruber, S., Krautblatter, M., Jaillet, S., Malet, E., Morra di Cella, U., Noetzli, J., Ravanel, L., Pogliotti, P., Verleysdonk, S., 2009. L’Aiguille du Midi (massif du Mont Blanc) : un site remarquable pour l’étude du permafrost des parois d’altitude. Collection EDYTEM, Cahiers de Géographie 8, 135-146.

Derksen, C., LeDrew, E., 2000. Variability and change in terrestrial snow cover: data acquisition and links to the atmosphere. Progress in Physical Geography 24, 469-498.

Dietrich, P., Helmig, R., Sauter, M., Hötzl, H., Köngeter, J., Teutsch, G., 2005. Flow and Transport in Fractured Porous Media. Springer, Berlin.

Dikau, R., 1996. Oberflächensysteme - ein altes oder neues ein Thema? Geographica Helvetica 61, 170-180.

Dikau, R., 2004a. Factor of safety. In: A. Goudie (Ed.), Encyclopedia of Geomorphology. Routledge, London, pp. 359-360.

Dikau, R., 2004b. Mass movements. In: A. Goudie (Ed.), Encyclopedia of Geomorphology. Routledge, London, pp. 644-653.

Dikau, R., 2006. Komplexe Systeme in der Geomorphologie. Mitteilungen der Österreichischen Geographischen Gesellschaft 148, 125-150.

Dixon, J.C., 2013. 4.14 Chemical Weathering in Cold Climates. In: J.F. Shroder (Ed.), Treatise on Geomorphology. Academic Press, San Diego, pp. 245-257.

Draebing, D., Krautblatter, M., 2012. P-wave velocity changes in freezing hard low-porosity rocks: a laboratory-based time-average model. The Cryosphere 6, 1163-1174.

Dramis, F., Govi, M., Guglielmin, M., Mortara, G., 1995. Mountain Permafrost and Slope Instability in the Italian Alps: the Val Pola Landslide. Permafrost and Periglacial Processes 6, 73-82.

Dwivedi, R.D., Soni, A.K., Goel, R.K., Dube, A.K., 2000. Fracture toughness of rocks under sub-zero temperature conditions. Int. J. Rock Mech. Min. Sci. 37, 1267-1275.

Dzhurik, V., Leshchikov, F.N., 1973. Experimental investigations of seismic properties of frozen soils. In: F. Sanger (Ed.), 2nd International Conference on Permafrost. USSR Contribution, Yakutsk, USSR, pp. 485-488.

Eberhardt, E., Stead, D., Coggan, J.S., 2004. Numerical analysis of initiation and progressive failure in natural rock slopes—the 1991 Randa rockslide. Int. J. Rock Mech. Min. Sci. 41, 69-87.

Eckerstorfer, M., Christiansen, H.H., L., R., Vogel, S., 2013a. The geomorphological effect of cornice fall avalanches in the Longyeardalen valley, Svalbard. The Cryosphere 7, 1361–1374.

Eckerstorfer, M., Christiansen, H.H., Vogel, S., Rubensdotter, L., 2013b. Snow cornice dynamics as a control on plateau edge erosion in central Svalbard. Earth Surf. Proc. Land. 38, 466–476.

Edelbro, C., 2003. Rock Mass Strength - A Review, Technical Report, Lulea University of Technology

Egli, L., 2008. Spatial variability of new snow amounts derived from a dense network of Alpine automatic stations. Annals of Glaciology 49, 51-55.

Embleton-Hamann, C., 2004. Proglacial landforms. In: A. Goudie (Ed.), Encyclopedia of Geomorphology. Routledge, London, pp. 810-813.

Engelhard, M., Hauck, C., Salzmann, N., 2010. Influence of atmospheric forcing parameters on modelled mountain permafrost evolution. Meteorologische Zeitschrift 19, 491-500.

Erismann, T.H., Abele, G., 2001. Dynamics of Rockslides and Rockfalls. Springer, Heidelberg.

Eslami, J., Grgic, D., Hoxha, D., 2010. Estimation of the damage of a porous limestone from continuous (P- and S-) wave velocity measurements under uniaxial loading and different hydrous conditions. Geophys. J. Int. 183, 1362-1375.

Essery, R., Pomeroy, J., 2004. Implications of spatial distributions of snow mass and melt rate for snow-cover depletion: theoretical considerations. Annals of Glaciology 38, 261-265.

Everett, D.H., 1961. The thermodynamics of frost damage to porous solids. Transactions of the Faraday Society 57, 1541-1551.

Ferrians, O.J., Hobson, G.D., 1973. Mapping and predicting permafrost in North America: A review, 1963-1973. In: F. Sanger (Ed.), 2nd International Conference on Permafrost. Northamerican Contribution, Yakutsk, USSR, pp. 479-498.

Fierz, C., Armstrong, R.L., Durand, Y., Etchevers, P., Greene, E., McClung, D.M., Nishimura, K., Satyawali, P.K., Sokratov, S.A., 2009. The International Classification for Seasonal Snow on the Ground, IHP-VII Technical Documents in Hydrology N°83, IACS Contribution N°1, UNESCO-IHP, Paris.

Fischer, L., 2010. Slope Instabilities on Perenially Frozen and Glacierised Rock Walls: Multi-Scale Observations, Analyses and Modelling, University of Zurich, Zürich.

Fischer, L., Amann, F., Moore, J.R., Huggel, C., 2010. Assessment of periglacial slope stability for the 1988 Tschierva rock avalanche (Piz Morteratsch, Switzerland). Engineering Geology 116, 32-43.

Fischer, L., Eisenbeiss, H., Kaab, A., Huggel, C., Haeberli, W., 2011. Monitoring Topographic Changes in a Periglacial High-mountain Face using High-resolution DTMs, Monte Rosa East Face, Italian Alps. Permafrost And Periglacial Processes 22, 140-152.

Fischer, L., Huggel, C., Kaab, A., Haeberli, W., 2013. Slope failures and erosion rates on a glacierized high-mountain face under climatic changes. Earth Surface Processes and Landforms 38, 836-846.

Fischer, L., Huggel, C., Lemy, F., 2007. Investigation and modelling of periglacial rock fall events in the European Alps. Geophys. Res. Abstr. 9, 08160.

Fischer, L., Kääb, A., Huggel, C., Noetzli, J., 2006. Geology, glacier retreat and permafrost degradation as controlling factors of slope instabilities in a high-mountain rock wall: the Monte Rosa east face. Natural Hazards and Earth System Sciences 6, 761–772.

Forster, C., Smith, L., 1989. The influence of groundwater-flow on thermal regimes in mountainous terrain - a model study. Journal of Geophysical Research-Solid Earth and Planets 94, 9439-9451.

Fortier, R., LeBlanc, A.M., Yu, W.B., 2011. Impacts of permafrost degradation on a road embankment at Umiujaq in Nunavik (Quebec), Canada. Canadian Geotechnical Journal 48, 720-740.

French, H., 2007. The Periglacial Environment. Chichester, Chichester.

Fukuda, M., 1983. The porewater pressure in porous rocks during freezing, 4th International Conference on Permafrost, Fairbanks, Alaska, pp. 322-327.

Galley, R.J., Trachtenberg, M., Langlois, A., Barber, D.G., Shafai, L., 2009. Observations of geophysical and dielectric properties and ground penetrating radar signatures for discrimination of snow, sea ice and freshwater ice thickness. Cold Regions Science and Technology 57, 29-38.

Geertsema, M., Clague, J.J., Schwab, J.W., Evans, S.G., 2006. An overview of recent large catastrophic landslides in northern British Columbia, Canada. Engineering Geology 83, 120-143.

Geilhausen, M., Otto, J.C., Schrott, L., 2012. Spatial distribution of sediment storage types in two glacier landsystems (Pasterze & Obersulzbachkees, Hohe Tauern, Austria). Journal of Maps 8, 242-259.

Gischig, V., Loew, S., Kos, A., Moore, J.R., Raetzo, H., Lemy, F., 2009. Identification of active release planes using ground-based differential InSAR at the Randa rock slope instability, Switzerland. Natural Hazards and Earth System Sciences 9, 2027-2038.

Gischig, V.S., Moore, J.R., Evans, K.F., Amann, F., Loew, S., 2011a. Thermomechanical forcing of deep rock slope deformation: 1. Conceptual study of a simplified slope. J. Geophys. Res.-Earth Surf. 116, F04010.

Gischig, V.S., Moore, J.R., Evans, K.F., Amann, F., Loew, S., 2011b. Thermomechanical forcing of deep rock slope deformation: 2. The Randa rock slope instability. J. Geophys. Res.-Earth Surf. 116, F04011.

Gobiet, A., Kotlarski, S., Beniston, M., Heinrich, G., Rajczak, J., Stoffel, M., in press. 21st century climate change in the European Alps - A review. Science of The Total Environment.

Gomez-Heras, M., Smith, B.J., Fort, R., 2006. Surface temperature differences between minerals in crystalline rocks: Implications for granular disaggregation of granites through thermal fatigue. Geomorphology 78, 236-249.

Goudie, A.S., 2006. The Schmidt Hammer in geomorphologlical research. Progress In Physical Geography 30, 703-718.

Graf, W.L., 1988. Fluvial Processes in Dryland Rivers. Springer, Berlin.

Gray, D.M., Landine, P.G., Granger, R.J., 1985. Simulating infiltration into frozen prairie soils in streamflow models. Can J Earth Sci 22, 464–472.

Gruber, S., 2005. Mountain permafrost: transient spatial modelling, model verification and the use of remote sensing, University of Zurich, Switzerland.

Gruber, S., 2012. Derivation and analysis of a high-resolution estimate of global permafrost zonation. Cryosphere 6, 221-233.

Gruber, S., Haeberli, W., 2007. Permafrost in steep bedrock slopes and its temperaure-related destabilization following climate change. J. Geophys. Res. 112, F02S18.

Gruber, S., Hoelzle, M., 2001. Statistical modelling of mountain permafrost distribution: local calibration and incorporation of remotely sensed data. Permafrost and Periglacial Processes 12, 69-77.

Gruber, S., Hoelzle, M., 2008. The Cooling Effect of Coarse Blocks Revisited: A Modeling Study of a Purely Conductive Mechanism. In: D.L. Kane, K.M. Hinkel (Eds.), 9th Int. Conf. on Permafrost. Institute of Northern Engineering, UAF, Fairbanks, US, pp. 557-561.

Gruber, S., Hoelzle, M., Haeberli, W., 2004a. Permafrost thaw and destabilization of Alpine rock walls in the hot summer of 2003. Geophysical Research Letters 31, 1-4.

Gruber, S., Hoelzle, M., Haeberli, W., 2004b. Rock-wall Temperatures in the Alps: Modelling their Topographic Distribution and Regional Differences. Permafrost and Periglacial Processes 15, 299-307.

Gruber, S., King, L., Kohl, T., Herz, T., Haeberli, W., Hoelzle, M., 2004c. Interpretation of geothermal profiles perturbed by topography: the alpine permafrost boreholes at Stockhorn Plateau, Switzerland. Permafrost and Periglacial Processes 15, 349-357.

Gruber, S., Peter, M., Hoelzle, M., Woodhatch, I., Haeberli, W., 2003. Surface temperatures in steep alpine rock faces. A strategy for regional-scale measurement and modelling. Proceedings of the Seventh International Conference on Permafrost 2003, Zurich, Switzerland, 325-330.

Grünewald, T., Schirmer, M., Mott, R., Lehning, M., 2010. Spatial and temporal variability of snow depth and ablation rates in a small mountain catchment. Cryosphere 4, 215-225.

Gubler, S., Fiddes, J., Keller, M., Gruber, S., 2011. Scale-dependent measurement and analysis of ground surface temperature variability in alpine terrain. Cryosphere 5, 431-443.

Guenzel, F.K., 2008. Shear strength of ice-filled rock joints. In: D.L. Kane, K.M. Hinkel (Eds.), 9th International Conference on Permafrost. INE-UAF, Fairbanks, Alaska, US, pp. 581-586.

Gunzburger, Y., Merrien-Soukatchoff, V., 2011. Near-surface temperatures and heat balance of bare outcrops exposed to solar radiation. Earth Surface Processes and Landforms 36, 1577-1589.

Günzel, F.K., 2012. Shear strength of rock joints filled with frozen sand. In: K.M. Hinkel (Ed.), 10th Int. Conf. on Permafrost, Salekhard, Russia, pp. 143-148.

Haeberli, W., 1973. Die Basis-Temperatur der winterlichen Schneedecke als möglicher Indikator für die Verbreitung von Permafrost. Zeitschrift für Gletscherkunde und Glazialgeologie 9, 221-227.

Haeberli, W., 2005. Investigating glacier-permafrost relationships in high mountain areas: historical background, selected examples and research needs. In: C. Harris, J.B. Murton (Eds.), Cryospheric Systems: Glaciers and Permafrost. Special Publications. Geological Society, London, pp. 29-37.

Haeberli, W., Huggel, C., Kääb, A., Zgraggen-Oswald, S., Polkvoj, A., Galushkin, I., Zotikov, I., Osokin, N., 2004. The Kolka-Karmadon rock/ice slide of 20 September 2002: an extraordinary event of historical dimensions in North Ossetia, Russian Caucasus. Journal of Glaciology 50, 533-546.

Haeberli, W., Noetzli, J., Arenson, L., Delaloye, R., Gartner-Roer, I., Gruber, S., Isaksen, K., Kneisel, C., Krautblatter, M., Phillips, M., 2010. Mountain permafrost: development and challenges of a young research field. Journal Of Glaciology 56, 1043-1058.

Haeberli, W., Wegmann, M., Vonder Muhll, D., 1997. Slope stability problems related to glacier shrinkage and permafrost degradation in the Alps. Eclogae Geol. Helv. 90, 407-414.

Hales, T.C., Roering, J.J., 2005. Climate-controlled variations in scree production, Southern Alps, New Zealand. Geology 33, 701-704.

Hales, T.C., Roering, J.J., 2007. Climatic controls on frost cracking and implications for the evolution of bedrock landscapes. J. Geophys. Res.-Earth Surf. 112, F02033.

Hales, T.C., Roering, J.J., 2009. A frost "buzzsaw" mechanism for erosion of the eastern Southern Alps, New Zealand. Geomorphology 107, 241-253.

Hall, K., 2013. 4.15 Mechanical Weathering in Cold Regions. In: J.F. Shroder (Ed.), Treatise on Geomorphology. Academic Press, San Diego, pp. 258-276.

Hall, K., André, M.-F., 2001. New insights into rock weathering from high-frequency rock temperature data: an Antarctic study of weathering by thermal stress. Geomorphology 41, 23-35.

Hall, K., Guglielmin, M., Strini, A., 2008. Weathering of granite in Antarctica: II. Thermal stress at the grain scale. Earth Surface Processes and Landforms 33, 475-493.

Hall, K., Thorn, C., 2011. The historical legacy of spatial scales in freeze-thaw weathering: Misrepresentation and resulting misdirection. Geomorphology 130, 83-90.

Hall, K., Thorn, C., Sumner, P., 2012. On the persistence of 'weathering'. Geomorphology 149, 1-10.

Hall, K., Thorn, C.E., 2014. Thermal fatigue and thermal shock in bedrock: An attempt to unravel the geomorphic processes and products. Geomorphology 206, 1-13.

Hall, K., Thorn, C.E., Matsuoka, N., Prick, A., 2002. Weathering in cold regions: some thoughts and perspectives. Prog Phys Geog 26, 577-603.

Halla, C., 2013. Bewegungsprozesse im Festgestein des Periglazials im Steintälli, Mattertal, Schweiz. Diploma Thesis, unpublished, Universität Bonn.

Halla, C., Krautblatter, M., Draebing, D., 2014. The interplay of predefined rock mechanics and permafrost forcing in a steep alpine rock crest (Steintaelli, Mattertal, Switzerland). Geophys. Res. Abstr. 16, EGU2014-5158.

Hallet, B., 2006. Geology - Why do freezing rocks break? Science 314, 1092-1093.

Hallet, B., Walder, J.S., Stubbs, C.W., 1991. Weathering by segregation ice growth in microcracks at sustained subzero temperatures: Verification from an experimental study using acoustic emissions. Permafrost Periglac. 2, 283-300.

Hanson, S., Hoelzle, M., 2004. The thermal regime of the active layer at the Murtel rock glacier based on data from 2002. Permafrost Periglac. 15, 273-282.

Harris, C., Arenson, L.U., Christiansen, H.H., Etzemuller, B., Frauenfelder, R., Gruber, S., Haeberli, W., Hauck, C., Holzle, M., Humlum, O., Isaksen, K., Kaab, A., Kern-Lutschg, M.A., Lehning, M., Matsuoka, N., Murton, J.B., Nozli, J., Phillips, M., Ross, N., Seppala, M., Springman, S.M., Muhll, D.V., 2009. Permafrost and climate in Europe: Monitoring and modelling thermal, geomorphological and geotechnical responses. Earth-Sci. Rev. 92, 117-171.

Harris, C., Cook, J.D., 1986. The detection of high altitude permafrost in Jotunheimen, Norway using seismic refraction rechniques: an assessment. Arctic Alpine Res. 18, 19-26.

Harris, C., Davies, M.C.R., Etzelmüller, B., 2001. The assessment of potential geotechnical hazards associated with mountain permafrost in a warming global climate. Permafrost Periglac. 12, 145-156.

Harris, C., Murton, J.B., 2005. Interactions between glaciers and permafrost: an introduction. In: C. Harris, J.B. Murton (Eds.), Cryospheric Systems: Glaciers and Permafrost. Geological Society. Special Pcublication 242, London, pp. 1-9.

Harris, S.A., Pedersen, D.E., 1998. Thermal regimes beneath coarse blocky materials. Permafrost And Periglacial Processes 9, 107-120.

Harrison, S., 2001. On reductionism and emergence in geomorphology. Transactions of the Institute of British Geographers 26, 327-339.

Hartmeyer, I., Keuschnig, M., Schrott, L., 2012. A scale-oriented approach for the long-term monitoring of ground thermal conditions in permafrost-affected rock faces, Kitzsteinhorn, Hohe Tauern range, Austria. Austrian Journal of Earth Science 105, 128-139.

Hasler, A., Gruber, S., Beutel, J., 2012. Kinematics of steep bedrock permafrost. J. Geophy. Res.-Solid Ea. 117, F01016.

Hasler, A., Gruber, S., Font, M., Dubois, A., 2011a. Advective Heat Transport in Frozen Rock Clefts: Conceptual Model, Laboratory Experiments and Numerical Simulation. Permafrost And Periglacial Processes 22, 378-389.

Hasler, A., Gruber, S., Haeberli, W., 2011b. Temperature variability and offset in steep alpine rock and ice faces. Cryosphere 5, 977-988.

Hauck, C., 2001. Geophysical methods for detecting permafrost in high mountains, Mitteilungen der Versuchsanstalt für Wasserbau, Hydrologie und Glaziologie, 171.

Hauck, C., Böttcher, M., Maurer, H., 2011. A new model for quantifying subsurface ice content based on geophysical data sets. The Cryosphere 5, 453-468.

Hauck, C., Isaksen, K., Muhll, D.V., Sollid, J.L., 2004a. Geophysical Surveys Designed to Delineate the Altitudinal Limit of Mountain Permafrost: An Example from Jotunheimen, Norway. Permafrost and Periglacial Processes 15, 191-205.

Hauck, C., Isaksen, K., Vonder Mühll, D., Sollid, J.L., 2004b. Geophysical surveys designed to delineate the altitudinal limit of mountain permafrost: an example from Jotunheimen, Norway. Permafrost Periglac. 15, 191-205.

Hauck, C., Kneisel, C., 2008a. Applied Geophysics in Periglacial Environments. Cambridge University Press, Cambridge.

Hauck, C., Kneisel, C., 2008b. Electrical methods. In: C. Hauck, C. Kneisel (Eds.). Cambridge University Press, Cambridge, pp. 3-27.

Hauck, C., Kneisel, C., 2008c. Quantifying the ice content in low-altitude scree slopes using geophysical methods. In: C. Hauck, C. Kneisel (Eds.), Applied Geophysics in Periglacial Environments. University Press, Cambridge, pp. 153-164.

Hauck, C., Vieira, G., Gruber, S., Blanco, J., Ramos, M., 2007. Geophysical identification of permafrost in Livingston Island, maritime Antarctica. J. Geophys. Res.-Earth Surf. 112, F02S19.

Hauck, C., Vonder Mühll, D., 2003a. Evaluation of geophysical techniques for application in mountain permafrost studies. Z. Geomorph. N. F. Suppl.-Vol. 132, 161-190.

Hauck, C., Vonder Mühll, D., 2003b. Inversion and Interpretation of Two-Dimensional Geoelectrical Measurements for Detecting Permafrost in Mountainous Regions. Permafrost and Periglacial Processes 14, 305-318.

Hausmann, H., Krainer, K., Brückl, E., Mostler, W., 2007. Internal structure and ice content of Reichenkar rock glacier (Stubai Alps, Austria) assessed by geophysical investigations. Permafrost Periglac. 18 351-367

Heap, M.J., Faulkner, D.R., Meredith, P.G., Vinciguerra, S., 2010. Elastic moduli evolution and accompanying stress changes with increasing crack damage: implications for stress changes around fault zones and volcanoes during deformation. Geophys. J. Int. 183, 225-236.

Heilig, A., Schneebeli, M., Eisen, O., 2009. Upward-looking ground-penetrating radar for monitoring snowpack stratigraphy. Cold Regions Science and Technology 59, 152-162.

Heilig, A., Schober, M., Schneebeli, M., Fellin, W., 2008. Next level for snow pack monitoring in real-time using Ground-Penetrating Radar (GPR) technology, International Snow Science Workshop Whistler, pp. 111-117.

Heim, A., 1932. Bergsturz und Menschenleben. Beiblatt zur Viertelsjahrschrift der Naturforschenden Gesellschaft Zürich, 77.

Heincke, B., Green, A.G., van der Kruk, J., Willenberg, H., 2006a. Semblance-based topographic migration (SBTM): a method for identifying fracture zones in 3D georadar data. Near Surf. Geophys. 4, 79-88.

Heincke, B., Maurer, H., Green, A.G., Willenberg, H., Spillmann, T., Burlini, L., 2006b. Characterizing an unstable mountain slope using shallow 2D and 3D seismic tomography. Geophysics 71, B241-B256.

Hencher, S.R., 1987. The implications of joints and structures for slope stability. In: M.G. Anderson, K.S. Richards (Eds.), Slope Stability. Wiley & Sons, Oxford, pp. 145-186.

Hilbich, C., 2010. Time-lapse refraction seismic tomography for the detection of ground ice degradation. Cryosphere 4, 243-259.

Hilbich, C., Fuss, C., Hauck, C., 2011. Automated Time-lapse ERT for Improved Process Analysis and Monitoring of Frozen Ground. Permafrost Periglac. 22, 306-319.

Hilbich, C., Hauck, C., Hoelzle, M., Scherler, M., Schudel, L., Voelksch, I., Muehll, D.V., Maeusbacher, R., 2008. Monitoring mountain permafrost evolution using electrical resistivity tomography: A 7-year study of seasonal, annual, and long-term variations at Schilthorn, Swiss Alps. J. Geophys. Res. 113, F01S90.

Hilbich, C., Marescot, L., Hauck, C., Loke, M.H., Mausbacher, R., 2009. Applicability of Electrical Resistivity Tomography Monitoring to Coarse Blocky and Ice-rich Permafrost Landforms. Permafrost And Periglacial Processes 20, 269-284.

Hoek, E., Brown, E.T., 1997. Practical estimates of rock mass strength. International Journal of Rock Mechanics and Mining Sciences & Geomechanics Abstracts 34, 1165-1186.

Hoelzle, M., 1994. Permafrost und Gletscher im Oberengadin. Grundlagen und Anwendungsbeispiele für automatisierte Schätzverfahren. VAW Mitteilungen, 132.

Hoelzle, M., Mittaz, C., Etzelmuller, B., Haeberli, W., 2001. Surface energy fluxes and distribution models of permafrost in European mountain areas: an overview of current developments. Permafrost And Periglacial Processes 12, 53-68.

Hoelzle, M., Wegmann, M., Krummenacher, B., 1999. Miniature temperature dataloggers for mapping and monitoring of permafrost in high mountain areas: first experience from the Swiss Alps. Permafrost and Periglacial Processes 10, 113-124.

Huggel, C., Clague, J.J., Korup, O., 2012. Is climate change responsible for changing landslide activity in high mountains? Earth Surface Processes and Landforms 37, 77-91.

Huggel, C., Gruber, S., Caplan-Auerbach, J., Wessels, R.L., Molnia, B.F., 2008. The 2005 Mt. Steller, Alaska, rock-ice avalanche: A large slope failures in cold permafrost. In: D.L. Kane, K.M. Hinkel (Eds.), 9th Int. Conf. on Permafrost. Institute of Northern Engineering, UAF, Fairbanks, USA, pp. 747-752.

Huggel, C., Salzmann, N., Allen, S., Caplan-Auerbach, J., Fischer, L., Haeberli, W., Larsen, C., Schneider, D., Wessels, R., 2010. Recent and future warm extreme events and high-mountain slope stability. Philosophical Transactions of the Royal Society A: Mathematical, Physical and Engineering Sciences 368, 2435-2459.

Huggel, C., Zgraggen-Oswald, S., Haeberli, W., Kaab, A., Polkvoj, A., Galushkin, I., Evans, S.G., 2005. The 2002 rock/ice avalanche at Kolka/Karmadon, Russian Caucasus: assessment of extraordinary avalanche formation and mobility, and application of QuickBird satellite imagery. Natural Hazards and Earth System Sciences 5, 173-187.

Ikeda, A., 2006. Combination of Conventional Geophysical Methods for Sounding the Composition of Rock Glaciers in the Swiss Alps. Permafrost Periglac. 17, 35-48.

Ikeda, A., Matsuoka, N., 2002. Degradation of talus-derived rock glaciers in the Upper Engadin, Swiss Alps. Permafrost And Periglacial Processes 13, 145-161.

Ikeda, A., Matsuoka, N., 2006. Pebbly versus bouldery rock glaciers: Morphology, structure and processes. Geomorphology 73, 279-296.

Inada, Y., Yokota, K., 1984. Some Studies of Low-Temperature Rock Strength. Int. J. Rock Mech. Min. Sci. 21, 145-153.

Intergovernmental Panel on Climate Change, 2007. IPCC Fourth Assessment Report. Climate Change 2007 - The Physical Science Basis. Cambridge University Press, Cambridge.

Ishikawa, M., 2003. Thermal regimes at the snow-ground interface and their implications for permafrost investigation. Geomorphology 52, 105-120.

ISRM, 1978. Suggested Methods for the quantitative description of discontinuities in rock masses. International Journal of Rock Mechanics and Mining Sciences & Geomechanics Abstracts 15, 319-368.

itmsoil, 2014a. E3 Digital Tape Extensometer - Datasheet.

itmsoil, 2014b. E3 Digital Tape Extensometer - User Manual.

Jaedicke, C., 2003. Snow mass quantification and avalanche victim search by ground penetrating radar. Surveys in Geophysics 24, 431-445.

Jaedicke, C., Sandvik, A.D., 2002. High resolution snow distribution data from complex Arctic terrain: a tool for model validation. Natural Hazards and Earth System Science 2, 147-155.

Jaeger, C., 2009. Rock mechanics and engineering. Cambridge University Press, Cambridge.

Jia, H., Xiang, W., Krautblatter, M., 2014. Observation of fatigue in sandstone samples exposed to repeated freeze-thaw cycles. Geophysical Research Abstracts 16, EGU2014-15170.

Johnston, J.E., Christensen, N.I., 1995. Seismic Anisotropy of Shales. J Geophys Res-Solid Ea 100, 5991-6003.

Juliussen, H., Humlum, O., 2008. Thermal regime of openwork block fields on the mountains Elgåhogna and Sølen, central-eastern Norway. Permafrost And Periglacial Processes 19, 1-18.

Kääb, A., Huggel, C., Fischer, L., Guex, S., Paul, F., Roer, I., Salzmann, N., Schlaefli, S., Schmutz, K., Schneider, D., Strozzi, T., Weidmann, Y., 2005. Remote sensing of glacier- and permafrost-related hazards in high mountains: an overview. Natural Hazards and Earth System Sciences 5, 527-554.

Kamai, T., Weisbrod, N., Dragila, M.I., 2009. Impact of ambient temperature on evaporation from surface-exposed fractures. Water Resources Research 45, W02417.

Keller, F., 1992. Automated mapping of mountain permafrost using the program PERMAKART within the geographical information system ARC/INFO. Permafrost And Periglacial Processes 3, 133-138.

Keller, F., 1994. Interaktionen zwischen Schnee und Permafrost. Eine Grundlagenstudie im Oberengadin, ETH Zürich.

Keller, F., Gubler, H., 1993. Interaction between snow cover and high mountain permafrost, Murtèl/Corvatsch, Swiss Alps, 6th International Conference on Permafrost, Beijing, pp. 332–337.

Kelly, M.A., Buoncristiani, J.F., Schluchter, C., 2004. A reconstruction of the last glacial maximum (LGM) ice-surface geometry in the western Swiss Alps and contiguous Alpine regions in Italy and France. Eclogae Geol. Helv. 97, 57-75.

Kemeny, J., 2003. The time-dependent reduction of sliding cohesion due to rock bridges along discontinuities: A fracture mechanics approach. Rock Mech. Rock Eng. 36, 27-38.

Kemna, A., 2000. Tomographic inversion of complex resistivity—Theory and application. Berichte des Instituts für Geophysik der Ruhr-Universität Bochum Reihe A, 65. Der Andere, Osnabrück.

Kenner, R., Phillips, M., Danioth, C., Denier, C., Thee, P., Zgraggen, A., 2011. Investigation of rock and ice loss in a recently deglaciated mountain rock wall using terrestrial laser scanning: Gemsstock, Swiss Alps. Cold Reg Sci Technol 67, 157-164.

King, M.S., 1966. Wave Velocities in Rocks as a Function of Changes in Overburden Pressure and Pore Fluid Saturants. Geophysics 31, 50-73.

King, M.S., 1977. Acoustic velocities and electrical properties of frozen sandstones and shales. Can. J. Earth Sci. 14, 1004-1013.

King, M.S., 1984. The influence of clay-sized particles on seismic velocity for Canadian Arctic permafrost. Can. J. Earth Sci. 21, 19-24.

King, M.S., Zimmerman, R.W., Corwin, R.F., 1988. Seismic and electrical properties of unconsolidated permafrost. Geophys. Prospec. 36, 349-364.

Kneisel, C., Emmert, A., Kästl, J., 2014a. Application of 3D electrical resistivity imaging for mapping frozen ground conditions exemplified by three case studies. Geomorphology 210, 71-82.

Kneisel, C., Hauck, C., 2003. Multi-method geophysical investigation of a sporadic permafrost occurrence. Zeitschrift für Geomorphologie / Supplement 132, 145-159.

Kneisel, C., Hauck, C., Fortier, R., Moorman, B., 2008. Advances in geophysical methods for permafrost investigations. Permafrost Periglac. 19, 157-178.

Kneisel, C., Rodder, T., Schwindt, D., 2014b. Frozen ground dynamics resolved by multi-year and year-round electrical resistivity monitoring at three alpine sites in the Swiss Alps. Near Surf. Geophys. 12, 117-132.

Koestel, J., Kemna, A., Javaux, M., Binley, A., Vereecken, H., 2008. Quantitative imaging of solute transport in an unsaturated and undisturbed soil monolith with 3-D ERT and TDR. Water Resources Research 44.

Kohl, T., 1999. Transient thermal effects at complex topographies. Tectonophysics 306, 311-324.

Kohl, T., Gruber, S., 2003. Evidence of palaeotemperature signals in mountain permafrost areas, 8th International Conference on Permafrost, Zurich, Switzerland. Extended Abstracts, pp. 83-84.

Konrad, J.M., Morgenstern, N.R., 1982. Prediction of frost heave in the laboratory during transient freezing. Canadian Geotechnical Journal 19, 250-259.

Kos, A., Strozzi, T., Stockmann, R., Wiesmann, A., Werner, C., 2011. Detection and characterization of rock slope instabilities using a portable radar interferometer (GPRI). Proceedings of the Second World Landslide Forum – 3-7 October 2011, Rome, pp. 325-329.

Krautblatter, M., 2008. Rock Permafrost Geophysics and its Explanatory Power for Permafrost-Induced Rockfalls and Rock Creep: a Perspective. In: D.L. Kane, K.M. Hinkel (Eds.), 9th Int. Conf. on Permafrost. INE-UAF, Fairbanks, Alaska, US, pp. 999-1004.

Krautblatter, M., 2009. Detection and quantification of permafrost change in alpine rock walls and implications for rock instability, Univerität Bonn, Bonn, 164 pp.

Krautblatter, M., 2010. Patterns of multiannual aggradation of permafrost in rock walls with and without hydraulic interconnectivity (Steintälli, Valley of Zermatt, Swiss Alps). In: J. Otto, R. Dikau (Eds.), Landform - Structure, Evolution, Process Control. Proceedings of the International Symposium on Landform organised by the Research Training Group 437. Lecture Notes in Earth Sciences 115. Springer Verlag, Heidelberg, pp. 199-219.

Krautblatter, M., Dikau, R., 2007. Towards a uniform concept for the comparison and extrapolation of rockwall retreat and rockfall supply. Geogr. Ann. 89, 21-40.

Krautblatter, M., Draebing, D., 2014. Pseudo 3D - P-wave refraction seismic monitoring of permafrost in steep unstable bedrock. J. Geophys. Res. Earth Surf. 119, 287-299.

Krautblatter, M., Funk, D., Günzel, F.K., 2013. Why permafrost rocks become unstable: a rock–ice-mechanical model in time and space. Earth Surface Processes and Landforms 38, 876-887.

Krautblatter, M., Hauck, C., 2007. Electrical resistivity tomography monitoring of permafrost in solid rock walls. J. Geophys. Res. 112, F02S20.

Krautblatter, M., Heißel, G., Moser, M., Nittel, P., Verleysdonk, S., 2009. Bliggferner - Tomographie einer Massenbewegung im Permafrostbereich zur Einschätzung des Gefährdungspotentials, 11. Geoforum Umhausen, Tirol, pp. 10-12.

Krautblatter, M., Huggel, C., Deline, P., Hasler, A., 2012. Research perspectives for unstable high-alpine bedrock permafrost: measurement, modelling and process understanding. Permafrost Periglac. 23, 80-88.

Krautblatter, M., Verleysdonk, S., Flores-Orozco, A., Kemna, A., 2010. Temperature-calibrated imaging of seasonal changes in permafrost rock walls by quantitative electrical resistivity tomography (Zugspitze, German/Austrian Alps). J. Geophys. Res. 115, F02003.

Krus, M., 1995. Feuchtetransport und Speicherkoeffizienten poröser mineralischer Baustoffe - theoretische Grundlagen und neue Meßtechniken. Fakultät für Bauingenieur- und Vermessungswesen. University of Stuttgart, Stuttgart.

Kukkonen, I.T., Safanda, J., 2001. Numerical modelling of permafrost in bedrock in northern Fennoscandia during the Holocene. Global and Planetary Change 29, 259-273.

Kurfurst, P.J., Hunter, J.A., 1977. Field and laboratory measurements of seismic properties of permafrost, Proceedings of a Symposium on Permafrost Geophysics, pp. 1-15.

LaBrecque, D.J., Miletto, M., Daily, W., Ramirez, A., Owen, E., 1996. The effects of noise on Occam's inversion of resistivity tomography data. Geophysics 61, 538-548.

Lachenbruch, A.H., Marshall, B.V., 1986. Changing climate - geothermal evidence from permafrost in the Alaskan Arctic. Science 234, 689-696.

Lanz, E., Maurer, H., Green, A.G., 1998. Refraction tomography over a buried waste disposal site. Geophysics 63, 1414-1433.

Lapen, D.R., Martz, L.W., 1996. An investigation of the spatial association between snow depth and topography in a Prairie agricultural landscape using digital terrain analysis. Journal of Hydrology 184, 277-298.

Leclaire, P., Cohen-Ténoudji, F., J., A.-P., 1994. Extension of Biot's theory of wave propagation to frozen porous media. J. Acoust. Soc. Am. 96, 3753-3768.

Lehning, M., 2005. Energy Balance and Thermophysical Processes in Snowpacks. In: M.G. Anderson, J.J. McDonnell (Eds.), Encyclopedia of the Hydrological Sciences. Wiley, Chichester, pp. 2475-2490.

Lehning, M., Bartelt, P., Brown, B., Fierz, C., 2002. A physical SNOWPACK model for the Swiss avalanche warning Part III: Meteorological forcing, thin layer formation and evaluation. Cold Regions Science and Technology 35, 169-184.

Lehning, M., Lowe, H., Ryser, M., Raderschall, N., 2008. Inhomogeneous precipitation distribution and snow transport in steep terrain. Water Resources Research 44, W07404.

Lehning, M., Volksch, I., Gustafsson, D., Nguyen, T.A., Stähli, M., Zappa, M., 2006. ALPINE3D: a detailed model of mountain surface processes and its application to snow hydrology. Hydrological Processes 20, 2111-2128.

Lipovsky, P., Evans, S., Clague, J., Hopkinson, C., Couture, R., Bobrowsky, P., Ekström, G., Demuth, M., Delaney, K., Roberts, N., Clarke, G., Schaeffer, A., 2008. The July 2007 rock and ice avalanches at Mount Steele, St. Elias Mountains, Yukon, Canada. Landslides 5, 445-455.

Lo, T.W., Coyner, K.B., Toksoz, M.N., 1986. Experimental-Determination of Elastic-Anisotropy of Berea Sandstone, Chicopee Shale, and Chelmsford Granite. Geophysics 51, 164-171.

Lock, G.S.H., 2005. The growth and decay of ice. Cambridge University Press, Cambridge.

Luetschg, M., 2005. A model and field analysis of the interaction processes between snow cover and Alpine permafrost, University of Zurich.

Luetschg, M., Bartelt, P., Lehning, M., Stoeckli, V., Haeberli, W., 2003. Numerical simulation of the interaction processes between snow cover and alpine permafrost. In: M. Phillips, S. Springman, L. Arenson (Eds.), 8th International Conference on Permafrost, Zurich, Switzerland, pp. 697-702.

Luetschg, M., Haeberli, W., 2005. Permafrost evolution in the Swiss Alps in a changing climate and the role of the snow cover. Norsk Geografisk Tidsskrift 59, 78-83.

Luetschg, M., Lehning, M., Haeberli, W., 2008. A sensitivity study of factors influencing warm/thin permafrost in the Swiss Alps. J. Glac. 54, 696-704.

Luetschg, M., Stoeckli, V., Lehning, M., Haeberli, W., Ammann, W., 2004. Temperatures in two boreholes at Flüela Pass, Eastern Swiss Alps: the effect of snow redistribution on permafrost distribution patterns in high mountain areas. Permafrost and Periglacial Processes 15, 283-297.

Machguth, H., Eisen, O., Paul, F., Hoelzle, M., 2006. Strong spatial variability of snow accumulation observed with helicopter-borne GPR on two adjacent Alpine glaciers. Geophysical Research Letters 33.

Mahmutoglu, Y., 1998. Mechanical Behaviour of Cyclically Heated Fine Grained Rock. Rock Mech. Rock Eng. 31, 169-179.

Marchand, W.D., Bruland, O., Killingtveit, A., 2001. Improved Measurements and Analysis of Spatial Snow Cover by Combining a Ground Based Radar System With a Differential Global Positioning System Receiver. Nordic Hydrology 32, 181-194.

Marchand, W.D., Killingtveit, A., 2001. Analyses of the Relation Between Spatial Snow Distribution and Terrain Characteristics, 58th Eastern Snow Conference, Ottawa, Ontario, Canada.

Marmy, A., Salzmann, N., Scherler, M., Hauck, C., 2013. Permafrost model sensitivity to seasonal climatic changes and extreme events in mountainous regions. Environmental Research Letters 8, 1-9.

Matsuoka, N., 1990a. Mechanisms of Rock Breakdown by Frost Action - an Experimental Approach. Cold Reg Sci Technol 17, 253-270.

Matsuoka, N., 1990b. The rate of bedrock weathering by frost action - field-measurements and a predictive model. Earth Surface Processes and Landforms 15, 73-90.

Matsuoka, N., 1991. A model of the rate of frost shattering: Application to field data from Japan, Svalbard and Antarctica. Permafrost And Periglacial Processes 2, 271-281.

Matsuoka, N., 2001a. Direct observation of frost wedging in alpine bedrock. Earth Surf. Proc. Land. 26, 601-614.

Matsuoka, N., 2001b. Microgelivation versus macrogelivation: towards bridging the gap between laboratory and field frost weathering. Permafrost and Periglacial Processes 12, 299-313.

Matsuoka, N., 2008. Frost weathering and rockwall erosion in the southeastern Swiss Alps: Long-term (1994-2006) observations. Geomorphology 99, 353-368.

Matsuoka, N., Hirakawa, K., Watanabe, T., Haeberli, W., Keller, F., 1998. The role of diurnal, annual and millenial freeze-thaw cycles in controlling alpine slope stability, 7th International Conference on Permafrost, Yellowknife, Canada, pp. 711-717.

Matsuoka, N., Hirakawa, K., Watanabe, T., Moriwaki, K., 1997. Monitoring of Periglacial Slope Processes in the Swiss Alps: the First Two Years of Frost Shattering, Heave and Creep. Permafrost And Periglacial Processes 8, 155-177.

Matsuoka, N., Murton, J., 2008. Frost weathering: Recent advances and future directions. Permafrost Periglac. 19, 195-210.

Matsuoka, N., Sakai, H., 1999. Rockfall activity from an alpine cliff during thawing periods. Geomorphology 28, 309-328.

Maurer, H., Hauck, C., 2007. Instruments and methods - Geophysical imaging of alpine rock glaciers. Journal of Glaciology 53, 110-120.

Mavko, G., Mukerji, T., Dvorkin, J., 2009. The Rock Physics Handbook. Cambridge University Press, Cambridge.

McColl, S.T., 2012. Paraglacial rock-slope stability. Geomorphology 153–154, 1-16.

McColl, S.T., Davies, T.R.H., 2013. Large ice-contact slope movements: glacial buttressing, deformation and erosion. Earth Surface Processes and Landforms 38, 1102-1115.

McColl, S.T., Davies, T.R.H., McSaveney, M.J., 2010. Glacier retreat and rock-slope stability: debunking debuttressing. Delegate Papers, Geologically Active, 11th Congress of the International Association for Engineering Geology and the Environment, Auckland, New Zealand, 467–474.

McGinnis, L.D., Nakao, K., Clark, C.C., 1973. Geophysical identification of frozen and unfrozen ground, Antarctica. 2nd International Conference on Permafrost 1973. Northamerican Contribution, Yakutsk, USSR, 136-146.

McGreevy, J.P., 1985. Thermal properties as controls on rock surface temperature maxima, and possible implications for rock weathering. Earth Surface Processes and Landforms 10, 125-136.

McGreevy, J.P., Whalley, W.B., 1982. The geomorphic significance of rock temperature-variations in cold environments - a discussion. Arctic and Alpine Research 14, 157-162.

McGreevy, J.P., Whalley, W.B., 1985. Rock moisture-content and frost weathering under natural and experimental conditions - a comparative discussion. Arctic and Alpine Research 17, 337-346.

Mellor, M., 1970. Phase composition of pore water in cold rocks, CRREL Res. Rep. 292.

Mellor, M., 1971. Strength and deformability of rocks at low temperature, CRREL Res. Rep. 294.

Mellor, M., 1973. Mechanical properties of rocks at low temperatures. 2nd International Conference on Permafrost. Northamerican Contribution 1973, Yakutsk, USSR, 334-344.

Melvold, K., 2008. Snow measurements using GPR: example from Amundsenisen, Svalbard. In: C. Hauck, C. Kneisel (Eds.), Applied Geophysics in Periglacial Environments. Cambridge University Press, pp. 207-216.

Messerli, B., 2006. From nature-dominated to human-dominated global environmental change in mountains of the world. In: M.F. Price (Ed.), Global Change in Mountain Regions. Sapiens Publishing, Duncow, pp. 3-5.

Minshull, T.A., Singh, S.C., Westbrook, G.K., 1994. Seismic Velocity Structure at a Gas Hydrate Reflector, Offshore Western Colombia, from Full-Wave-Form Inversion. J. Geophys. Res. 99, 4715-4734.

Mittaz, C., Hoelzle, M., Haeberli, W., 2000. First results and interpretation of energy-flux measurements over Alpine permafrost. Annals of Glaciology 31, 275-280.

Mittaz, C., Imhof, M., Hoelzle, M., Haeberli, W., 2002. Snowmelt evolution mapping using an energy balance approach over an alpine terrain. Arctic, Antarctic and Alpine Research 34, 264-281.

Moore, J.R., Gischig, V., Katterbach, M., Loew, S., 2011. Air circulation in deep fractures and the temperature field of an alpine rock slope. Earth Surface Processes and Landforms 36, 1985-1996.

Moorman, B., 2005. Glacier-permafrost hydrological interconnectivity: Stagnation Glacier, Bylot Island, Canada. In: C. Harris, J.B. Murton (Eds.), Cryospheric systems: Glaciers and Permafrost. Special Publication. Geological Society, London, pp. 63-74.

Morán-Tejeda, E., López-Moreno, J.I., Beniston, M., 2013. The changing roles of temperature and precipitation on snowpack variability in Switzerland as a function of altitude. Geophysical Research Letters 40, 2131-2136.

Moser, M., Wunderlich, T.A., Meier, H., 2009. Kinematische Analyse der Bergzerreißung Hornbergl – Reutte (Tirol). Jahrbuch der Geologischen Bundesanstalt 149, 177-193.

Mott, R., Faure, F., Lehning, M., Löwe, H., Hynek, B., Michlmayer, G., Prokop, A., Schöner, W., 2008. Simulation of seasonal snow-cover distribution for glacierized sites on Sonnblick, Austria, with the Alpine3D model. Annals of Glaciology 49, 155-160.

Mott, R., Schirmer, M., Bavay, M., Grunewald, T., Lehning, M., 2010. Understanding snow-transport processes shaping the mountain snow-cover. Cryosphere 4, 545-559.

Muller, S.W., 2008. Frozen in Time. Permafrost and Engineering Problems. ASCE, Reston.

Murton, J.B., Coutard, J.-P., Lautridou, J.-P., Ozouf, J.-C., Robinson, D.A., Williams, R.B.G., 2001. Physical Modelling of Bedrock Brecciation by Ice Segregation in Permafrost. Permafrost and Periglacial Processes 12, 255–266.

Murton, J.B., Coutard, J.P., Lautridou, J.P., Ozouf, J.C., Robinson, D.A., Williams, R.B.G., Guillemet, G., Simmons, P., 2000. Experimental design for a pilot study on bedrock weathering near the permafrost table. Earth Surf. Proc. Land. 25, 1281-1294.

Murton, J.B., Peterson, R., Ozouf, J.C., 2006. Bedrock fracture by ice segregation in cold regions. Science 314, 1127-1129.

Musil, M., Maurer, H., Green, A.G., Horstmeyer, H., Nitsche, F., Vonder Mühll, D., Springman, S., 2002. Shallow seismic surveying of an Alpine rock glacier. Geophysics 67, 1701-1710.

Nakano, Y., Smith, M., Martin, R.J., 1972. Ultrasonic Velocities of Dilatational and Shear Waves in Frozen Soils. Water Resources Research 8, 1024-1030.

Nixon, J.F., 1982. Field frost heave predictions using the segregation potential concept. Canadian Geotechnical Journal 19, 526-529.

Noetzli, J., 2008. Modeling Transient Three-dimensional Temperature Fields in Mountain Permafrost, Mathematisch-naturwissenschaftliche Fakultät der Universität Zürich.

Noetzli, J., Gruber, S., 2009. Transient thermal effects in Alpine permafrost. The Cryosphere 3, 85-99.

Noetzli, J., Gruber, S., 2012. Permafrost Temperatures, Analytical Models. Lecture on Quantification and modeling of spatial processes in high mountain areas GEO 413.2, GEO 814, University of Zurich.

Noetzli, J., Gruber, S., Kohl, T., Salzmann, N., Haeberli, W., 2007. Three-dimensional distribution and evolution of permafrost temperatures in idealized high-mountain topography. Journal of Geophysical Research 112, F02S13.

Noetzli, J., Hoelzle, M., Haeberli, W., 2003. Mountain permafrost and recent Alpine rock-fall events: a GIS-based approach to determine critical factors In: M. Phillips, S. Springman, L. Arenson (Eds.), 8th International Conference on Permafrost Zurich, Switzerland, pp. 827-832.

Nogués-Bravo, D., Araújo, M.B., Errea, M.P., Martínez-Rica, J.P., 2007. Exposure of global mountain systems to climate warming during the 21st Century. Global Environ. Chan. 17, 420-428.

NRC-Permafrost-Subcommitee, 1988. Glossary of Permafrost and related ground-ice terms. NRC Technical Memorandum 142, 1-156.

Nur, A., Simmons, G., 1969. Effect of Saturation on Velocity in Low Porosity Rocks. Earth Planet. Sci. Lett. 7, 183-193.

O'Neill, R.V., DeAngelis, D.L., Waide, J.B., Allen, T.F.H., 1986. A Hierarchical Concept of Ecosystems. Princeton University Press, Princeton.

Oertel, D., 2009. Paraglacial rock and glacier forefield dynamics in the Turt-mann and Matter Valleys, Valais, Switzerland. Dipl. Thesis, unpublished, University of Bonn.

Oke, T.R., 1987. Boundary Layer Climates. Methuen, London, New York.

Oppikofer, T., Bunkholt, H.S.S., Fischer, L., Saintot, A., Hermanns, R.L., Carrea, D., Longchamp, C., Derron, M.H., Michoud, C., M., J., 2012. Investigation and monitoring of rock slope instabilities in Norway by terrestrial laser scanning. In: E. Eberhardt, C. Froese, K. Turner, S. Leroueil (Eds.), Landslides and Engineered Slopes: Protecting Society through Improved Understanding. Routledge, New York, pp. 1235-1241.

Oppikofer, T., Jaboyedoff, M., Keusen, H.-R., 2008. Collapse at the eastern Eiger flank in the Swiss Alps. Nature Geoscience 1, 531-535.

Ortlieb, C., 2012. Der Einfluss periglazialer Phänomene auf kriechende Felshänge im Turtmanntal, Wallis, Schweiz. Dipl. Thesis, unpublished, University of Bonn.

Osterkamp, T.E., 1983. Response of Alaskan permafrost to climate, 4th International Conference on Permafrost, Fairbanks, Alaska, pp. 145-152.

Otto, J.-C., Dikau, R., 2004. Geomorphic system analysis of a high mountain valley in the Swiss Alps. Zeitschrift für Geomorphologie N.F. 48, 323-341.

Otto, J.C., Keuschnig, M., Götz, J., Marbach, M., Schrott, L., 2012. Detection of mountain permafrost by combining high resolution surface and subsurface information - an example from the Glatzbach catchment, Austrian Alps. Geografiska Annaler Series A-physical Geography 94A, 43-57.

Otto, J.C., Sass, O., 2006. Comparing geophysical methods for talus slope investigations in the Turtmann valley (Swiss Alps). Geomorphology 76, 257-272.

Ottowitz, D., Jochum, B., Supper, R., Römer, A., Pfeiler, S., Keuschnig, M., 2012. Permafrost monitoring at Mölltaler Glacier and Magnetköpfl. Berichte Geol. B.-A. 93, 57-64.

Overduin, P.P., Westermann, S., Yoshikawa, K., Haberlau, T., Romanovsky, V., Wetterich, S., 2012. Geoelectric observations of the degradation of nearshore submarine permafrost at Barrow (Alaskan Beaufort Sea). J. Geophys. Res.-Earth Surf. 117, F02004.

Pälli, A., Kohler, J.C., Isaksson, E., Moore, J.C., Pinglot, J.F., Pohjola, V.A., Samuelsson, H., 2002. Spatial and temporal variability of snow accumulation using ground-penetrating radar and ice cores on a Svalbard glacier. Journal of Glaciology 48, 417-424.

Palmström, A., 1982. The Volumetric Joint Count – a useful and simple measure of the degree of Rock Mass Jointing, Proceedings of the IV Congress International Association of Engineering Geology, New Delhi.

Pandit, B.I., King, M.S., 1979. A study of the effects of pore-water salinity on some physical properties of sedimentary rocks at permafrost temperatures. Can. J. Earth Sci. 16, 1566-1580.

Patton, F.D., 1966. Multiple modes of shear failure in rock, 1st Congress of the International Society for Rock Mechanics, Laboratory of Civil Engineering, Lisbon, pp. 509–513.

Pearson, C., Murphy, J., Hermes, R., 1986. Acoustic and Resistivity Measurements on Rock Samples Containing Tetrahydrofuran Hydrates - Laboratory Analogs to Natural-Gas Hydrate Deposits. J. Geophys. Res.-Solid 91, 14132-14138.

PERMOS, 2013. Permafrost in Switzerland 2008/2009 and 2009/2010. In: J. Noetzli (Ed.), Glaciological Report (Permafrost) No. 10/11 of the Cryospheric Commission of the Swiss Academy of Sciences, Zürich.

Petschik, M., 2014. Zeitliche Hangstabilitätsanalyse und vorbereitende/auslösende Faktoren anhand der Bewegungszeitreihen am Hornbergl seit 1996. MSc, TU München.

Phillips, J.D., 1999. Earth Surface Systems, Oxford.

Phillips, M., 2000. Influences of snow supporting structures on the thermal regime of the ground in alpine permafrost terrain, Eidgenössisches Institut für Schnee- und Lawinenforschung, Davos.

Pielmeier, C., Schneebeli, M., 2003. Developments in the Stratigraphy of Snow. Surveys In Geophysics 24, 389-416.

Pirulli, M., 2009. The Thurwieser rock avalanche (Italian Alps): Description and dynamic analysis. Engineering Geology 109, 80-92.

Pogrebiskiy, M.I., Chernyshev, S.N., 1977. Determination of the permeability of the frozen fissured rock massif in the vicinity of the Kolyma Hydroelectric Power Station. Cold Regions Research and Engineering Laboratory - Draft Translation 634, 1-13.

Prick, A., 1997. Critical Degree of Saturation as a Threshold Moisture Level in Frost Weathering of Limestones. Permafrost And Periglacial Processes 8, 91-99.

Priest, S.D., 1993. Discontinuity Analysis for Rock Engineering. Chapman & Hall, London, Glasgow.

Prinz, H., Strauß, R., 2011. Ingeniergeologie. Spektrum, Heidelberg.

Prokop, A., 2008. Assessing the applicability of terrestrial laser scanning for spatial snow depth measurements. Cold Regions Science and Technology 54, 155-163.

Prokop, A., Schirmer, M., Rub, M., Lehning, M., Stocker, M., 2008. A comparison of measurement methods: terrestrial laser scanning, tachymetry and snow probing for the determination of the spatial snow-depth distribution on slopes. Annals of Glaciology 49, 210-216.

Rabatel, A., Deline, P., Jaillet, S., Ravanel, L., 2008. Rock falls in high-alpine rock walls quantified by terrestrial lidar measurements: A case study in the Mont Blanc area. Geophysical Research Letters 35, L10502.

Ravanel, L., Allignol, F., Deline, P., Gruber, S., Ravello, M., 2010. Rock falls in the Mont Blanc Massif in 2007 and 2008. Landslides 7, 493-501.

Ravanel, L., Deline, P., 2008. La face ouest des Drus (massif du Mont-Blanc). Évolution de l'instabilité d'une paroi rocheuse dans la haute montagne alpine depuis la fin du petit age glaciaire. Géomorphologie : relief, processus, environnement 4, 261-272.

Ravanel, L., Deline, P., 2010. Climate influence on rockfalls in high-Alpine steep rockwalls: The north side of the Aiguilles de Chamonix (Mont Blanc massif) since the end of the 'Little Ice Age'. Holocene 21, 357-365.

Ravanel, L., Deline, P., Lambiel, C., Vincent, C., 2013. Instability of a High Alpine Rock Ridge: the Lower Arete Des Cosmiques, Mont Blanc Massif, France. Geografiska Annaler Series A-physical Geography 95A, 51-66.

Rees, W., G., 2006. Remote Sensing of snow and ice. Taylor & Francis, Boca Raton.

Remy, J.M., Bellanger, M., Homandetienne, F., 1994. Laboratory Velocities and Attenuation of P-Waves in Limestones During Freeze-Thaw Cycles. Geophysics 59, 245-251.

Richter, D., Simmons, G., 1974. Thermal expansion behavior of igneous rocks. International Journal of Rock Mechanics and Mining Sciences & Geomechanics Abstracts 11, 403-411.

Rodder, T., Kneisel, C., 2012. Permafrost mapping using quasi-3D resistivity imaging, Murtel, Swiss Alps. Near Surf. Geophys. 10, 117-127.

Roethlisberger, H., 1960. Seismic refraction soundings in permafrost near Thule, greenland. In: G.O. Raasch (Ed.), Proceedings of the first International Symposium on Arctic Geology. University of Toronto Press, Calgary, Alberta, pp. 970-980.

Rosset, E., Hilbich, C., Schneider, S., Hauck, C., 2013. Automatic filtering of ERT monitoring data in mountain permafrost. Near Surf. Geophys. 11, 423-433.

Salzmann, N., Nötzli, J., Hauck, C., Gruber, S., Hoelzle, M., Haeberli, W., 2007. Ground surface temperature scenarios in complex high-mountain topography based on regional climate model results. Journal of Geophysical Research 112, F02S12.

Sand, K., Bruland, O., 1998. Application of georadar for snow cover surveying. Nordic Hydrology 29, 361-370.

Sand, K., G., W.J., D., M., O., B., Melvold, K., 2003. Regional Variations of Snow Accumulation on Spitsbergen, Svalbard, 1997-99. Nordic Hydrology 34, 17-32.

Sandmeier, K.J., 2008. REFLEXW Version 5.5. Manual. Karlsruhe.

Sass, O., 1998. Die Steuerung von Steinschlagmenge und -verteilung durch Mikroklima, Gesteinsfeuchte und Gesteinseigenschaften im westlichen Karwendelgebirge (Bayerische Alpen). Münchner Geogr. Abh. 29B, 1-175.

Sass, O., 2003. Moisture distribution in rockwalls derived from 2D-resistivity measurements. Z. Geomorph. N.F. Suppl.-Vol. 132, 51-69.

Sass, O., 2004. Rock Moisture Fluctuations During Freeze-thaw Cycles: Preliminary Results from Electrical Resistivity Measurements. Polar Geography 28, 13-31.

Sass, O., 2005a. Rock moisture measurements: techniques, results, and implications for weathering. Earth Surf. Proc. Land. 30, 359-374.

Sass, O., 2005b. Spatial patterns of rockfall intensity in the northern Alps. Z. Geomorph. N. F. Suppl.-Bd. 138, 51-65.

Schaffhauser, A., Adams, M., Fromm, R., Jörg, P., Luzi, G., Noferini, L., Sailer, R., 2008. Remote sensing based retrieval of snow cover properties. Cold Regions Science and Technology 54, 164-175.

Schär, C., Vidale, P.L., Lüthi, D., Frei, C., Häberli, C., Liniger, M.A., Appenzeller, C., 2004. The role of increasing temperature variability in European summer heatwaves. Nature 427, 332-336.

Scherler, M., Hauck, C., Hoelzle, M., Salzmann, N., 2013. Modeled sensitivity of two alpine permafrost sites to RCM-based climate scenarios. J. Geophys. Res.-Earth Surf. 118, 780-794.

Scherler, M., Hauck, C., Hoelzle, M., Stähli, M., Völksch, I., 2010. Meltwater infiltration into the frozen active layer at an alpine permafrost site. Permafrost And Periglacial Processes 21, 325-334.

Schirmer, M., Wirz, V., Clifton, A., Lehning, M., 2011. Persistence in intra-annual snow depth distribution: 1. Measurements and topographic control. Water Resources Research 47, W09516.

Schmid, M.O., Gubler, S., Fiddes, J., Gruber, S., 2012. Inferring snowpack ripening and melt-out from distributed measurements of near-surface ground temperatures. Cryosphere 6, 1127-1139.

Schmidt, M., 2010. Snow Cover Duration in Relation to Topography in the Loetschental, Switzerland. In: J.C. Otto, R. Dikau (Eds.), Landform - Structure, Evolution, Process Control. Proceedings of the International Symposium on Landform organised by the Research Training Group 437. Lecture Notes in Earth Sciences 115. Springer Verlag, Heidelberg, pp. 151-164.

Schmidt, S., 2009. Die reliefabhängige Schneedeckenverteilung im Hochgebirge - ein multiskaliger Methodenverbund am Beispiel des Lötschentals (Schweiz). Bonner Geographische Abhandlungen 123.

Schmidt, S., Weber, B., Winiger, M., 2009. Analyses of seasonal snow disappearance in an alpine valley from micro- to meso-scale (Loetschental, Switzerland). Hydrological processes 23, 1041-1051.

Schneider, S., Daengeli, S., Hauck, C., Hoelzle, M., 2013. A spatial and temporal analysis of different periglacial materials by using geoelectrical, seismic and borehole temperature data at Murtèl–Corvatsch, Upper Engadin, Swiss Alps. Geographica Helvetica 63, 265-280.

Schneider, S., Hoelzle, M., Hauck, C., 2012. Influence of surface and subsurface heterogeneity on observed borehole temperatures at a mountain permafrost site in the Upper Engadine, Swiss Alps. Cryosphere 6, 517-531.

Schoeneich, P., Hantz, D., Vengon, M., Frayssines, M., Deline, P., Amelot, F., Savary, J., 2004. A new Alpine rockfall inventory. Swiss Geoscience Meeting, Lausanne.

Schrott, L., Otto, J.C., Keller, F., 2012. Modelling alpine permafrost distribution in the Hohe Tauern Region, Austria. Austrian Journal of Earth Sciences 105, 169-183.

Schrott, L., Sass, O., 2008. Application of field geophysics in geomorphology: Advances and limitations exemplified by case studies. Geomorphology 93, 55-73.

Schumm, S.A., 1973. Geomorphic thresholds and complex response of drainage systems In: M. Morisawa (Ed.), Fluvial Geomorphology: Proc. of the 4th Annual Geomorphology Symposium, Binghamton, New York, pp. 299-310.

Schumm, S.A., 1991. To interpret the earth. Ten ways to be wrong, Cambridge.

Schumm, S.A., Lichty, R.W., 1965. Time space and causality in geomorphology. American Journal of Science 263, 110-119.

Schweizer, J., Kronholm, K., Jamieson, J.B., Birkeland, K.W., 2008. Review of spatial variability of snowpack properties and its importance for avalanche formation. Cold Regions Science and Technology 51, 253-272.

Scott, W.J., Sellmann, P.V., Hunter, J.A., 1990. Geophysics in the study of permafrost. In: S. Ward (Ed.), Geotechnical and Environmental Geophysics. Soc. of Expl. Geoph., Tulsa, pp. 355-384.

Selby, M.J., 1980. A rock mass strength classification for geomorphic purposes: with tests from Antarctica amd New Zealand. Z. Geormorph. N.F. 24, 31-51.

Seligman, G., 1980. Snow structure and ski fields : beeing an account of snow and ice forms met with in nature and a study on avalanches and snowcraft. Forster & Jagg, Cambridge.

Seyfried, M.S., Murdock, M.D., 1997. Use of air permeability to estimate infiltrability of frozen soil. Journal of Hydrology 202, 95-107.

Siegesmund, S., Mosch, S., Scheffzuk, C., Nikolayev, D.I., 2008. The bowing potential of granitic rocks: rock fabrics, thermal properties and residual strain. Environmental Geology 55, 1437-1448.

Siewert, M.B., Krautblatter, M., Christiansen, H.H., Eckerstorfer, M., 2012. Arctic rockwall retreat rates estimated using laboratory-calibrated ERT measurements of talus cones in Longyeardalen, Svalbard. Earth Surface Processes and Landforms 37, 1542-1555.

Sjogren, B., 1984. Shallow Refraction Seismics. Chapman & Hall, London.

Sjogren, B., Ofsthus, A., Sandberg, J., 1979. Seismic Classification of Rock Mass Qualities. Geophys. Prospec. 27, 409-442.

Slater, L., Binley, A.M., Daily, W., Johnson, R., 2000. Cross-hole electrical imaging of a controlled saline tracer injection. Journal of Applied Geophysics 44, 85-102.

Slaymaker, O., 2009. Proglacial, periglacial or paraglacial? In: J. Knight, S. Harrison (Eds.), Periglacial and Paraglacial Processes and Environments. Geological Society Special Publications. The Geological Society: London, pp. 268–288.

Slaymaker, O., Kelly, R.E.J., 2007. The Cryosphere and global environmental change. Environmental systems and global change series. Blackwell, Oxford.

Soldati, M., 2004. Deep-seated gravitational slope deformation. In: A. Goudie (Ed.), Encyclopedia of Geomorphology. Routledge, London, pp. 226-228.

Sondergeld, C.H., Rai, C.S., 2007. Velocity and resistivity changes during freeze-thaw cycles in Berea sandstone. Geophysics 72, E99-E105.

Sosio, R., Crosta, G.B., Hungr, O., 2008. Complete dynamic modeling calibration for the Thurwieser rock avalanche (Italian Central Alps). Engineering Geology 100, 11-26.

Springman, S.M., Arenson, L.U., Yamamoto, Y., Maurer, H., Kos, A., Buchli, T., Derungs, G., 2012. Multidisciplinary investigations on three rock glaciers in the Swiss Alps: legacies and future perspectives. Geografiska Annaler: Series A, Physical Geography 94, 215-243.

Stähli, M., 2005. Freezing and thawing phenomena in soils. In: M.G. Anderson, J.J. McDonnell (Eds.), Encyclopedia of the Hydrological Sciences. Wiley, Chichester, pp. 1069-1077.

Stocker-Mittaz, C., Hoezle, M., Haeberli, W., 2002. Modelling alpine permafrost distribution based on energy-balance data: a first step. Permafrost And Periglacial Processes 13, 271-282.

Strozzi, T., Ambrosi, C., Raetzo, H., 2013. Interpretation of Aerial Photographs and Satellite SAR Interferometry for the Inventory of Landslides. Remote Sensing 5, 2554-2570.

Strozzi, T., Delaloye, R., Kaab, A., Ambrosi, C., Perruchoud, E., Wegmuller, U., 2010. Combined observations of rock mass movements using satellite SAR interferometry, differential GPS, airborne digital photogrammetry, and airborne photography interpretation. J. Geophys. Res.-Earth Surf. 115, F01014.

Sturm, M., Holmgren, J., Konig, M., Morris, K., 1997. The thermal conductivity of seasonal snow. Journal of Glaciology 43, 26-41.

Supper, R., Ottowitz, D., Jochum, B., Roemer, A., Pfeiler, S., Kauer, S., Keuschnig, M., Ita, A., 2014. Geoelectrical monitoring of frozen ground and permafrost in alpine areas: field studies and considerations towards an improved measuring technology. Near Surf. Geophys. 12, 93-115.

Taber, S., 1929. Frost Heaving. The Journal of Geology 37, 428-461.

Taber, S., 1930. The Mechanics of Frost Heaving. The Journal of Geology 38, 303-317.

Takeuchi, S., Simmons, G., 1973. Elasticity of Water-Saturated Rocks as a Function of Temperature and Pressure. J. Geophy. Res.-Solid Ea. 78, 3310-3320.

Terzaghi, 1962. Stability of steep slopes in hard unweathered rock. Geotechnique 12, 251–270.

Tharp, T.M., 1987. Conditions for crack propagation by frost wedging. Geological Society of America Bulletin 99, 94-102.

Thomsen, L., 1986. Weak Elastic-Anisotropy. Geophysics 51, 1954-1966.

Tiab, D., Donaldson, E.C., 2004. Petrophysics. Theory and practice of measuring reservoir rock and fluid transport properties. Elsevier, Oxford.

Tice, A.R., Burrous, A.M., Anderson, D.M., 1978. Determination of unfrozen water in frozen soil by pulsed nuclear magnetic resonance, 3rd International Conference on Permafrost, Edmonton, Canada, pp. 149-155.

Timur, A., 1968. Velocity of compressional waves in porous media at permafrost temperatures. Geophysics 33, 584-595.

Toksöz, M.N., Cheng, C.H., Timur, A., 1976. Velocities of Seismic-Waves in Porous Rocks. Geophysics 41, 621-645.

Tricart, J., 1970. Geomorphology of Cold Regions, London.

Varnes, D.J., 1978. Slope Movement Types and Processes. In: R.L. Schuster, R.J. Krizek (Eds.), Landslides, Analysis and control. Transportation Research Board, Special Report National Research Council, Washington, D.C., pp. 11-33.

Verleysdonk, S., Krautblatter, M., Dikau, R., 2011. Sensitivity and path dependence of mountain permafrost systems. Geogr. Ann. 93A, 113-135.

Vernik, L., Nur, A., 1992. Ultrasonic Velocity and Anisotropy of Hydrocarbon Source Rocks. Geophysics 57, 727-735.

Viles, H., Goudie, A., Grab, S., Lalley, J., 2011. The use of the Schmidt Hammer and Equotip for rock hardness assessment in geomorphology and heritage science: a comparative analysis. Earth Surface Processes and Landforms 36, 320-333.

Viles, H.A., 2001. Scale issues in weathering studies. Geomorphology 41, 63-72.

Viles, H.A., 2013a. 4.2 Synergistic Weathering Processes. In: J.F. Shroder (Ed.), Treatise on Geomorphology. Academic Press, San Diego, pp. 12-26.

Viles, H.A., 2013b. Linking weathering and rock slope instability: non-linear perspectives. Earth Surface Processes and Landforms 38, 62-70.

Viles, H.A., Naylor, L.A., Carter, N.E.A., Chaput, D., 2008. Biogeomorphological disturbance regimes: progress in linking ecological and geomorphological systems. Earth Surface Processes and Landforms 33, 1419-1435.

Vlahou, I., Worster, M.G., 2010. Ice growth in a spherical cavity of a porous medium. Journal of Glaciology 56, 271-277.

Vogel, S., Eckerstorfer, M., Christiansen, H.H., 2012. Cornice dynamics and meteorological control at Gruvefjellet, Central Svalbard. Cryosphere 6, 157-171.

Vonder Mühll, D., Hauck, C., Gubler, H., 2002. Mapping of mountain permafrost using geophysical methods. Progress in Physical Geography 26, 643-660.

Vonder Mühll, D., Hauck, C., Gubler, H., McDonald, R., Russill, N., 2001. New geophysical methods of investigating the nature and distribution of mountain permafrost with special reference to radiometry techniques. Permafrost Periglac. 12, 27-38.

Vosteen, H.D., Schellschmidt, R., 2003. Influence of temperature on thermal conductivity, thermal capacity and thermal diffusivity for different types of rock. Phys. Chem. Earth 28, 499-509.

Walder, J., Hallet, B., 1985. A Theoretical-Model of the Fracture of Rock During Freezing. Geological Society of America Bulletin 96, 336-346.

Walder, J.S., Hallet, B., 1986. The Physical Basis of Frost Weathering - toward a More Fundamental and Unified Perspective. Arctic Alpine Res. 18, 27-32.

Wang, Z.J., 2001. Fundamentals of seismic rock physics. Geophysics 66, 398-412.

Ward, S., 2004. Sackung. In: A. Goudie (Ed.), Encyclopedia of Geomorphology. Routledge, London, pp. 890-892.

Wassermann, J., Senfaute, G., Amitrano, D., Homand, F., 2009. Evidence of dilatant and non-dilatant damage processes in oolitic iron ore: P-wave velocity and acoustic emission analyses. Geophys. J. Int. 177, 1343-1356.

Watanabe, T., Matsuoka, N., Christiansen, H.H., 2012. Mudboil and ice-wedge dynamics investigated by electrical resistivity tomogrpahy, ground temperatures and surface movements in Svalbard. Geografiska Annaler Series A-physical Geography 94A, 445-457.

Weertman, J., 1973. Creep of ice. In: E. Whalley, S.J. Jones, L.W. Gold (Eds.), Physics and Chemistry of Ice. Royal Soc. of Canada, Ottawa, pp. 320-337.

Wegmann, M., 1998. Frostdynamik in hochalpinen Felswänden am Beispiel der Region Jungfraujoch - Aletsch., Zürich.

Wegmann, M., Gudmundsson, G.H., 1999. Thermally induced temporal strain variations in rock walls observed at subzero temperatures. In: K. Hutter, Y. Wang, H. Beer (Eds.), Advances in Cold-Region Thermal Engineering and Sciences. Lecture Notes in Physics. Springer Berlin, Heidelberg, pp. 511-518.

Wegmann, M., Gudmundsson, G.H., Haeberli, W., 1998. Permafrost Changes in Rock Walls and the retreat of alpine glaciers: a Thermal Modelling Approach. Permafrost and Periglacial Processes 9, 23-33.

Weisbrod, N., Dragila, M.I., 2006. Potential impact of convective fracture venting on salt-crust buildup and ground-water salinization in arid environments. J. Arid. Environ. 65, 386-399.

Weisbrod, N., Dragila, M.I., Nachshon, U., Pillersdorf, M., 2009. Falling through the cracks: The role of fractures in Earth-atmosphere gas exchange. Geophysical Research Letters 36.

Wettlaufer, J.S., Worster, M.G., 1995. Dynamics of premelted films - frost heave in a capillary. Physical Review E 51, 4679-4689.

Whalley, W.B., 1974. The mechanics of high-magnitude low-frequency rock failure. Reading Geographical Papers 27.

Whalley, W.B., 1984. Rockfalls. In: D. Brundsden, D.B. Prior (Eds.), Slope Instability. Wiley, Chichester, pp. 217–256.

Willenberg, H., Evans, K.F., Eberhardt, E., Spillmann, T., Loew, S., 2008. Internal structure and deformation of an unstable crystalline rock mass above Randa (Switzerland): Part II - Three-dimensional deformation patterns. Engineering Geology 101, 15-32.

Williams, P.J., Smith, M.W., 1989. The Frozen Earth. Fundamentals of Geocryology. Cambridge University Press, Cambridge.

Winkler, K.W., 1983. Frequency-dependent ultrasonic properties of high-porosity sandstones. J. Geophy. Res. 88, 9493-9499.

Winstral, A., Elder, K., Davis, R.E., 2002. Spatial snow modeling of wind-redistributed snow using terrain-based parameters. J. Hydrometeorol. 3, 524-538.

Wirz, V., Gruber, S., Gubler, S., Purves, R.S., 2014. Estimating velocity from noisy GPS data for investigating the temporal variability of slope movements. Nat. Hazards Earth Syst. Sci. Discuss. 2, 1153-1192.

Wirz, V., Schirmer, M., Gruber, S., Lehning, M., 2011. Spatio-temporal measurements and analysis of snow depth in a rock face. Cryosphere 5, 893-905.

Witherspoon, P.A., 2000. Inverstigations at Berkeley on Fracture Flow in Rock: From Parallel Plate Model to Chaotic Systems. In: B. Faybishenko, P.A. Witherspoon, S.M. Benson (Eds.), Dynamics of fluids in fractured rocks. American Geophysical Union, Washington D.C., pp. 1-58.

Witherspoon, P.A., 2013. Investigations at Berkeley on Fracture Flow in Rocks: From the Parallel Plate Model to Chaotic Systems, Dynamics of Fluids in Fractured Rock. American Geophysical Union, pp. 1-58.

Wohlenberg, J., 2012. 1.2 Densities of rocks. In: G. Angenheister (Ed.), Springer Materials - The Landolt-Börnstein Database (http://www.springermaterials.com).

Woodward, J., Burke, M.J., 2007. Applications of ground-penetrating radar to glacial and frozen materials. Journal of Environmental and Engineering Geophysics 12, 69-85.

Worsley, P., 2004. Periglacial Geomorphology. In: A. Goudie (Ed.), Encyclopedia of Geomorphology. Routledge, London, pp. 772-776.

Worster, M.G., Wettlaufer, J.S., 1999. The fluid mechanics of premelted liquid films. In: W. Shyy (Ed.), Fluid Dynamics at Interfaces. Cambridge Univ. Press, Cambridge, pp. 339-351.

Wyllie, D.C., Mah, C.W., 2004. Rock Slope Engineering: Civil and Mining. Spon Press, London.

Wyllie, M.R.J., Gregory, A.R., Gardner, L.W., 1956. Elastic wave velocities in heterogeneous and porous media. Geophysics 21, 41-70.

Wyllie, M.R.J., Gregory, A.R., Gardner, L.W., 1958. An experimental investigation of factors effecting elastic wave velocities in porous media. Geophysics 23, 459-493.

Yoshikawa, K., Leuschen, C., Ikeda, A., Harada, K., Gogineni, P., Hoekstra, P., Hinzman, L., Sawada, Y., Matsuoka, N., 2006. Comparison of geophysical investigations for detection of massive ground ice (pingo ice). Journal of Geophysical Research-Planets 111, E06S19.

Zangerl, C., Prager, C., Brandner, R., Brückl, E., Eder, S., Fellin, W., Tentschert, E., Poscher, G., Schönlaub, H., 2008. Methodischer Leitfaden zur prozessorientierten Bearbeitung von Massenbewegungen. Geo.Alp 5, 1-51.

Zhang, T.J., 2005. Influence of the seasonal snow cover on the ground thermal regime: An overview. Rev. Geophys. 43, RG4002.

Zimmerman, R.W., King, M.S., 1986. The effect of the extent of freezing on seismic velocities in unconsolidated permafrost. Geophysics 51, 1285-1290.